INVESTIGATING ELECTRONIC, OPTICAL AND STRUCTURAL PROPERTIES OF MATERIALS/STRUCTURES FOR OPTOELECTRONIC AND PHOTOCATALYTIC APPLICATIONS

A Thesis Submitted
In Partial Fulfillment of the Requirements for the Degree of

DOCTOR OF PHILOSOPHY

by

ASHISH RATURI
(2K19/PHDEC/15)

Under the Supervision of

Joint Supervisor	Supervisor
Dr. Sudhanshu Choudhary	**Prof. Poornima Mittal**
Instructor, SEECS, UND, USA	**Professor, ECE, DTU, India**

Department of Electronics and Communication Engineering

DELHI TECHNOLOGICAL UNIVERSITY
(Formerly Delhi College of Engineering)
Shahbad Daulatpur, Main Bawana Road, Delhi-110042. India

March, 2025

ACKNOWLEDGEMENTS

possible. Their willingness to participate and engage in meaningful discussions enriched my research and provided me with valuable data. I also express my thanks all the staff members of the department for their continuous support in our academic activities.

Lastly, I would like to thank my family for their kindness, support, and patience throughout my journey. Their belief in me has kept my spirits and motivation high during this process. Their understanding, love, and encouragement have been a constant source of motivation, and I am truly grateful for their presence in my life.

To all those who have directly or indirectly contributed to my doctoral thesis, I extend my deepest gratitude. Your support, whether big or small, has played a significant role in shaping my academic and personal growth. I am profoundly grateful for your presence in my life and for the impact you have had on my journey as a researcher.

<div align="right">

ASHISH RATURI
(Roll No. 2K19/PHDEC/15)

</div>

CANDIDATE'S DECLARATION

I **Ashish Raturi (Roll No. 2K19/PHDEC/15)** student of Ph.D., hereby certify that the work which is being presented in the thesis entitled **"Investigating Electronic, Optical and Structural Properties of Materials/Structures for Optoelectronic and Photocatalytic"**, in partial fulfillment of the requirements for the award of the Degree of **Doctor of Philosophy**, submitted in the Department of **Electronics and Communication Technology**, Delhi Technological University is an authentic record of my own work carried out during the period from **Aug 2019** to **March 2025** under the supervision **of Prof. Poornima Mittal, Professor, Department of Electronics and Communication Engineering, Delhi Technological University, Delhi, India** and **Dr. Sudhansu Choudhary, School of Electrical Engineering and Computer Science (SEECS), University of North Dakota (UND), USA**.

The matter presented in the thesis has not been submitted by me for the award of any other degree of this or any other Institute.

Date: 27-03-2025   **ASHISH RATURI**

                                                                                (Roll No. 2K19/PHDEC/15)

This is to certify that the student has incorporated all the corrections suggested by the examiners in the thesis and the statement made by the candidate is correct to the best of our knowledge.

Signatiure of Supervisor (s)   **Signature of External Examiner**

CERTIFICATE

Certified that **Ashish Raturi** (**2K19/PHDEC/15**) has carried out their search work presented in this thesis entitled **"Investigating Electronic, Optical and Structural Properties of Materials/Structures for Optoelectronic and Photocatalytic"** for the award of **Doctor of Philosophy** from Department of Electronics and Communication Engineering, Delhi Technological University, Delhi, under our supervision. The thesis embodies results of original work, and studies are carried out by the student himself and the contents of the thesis do not form the basis for the award of any other degree to the candidate or to anybody else from this or any other University/Institution.

Date: 27-03-2025

Dr. SUDHANSHU CHOUDHARY   **Prof. POORNIMA MITTAL**

Joint Supervisor   Supervisor

School of EE and CS   Department of ECE

University of North Dakota   Delhi Technological University

North Dakota, USA   Delhi, India

ABSTRACT

Perovskite and two-dimensional materials have emerged as a revolutionary class of material in optoelectronics, characterized by their remarkable light-harvesting capacity, tuneable bandgap, and high charge-carrier mobility. These materials are extensively utilized in the fabrication of solar cells, due to high power conversion efficiencies with cost effective and scalable fabrication. Their utilization in photovoltaics and optoelectronic circuits make them a potential candidate for next-generation electronic and photonic applications. The present work researches into modulating the structural, electronic, and optical properties of perovskites (LiNbO$_3$, SrTiO$_3$) and two-dimensional materials (SnS, SnSe, ZnS, ZnSe) for optoelectronic applications. This research focuses on three key techniques: doping, strain, and layering for bandgap modulation of the materials and subsequently improving the visible region absorption. The aim is to improve the optical properties by employing techniques doping, strain, and layering and making them suitable for advanced optoelectronic, photovoltaic, and solar applications.

This work investigates the electronic and optical properties of the oxide perovskites SrTiO$_3$ and LiNbO$_3$ under the influence of doping and strain by utilizing density functional theory (DFT). The pristine LiNbO$_3$ is a wide bandgap material with bandgap value of 3.56 eV, having optical absorption primarily in the UV region of optical spectrum. The hexagonal unit cell of pristine LiNbO$_3$ is doped with various metal dopants. Due to the metal doping, the bandgap of LiNbO$_3$ is reduced in comparison to the pristine cell. Specifically, the doping of plasmonic metal dopants such as gold, silver, aluminum, and copper leads to a significant reduction in the bandgap. The decrease in the bandgap is highest for silver-doped and gold-doped LiNbO$_3$ with values 2.38 eV and 2.45 eV, respectively. This shift extends optical absorption into the visible spectrum, making it more suitable for optoelectronic applications. Additionally, to investigate the impact of doping on the optical properties, the refractive index and dielectric constant are also calculated for pristine and doped structures. The dielectric constant and refractive index increase upon doping, with silver-doped LiNbO$_3$ exhibiting the highest enhancement. These findings indicate that metal-doped LiNbO$_3$ can be a promising material for applications in photovoltaics, photonic, and optoelectronics.

Likewise, pristine SrTiO$_3$, characterized by a wide bandgap of 3.20 eV, predominantly absorbs ultraviolet (UV) light within the 300–400 nm range, which limits its applicability in visible-

light-driven technologies such as photovoltaics and photocatalysis. To overcome this limitation, metal doping with plasmonic metal dopants such as Ag, Al, Au, and Cu has been employed to modify the bandgap and optical properties of $SrTiO_3$. Among these dopants, Cu has been found the most effective dopant in reducing the bandgap, lowering it to 2.0 eV, thereby extending its optical absorption into the visible spectrum (380–800 nm). Additionally, Au and Ag doping enhance visible-light absorption through surface plasmon resonance effects, improving the efficiency of light energy conversion into electronic transitions. These doping-induced modifications noticeably improve the optoelectronic performance of $SrTiO_3$, making it a highly promising candidate for applications in photocatalysis, solar cells, and other energy-harvesting technologies.

Further, Strain engineering plays a crucial role in modifying the electronic and optical properties of oxide perovskite like $SrTiO_3$ and $LiNbO_3$, enabling their application in optoelectronics and photovoltaics. The application of biaxial tensile and compressive strains on pristine $SrTiO_3$ significantly enhances its optical absorption by shifting the absorption spectrum into the visible range. Under 20% compressive strain, $SrTiO_3$ exhibited absorption peaks in the visible spectrum (380–800 nm), with a significant redshift and increased absorption intensity. Similarly, pristine $LiNbO_3$, with an intrinsic bandgap of 3.56 eV and UV-only absorption, showed remarkable improvements under strain. Application of 20% tensile strain shift its absorption into the visible range (400–800 nm), with a peak absorption coefficient of ~500 k at 600 nm. These structural modifications also resulted in enhancement in dielectric constants and refractive indices, improving light propagation and optical performance. Comparatively, unstrained $SrTiO_3$ and $LiNbO_3$ exhibited negligible absorption in the visible spectrum, underscoring the transformative impact of strain on their optical properties. These enhancements demonstrate that strain engineering not only narrows the bandgap but also expands the utility of these materials to better utilize solar energy, paving the way for advanced applications in energy and photonics.

Furthermore, the coexistence of strain and doping demonstrated an even greater effect on the optical performance of these materials. In $SrTiO_3$, doping with metals such as copper (Cu), silver (Ag), aluminum (Al), and gold (Au) introduced impurity bands that significantly reduced the bandgap. For instance, Cu-doped $SrTiO_3$ under 20% compressive strain exhibited absorption peaks throughout the visible spectrum, with an absorption coefficient of ~650 k. Similarly, for $LiNbO_3$, metal doping combined with strain yielded extraordinary improvements.

Au-doped LiNbO₃, with an initial bandgap of 1.36 eV (near the Shockley-Queisser limit), exhibited a further redshift when subjected to 20% tensile strain, enhancing visible light absorption to ~550 k. Ag-doped LiNbO₃ under 20% compressive strain also showed peak absorption values of ~650 k in the visible range, demonstrating comparable optical performance to Cu-doped structures. Additionally, Cu-doped LiNbO₃, under both compressive and tensile strains, exhibited a peak absorption intensity of ~500 k, making it another strong candidate for optoelectronic applications. These enhancements, attributed to the synergistic effects of strain and doping, position SrTiO₃ and LiNbO₃ as leading materials for photovoltaic and optoelectronic technologies.

Additionally, the two-dimensional materials, pristine monolayers of SnS, SnSe, ZnS, and ZnSe exhibit bandgaps of 1.70 eV, 1.46 eV, 2.35 eV, and 1.46 eV, respectively. The SnS and SnSe, with their relatively low bandgaps, absorb photons in the 350–600 nm range (part of the visible spectrum), while ZnS and ZnSe, with their wide bandgaps, absorb primarily in the UV range (100–300 nm) with zero visible-light absorption. The application of strain modifies their bandgaps and optical properties, enabling significant redshifts in absorption. The tensile strain of 10% reduces the bandgap of ZnSe from 1.46 eV to 0.58 eV, shifting absorption entirely into the visible region (400–700 nm). Similarly, ZnS exhibits a bandgap reduction from 2.35 eV to 1.35 eV under 10% tensile strain, with absorption extending into the visible spectrum. Strain also improves optical parameters such as the refractive index and dielectric constant, enabling efficient photon interaction and energy absorption in the visible range. These results highlight strain engineering as a versatile tool for tailoring the optoelectronic properties of 2D materials.

In this work, the formation of van der Waals heterostructures, such as SnS/SnSe, SnS/ZnS, and SnS/ZnSe, provides an additional strategy for optimizing optical absorption. For instance, combining SnS (bandgap: 1.70 eV) with SnSe (bandgap: 1.46 eV) results in a heterostructure with a reduced bandgap of 1.04 eV, shifting absorption peaks into the visible region. Similarly, SnS/ZnS and SnS/ZnSe heterostructures exhibit bandgaps of 0.6 eV and 0.9 eV, respectively, enabling complete absorption within the visible spectrum (350–650 nm). The heterostructures also demonstrate enhanced and broad optical absorption compared to individual monolayers, owing to synergistic effects from combining the properties of the constituent layers. The peaks of energy-dependent absorption coefficients for heterostructures are concentrated in the 1.0– 4.0 eV range, indicating superior absorption performance in the visible region. Furthermore,

these heterostructures exhibit improvements in refractive index and dielectric constant, essential for optoelectronic device performance.

In summary, this research work demonstrates the transformative potential of metal doping, strain engineering, and heterostructure formation in tailoring the electronic and optical properties of perovskites and 2D materials. The oxide perovskite is doped with the metal dopants and further strain is applied to tune the optical properties for optoelectronic applications. In monolayers of 2D materials the layering and strain is utilized to modulate the electronic and optical properties. The reduction in bandgap and redshifts in optical absorption induced by these modifications enable efficient visible-light absorption and energy conversion, making these materials suitable for advanced applications in photovoltaics, photodetectors, and optoelectronic devices. These findings pave the way for next-generation materials with precisely tuned properties to meet diverse technological needs.

TABLE OF CONTENTS

LIST OF TABLES

LIST OF FIGURES

List of Abbreviations

Symbol/Abbreviation	Full Form
Ag	Silver
Al	Aluminum
ATK	Atomistix ToolKit
Au	Gold
CNT	Carbon Nanotube
Cu	Copper
DFT	Density Functional Theory
DOS	Density of States
Fe	Iron
GGA	Generalized Gradient Approximation
GPa	Gigapascal
HSE	Heyd-Scuseria-Ernzerhof hybrid functional
LBFGS	Limited-memory Broyden–Fletcher–Goldfarb Shanno
LDA	Local Density Approximation
LED	Light Emitting Diode
$LiNbO_3$/ LN	Lithium Niobate
m-GGA	Meta Generalized Gradient Approximation
Mn	Manganese
Mo	Molybdenum
Ni	Nickel
PBE	Perdew–Burke–Ernzerhof

PDOS	Partial Density of States
Sn	Tin
SnS	Tin Sulfide
SnSe	Tin Selenide
SrTiO3/ STO	Strontium Titanate
TDOS	Total Density of States.
TMD	Transition-metal dichalcogenide
UV	Ultraviolet
VdW	Van der Waals
VNL	Virtual NanoLab
XC	Exchange Correlation
Zn	Zinc
ZnS	Zinc Sulfide
ZnSe	Zinc Selenide
2D	2-Dimensional

CHAPTER – 1
INTRODUCTION

Nanotechnology is a multidisciplinary field that entails the augmentation of the physical properties of materials at atomic and molecular scales, generally within the nanoscale range of 1–100 nanometers. It can facilitate the synthesis of novel materials with superior attributes, including increased strength, conductivity, and reactivity. Nanotechnology has vast applications in medicine, electronics, energy, environmental science, and optoelectronics. The perovskites have emerged as a pivotal material among the nanomaterials due to their remarkable optoelectronic characteristics. In the fields of energy conversion, flexible electronics, and environmental protection, perovskite nanoparticles have changed the way solar cells, LEDs, and sensors work by making them more efficient and cost-effective. This chapter highlights a comprehensive introduction of the nanomaterials, specifically perovskites, followed by the explanation of various properties of perovskites. Subsequently, the chapter delves into the methods used to tune the properties of perovskites for use in optoelectronic applications.

The chapter presented here is divided into eight sections. The first section provides an overview of the perovskites. Second section elaborates on the electronic and optical properties of perovskites and explains their role in optoelectronic applications. The application of density functional theory (DFT) in material chareterization is presented in third section. Fourth section discusses various techniques utilized for tuning the properties of perovskites for optoelectronic and photovoltaic applications. Subsequently, fifth section includes the problem statement derived for the research. In the section six, the objectives formulated to solve the identified technical gap during the research work are illustarated. Seventh section explains the DFT computations and the methodology used to achieve the formulated research objectives. Finally, section eight illustrates the structure of the thesis.

1.1 INTRODUCTION

In the modern era, nanomaterials are essential for societal advancement, with historical civilizations often characterized by their primary materials, such as bronze and iron [1, 2]. To achieve the technological breakthrough in the field of material science, it is essential to identify the novel materials for various applications. To foster an electronic revolution, it is critical to

deeply understand the electronic and optical properties of materials and to identify the materials with properties desired for various applications [3]. Computational modeling has become an important tool for studying the impact of changes in material properties over time and for identifying new novel materials [4, 5, 9]. It lets researchers to complete the complicated experimental processes that are hard to study using traditional lab methods with limited time frame. By systematically analyzing a wide range of possible material combinations, computational methods speed up research timelines, turning what would usually take years of experimentation into a more efficient and manageable process [6].

| (a) | (b) | (c) |
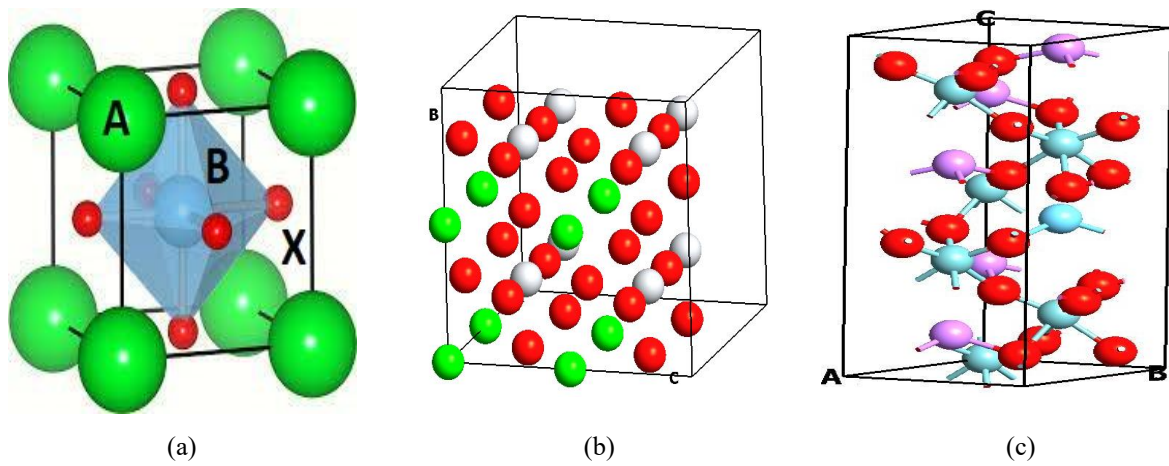
Fig. 1.1. Schematic representation of (a) Perovskite Structure, (b) $SrTiO_3$ Crystal and (c) $LiNbO_3$ Crystal.

In the broad variety of available nanomaterials, perovskite is a distinctive category of mineral defined by the crystal structure, ABX_3. Where "A" and "B" indicate cations of varying sizes and "X" denotes an anion, commonly oxygen or halogen [11]. The crystal structure of perovskite is illustrated in Fig. 1.1 (a). Most of the elements of the periodic table can be utilized at the A or B sites of perovskites, which makes perovskites exceptionally adaptable and opens up new dimensions for material discovery. Perovskites possess remarkable optoelectronic characteristics, making them suitable for a variety of applications like solar cells, light-emitting diodes (LEDs), lasers, and photodetectors [36]. The chemical composition and structural arrangement of perovskites can tune their band gap, a well-identified attribute, facilitating the optimization of their optical characteristics for particular applications. The distinctive characteristics and flexible uses of perovskites make them a critical material for research, with the capacity to propel advancements in optoelectronics and other fields.

Based on the X anion, perovskite can be classified into two categories, i.e., oxide and halide perovskite. Oxide perovskites are favored in various applications over halide perovskites due to their high stability, good thermal and environmental durability, strong chemical bonds, and

remarkable optical properties. Among the variety of available pervoskites, lithium niobate (LiNbO$_3$) is an oxide perovskite material that is known for its unique electro-optic, nonlinear optical, and ferroelectric properties. These properties make it very useful for many applications in optics and photonics. The crystalline structure of LiNbO$_3$ is depicted in Fig. 1.1 (b). Along with LiNbO$_3$, the strontium titanate (SrTiO$_3$) is a perovskite oxide that demonstrates good dielectric, ferroelectric, and optoelectronic properties (Fig. 1.1 (c)). It is the wide band gap of these two oxide pervoskites (LiNbO$_3$ and SrTiO$_3$), that restricts their absorption to the ultraviolet (UV) region of the optical spectrum only with almost zero absorption in the visible region. Despite so many advantageous properties, the limited visible region absorption due to large bandgap poses challenges for applicability of LiNbO$_3$ and SrTiO$_3$ in solar and optoelectrnic applications.

(a)	(b)	(c)	(d)
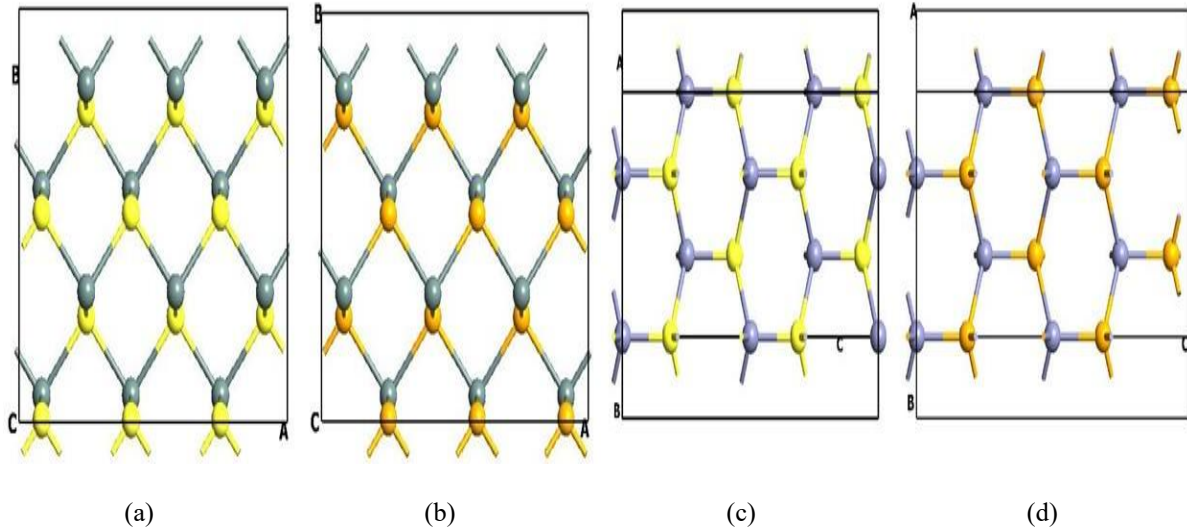
Fig. 1.2. Structure of monolayers of (a) SnS, (b) SnSe, (c) ZnS and (d) ZnSe.

In addition to bulk materials, monolayers of two-dimensional (2D) materials, including transition metal dichalcogenides (TMDs), graphene, and black phosphorus, play a vital role in various optoelectronic applications because of their distinctive features [19]. In these monolayers, the distinguished class of transition metal dichalcogenides, such as MoS$_2$ and WSe$_2$, possess direct band gaps that may be modulated by varying the layer count, making them suitable for photodetectors, LEDs, and other photonic applications. Furthermore, in the wide variety of 2D materials, the monolayers of zinc monochalcogenides (ZnS and ZnSe) and tin monochalcogenides (SnS and SnSe) are attracting the interest of researchers due to their extraordinary optoelectronic characteristics [20]. The schematic of the monolayer of SnS, SnSe, ZnS, and ZnSe are shown in Fig. 1.2. The distinctive optical and electronic properties of

these monolayers are essential for the advancement of next-generation optoelectronic devices, such as flexible displays and sophisticated solar cells, hence propelling continuous research in their manufacturing and integration. Despite having good optical properties, some of these monolayers have wide bandgaps and absorption limited only to the ultraviolet region of the optical spectrum.

1.2 ELECTRONIC AND OPTICAL PROPERTIES OF MATERIALS

Materials are important in everyday life because of their versatile structural properties. Other than structural properties, materials are significant due to their physical properties [4], including magnetic properties, thermal properties, electrical properties, electronic properties, and optical properties. To identify the novel materials for a variety of optoelectronic and photovoltaic applications, it is essential to understand the optoelectronic properties of the materials [3].

Among the various electronic properties of the material, the key property of any material is its bandgap, which decides the emission wavelengths of optical devices fabricated from the respective material. The higher the energy, the shorter the wavelength. Photodiodes and other semiconductor photodetectors fabricated from the material can have a substantial responsivity only for photon energies above the band gap energy of the materials utilized [5]. Similarly, solar cells can only utilize light with photon energies above the band gap of the materils utilized in the fabaication. Further, the band gap also determines what portion of the solar spectrum a photovoltaic cell absorbs. A semiconductor will not absorb photons of energy less than the bandgap, and the energy of the electron-hole pair produced by a photon is equal to the bandgap energy. Due to the above reasons, the bandgap plays a key role in identifying the properties of materials for various applications [9].

The changes that light undergoes upon interacting with a particular substance are known as the optical properties of that substance. The optical properties of composite materials comprise an interesting field of study, since these properties may differ significantly from those of the constituents [11]. Due to this fact, one may design materials with properties meeting a set of desirable conditions. To achieve this goal, two requirements must be met: suitable constituent materials must be found and characterized, and relationships predicting the effective optical parameters of a composite must be determined. The optical properties of the materials can be utilized in many applications, like domestic, health, astronomy, and manufacturing.

Along with electronic and optical properties, in materials, structural properties such as lattice constant and formation energy are also imprprtant to evelaute and play a crucial role in determining the performance and stability. The lattice constant measures the periodic distance between atoms in a crystal structure and significantly influences electronic and optical properties. Variations in lattice constants can lead to changes in band gap energy and carrier mobility, which are essential for deciding the efficiency of devices like light-emitting diodes (LEDs) and lasers. Further, the formation energy indicates the thermodynamic stability of a material, with lower formation energies suggesting that a material is less likely to degrade or undergo phase transitions under operational conditions. This stability is especially important in environments that expose devices to varying temperatures and conditions. By carefully optimizing lattice constants and minimizing formation energy, optoelectronic materials that exhibit superior performance and reliability can be designed.

1.3 DENSITY FUNCTIONAL THEORY FOR MATERIAL CHARACTERIZATION

Density Functional Theory, widely recognized as DFT, is a quantum mechanical approach employed on the materials to investigate various properties. The DFT is based on the traditional Kohn-Sham (KS) equation, which simplifies the many-body electron interaction by employing non-interacting electrons that replicate the actual electron density of a system. In DFT, the accuracy of the calculated results depends on the choice of the exchange-correlation (XC), functional capturing the effects of electron exchange (Pauli exclusion principle) and correlation (electron interactions) [34]. Along with exchange correlation, the choice of approximations, including the Local Density Approximation (LDA) and Generalized Gradient Approximation (GGA), plays a vital role in deciding the computational efficiency. DFT is essential in materials research for forecasting features such as conductivity, magnetism, and structural stability, facilitating material design and discovery [15, 42].

More advanced functionals, such as hybrid functionals, incorporate exact exchange from Hartree-Fock theory, while meta-GGA functionals include additional information like kinetic energy density. Beyond standard DFT, extensions like DFT+U improve the treatment of strongly correlated systems, while the GW approximation refines quasiparticle energy calculations. The accuracy of DFT strongly depends on the choice of XC functional, influencing its effectiveness in various applications, including band structure calculations,

catalysis, energy storage, and mechanical property predictions. Despite its approximations, DFT, particularly through the Kohn-Sham formalism, remains a cornerstone of modern materials science, enabling the design and discovery of new materials with tailored properties.

In the past few years, DFT has also been utilized by the researchers for forecasting the electronic and optical properties of materials. The band structure and the light interaction of the materials can be accurately computed by applying the DFT on ATK VNL. Although the exchange-correlation functional used in the initial days of DFT, i.e., LDA, faced many accuracy issues in the prediction, the discovery of accurate exchange-correlation (XC) functionals, many-body perturbation theories (e.g., GW), and machine learning (ML) allowed DFT to predict accurate results and to identify novel materials for a variety of applications. In conclusion, DFT-based methods form the foundation of contemporary computational investigations into the bandgap, absorption, dielectric, and refractive properties. Progress in hybrid functionals, many-body corrections, and machine learning-driven models persists in closing the gaps between theory and experiment. These innovations facilitate the systematic design of advanced materials for energy, sensing, and quantum and optical technologies.

1.4 TECHNIQUES FOR TUNING THE PROPERTIES OF MATERIALS

Perovskite materials demonstrate superior optoelectronic properties, and their performance can be further enhanced by using the techniques like doping, strain engineering, and layering. Doping alters the band structure by incorporating foreign atoms at the A, B, or X sites, enhancing charge transfer, stability, and absorption. Strain engineering, applied externally, modifies the lattice structure, resulting in bandgap adjustment and improved carrier mobility. Layering (heterostructuring) entails the amalgamation of perovskites with alternative materials to establish adjustable band alignment, enhance charge separation, and optimize optical absorption. These techniques provide exact regulation of perovskite characteristics, rendering them optimal for high-performance solar cells, LEDs, and photodetectors.

1.4.1 Doping for bandgap modulation of perovskite

Doping can make the electronic and optical properties of perovskites (ABX structure) much better, which makes them more useful for many optoelectronic applications. Adding foreign atoms to the A or B site of perovskite changes the bandgap and makes the charge transfer, stability, and optoelectronic properties better. The A-site doping in the perovskite primarily

influences the crystal symmetry, ionic mobility, and defect passivation. The B-site doping, on the other hand, allows bandgap engineering and improves the properties of the perovskite that is being used in optoelectronics. In the same way, halide perovskites are sometimes doped at the X site as well. This may cause a shift in absorption toward the blue spectrum, which is good for tandem solar cells.

In oxide perovskites, the doping at the O site generates an oxygen vacancy, thereby augmenting the catalytic activity and conductivity of the targeted perovskite. The doping percentage, along with the choice of doping site and type of dopant, influences how doping affects the properties of perovskites. Among the variety of dopants, the metal doping in perovskites significantly alters optical, electrical, and structural characteristics. It further improves the bandgap modulation, charge transport, and stability. The right amount of metal dopants makes perovskites more useful in photovoltaics, photocatalysis, and optoelectronics by increasing their conductivity and absorbance in the visible region.

1.4.2 Strain Engineering for perovskites

Strain engineers have become a powerful tool for modulating the optical properties of materials in recent times. The application of the strain on perovskites directly affects the electronic structure and defect dynamics. Strain can generate structural phase transitions, modifying optical absorption and emission characteristics. The type and intensity of the applied strain determine its implications. The applied tensile strain expands the lattice and typically results in a decrease in the bandgap. This untimely shift the absorption towards the visible region from the undesired ultraviolet region (redshift). Putting compressive strain on the other hand makes the lattice smaller, which increases the bandgap and moves the absorption toward shorter wavelengths (blueshift). This approach is truly advantageous for optimizing the properties of perovskite for various optoelectronic, photovoltaic, and solar applications. Additionally, the applied strain on perovskite can either enhance or suppress radiative recombination, thereby influencing the intensity of photoluminescence. Strain can also modify the defect densities and trap states, influencing carrier lifetimes. A well-thought-out strain field can reduce non-radiative recombination and boost photocarrier transmission in perovskites.

1.4.3 Layering of Tin and Zinc Monochalcogenides

The formation of heterostructures by stacking monolayers of various materials is a viable technique for enhancing optical properties and evolving novel structures for next-generation

optoelectronic applications. The monolayers of monochalcogenides of Sn and Zn, including SnS, SnSe, ZnS, and ZnSe, are extensively studied by the researchers due to their tuneable bandgap and superior optical properties. The tin monochalcogenides have considerable absorption in the visible region. However, the zinc monochalcogenides have absorption limited only to the ultraviolet region of the optical spectrum, which limits their usability in optoelectronic and photovoltaic applications. The formation of a heterostructure of SnS with SnSe, ZnS, and ZnSe results in manipulation in the bandgap, which is crucial in defining their optical absorption and emission properties. The layered architecture facilitates quantum confinement phenomena, wherein diminished dimensionality amplifies exciton binding energy, resulting in intensified light-matter interactions.

Furthermore, strain engineering in these heterostructures can adjust the bandgap by applying compressive or tensile strain, thereby successfully modifying photoluminescence emission and absorption thresholds. Furthermore, the development of heterostructures can mitigate defect states and diminish non-radiative recombination centers, resulting in enhanced luminescence efficiency. The capability for bandgap modulation in these heterostructures facilitates applications throughout a broad spectral range, from visible to infrared, rendering them appealing for telecommunications, infrared detection, and photonic integration. Another advantage is their eco-friendly and lead-free characteristics, providing a sustainable alternative to traditional optoelectronic materials. These heterostructures have superior stability relative to their constituent components, minimizing deterioration under light exposure or environmental conditions, which is essential for prolonged device operation. These enhancements render them exceptionally appropriate for sophisticated applications in photodetectors, LEDs, solar cells, and various optoelectronic technologies.

1.5 PROBLEM STATEMENT

Investigation into the structural, optical, and electronic properties of perovskites is essential for improving their acceptability for optoelectronic applications and designing the novel materials. In the wide variety of oxide perovskites, lithium niobate ($LiNbO_3$) and strontium titanate ($SrTiO_3$) are prominent members of the perovskite family largely recognized due to their extraordinary electronic and optical properties. These perovskites are extensively utilized in a variety of applications like photonics, optoelectronics, and nonlinear optics. Nonetheless, the fundamental bottleneck of $LiNbO_3$ and $SrTiO_3$ is their wide bandgap, which limits their absorption in the ultraviolet region of the optical spectrum only. The value of the direct bandgap

for LiNbO$_3$ is 3.8 eV, while it is 3.2 eV for SrTiO$_3$. Due to these wide bandgaps, the absorption is found in the lower energy ranges only (ultraviolet region). This limits the efficient utilization of LiNbO$_3$ and SrTiO$_3$ for the visible and infrared-based applications and results in diminishing their efficacy in numerous practical applications that necessitate robust absorption throughout a wider spectral range.

Specifically, in the photovoltaic and photocatalytic-based applications, the material having capabilities of absorbing only UV photons is discouraged as the UV region is only 3-5% of the entire optical spectrum. The restricted light absorption of LiNbO$_3$ and SrTiO$_3$ indicates that only a little fraction of the solar spectrum or artificial light may be utilized, making them less efficient for energy conversion applications such as solar cells, photocatalysis, and light-harvesting. Furthermore, the broad bandgap of these perovskites degrades their electrical and optoelectronic efficacy. In photodetectors and optoelectronic devices, materials having a broad absorption spectrum are favored as they can produce charge carriers under lower-energy (visible and near-infrared) illumination. To improve the visible region absorption of LiNbO$_3$ and SrTiO$_3$, bandgap engineering can be performed by using various techniques, including doping, strain engineering, and heterostructuring (layering). Doping involves incorporating foreign atoms into the perovskite lattice to introduce new electronic states, modify band edges, or induce structural changes that improve visible light absorption.

Strain engineering exploits lattice distortions to modify the electronic band structure, reducing the bandgap and enhancing optical absorption. Applying strain changes the crystal symmetry and influences orbital interactions, effectively shifting the absorption edge toward longer wavelengths. Notwithstanding these problems, LiNbO$_3$ and SrTiO$_3$ continue to be esteemed materials owing to their remarkable ferroelectric, piezoelectric, and nonlinear optical characteristics. Their application in frequency conversion, electro-optic modulation, and photonic devices remains a significant focus of study. For applications demanding high optical efficiency in the visible and infrared spectra, changes or alternative materials with reduced bandgaps are essential to enhance performance. Layering perovskites with other materials or designing heterostructures is another effective method to extend optical absorption into the visible and near-infrared regions.

By combining different materials, band alignment and charge separation properties can be optimized. The integration of monolayers of Zn and Sn monochalcogenides into heterostructures offers pathways for novel optical and electronic phenomena. Analyzing the

interfacial interactions and electronic band alignments in such systems is critical for realizing advanced devices that exploit their unique properties and thus address challenges in the field of optoelectronics.

Therefore, the overall problem addressed in this work is tuning the optical and electronic properties of perovskites by means of doping and strain. Further, the heterostructure of Zn and Sn monochalcogenides is also formed to investigate the impact of layering on optical and electronic properties. The strategies of doping, strain, and layering eventually modify the electronic structure and result in improving the visible light absorption, which ultimately enhances the performance of perovskites in optoelectronic applications.

1.6 OBJECTIVES

The main objective of this work is to tune the electronic and optical properties of materials by employing techniques like doping, strain, and layering. To evaluate the impact, firstly, the electronic and optical properties of pristine $SrTiO_3$ and $LiNbO_3$ are calculated using DFT computations. The same properties are calculated for the monolayers of ZnS, ZnSe, SnS, and SnSe. To analyze the electronic structure, the bandgap is calculated; however, the optical behavior is analyzed by calculating the optical parameters like refractive index, dielectric function, and absorption coefficient.

All the DFT computations are performed on ATK VNL with the exchange correlation functional of LDA and GGA for the calculations of electronic properties and geometry optimization. However, optical properties are calculated using meta-GGA to achieve the accuracy in the calculated result. In doping, various plasmonic dopants like Au, Ag, Al, and Cu with different doping concentrations are utilized. In strain, compressive and tensile strains of varying intensities are applied to modulate the properties for desired applications. Furthermore, the heterostructures of SnS is formed with ZnSe, SnSe, and ZnS to engineer the optical properties for optoelectronic and photovoltaic applications. To accomplish the proposed work, the following objectives are framed:

Objective 1:

Analyzing the effect of metal doping (M= Au, Ag, Cu, Al, Mn, Mo, Ni, and Fe) on electronic and optical properties of lithium niobate ($LiNbO_3$) crystal for optoelectronic applications: A First-principles Calculation.

Objective 2:

Determining the structural, electronic, and optical Properties on strontium titanate ($SrTiO_3$) crystal. Tuning the electronic and optical properties of $SrTiO_3$ through plasmonic metal doping for optoelectronic and photocatalytic applications.

Objective 3:

Investigating the structural stability of the doped $LiNbO_3$ and doped $SrTiO_3$ using formation energy. Exploring the evaluation of improved visible light absorption and photocatalytic behaviour by application of strain.

Objective 4:

Analysing the structural, electronic, & optical properties of heterostructures of metal oxides/alkali metals/2D materials and tuning their properties for optoelectronic and photocatalytic applications.

1.7 METHODOLOGY

To calculate the electronic and optical properties, the density functional theory calculations are executed on ATK VNL. Overall, the following methodology has been performed to investigate the electronic, optical, and structural properties of materials and structures and to investigate the influence of doping, strain, and layering on these properties

- The geometry of the pristine structure/layer is optimized to minimize the energy.
- Electronic and optical properties of pristine structure/layer are calculated using density functional theory.
- The crystal is modified by mean of doping/strain/heterostructure to achieve the desired properties for optoelectronic applications.
- Further the stability analysis is carried out using calculations of formation energy.
- For $SrTiO_3$ the photovoltaic behavior is also investigate using band edge alignment.

The DFT calculations are performed using a plane-wave basis set, ideal for periodic systems like crystals, via the Quantum-ATK toolkit, which specializes in simulating electronic properties. Geometry optimization employs the Perdew–Burke–Ernzerhof (PBE) version of the Generalized Gradient Approximation (GGA) for the exchange-correlation functional, utilizing

a Monkhorst-Pack sample in the Brillouin zone. The LBFGS optimization method ensures that atomic forces remain below 0.02 eV/Å and stress below 0.004 GPa. For electronic property calculations, the GGA method is applied to maintain consistency with prior research, while optical properties are assessed using the meta-GGA (TB09) approach, also employing the same k-point sampling.

For the material, a relationship among the dielectric constant (εr), response coefficients, polarizability (α), optical conductivity (σ), and susceptibility (χ) is given as:

$$\varepsilon_r = 1 + \chi(\omega) \tag{1.1}$$

$$\alpha(\omega) = V\varepsilon_0\chi(\omega) \tag{1.2}$$

$$\sigma(\omega) = -img(\omega\varepsilon_0\chi(\omega)) \tag{1.3}$$

The refractive index (η), extinction coefficient (k), and dielectric constant (εr) are related as:

$$\eta + i\kappa = \sqrt{\varepsilon_r} \tag{1.4}$$

Refractive index (η) and extinction coefficient (k) can be represented in terms of real (ε_1) and imaginary parts (ε_2) of dielectric function, as:

$$\eta = \sqrt{\frac{\sqrt{\varepsilon_1{}^2 + \varepsilon_2{}^2} + \varepsilon_1}{2}} \tag{1.5}$$

$$\kappa = \sqrt{\frac{\sqrt{\varepsilon_1{}^2 + \varepsilon_2{}^2} - \varepsilon_1}{2}} \tag{1.6}$$

Coefficient of optical absorption and coefficient of extinction are related as:

$$\alpha_a = 2\frac{\omega}{c}\kappa \tag{1.7}$$

Wavelength (λ) and photon energy (E) are related as:

$$\lambda(\mu m) = \frac{1.2398}{E(eV)} \tag{1.8}$$

The strain is applied in the biaxial directions and is defined below.

$$\varepsilon = \frac{a - a_0}{a_0} \times 100\ \% \tag{1.9}$$

In the equation given above, ao is the value of the lattice constant (relaxed and without strain) and a represents the lattice constant with strain. The positive value of ε represents the tensile strain and the negative value represents the compressive strain. Further, to investigate the structural stabilities of doped structures the total energy calculations are performed on pristine and doped SrTiO3. with the relation given below.

$$E_{Binding} = -\frac{(E_T - xE_{Sr} - yE_{Ti} - zE_O - kE_{M(Au,Al,Au,Cu)})}{x+y+z} \qquad (1.10)$$

In the equation given above ET is the computed energy, Esr is the computed energy of Sr, E is the computed energy of O, ETi is the computed energy of Ti, and Em is the computed energy of the dopant. x, y, z, k, and N are the number of atoms. The formation energy is calculated by using the equation given below.

$$E_{Formation} = -\frac{(E_{Doped} - E_{Pristine} - xE_{M(Au,Al,Au,Cu)})}{N} \qquad (1.11)$$

In the equation given above S, Epristine is the computed energy of pure crystal, and EM is the computed energy of the dopant. x and N are the total numbers of dopant atoms and the total number of atoms in the nanocrystal respectively.

1.8 THESIS ORGANIZATION

The thesis is organized into seven chapters, beginning with the first chapter dedicated to the introduction. In the second chapter, an overview of different perovskites and their properties is presented. Chapters three to six are dedicated to the four objectives identified based on the technical gaps. Finally, in chapter seven, the key findings are summarized, and the future of the work is presented. A brief overview of the contents of each chapter is as follows:

Chapter 1: Introduction

This chapter highlights the origin, structure, and electronic and optical properties of perovskites. It provides an overview of key topics covered in the thesis, including the structure of perovskites and monolayers, their electronic and optical characteristics, methods for tuning material properties, and an introduction to density functional theory. Additionally, the significance of these topics and current research trends are highlighted, offering a comprehensive foundation for the discussions that follow.

Chapter 2: Literature Review

In this chapter, a detailed literature review of the perovskites and heterostructures for optoelectronic applications is presented. The origin, structure, and properties of perovskite lithium niobate and strontium titanate are reported in the literature. Their structural, electronic properties, and optical properties are reviewed for optoelectronic-based applications. Subsequently, the impact of doping, strain, and layering on the optical and electronic properties of various materials is reviewed for optoelectronic applications. Further, a detailed review is carried out on the stability analysis of perovskites and the photovoltaic behavior of perovskites. Additionally, materials like ZnS, ZnSe, SnS, and SnSe are also reviewed, offering advantageous properties for optoelectronic applications. Heterostructures formed by stacking different monolayers combine diverse electronic and optical properties, enhancing device functionality.

Chapter 3: Metal Doping for Improving Optical Properties of Lithium Niobate

In this chapter, the structural, electronic, and optical properties of pristine lithium niobate (LiNbO$_3$) and its metal-doped variants are illustrated using first-principles Density Functional Theory (DFT) calculations. Various transition and plasmonic metals (e.g., Al, Cu, Ag, Au) are examined to determine their impact on reducing the bandgap and enhancing optical properties for optoelectronics applications. The study utilizes a hexagonal unit cell model with 40 atoms, applying a 5% doping concentration. Key findings include changes in lattice constants and significant reductions in bandgap, alongside an improvement in the optical properties.

Chapter 4: Tuning the Optical Properties of SrTiO$_3$ for Optoelectronic and Photocatalytic Applications

This chapter presents the structural, electronic, and optical properties of strontium titanate (STO) doped with plasmonic metals (Ag, Al, Au, and Cu) using density functional theory (DFT) utilizing Quantum-ATK. Doping occurs at a 5% concentration targeting titanium sites. Results show enhanced electronic and optical properties in M-STO, suggesting promising applications in optoelectronics and photocatalysis, particularly in relation to water redox potential.

Chapter 5: Strain Engineering for Tuning the Optoelectronic Properties of Perovskites

This chapter focuses on the impact of compressive and tensile strain on structural, electronic, and optical properties. The pristine and doped crystal of strontium titanate ($SrTiO_3$) and lithium niobate (LiNb) is applied with the compressive and tensile strain of varying intensities (10% and 20%). Further, the impact of varying strains (compressive and tensile) on the optical and electronic properties of pristine and doped crystals is explored.

Chapter 6: Layering and Strain for Tuning the Optical Properties of Monolayers

This chapter employs density functional theory (DFT) to analyze the electronic, structural, and optical properties of monolayers of tin-monochalcogenides (SnS and SnSe) and zinc-monochalcogenides (ZnS and ZnSe). Heterostructures are formed by combining SnS with SnSe, ZnS, and ZnSe, enabling bandgap engineering to optimize absorption and shift optical properties into the visible range. The resulting SnS-based heterostructures exhibit enhanced optoelectronic characteristics, demonstrating significant potential for applications in solar cells, optoelectronic devices, and photovoltaic technologies.

Chapter 7: Conclusions and Future Scope

In this chapter, the key findings of each chapter are summarized point-by-point to explain how each objective is achieved and their key features are reiterated. In the future scope section, the different aspects that can be worked upon are highlighted. Also, different possible aspects for memory improvement are identified.

The chapters are followed by the list of publications and references. All the papers published, submitted, and in progress for the completion of this work are listed in section – List of Publications. While all the books and papers that were referred to during the study to form the basis for this work are listed in the reference section.

CHAPTER-2
LITERATURE REVIEW

This chapter focuses on perovskites and explores various techniques utilized to tune their properties for diverse applications. Among the different types, oxide perovskites, known for their wide bandgap and exceptional optical properties, are extensively reviewed based on their characteristics. The chapter presents a comprehensive literature review on perovskites, covering their origin, properties, and applications. In recent years, researchers have been actively investigating techniques to modulated the electronic and optical properties of materials. The chapter highlights key techniques such as doping, strain engineering, and layering, which play a crucial role in material modeling. As the demand for advanced materials in next-generation optoelectronics continues to grow, discovering innovative approaches for material optimization has become essential.

These techniques allow researchers to precisely tailor material properties without altering their fundamental composition. Doping introduces foreign elements into the material structure, improving electrical conductivity and optical behavior. Strain engineering manipulates lattice distortions to optimize mechanical stability and electronic properties, while layering enables better control over material interfaces, enhancing overall functionality. By varying the layers, properties like electrical conductivity, thermal resistance, and mechanical strength can be customized. Layered heterostructures, especially in 2D materials, allow for quantum effects that enable novel functionalities.

This chapter is divided into eleven sections, each covering a distinct aspect of perovskite materials. It begins with an introduction in section one, followed by second section, which elucidate the evolution of perovskites. Section three discusses the crystal structure of perovskites, while section four explains the crystal stability of perovskites, while Section five explains their key properties. Section six highlights the use of Density Functional Theory (DFT) in assessing material characteristics, and Section seven illustrate the effects of doping on the electronic and optical properties of perovskites. The influence of strain on these properties across various materials is explained in Section eight. Section nine explores layering and heterostructures as a means to modulate the bandgap and absorption characteristics of bulk

and layered materials. Section ten reviews the diverse applications of perovskites, and finally, Section eleven identifies technical gaps in the field based on the literature review.

2.1 INTRODUCTION

The last few decades played a vital role in the evolution of nanotechnology and flourished it to a large extent. Nowadays, many types of research are being carried out by the researchers in the field of nanotechnology. The advancement in the field of nanotechnology in the past few decades is mainly concentrated on developing the crystal of nanomaterial, synthesis and characterization, and further augmentation in the size and shape of the synthesized nanomaterial at the nanoscale for desired characteristics [1, 9, 10]. In the field of material science, the word nano is taken from the Greek word nanos or the Latin word nanus. The meaning of nanos or nanus is dwarf, which is a mixture of chemistry, physics, solid state, and material science [2]. The study of nanomaterials involves the study of physics, chemistry, and its derived field, material science, and solid state [3]. Nanoscience study also involves the understanding of the arrangement of atoms in the materials and the synthesis of the novel materials along with characterization [4, 13].

In the past few decades, the advancement in the field of nanotechnology gained the attention of the industry and is responsible for the widespread use of nanotechnology in the manufacturing of optoelectronic devices [5-7]. The nanotechnology evolved with the vast applications in engineering, environment, electronics, and defense [8, 14]. Even though a lot of advancement has happened in nanotechnology in the past few years, there is still a scope in identifying the new novel nanomaterials for various applications. By seeing the ongoing development in the field of nanotechnology, it can be anticipated that in the upcoming years, the devices based on nanotechnology will control the living environment and communication [11, 12]. This increases the interest of the research community to elaborate on the topics of nanotechnology in detail.

The fundamental element of the nanotechnology is the nanomaterial, used for the fabrication of various electronic and optical devices for potential applications [15, 16]. The materials having crystals with a size less than 100 nm and with at least one dimension are considered nanomaterials [22-24]. The fundamental characteristics of the nanometers are primarily decided by the arrangement of the atoms and the shape and size of the material. Advantageously, the nanomaterials are capable of producing new characteristics and properties

by modification in the arrangement of atoms and the shape and size of the material at the nanoscale [25, 26]. Largely, all the nanomaterials can be classified in the category of nanosheets, nanoparticles, nanotubes, and nanorods based on the shape of the nanomaterial. Additionally, the classifications of the nanomaterials can also be carried out based on their dimensionality [27, 28]. The nanoparticles, quantum dots, have zero dimension; the nanorods and nanotubes are one-dimensional; and films and layers are two-dimensional [21, 28]. The two or more may be combined to form the three-dimensional nanomaterials.

The classification of nanomaterials based on dimensionality is illustrated in Fig. 2.1. In the zero-dimensional nanomaterials, all the dimensions are in the range of nanoscale [29]. In one-dimensional nanomaterials, one dimension is in the range of nanoscale, and the other two are out of the nanoscale range [27]. In two-dimensional nanomaterials, two dimensions are in the range of nanoscale, and one is out of the nanoscale range. In three-dimensional nanomaterials, all the dimensions are not in the range of nanoscale (>100 nm scale) [28].
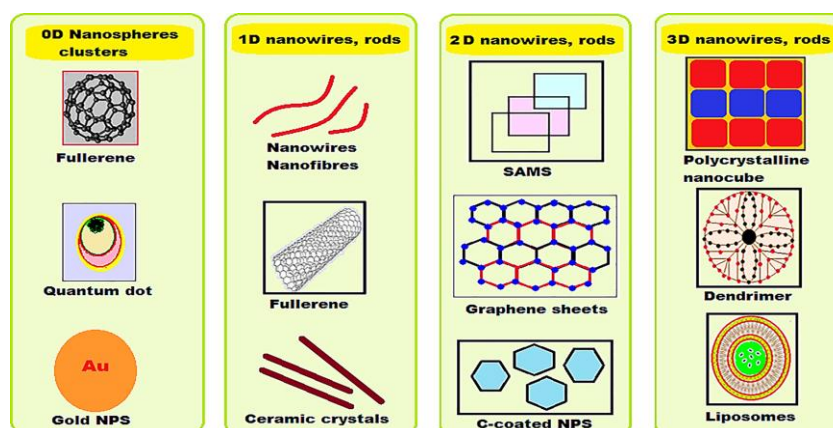
Fig. 2.1 Classification of perovskite on Dimensionality.

Nanomaterials can be further classified as carbon-based nanomaterials, semiconductor nanomaterials, polymeric nanomaterials, and metal nanoparticles based on their constitution. In the carbon-based nanomaterials, as the name suggests, the primary constituent is carbon. The carbon nanotube (CNT) and fullerenes are examples of carbon-based nanomaterials [30]. These are far stronger than the steel and are useful in the enhancement of structural properties. The CNTs are classified as single- or multi-walled and have extraordinary conductivity, electrical properties, high strength, and electron affinity [31, 32]. The metal-based nanomaterials are made of divalent and trivalent metal ions. The metal-based nanomaterials have high good absorption ability due to high surface area. The properties of metal-based nanomaterials can be changed by doping them with different elements with varying

18

constitution. Semiconductor nanomaterials have both metallic and non-metallic properties with a wide bandgap and are utilized in the fabrication of electronic and optical devices [33]. Oxides, sulfides, and phosphates of various group II-VI and group III-V elements come under semiconductor nanomaterials.

In recent decades, semiconductor graphene nanocomposite has evolved as a promising candidate for the fabrication of electronic and optical components [34]. Along with the above nanomaterials, the nanocomposite has a high value of surface to volume, which is advantageous for many applications. Among the available nanomaterials, there is a superior class of materials, known as Perovskite having chemical composition like calcium titanate ($CaTiO_3$), identified in 1939 by Gustavus Rose mineralogist of University of Berlin, in the Ural Mountains of Russia [35]. The schematic of the perovskite is shown in Fig. 2.2. The mineral was named after the renowned noble man Russian mineralogist Lev Perovski and is found in Russia, and various geographical locations like Arkansas, Italy, and Switzerland [36, 37].

2.2 EVOLUTION OF PEROVSKITES

Perovskites have emerged as transformative materials in modern technology, combining exceptional optoelectronic properties with versatile fabrication techniques. Known for their high-efficiency light-harvesting capabilities, they have revolutionized solar energy by enabling ultra-thin, flexible panels and tandem cells that surpass traditional efficiency limits. Their rapid development underscores a paradigm shift in renewable energy and next-generation optoelectronics, blending performance with adaptability for a brighter technological future. Past studies revealed that the elements with a perovskite structure have excellent physical, electronic, chemical, and optical properties like a high absorption coefficient, high mobility, and a high carrier lifetime, which make them suitable for optoelectronic applications [38].

They also identified good photocatalytic, magnetic, thermoelectric, and dielectric behavior along with excellent chemical and thermal stability [39]. Because of their unique qualities, perovskite materials are very appealing for a range of optoelectronic and photovoltaic device applications. Due to their remarkable light absorption, adjustable bandgaps, and high charge-carrier mobilities, solar energy technologies have advanced significantly. Examples of these developments include the creation of flexible, ultra-thin panels and tandem cells that outperform conventional efficiency thresholds. [40].

One of the predominating applications of perovskites is in the fabrication of light-harvesting devices, such as photodetectors [41]. The creation of high-performance photodetection systems has been made easier by perovskite materials' effective ability to transform incident photons into free charge carriers. They are effective in photodetection applications because of their remarkable optoelectronic characteristics, which include long carrier diffusion lengths and high absorption coefficients [42]. Along with the utilization in the fabrication of photodetectors, perovskites are also widely utilized in the fabrication of devices for various optoelectronic applications, including light-emitting diodes and optical sensors [43]. Beyond optoelectronics, perovskites have also proved great potential in sensing applications due to their exceptional structural characteristics and excellent sensing performance towards diverse chemical and biological species, both in solid and solution states.

The extraordinary optical, electronic, physical, structural, and chemical properties of the perovskites make them broadly acceptable and highly versatile in the fabrication of a variety of devices in the modern era. The versatility of perovskites is further highlighted by their ability to be modified through phase, dimension, composition, and geometry [44]. These modifications allow perovskites to be customized for particular uses, improving their functionality in a range of optoelectronic devices. This allows researchers to tune their properties to meet the specific requirements of various applications, unlocking a wide range of possibilities for the future of perovskite-based technologies. However, the large bandgap of perovskites limits their usability for optoelectronics applications. Due to wide bandgap of perovskites, they can only absorb the light of low wavelength in the ultraviolet region, which limits their optoelectronic efficiency [35].

In recent times, there were several reviews conducted to elucidate the applicability of perovskite structures in optoelectronic applications [40, 42, 45]. Elangovan *et al.* [46] in 2019 examined the characteristics, production, and classification of perovskites with an emphasis on their uses in photovoltaics, biological sensing, and catalysis. A thorough review of perovskite applications, such as solar cells, LEDs, photodetectors, lasers, and new neuromorphic devices, was given by Zhang *et al.* [40] in 2023 highlighted stability enhancements and material engineering breakthroughs for commercialization. Fu *et al*. [43] in 2017 discussed the synthesis techniques, photophysical characteristics, and optoelectronic applications of perovskite nanocrystals and highlighted their adjustable emission and high photoluminescence quantum yield for lasers and LEDs.

Chouhan *et al.* [47] performed an extensive review on the synthesis, optoelectronic characteristics, and uses of halide perovskites. They investigated diverse synthesis techniques for these materials, highlighting the impact of halide content on their bandgap and optical properties. The research emphasized the capabilities of halide perovskites in high-efficiency solar cells, luminous LEDs, and lasers. It has been concluded in the past studies that the optical properties of perovskite are completely dependent on their electronic structure, which significantly varies due to its dependency on surface atoms.

2.3 PEROVSKITE: CRYSTAL STRUCTURE AND CATEGORIZATION

Perovskite is a very unique class of material with exceptional structure and chemical composition, which differentiates it from other materials. The extraordinary properties of the composition of perovskites make them suitable for a wide range of applications. The perovskites are identified with the composition ABX_3, where A is the representation of a large cation and B represents a metal cation [35, 36, 47]. X is a representation of an anion, which is either a halide ion or oxygen. The unique and versatile composition of perovskites makes it suitable for a variety of applications [38, 40, 45].

In this section, the basic structure and properties of perovskites are described. The focus is on the various properties of perovskites illustrated in the previous research. In perovskite, where there is a presence of a cubical structure of A, B, and X sites [35, 38, 45, 47]. The B site and X site of perovskite form an octahedron with one B atom surrounded by the six A atoms [39]. A site is located in the octahedra and maintains the charge neutrality. The idea of a cubic structure of perovskite can be transformed to tetragonal, orthorhombic, or rhombohedral phases due to variation in the structure and properties of A, B, and X sites.

Based on the type of A site, B site, and X ion, perovskite can be broadly categorized into organic-inorganic hybrid perovskite, inorganic perovskites, and oxide perovskites [48, 49]. The organic-inorganic hybrid perovskite has either organic or inorganic elements on the A and B sites. Due to their high absorption coefficient and tunable bandgap, they have promising applications in optoelectronics and photovoltaics [50]. The common example of hybrid perovskite is methylammonium lead iodide ($MAPbI_3$), where the organic cation is methylammonium ($CH_3NH_3^+$) and the inorganic component is lead iodide (PbI_3).
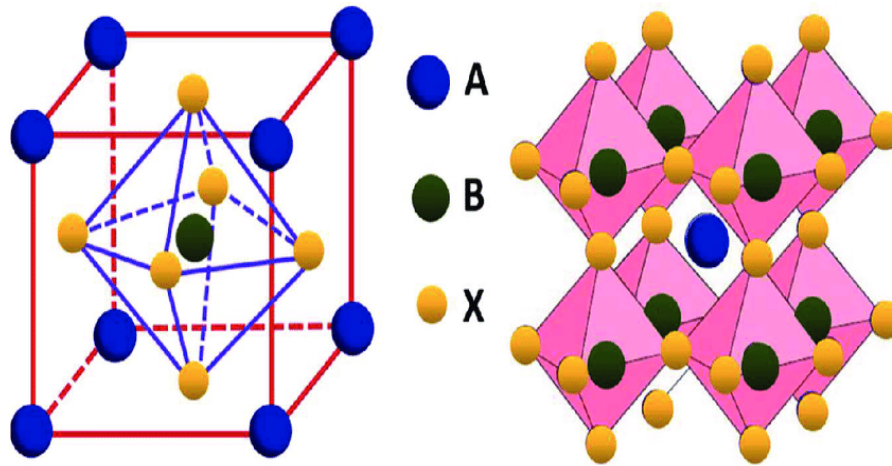
Fig. 2.2 Crystal structure of the unit cell perovskite.

Egger *et al.* [50] in 2016 investigate the dynamic structural effects of hybrid organic-inorganic perovskites (HOIPs) and their influence on optoelectronic properties and applications. HOIPs have remarkable semiconducting and light-absorption properties, rendering them suitable for photovoltaics, LEDs, and various optoelectronic devices. The research emphasizes the structural adaptability of HOIPs, wherein substantial molecular and octahedral reconfigurations affect charge transfer, carrier lifetimes, and optical absorbance. In inorganic perovskite, the A-site cation is an inorganic ion like cesium (Cs^+). The inorganic perovskites have excellent thermal stability and are utilized for applications with the requirement of robust operational performance [51].

Tai *et al.* [52] in 2019 examine the structural and compositional characteristics of inorganic perovskites, specifically $CsPbX_3$ (X = Cl, Br, I). The paper underscores the stability advantage of cesium-based perovskites compared to hybrid organic-inorganic variants, accentuating their resilience to moisture and temperature deterioration. The research investigates halide variation and doping techniques to modify optical characteristics, augment charge transport, and extend device lifespan.

On the other hand, in the oxide and halide perovskites, the X anion is always oxygen or halogen (chlorine, bromine, or iodine), respectively [35, 53]. The $CaTiO_3$, $SrTiO_3$, and $LiNbO_3$ are examples of the oxide perovskites. $MAPbI_3$, $CsPbI_3$, and $CsSnBr_3$ are examples of hailed perovskites. This section summarizes two broad classes of perovskites: halide perovskites and oxide perovskites. Due to variation in chemical and structural characteristics of oxide and halide perovskite, there is variation in the optoelectronic properties. The halide perovskite has

high performance, but the stability is a main concern in the halide perovskites. On the other hand, the oxide perovskites have stable structures with wide bandgaps.

Table 2.1 Properties and applications of halide and oxide perovskites.

S. No.	Property/Application	Oxide Perovskites	Halide Perovskites
1.	Band Gap	Wide (>2.5 eV), limiting solar efficiency	Narrow (1.2 to 2.3 eV), ideal for photovoltaics and LEDs
2.	Absorption Coefficient	Generally lower than halides	High (~10^5 cm^{-1}), excellent for light absorption
3.	Charge Carrier Diffusion	Often lower due to stronger electron-phonon interactions	Long diffusion lengths (>1 μm), benefiting optoelectronics
4.	Photoluminescence Quantum Efficiency (PLQE)	Lower due to higher non-radiative recombination	High PLQE, making them ideal for light-emitting applications
5.	Thermal Stability	Excellent, can withstand high temperatures	Poor, degrades under heat
6.	Chemical Stability	Stable in humid and oxygen-rich environments	Degrades in moisture, requiring encapsulation
7.	Toxicity	Lead-free and environmentally friendly	Contains toxic Pb, raising sustainability concerns
8.	Longevity	Long-lasting, suitable for industrial applications	Shorter lifespan without protective measures
9.	Processing Temperature	Requires high temperatures (~600 °C)	Processable at low temperatures (~100 °C)
10.	Fabrication Methods	Primarily solid-state reactions or vapor deposition	Solution-processed, enabling scalable and low-cost manufacturing
11.	Structural Flexibility	Difficult to modify due to rigid bonding	Highly tunable via composition and dimensionality adjustments
12.	Photovoltaics	Limited use due to wide band gap, but improving	Leading material with record efficiencies (>25%)
13.	Light-Emitting Diodes (LEDs)	Less efficient due to low PLQE	Excellent candidates for LEDs and display technologies
14.	Spintronics & Memory	Strong candidate due to ferroic properties	Limited due to soft lattices and low stability
15.	Sensors & Actuators	Highly durable, used in industrial applications	Less explored but potential exists

The compression of the properties of halide and oxide perovskite is illustrated in Table 2.1. The distinct structural and chemical characteristics of halide and oxide perovskites lead to varying functionalities. While halide perovskites excel in optoelectronic applications, their long-term stability remains a challenge. Oxide perovskites, on the other hand, offer unparalleled thermal and chemical stability, making them suitable for energy storage and electronic devices [56, 57].

2.4 PEROVSKITE: CRYSTAL STABILITY

The utilization of any material for various applications is decided by its stability. In the same way, the stability of the perovskite decides its applicability in a variety of applications. To predict the structural stability of the perovskite, the Goldschmidt tolerance factor (t) is used and is defined as below [58].

$$t = \frac{r_A + r_X}{\sqrt[2]{2} * (r_B + r_X)} \tag{2.1}$$

In the above equation, r_A, r_B, and r_X, represents the ionic radii of A, B, and X, respectively. A is the representation of the tolerance factor. The value of tolerance factor lies in the range of 0.8 to 1.0 for stable perovskite structure. In the case of halide perovskites, due to their ionic nature, stability is also determined by environmental factors such as moisture, heat, and UV radiation. For utilizing the perovskites in various optoelectronic applications, various techniques like cation and anion engineering are used to enhance stability. Cation engineering is used for improving the thermal and phase stability by replacing the organic cations with inorganic ones. In anion substitution, the mixed halides, such as Br^-/I^-, provide a balance between stability and bandgap tunability. Further, the process of additives and passivation is also used to improve the stability [58, 59]. In this process, the stability is achieved by incorporating the passivating agents to form the defects that enhance longevity.

It is evident from the previous research that the halide perovskites suffer from the stability concerns due to moisture, heat, light, and oxygen exposure [59]. The availability of the moisture results in the degradation of the material, whereas the heat changes the phase, making the halide perovskite unstable. Due to illumination, the ion migration and phase separation take place in halide perovskites and result in instability and performance degradation. However, the perovskite oxides show good stability due to their resilient crystal structure, characterized by a versatile arrangement of corner-sharing octahedra. The main reasoning behind their stability is the strong covalent bonding between their oxygen and metal cations [60]. The stable structure of oxide perovskites makes them highly suitable for high-temperature and high-frequency applications.

2.5 PEROVSKITE: ELECTRONIC AND OPTICAL PROPERTIES

To understand the fundamentals and to optimize the utilization, it is mandatory to understand various properties of perovskites like bandgap, refractive index, dielectric constant, and

absorption coefficient. The crystal structure, composition, and environmental factors play a vital role in deciding these properties. The performance of the devices fabricated from the material is directly dependent on these properties. In electronic properties, bandgap is a key factor that decides the ability of a material to absorb light and conduct electricity. It also decides the energy of the photon to jump from the valence band to the conduction band. In vast varieties of perovskites, the halide perovskites, with a bandgap in the range of 1.2 to 3 eV, can absorb the photon of high energy. The bandgap of these halide perovskites can be modified through compositional changes.

This is evident from the previous research that the bandgap of perovskites can be tuned by replacing a cation or anion with some other element. In optical properties, the refractive index also plays a vital role in deciding the usability of perovskites for optoelectronic applications. The refractive index of any material is an indication of its interaction with light and ultimately decides its reflection and refraction behavior. It is evident from the past studies that the halide perovskites have a high value of refractive index, generally greater than 2. The previously reported values of electronic and optical properties of various halide and oxide perovskites along with their absorption are tabulated in Table 2.2.

In a wide variety of perovskites, the oxide perovskites are examined by several researchers in past years for their stability, adjustable bandgaps, ferroelectric characteristics, and photocatalytic capabilities. They are essential for energy storage, optoelectronics, sensors, and superconductors, providing many uses in sustainable energy and technological devices. The study on oxide pervoskite $LiNbO_3$ highlights its wide bandgap (3.78 eV) and strong absorption in the UV-visible region (~350 nm). It exhibits high absorption coefficients (~10^5 cm^{-1}) at 4.5 eV and 3.2 eV, with a refractive index of 2.29 and a dielectric constant of 85.2. Its optical response varies with energy, peaking in the UV range, making it suitable for nonlinear optics and photonic applications [61, 69, 77].

The Chinedu et al. [63] performed calculations to analyze the electrical, structural, elastic, and optical characteristics of cubic $SrTiO_3$ perovskite, utilizing the Bagayoko-Zhao-Williams (BZW) technique inside the generalized gradient approximation (GGA) framework. A significant finding was the forecast of an indirect band gap of 3.24 eV at the experimental lattice constant (3.91 Å) and 3.21 eV at the calculated equilibrium lattice constant (3.92 Å), which corresponds closely with experimental outcomes. The direct band gap was determined to be 3.43 eV. It is also reported that the $SrTiO_3$ demonstrates considerable absorption at the

UV-visible threshold, with pronounced absorption at around 3.24 eV and a peak around 380 nm, rendering it suitable for ultraviolet and near-visible light applications. Nonetheless, its substantial bandgap restricts effective absorption in the visible spectrum, diminishing its efficacy for photovoltaic and photocatalytic applications.

Table 2.2 Electronic and optical properties of perovskite.

S. No.	Perovskite	Bandgap (eV)	Absorption Coefficient	Wavelength of Absorption (nm)	Refractive Index	Dielectric Constant	References
1.	LiNbO3	3.78	~10^5 at 4.5 eV	350 nm (UV-Visible region)	2.29	85.2	[61, 67, 70]
2.	BaTiO3	3.2	~10^5 at ~3.2 eV	~200-450 nm range. Peak at ~387 nm.	-	High	[62]
3.	SrTiO3	3.24	Strong absorption near 3.24 eV	380 nm (UV-Visible edge)	2.45	4.75	[63, 66, 69]
4.	KTaO3	3.57	1.8×10^5 at 5.1 eV	348 nm (UV region)	2.33	5.8	[64]
5.	MAPbI3	1.55	~1.5×10^5	750 nm (Near-Infrared)	2.5	25	[65]
6.	MAPbBr3	2.23	~1.8×10^5	550 nm (Visible - Green)	2.3	20	[65]
7.	CsPbBr3	2.3	~1.8×10^5	450 - 530 nm	2.3	6.1	[68, 71]
8.	CsPbI3	1.73	~1.5×10^5	600 - 700 nm	2.5	7.2	[68, 75]
9.	MAPbI3	1.55	~1.4×10^5	400 - 800 nm	2.6	7.5	[68, 71]
10.	FAPbBr3	2.2	1.7×10^5 at 2.2 eV	560 nm (Visible)	2.3	20	[71]
11.	CsSnBr3	0.614	~10^5 at ~1.75 eV	~400-800 nm range. Peak at ~700 nm	-	High	[72]
12.	LiNbO3 (0 GPa)	3.542	~10^5 at ~4.8 eV	~200-320 nm range. Peak at ~260 nm	2.3	5.3 at 0 eV,	[73]
13.	C4N2H14PbBr4	2.93	~10^5 at ~2.93 eV	~350-550 nm range. Peak at ~475 nm	-	-	[74]
14.	C4N2H14PbCl4	3.1	~9×10^4 at ~3.1 eV	~300-500 nm range. Peak at ~420 nm	-	-	[74]
15.	C5H16N2Pb2Br6	2.85	~8×10^4 at ~2.85 eV	~350-600 nm range. Peak at ~500 nm	-	-	[74]
16.	CsPbI3	1.73	~10^5 at ~1.73 eV	~400-780 nm range. Peak at ~720 nm	-	-	[75]
17.	FAPbI3	1.45	~10^5 at ~1.45 eV	~400-900 nm range. Peak at ~830	-	Enhanced	[75]

The Md. Moazzem Hossain *et al.* [67] investigates the structural, elastic, electrical, and optical properties of LiNbO₃ utilizing Density Functional Theory (DFT). It has been concluded in the

work that with a 3.54 eV band gap, high mechanical stability, and strong optical response, $LiNbO_3$ is ideal for nonlinear optics, electro-optic modulators, and photonics. $LiNbO_3$ shows strong absorption starting at ~3.40 eV with a peak at 6.02 eV, but its large bandgap limits visible light absorption, restricting its effectiveness for optoelectronic applications. In the review conducted, Liu *et al.* [76] investigated the exceptional photoelectric efficiency, elevated carrier mobility, and robust light absorption of various perovskite materials, thereby advancing solar cells, LEDs, visible light communication (VLC), and optical memristors. They emphasized the perovskite-based neuromorphic computing, encryption, and resistive switching devices, demonstrating significant potential in optoelectronics and artificial intelligence applications.

Benrekia *et al.* [64] utilized DFT and GW approximation to study the structural, electrical, vibrational, and optical characteristics of cubic $SrTiO_3$ and $KTaO_3$. They predicted lattice parameters, bulk modulus, and elastic constants accurately, matching experimental results. The band structure study showed indirect band gaps of 3.82 eV ($SrTiO_3$) and 3.57 eV ($KTaO_3$). Dielectric function analysis revealed interband transitions, including absorption peaks at 4.12 eV ($SrTiO_3$) and 4.32 eV ($KTaO_3$), mostly in the UV range. In many researchers, as illustrated above, the oxide perovskites are examined for their stability, ferroelectricity, superconductivity, and photocatalytic characteristics, rendering them advantageous in energy, electronics, and photonics.

Nonetheless, their substantial bandgap and minimal apparent absorption constrain their efficacy in solar cells and optoelectronics, necessitating bandgap engineering and defect modulation to enhance performance. Further, researchers investigate halide perovskites for optoelectronic applications owing to their low bandgap and robust visible light absorption, rendering them exceptionally efficient for light-harvesting purposes. Their absorption coefficients (~10^5 cm^{-1}) provide robust absorption in the visible band from 400 to 800 nm, encompassing the majority of the solar spectrum. This improves charge transfer and exciton dissociation, rendering them optimal for solar cells, LEDs, lasers, and photodetectors. Their adjustable bandgaps (1.2–2.3 eV) and solution processability facilitate the development of cost-effective, adaptable, and high-performance optoelectronic devices. Kholil *et al.* [72] examine the structural, optical, electrical, and mechanical properties of pristine $CsSnBr_3$ for optoelectronic applications. $CsSnBr_3$ exhibits a cubic perovskite structure characterized by a lattice value of 5.881 Å with a direct bandgap of 0.614 eV (DFT) and an experimental bandgap of 1.75 eV, rendering it appropriate for light absorption. The material demonstrates modest

absorption of visible light but possesses diminished conductivity, restricting its direct application in high-performance optoelectronic devices.

Rahaman *et al.* [74] investigated the optical characteristics of 1D molecular metal halides $C_4N_2H_{14}PbBr_4$, $C_4N_2H_{14}PbCl_4$, and $C_5H_{16}N_2Pb_2Br_6$ and found their potential use in optoelectronics. It is reported that these materials absorb strongly in the visible range and had bandgap tunability adjusted by metal halide octahedra's corner-sharing, edge-sharing, and face-sharing configurations. The presence of self-trapped excitons (STEs) in these perovskites, resulting from strong electron–phonon coupling and structural distortions, contributes to broadband photoluminescence (PL) emissions, ranging from blue to yellow.

The Sharif *et al.* [75] reviewed the current progress and advancement in perovskite solar cells. The study analyzes the optical properties of $MAPbI_3$, $CsPbI_3$, and $FAPbI_3$, investigating their absorption and charge transfer efficiency. The $MAPbI_3$ (1.53 eV) exhibits significant absorption (~550 nm) over 400-850 nm, while the $CsPbI_3$ (1.73 eV) exhibits stable absorption (~530 nm) but lower near-$FAPbI_3$ (1.45 eV) is suited for high-efficiency solar cells due to its broad absorbance (400-900 nm) and increased charge transport. The findings show that cation tweaking optimizes perovskite performance.

The above review highlights the significant potential of oxide and halide perovskites in optoelectronics, photovoltaics, and nonlinear optics. Oxide perovskites, like $LiNbO_3$ and $SrTiO_3$, offer high stability and strong optical responses but suffer from limited visible light absorption. In contrast, halide perovskites excel in light harvesting due to their tunable bandgaps and high absorption coefficients, making them ideal for solar cells, LEDs, and photodetectors. Despite their promise, challenges like stability and efficiency persist, requiring further research in bandgap engineering and material optimization for enhanced performance in energy and electronic applications.

2.6 ASSESSING MATERIAL CHARACTERISTICS

The Hohenberg-Kohn theorems and Kohn-Sham equations created a revolution in the field of Density Functional Theory (DFT) by facilitating the researchers to efficiently predict various electronic and optical properties of materials [78-80]. In the past decades, there has been a transition from the conventional experimental framework to a DFT-based theoretical setup for identifying materials for various applications [35, 63, 64, 70, 73, 77, 80]. This transition is supported by the discovery of exchange-correlation (XC) functionals and computer methods

utilized in performing the DFT computations [78]. Initially, Local Density Approximation (LDA) was utilized as XC for the calculations; however, its accuracy limits its utilization [81, 82]. Nevertheless, the discovery of Generalized Gradient Approximation (GGA), hybrid functionals, and many-body corrections (e.g., GW) has drastically improved the predictive efficacy of the DFT framework [77, 79, 80, 83]. It is necessary to calculate electronic properties like bandgap accurately for designing the novel materials for photovoltaic and optoelectronic applications.

2.6.1 BANDGAP CALCULATIONS OF MATERIALS

The DFT method has been extensively employed to determine the electronic structural characteristics of molecules and nanostructured materials. The optical properties of large nanoparticles are typically calculated by solving the classical Maxwell equations through Mie theory, the discrete dipole approximation (DDA), or the finite difference time domain technique. Numerous authors have indicated that when particle sizes fall below 5 to 10 nm or when the interstitial distance between two nanoparticles approaches the sub-nanometer scale, quantum mechanical effects predominate, rendering classical treatments of these nanoparticles ineffective.

In these cases, DFT has been widely utilized to calculate the properties of materials. It is evident from the past studies that DFT has played a pivotal role in the field of material science towards achieving experimental precision with improvements in exchange-correlation (XC) functionals. In the initial time of DFT, the LDA was utilized as an exchange-correlation functional [78, 82-84]. Though the inception of LDA was groundbreaking in the field of computational science, the estimation of the bandgap by LDA motivated researchers to discover new and accurate exchange correlation functionals [84], [85]. The authors evaluate the reliability of DFT-based Local Density Approximation (LDA) computations in comparison to Empirical Tight Binding (ETB) and Empirical Pseudopotential (EPS) approaches.

DFT simulations indicate that the bandgap in Si nanoclusters increases with size due to confinement, with LDA underestimating the bandgap by approximately 0.6 eV, necessitating quasiparticle corrections such as the GW approximation. LDA simulations for hydrogen-terminated Si nanoclusters indicate a bandgap of approximately 2.1 eV for 3 nm clusters, which is inferior to the experimental values of around 2.9 eV. Due to DFT's limitations in accurately predicting bandgaps due to self-energy errors and lack of excitonic effects, requiring GW

corrections for precise optical property estimations. Kang and Hybertsen (2010) employ DFT-LDA to compute the bandgaps of TiO_2, forecasting 2.08 eV for rutile and 1.75 eV for anatase, which considerably underrepresents the observed results. GW corrections enhance accuracy to 3.38 eV for rutile and 3.56 eV for anatase, consistent with experimental values (~3.3 eV) [86]. BSE indicates an exciton binding energy of approximately 0.13 eV, above the experimental value of around 0.03 eV.

Table 2.3 Benchmarking DFT Bandgap Predictions.

Year	Material	Bandgap Theoretical (eV)			Bandgap Experimental (eV)	Reference
		LDA	GGA	HSE		
2001	ScN	1.58	0.85	-	1.6	[87, 88]
	YN	1.09	1.15	-	-	
2012	ScN	0.79	0.88	-	0.9	[89]
2014	ZnS (Wurtzite)	2.32	2.46	-	3.91	[98]
2016	CdTe (Zinc Blende)	0.51	0.56	1.46	1.44	[99]
	HC(NH2)2PbI3 (FAPI)	1.283	1.368	2.886	1.55	
2017	CH3NH3PbI3 (MAPI)	1.321	1.401	2.448	1.6	[90]
	CH3NH3PbI3 (MAPI)	-	1.57	2.17	1.6	
2018	HC(NH2)2PbI3 (FAPI)	-	1.48	2.14	1.55	[91]
	AlAs	1.43	1.52	-	2.23	
2019	BAs	1.45	1.55	-	2.28	[92]
2019	LiFePO4	-	-	3.6	6.34	[93]
2019	FePO4	-	-	2.1	3.2	[93]
2021	CH3NH3PbI3 (MAPI)	1.321	1.401	2.448	1.6	[94]
2021	ZnO	0.79	0.83	2.46	3.4	[95]
2021	ZnO	0.79	0.83	2.46	3.4	[96]
2022	Zn-doped MgO	-	3.94	-	4.02	[97]
	BaTiO3	2	2.5	3.5	3.4	[100]
	CaTiO3	2.3	2.8	3.7	3.6	
2022	PbTiO3	1.8	2.2	3.1	3	
2024	SrTiO3	1.9	1.73	3.25	3.25	[101]

Kabita *et al.* [99] employed DFT utilizing LDA, GGA, and mBJ to investigate the bandgap and optical characteristics of CdTe. LDA/GGA underestimated band gaps, but mBJ yielded 1.46 eV, closely aligning with experimental results. The mBJ-GGA exchange correlation is employed to accurately characterize the electronic structure. Derkaoui *et al.* [101] examined

the cubic phase of $SrTiO_3$ utilizing density functional theory (DFT) with generalized gradient approximation (GGA/PBE), local density approximation (LDA), and the Coulomb interaction correction (Hubbard U). LDA/GGA underestimated bandgaps (1.73–1.90 eV), whereas DFT+U adjusted them to align with experimental values (3.20–3.25 eV). The optical qualities were contingent upon modifications in the electrical structure.

Hernández-Haro *et al.* [91] evaluated DFT functionals for the bandgaps of organic-inorganic perovskites. It has been reported that the LDA/GGA underestimated band gaps, but hybrid methods (HSE06, B3LYP) enhanced accuracy. It is also observed in the work that PBE and RPBE exhibit a compromise between accuracy and computational expense. Spin-orbit coupling and dispersion corrections influenced electronic structures. NAO-based computations surpassed plane-wave pseudopotentials.

Pela and colleagues utilized DFT (LDA, LDA-1/2, mBJ, HSE06) for InAlN nanorods. LDA underestimated bandgaps, but mBJ and HSE06 enhanced accuracy [102]. The optical properties, such as dielectric function and refractive index, were well predicted by HSE06 and mBJ, closely aligning with the results of the Bethe-Salpeter equation (BSE). Li *et al.* [100] employed DFT (LDA/GGA) and machine learning to analyze the bandgaps of oxide perovskites. LDA/GGA underestimated band gaps by around 1.5 eV. HSE06 enhanced predictions, incorporating 1 eV adjustment from valence band downshift and 0.5 eV adjustment from conduction band uplift. Machine learning adjusted DFT-GGA bandgaps with an inaccuracy of 0.16 eV.

The detail of the work done on calculations of bandgap using DFT with different exchange correlations is tabulated in Table 2.3. Each work underscores the shortcomings of LDA/GGA in predicting bandgap and optical properties, with enhancements observed from LDA and GGA to HSE. The inaccuracies in GGA and LDA opened the scope for the hybrid functionals HSE06 (Heyd-Scuseria-Ernzerhof), which combine a portion of precise Hartree-Fock (HF) into the computations. But the cost of accuracy with hybrid functional is in the form of computational time. Further computational accuracy has been improved with the utilization of Meta-GGA functionals and Tran-Blaha (TB09).

2.6.2 OPTICAL PROPERTIES OF MATERIALS

In the past few decades, DFT has also been adopted by the researchers as an essential tool for forecasting the optical properties for understanding the light interaction of the materials.

Various optical properties of materials, like absorption coefficient, dielectric constant, and refractive index, are very significant in designing the material for various optoelectronic applications such as solar cells, light-emitting diodes (LEDs), and photonic crystals. Although the exchange correlation functional used in the initial days of DFT, i.e., LDA, faced many accuracy issues in the prediction, the discovery of accurate exchange-correlation (XC) functionals, many-body perturbation theories (e.g., GW), and machine learning (ML) allowed DFT to predict accurate results. The absorption coefficient (α), an essential parameter in optoelectronics and photovoltaics, measures the intensity with which a material absorbs light at a specific wavelength. The precise forecasting of absorption is crucial for the development of solar cells, photodetectors, and light-emitting devices.

In recent decades, Density Functional Theory (DFT) and its expansions have emerged as essential instruments for estimating α, allowing researchers to connect theoretical predictions with experimental findings. For the design and discovery of novel materials, the prediction of dielectric constants and refractive indices is also essential along with the prediction of absorption. The initial DFT methods like LDA underestimate the dielectric constants due to an inadequate treatment of electron interactions. The underestimation is reduced in GGA and further improved in hybrid functionals, such as HSE06. The refractive index, which is derived from the dielectric constant ($n = \epsilon$), is enhanced by analogous methodologies. Anisotropic materials, such as layered compounds, necessitate the use of meta-GGA functionals, including SCAN or TB09, to accurately represent directional variations. The computational cost is increased by adopting the higher-order exchange correlation functionals.

Kar et al. [70] employed OLCAO-MGGA-TB09+c and OLCAO-GGA-PBES + U under the framework of density functional theory (DFT) for the calculations of optical absorption, reflectance, refractive index, and dielectric function of $LiNbO_3$. The reported bandgap was 3.79 eV, a little underestimated by LDA. Liu *et al.* [76] conducted DFT calculations that demonstrated significant light absorption, elevated photoluminescence quantum yield (PLQY), and adjustable bandgaps in perovskite materials. It is concluded that the exchange-correlation functionals influence optical transitions, with hybrid functionals such as HSE06 enhancing precision. The research highlighted the applications of perovskites in visible light communication, optical encryption, and neuromorphic computing. Alarab *et al.* [66] calculated the optical absorption and dielectric characteristics of $SrTiO_3$ by utilizing DFT and XPS/UPS methodologies. It is found in the work that the GGA underestimated the dielectric constant,

whereas HSE06 and GW yielded superior estimates of the optical gap, consistent with experimental ellipsometry results.

Table 2.4 Comparison of exchange correlation functionals of DFT.

XC Functional	Type	Description	Accuracy	Computing cost
B3LYP	Hybrid	Provides accurate predictions for geometrical, optoelectronic, and charge transfer properties of organic dyes.	Moderate (better for organic molecules than solids)	Moderate
BHandHLYP	Hybrid	Improves time-dependent DFT (TD-DFT) results for organic dyes due to higher Hartree-Fock exchange.	High for molecules, moderate for solids	High
CAM-B3LYP	Range-separated hybrid	Provides accurate optical properties, particularly for charge-transfer excitations.	High	High
LC-ωPBE	Range-separated hybrid	Yields results comparable to experimental optical data for organic dyes.	High	High
PBE	GGA	Underestimates band gaps but combined with GW gives reliable optical properties.	Low (severe underestimation of band gaps)	Low
HSE06	Hybrid	Provides accurate band gaps for many materials, improving upon standard GGA.	High	High
mBJ	Meta-GGA	Band gaps comparable to hybrid functionals like HSE06; good for optical properties of solids.	High	Moderate

It is found in all the studies that standard LDA/GGA underestimated bandgaps, altering optical transitions. However, the meta-GGA and HSE06 functionals enhanced the correlation with experimental refractive indices and second-harmonic generation characteristics, crucial for integrated optics. The challenge of maintaining the balance between computational cost and accuracy is always faced by the researchers in predicting the properties of materials. The compression of the accuracy and computational cost of different exchange correlations available with DFT is tabulated in Table 2.4 [67]. In conclusion, DFT-based methods form the foundation of contemporary computational investigations into the bandgap, absorption, dielectric, and refractive properties. Progress in hybrid functionals, many-body corrections, and machine learning-driven models persists in closing the gaps between theory and experiment. These innovations facilitate the systematic design of advanced materials for energy, sensing, and quantum technologies.

2.7 DOPING FOR TUNING THE PROPERTIES OF MATERIALS

In the past few years, doping has proved itself a key method for tuning the properties of perovskite, facilitating enhancement in their stability, bandgap, and optical absorption. Doping halide and oxide perovskites is crucial for tailoring their bandgap, optical absorption, dielectric properties, and stability for applications in solar cells, photodetectors, and photocatalysis. Due to the incorporation of dopants at various sites of the perovskite lattice, the device performance improves drastically for a variety of applications like emitting diodes (LEDs), photodetectors, and solar cells. Doping is a crucial method for modifying the optoelectronic properties of perovskite materials, facilitating improvements in their structural stability, optical emissions, and electrical attributes.

It has been observed from the available literature that by meticulously selecting various dopants with varying doping concentrations, the desired enhancements in the electronic and optical properties are attained, hence broadening the utilization of perovskites in diverse optoelectronic applications. For the optoelectronic applications, the absorption is desired in the lower energy ranges or in the visible region. It is evident from the study that doping has proven itself as an important technique for improving the visible region absorption of perovskite materials. This ultimately results in the efficient utilization of the perovskites in the fabrication of optoelectronic devices and solar cells. Due to the incorporation of dopants with optimum doping concentration, the lattice structure of perovskite adjusts proficiently and results in an enhancement in the visible region absorption.

The light-matter interaction and device performance of any material are directly influenced by the refractive index. The doping can be utilized to effectively alter the refractive index, hence improving the light interaction and optical properties. In many optoelectronic applications, the elevated refractive index enhances the light trapping, reduces the losses, and increases the absorption length. The changes in the refractive index can improve the optical efficiency and increase the brightness of the materials. The halide doping is a widely used technique for modulating the refractive index of perovskites. In optical properties, the dielectric constant is considered an essential property of the material that decides the recombination losses and charge separation. The improvement in the value of the dielectric constant directly impacts the device's performance, energy conservation, and sensitivity. The past research on material properties indicates that the introduction of any dopant in any perovskite enhances the value of the dielectric constant, improves the ability to withstand electric fields, and reduces the

recombination losses. The meticulous selection of dopant and doping concentration can modulate the dielectric constant of perovskite for a variety of applications. Overall, doping optimizes both halide and oxide perovskites, enhancing visible light absorption, bandgap tunability, photoluminescence, and electronic properties, advancing their role in next-generation optoelectronic and energy applications.

2.7.1 Tuning electronic and optical properties using doping

To examine the impact of doping the absorption, a study was published in 2014 by Joseph and Venkateswaran *et al.* [103] performing the bandgap engineering in ZnO using doping with 3d transition metal ions (Cr, Mn, Fe, Co, Ni) and investigating its effects on optical characteristics. In the work, the doping-induced alterations in the bandgap were reported, with Cr, Fe, and Ni resulting in a red shift, whereas Mn and Co-produced a blue shift. For the pure ZnO, the value of the bandgap is reported to be 3.37 eV. However, due to the doping with Fe, it was reduced to 2.09 eV, indicating a tunability. Figure 2 depicts the fluctuation in the bandgap of ZnO before and after doping with Cr, Mn, Fe, Co, and Ni.
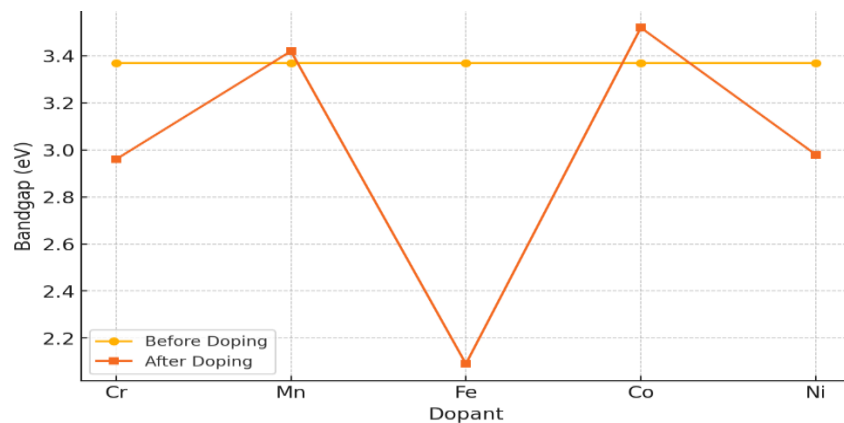
Fig. 2.3 Bandgap of ZnO before and after doping.

The unadulterated ZnO bandgap is consistently 3.37 eV, whereas doping induces considerable alterations. Fe-doped ZnO exhibits a significant drop to 2.09 eV, signifying a pronounced red shift into the visible spectrum. Doping with Mn and Co induces a blue shift, elevating the bandgap to 3.42 eV and 3.52 eV, respectively. Doping with Cr and Ni induces a mild redshift. This is due to the production of a single-phase ZnO structure due to dopants Mn and Co, while dopants Cr, Fe, and Ni led to the formation of secondary phases such as $ZnCr_2O_4$ and NiO. The investigation on optical absorption indicates that there is a shift towards the visible spectrum with dopants Cr and Ni. While Co and Mn exhibited a shift towards the ultraviolet spectrum. These alterations are the result of sp-d exchange interactions, the Burstein-Moss effect, and

polaronic interactions. The ability of bandgap and absorption alteration due to doping advocates the enhanced utility of ZnO in optoelectronics, spintronics, and magneto-optical systems. The variation of bandgap of ZnO on doping is illustrate in Fig. 2.3.

The research work conducted by Sheetal *et al.* [106] in 2014 investigates the optical characteristics of Eu-doped $CaZrO_3$ phosphor, emphasizing its bandgap, absorption, and luminescence. The pristine $CaZrO_3$ perovskite has significant UV absorption with a peak at ~279 nm, which shifts towards 576-656 nm with a strong red emission peak at 616 nm. After doing so, the bandgap remains wide, signifying a small alteration in the electrical structure of the $CaZrO_3$ perovskite. Before doping, the absorption is predominantly in the ultraviolet spectrum, which changes to the visible spectrum, especially in the red region, after doping. This transition arises from the electric dipole transition of Eu^{3+} ions, enhancing photoluminescence efficiency. The research verifies that Eu doping improves the optical response without markedly altering the bandgap, which is appropriate for display technologies, optical coatings, and LED phosphors. The material's stability and intense luminosity render it a formidable prospect for next-generation red phosphors in optoelectronic applications.

Table 2.5 Tuning electronic properties of materials using doping.

Year	Perovskite Material	Dopant(s)	Bandgap (Before Doping)	Bandgap (After Doping)	Applications	References
2011	ZnO	Cr, Mn, Fe, Co, Ni	3.37	Cr: 2.96, Mn: 3.42, Fe: 2.09, Co: 3.52, Ni: 2.98	Optoelectronics, Spintronics, Magneto-optical Devices	[103]
2012	CdS	Cu	2.5	2.2 eV (Cu-doped CdS)	Solar Cells, Photodetectors	[104]
2013	TiO2 (Anatase)	N, Ta (Co-doping)	3.2 eV	2.72 eV	Photocatalysis, environmental pollutant degradation	[105]
2014	CaZrO3	Eu	4.5	Maintained with red emission peaks	Display devices, Optical materials	[106]
2015	Mn-Fe co-doped SrTiO3	Mn, Fe	3.2 eV	Reduced	Spintronics, optoelectronics	[107]
2016	SnS Thin Films	Al	1.31 eV	Decreases to 1.20 eV (2% Al-doped)	Solar Cells, Thin-Film Photodetectors, Photovoltaics	[108]
2017	$CsPbCl_3$ Nanocrystals	Ce^{3+}, Sm^{3+}, Eu^{3+}, Tb^{3+}, Dy^{3+}, Er^{3+}, Yb^{3+}	~3.0 eV	Increases due to lattice contraction	Optoelectronics, Light-Emitting Devices, Photonic Materials	[109]

2019	Rh-doped SrTiO3	Rh	3.2 eV	Reduced.	Photocatalysis, hydrogen production	[110]
2019	Cu-doped SrTiO3	Cu	1.812 eV	1.788 eV	Photocatalysis, optoelectronics	[111]
2019	Zn-doped SrTiO3	Zn	3.2 eV	1.44 eV	Optoelectronics	[112]
2020	Subphthalocyanine (SubPc) Derivatives	Various acceptor groups (A1-A4)	2.49 eV	Y1: 2.30 eV, Y2: 2.56 eV, Y3: 2.12 eV, Y4: 2.28 eV	Organic photovoltaics	[113]
2020	Fe-doped CdS Nanostructure	Iron (Fe)	2.42 eV	2.47 eV (Spin up), 0.5 eV (Spin down)	Solar cells, optoelectronics, spintronics	[114]
2020	CdS	Sc, Ti, V, Cr, Mn	2.42 eV	Sc: 2.38 eV, Ti: 2.52 eV, V: 2.31 eV, Cr: 2.39 eV, Mn: 2.24 eV	Photovoltaics, photodetectors	[115]
2020	Monodoped and Codoped SrTiO3	Mn, N (codoped)	3.2 eV	MnTiNO: 1.94 eV, MnSrNO: 2.34 eV	Photocatalysis, water splitting	[116]
2020	SrTiO3	Ru	3.2 eV	Extended absorption up to 750 nm	Photocatalysis, hydrogen production	[117]
2020	Eu-doped LiNbO3	Eu3+	3.8 eV	Reduced	Optoelectronic devices, photonics	[118]
2021	Zn-Doped CsPbBr3	Mn	2.31 eV	2.08 eV	Photodetectors, light-emitting devices	[120]
2021	Fe2O3	Rh	2.1 eV	1.8 eV	PEC water splitting	[121]
2021	Nb-doped SrTiO3	Nb	3.2 eV	Reduced	Transparent conductive materials, photocatalysis	[122]
2023	Al-Doped Titania	Al	3.38 eV	3.18 eV	Perovskite solar cells, photoactive textiles	[124]
2023	Anatase TiO2	Au and N	3.09 eV	2.78 eV (Au), 1.71 eV (Au-N)	Photocatalysis, water splitting	[125]
2024	Bi2O3	Zn	3.96 eV	2.79 eV	Optoelectronic devices, solar cells	[126]

Kafashan *et al.* [108] in 2016 attempted to investigate the structural and optical impacts of aluminum doping on tin sulfide thin films, which were deposited using electrodeposition on fluorine-doped tin oxide substrates. The work conducted aimed to improve the characteristics of the material for solar cell and optoelectronic applications. The pristine SnS exhibits a direct bandgap of 1.31 eV, which lessened to 1.20 eV due to the doping of Al at the Sn site. X-ray diffraction (XRD) examination verified that the films maintained a polycrystalline orthorhombic structure, exhibiting enhanced crystallinity attributed to superior Sn vacancy

filling. Photoluminescence (PL) spectra exhibited a red shift with increased Al concentration, signifying alterations in the electronic structure. The UV-Vis absorption spectra indicated increased absorption in the visible spectrum (450–700 nm), with an absorption coefficient above 10^4 cm^{-1}, illustrating effective light-harvesting efficiency. Scanning electron microscopy (SEM) demonstrated a reduction in grain size and enhanced surface uniformity with elevated Al concentration.

Table 2.6 Tuning optical properties of materials using doping.

Year	Perovskite	Dopant	Absorption Before Doping	Absorption After Doping	Effect on Visible Region Absorption	References
2011	ZnO	Cr, Mn, Fe, Co, Ni	Cr: Red, Mn: Blue, Fe: Red, Co: Blue, Ni: Red	Cr: 720-525 nm; Mn: No distinct peaks; Fe: No distinct peaks; Co: ~640-530 nm; Ni: 585-515 nm	Cr, Fe, Ni: Toward Visible; Mn, Co: Toward UV. Cr: 525-720, Mn: No shift, Fe: No shift, Co: 530-640, Ni: 515-585	[103]
2012	CdS	Cu	UV Region (~300-500 nm)	Shift toward visible region. ~550 nm	Enhanced absorption in visible range. Shift toward visible region (500-550 nm)	[104]
2013	TiO2 (Anatase)	N, Ta (Co-doping)	UV region	Red-shifted into visible light 457.6 nm	Improved band alignment, enhanced photocatalytic efficiency. Enhanced photocatalytic activity	[105]
2014	CaZrO3	Eu	UV region	Strong red emission at 616 nm. 576-656 nm (red emission at 616 nm)	Strong red luminescence due to Eu doping	[106]
2015	Mn-Fe co-doped SrTiO3	Mn, Fe	UV range	Extended into visible region (Red shift). 450-650 nm	Ferrimagnetic behavior, enhanced extinction coefficient. Improved magnetic and optical properties	[107]
2016	SnS Thin Films	Al	UV-Visible (~400-600 nm)	Higher absorption in visible, extended absorption (~450-700 nm)	Increased absorption, red shift observed in photoluminescence (PL) spectra	[108]
2017	CsPbCl₃ Nanocrystals	Ce^{3+}, Sm^{3+}, Eu^{3+}, Tb^{3+}, Dy^{3+}, Er^{3+}, Yb^{3+}	UV-Visible (~270-420 nm)	Enhanced emissions from visible to near-infrared (NIR), specific peaks for each lanthanide	Increased emission efficiency, high photoluminescence quantum yield (QY)	[109]

2019	Rh-doped SrTiO3	Rh	UV region. Peak at 387 nm	Extended into visible region (red shift). 500-700 nm	Enhanced water splitting efficiency. Z-scheme water splitting, high dispersibility	[110]
2019	Cu-doped SrTiO3	Cu	UV region	Visible light absorption improved (red shift). 420-550 nm	Enhanced photocatalytic activity and photo-conductivity. enhanced electron-hole recombination	[111]
2019	Zn-doped SrTiO3	Zn	UV range	Significant red shift observed with peak at 860 nm	Improved optoelectronic properties, better conductivity	[112]
2020	Subphthalo cyanine (SubPc) Derivatives	Various acceptor groups (A1-A4)	Visible region	Enhanced absorption in visible region.	Higher efficiency in solar cells. Better charge transfer, increased dipole moments	[113]
2020	Fe-doped CdS Nanostructure	Iron (Fe)	UV-visible region (512.4 nm) (409.92 - 512.4 nm)	Enhanced absorption in visible range (502.02 nm) (401.62 - 502.02 nm)	Semiconducting nature, spin-polarized band structure, improved optoelectronic properties	[114]
2020	CdS	Sc, Ti, V, Cr, Mn	UV range	Enhanced visible absorption. 550-750 nm	Improved photocatalytic and optoelectronic properties	[115]
2020	Monodope d and Codoped SrTiO3	Mn, N (codope d)	UV range	Extended absorption in visible light. MnTiNO: 640 nm, MnSrNO: 530 nm	Enhanced charge carrier mobility and photocatalytic efficiency. Suppressed recombination, better stability	[116]
2020	SrTiO3	Ru	UV range (380 nm)	Visible light absorption up to 750 nm	Drastically improved photocatalytic activity	[117]
2020	Eu-doped LiNbO3	Eu3+	UV range (326 nm)	Enhanced red emission observed. 600-700 nm	Increased remnant polarization, enhanced optical properties	[118]
2021	ZnO Thin Films	Al	Peaks in UV region (280-350 nm). Peak at 350 nm	Extended into visible region (350-600 nm). Extended to 420 nm	Increased intensity, higher photoconductivity. Redshift observed, better UV detector response	[131]
2021	Zn-Doped CsPbBr3	Mn	Peaks in UV region, weak visible absorption (300-400 nm). Peak at 400 nm	Significant redshift. Peak shift to 470 nm. Enhanced absorption in visible range (400-700 nm).	Increased dielectric function, improved photoluminescence properties	[120]
2021	Fe2O3	Rh	500-700 nm	600-900 nm	Increased absorption, better photocurrent response	[121]

2021	Nb-doped SrTiO3	Nb	UV region	Improved visible light absorption. 400-600 nm	Enhanced photocatalytic efficiency. n-type conductivity, bandgap narrowing	[122]
2023	Al-Doped Titania	Al	UV region (< 400 nm). Peak at 380 nm	Shift to 450 nm. Shifted towards visible range (400-700 nm)	Enhanced efficiency in perovskite solar cells. Higher thermal stability, improved conductivity, better charge transport	[124]
2023	Anatase TiO2	Gold (Au) and Nitrogen (N)	UV region	Enhanced visible light absorption (446.04 nm) (356.83 - 446.04 nm)	Enhanced water splitting efficiency, reduced electron-hole recombination	[125]
2024	Bi2O3	Zn	Peak at 320 nm (UV region)	Extended into visible region, peak shift to 450 nm. Red shift observed	Higher electrical conductivity, enhanced photocatalytic efficiency	[126]

Gillani *et al.* [112] in 2019 executed the first-principles computation by utilizing density functional theory (DFT) to examine the structural, electrical, optical, and thermal characteristics of Zn-doped $SrTiO_3$ (STO). The work demonstrates that doing the STO with Zn decreases the ionic radii between Zn and Sr and ultimately reduces the unit volume. The wide bandgap of STO is 3.20 eV, which narrowed down to 1.443 eV due to Zn doping. The optical characteristics exhibited a red shift in the absorption spectrum, signifying increased visible light absorption. The values of dielectric constant and refractive index are also calculated and found to be increased due to doping. The research also demonstrated alterations in energy loss function and reflectivity spectra, indicating enhanced optical responsiveness. The observation of the research indicates that Zn-doped STO is a potential material for optoelectronic applications, such as photocatalysis, thermoelectrics, and energy storage devices.

Recent studies have advanced perovskite and oxide materials for applications in solar cells, photodetectors, and photocatalysis, building on prior research in bandgap engineering and the enhancement of optical properties. Table 2.6 illustrates the summary of the work conducted on tuning the electronic and optical properties of various materials for optoelectronic applications using doping. In the recent works, Doni Pon *et al.* [131] in 2021 demonstrated Al-doped ZnO thin films and reported the drop in the bandgap from 3.26 eV to 3.08 eV, with absorption shifting from the ultraviolet region (280-350 nm) to the visible spectrum (350-600 nm), peaking at 420 nm. Similarly, Su *et al.* [120] in 2021 doped the $CsPbBr_3$ perovskite with an Mn atom and observed the lessening of the bandgap from 2.31 eV to 2.08 eV, with absorption extending from 400 nm to 470 nm within the visible spectrum (400-700 nm). The

improvements in the dielectric function and photoluminescence are also observed, which is advantageous for light-emitting devices.

Au-doped TiO_2 (Kanoun *et al.* [125] in 2023 and Nair *et al.* [123] in 2022) demonstrates a narrowing of the bandgap from 3.09 eV to 2.78 eV, which eventually results in a shift in absorption from ultraviolet (<400 nm) to visible light (400-700 nm). Due to Au doping on TiO_2, markedly improves the charge separation, dielectric constant, and photocatalytic effectiveness for water splitting. A similar kind of effect has been reported by Alsulami *et al.* [124] in 2023 when doing the same base material TiO_2 with Al.

Recently, Khan *et al.* [126] in 2024 doped the Bi_2O_3 with zinc and experienced a reduction in bandgap from 3.96 eV to 2.79 eV, accompanied by a shift in the UV absorption peak from 320 nm to 450 nm, resulting in enhanced electrical conductivity, improved dielectric properties, and increased photocatalytic efficiency. The investigations listed in this section indicate that doping can augment the dielectric constant and relocate optical absorption into the visible spectrum, which is essential for next-generation renewable energy and optoelectronic applications. Further, improvement observed in the refractive index and dielectric characteristics due to doping can support improving the light-harvesting efficiency and charge transfer, illustrating the ongoing development of doped functional materials for more efficient and reliable energy solutions.

2.7.2 Impact of doping concentration on properties of materials

In this section, the attempt is made to collectively examine the impact of doping concentration on the optical and electronic characteristics of a variety of materials. The focus is to analyze and review the choice of dopants and their concentrations to significantly alter the properties, hence impacting their possible utilization. The summary on the impact of doping of varying concentration on the bandgap and absorption of a variety of materials is tabulated in Table 2.7. The work accomplished by Lu Yao *et al.* [127] evaluates the Ca doping on the properties of $BiFeO_3$. The impact of increasing the concentration of Ca from 0% to 20% is also evaluated. It has been reported that increasing the concentration of Ca from 0% to 20% results in widening of the bandgap from 2.18 eV to 2.36 eV. This increase is attributed to lattice distortion and modifications in the electronic structure, which limit defect states and enhance energy separation between conduction and valence bands. The widening of the bandgap is linked with the observed shift in the absorption towards low wavelengths (blue shift). This shift is the

demonstration of the reduction in the absorption of the visible light. Additionally, the refractive index decreases with increasing Ca concentration, primarily due to the reduction in grain size, which alters light propagation and material transparency.

Table 2.7 Optical properties variation due to doping concentration.

Material	Dopant	Doping percentage	Bandgap before doping	Bandgap after doping	Optical & Dielectric Properties	References
$BiFeO_3$	Ca	0.00, 0.05, 0.10, 0.15, 0.20	2.18 eV	2.18 eV (0.00), 2.19 eV (0.05), 2.23 eV (0.10), 2.35 eV (0.15), 2.36 eV (0.20)	Visible region (~570 nm). Ca doping shifts absorption to lower wavelengths.	[127]
$SrTiO_3$	La	5, 15, 25	3.2 eV	3.33 eV (5%), 3.45 eV (15%), 3.53 eV (25%)	Near UV (~387 nm). La doping reduces visible light absorption.	[128]
TiO_2	Cr	3, 6, 9, 12	3.16 eV	1.90 eV (3%), 1.63 eV (6%), 1.57 eV (9%), 1.43 eV (12%)	Enhanced visible light	[129]
$SrTiO_3$	Rh	1, 2.5, 5, 7.5, 10	3.2 eV	No significant change for x ≦ 0.05, decreases for x > 0.05	Strong absorption in visible range, additional peaks at 580 nm due to Rh states.	[130]
ZnO	Al	0, 1, 3	3.35 eV	3.18 eV (1%), 3.31 eV (3%)	Enhanced UV absorption, bandgap narrowing with Al doping.	[131]
ZnO	Mo	0, 3.125, 6.25, 12.5	3.37 eV	Varies with Mo concentration, shows Burstein-Moss shift	Increased with Mo doping, transmittance decreased.	[132]
$SrTiO_3$	V	0.5, 1.0, 1.5, 2.0	3.2 eV	2.7 eV (0.5%), 2.54 eV (1.0%), 2.29 eV (1.5%), 2.13 eV (2.0%)	Visible light extension with V doping, strong photocatalytic activity.	[133]

Similarly, Miri Choi *et al.* [128] investigated the impact of La doping on $SrTiO_3$, emphasizing how increasing the intensity of doping influences the electronic and optical properties. A significant observation was the bandgap increase from 3.2 eV to 3.53 eV, a phenomenon

explained by the Burstein-Moss effect. In this effect, the introduction of excess charge carriers (due to La doping) shifts the Fermi level, making electronic transitions require more energy, thus widening the bandgap. The increase in the bandgap shifts the absorption edges towards shorter wavelengths, reducing visible light absorption (blue shift). The values of the dielectric constant also change due to the increase of the doping concentration and modify the polarization behavior and the ability of the material to store electrical energy. These effects suggest that La doping provides a mechanism to tune $SrTiO_3$ for applications in transparent conductive oxides and optoelectronic devices.

Contrarily, the V. R. Akshay *et al.* [129] investigated the Cr-doped TiO_2, which shows a decrease in bandgap with an increase in the concentration of Cr. The bandgap is reduced from 3.16 eV to 1.43 eV for the doping concentration of 3% to 12%. The decrease is due to the formation of intermediate states within the bandgap caused by Cr doping, facilitating the improved absorption in the visible range. The improvement in the visible region absorption makes it suitable for photocatalysis applications.

Further, Borbala Kiss *et al.* [130] examined the Rh-doped $SrTiO_3$ for visible-light-driven photocatalysis by altering the concentration of Rh. Contrasting with the findings of the previous works, where the bandgap linearly changes with the doping concentration, here, the changes in properties are a nonlinear function of the Rh concentration. For the Rh concentration less than 5%, the bandgap remains unaffected and starts decreasing for the Rh concentration greater than 5%. For Rh concentrations greater than 5%, the visible region absorption is improved along with improvement in the dielectric constant. Additionally, improvements in the refractive index were also reported, which highlights the potential applicability of Rh-doped $SrTiO_3$ in environmental applications such as water purification and organic pollutant degradation.

Recent studies by Doni Pon *et al.* [131] in 202, Li *et al.* [132] in 2020, and Bantawala *et al.* [133] in 2020 have systematically explored how dopant type and concentration influence the bandgap, optical absorption, dielectric behavior, and refractive index in ZnO and $SrTiO_3$-based materials, revealing doping-dependent trends that govern material performance [119]. Doni Pon *et al.* [131] investigated the Al-doped ZnO thin films for ultraviolet photodetector applications, produced using nebulizer spray pyrolysis. Doping with aluminum altered the bandgap, initially reducing it from 3.35 eV to 3.18 eV (1% Al) before increasing to 3.31 eV (3% Al). This fluctuation indicates that modest doping improves carrier mobility, whereas

severe doping leads to defect-induced dispersion. The absorption edge migrated into the ultraviolet area, enhancing photoresponsivity.

Bantawala *et al.* [133] investigated V-doped SrTiO₃, finding that an increase in V doping decreased the bandgap from 3.16 eV to 2.13 eV (2% V), hence enhancing visible-light absorption, charge mobility, and photocatalytic efficacy. Collectively, the work tabulated in Table 2.7 and illustrated above investigates the influence of doping concentration on the engineering of the material properties. The correlation of the dopant concentration and type with the tuned properties may be beneficial for finding novel materials for a variety of applications. Further, the doping concentration and type may be utilized with other techniques like defect engineering and co-doping to further optimize the materials for advanced optoelectronic and photocatalytic applications.

2.8. STRAIN FOR TUNING THE PROPERTIES OF MATERIALS

The progress in the discovery of next-generation novel materials for various applications depends on the ability to control the electronic and optical properties of the existing materials using some external factors. Among the available techniques for tuning the properties of materials, strain engineering has evolved as a potent and flexible technique for modulating the properties by changing the atomic structure and carrier dynamics. On the application of mechanical strain, either tensile or compressive, the properties like band gaps, charge carrier mobility, optical absorption, and emission characteristics can be fine-tuned without impacting the chemical makeup of the material. In the past few years, researchers have investigated a range of materials, including semiconductors, two-dimensional (2D) materials, perovskites, and complex oxides for strain-induced changes.

The strain can drastically impact the bandgap and exciton binding energy, particularly of transition metal dichalcogenides (TMDs) for applications in flexible electronics and strain sensors. Similarly, in the past, strain tuning has been extensively used with perovskites to improve the photovoltaic and light-emitting characteristics, hence improving the solar cell efficiency. This section of the review illustrates a thorough review of the recent computational and experimental developments in strain engineering for improvement of the electrical and optical characteristics. Further, the impact of the type and intensity of the strain on the optical and electronic properties of the material is also reviewed in detail.

2.8.1 Electronic and optical property modulation using strain

Strain engineering has become a critical approach in the past many years to modify the band structure, optical response, and electrical transport characteristics of materials. In the studies conducted on strain, Mohan *et al.* [136] investigated the impact of strain on silicene for enhancements in electrical and optical characteristics. Silicene has a zero bandgap without strain; nevertheless, at a uniaxial tensile strain of 4%, a bandgap is found at 75 meV, and a compressive strain of up to 6% increases the bandgap to 389 meV. This indicates a shift in the nature of silicene from a Dirac semimetal to a tunable semiconductor due to strain. Experiments conducted for the calculations of optical absorption indicated that absorption initially peaked at 1.8 eV (~689 nm, red light) and shifted toward longer wavelengths (redshift) under tensile strain, but compressive strain resulted in a blueshift, elevating the absorption peak to higher energy. These findings indicate the potential utilization of silicene for transistors and optoelectronic applications. The work performed to examine the impact of doping on electronic and optical properties of materials is illustrated in Table 2.8.

In perovskites, Miri Choi *et al.* [128] investigated the strain-dependent alterations in carrier mobility and optical absorbance of La-doped $SrTiO_3$ thin film. The measured bandgap of La-doped $SrTiO_3$ is 3.30 eV without strain, whereas tensile strain lessened it by changing the electronic state, causing the absorption edge to shift from 375 nm (ultraviolet region) to longer wavelengths (redshift). In a similar vein, Shengxue Yang *et al.* [137] investigated the $ReSe_2$ monolayer, indicating that tensile strain reduces the bandgap from 1.36 eV to 1.28 eV at +4% strain, resulting in a shift in absorbance from 910 nm (near-IR) to 970 nm. The findings of the work conducted demonstrated noticeable polarization-dependent optoelectronic characteristics, which are advantageous for infrared photodetectors. Likewise, Hao Huan *et al.* [140] analyzed the nanowire of cadmium selenide and observed bandgap modulation upon applied strain. The bandgap reduced from 3.30 eV to 3.15 eV with +6% tensile strain, whereas -6% compressive strain resulted in a minor reduction in bandgap to 3.27 eV. The absorbance originally reached a maximum at 4.99 eV (~248 nm, deep UV), then red-shifting to 4.69 eV (~264 nm) under tensile strain.

Further, Jose Angel Silva-Guillén *et al.* [142] applied 10% tensile strain and compressive strain on monolayer TiS_3. The bandgap of TiS_3 is 1.12 eV (HSE06 corrected), which increases on application of 10% with tensile strain and reduces under compressive strain. The initial absorption peak, located at 1.8 eV (~689 nm, red light), exhibited a blueshift under tensile

strain and a redshift under compression, indicating its applicability in anisotropic photodetectors. Monolayers of Janus Ga$_2$SSe, investigated by Hamad Rahman Jappor *et al.* [144], demonstrated strain-dependent fluctuations in bandgap. The bandgap decreased from 2.04 eV to 1.42 eV under +6% strain and to 1.74 eV under -6% strain. Optical absorption, initially in the visible spectrum (~608 nm, orange-red), transitioned to the near-infrared (~870 nm) with tensile strain, whereas compressive strain maintained its visible absorption characteristics, rendering it appropriate for UV photodetectors. Tuan V. Vu *et al.* [149] investigated WSSe bilayers, in which strain prompted a semiconductor-to-metal transition.

Table 2.8 Tuning electronic and optical properties of materials using strain.

Year	Material Name	Type and Intensity of Strain	Bandgap Before (eV)	Bandgap After (eV) for each strain	Absorption Before Strain (Wavelength Range)	Absorption After Strain (Wavelength Range) for each strain	References
2012	CuAlO2	Biaxial strain (-10.71% to 9.13%)	3.9	-10.71% strain: 3.6 eV, +9.13% strain: 4.2 eV	600-1600 nm	-10.71% strain: 650-1700 nm (Red-shift), +9.13% strain: 590-1500 nm (Blue-shift)	[135]
2013	SrTiO3	Epitaxial strain	3.2	Varies with La doping and strain	Near 387 nm	350-410 nm	[128]
2014	Silicene	Uniaxial & Biaxial strain (4% to 16%)	0	4% strain: 0.075 eV, 8% strain: 0.238 eV, 12% strain: 0.335 eV	317-10600 nm	4% strain: 400-700 nm (Red-shift), 8% strain: 280-600 nm (Blue-shift)	[136]
2015	ReSe2	Local Wrinkle Formation	1.15	Wrinkle-induced strain: Red-shifted bandgap	~1078 nm	1100-1250 nm (Red-shift)	[137]
2016	LaNiO3	Tensile & Compressive Strain (-2% to -7%)	1.5	Tensile: Reduction in bandgap tendency, Compressive: Slight bandgap widening	1.5 eV (827 nm) to 5.5 eV (225 nm)	Tesnile: Shift to longer wavelengths nm) Comresive: Peaks shift higher	[138]
2016	InN	Tensile (+2%, +6%), Compressive (-2%, -6%)	0.909	Tensile (+2%): 0.926, Tensile (+6%): 0.809, Compressive (-2%): 0.829, Compressive (-6%): 0.437	1.36 μm (0.909 eV)	Tensile (+2%): 1.34 μm (0.926 eV), Tensile (+6%): 1.53 μm (0.809 eV), Compressive (-2%): 1.50 μm (0.829 eV), Compressive (-6%): 2.83 μm (0.437 eV)	[139]

Year	Material	Strain type	Bandgap	Bandgap under strain	Absorption	Absorption under strain	Ref
2017	CdSe Nanowires (D12)	Tensile (+6%) and Compressive (-6%)	3.3	Tensile (+6%): 3.15 and Compressive (-6%): 3.27	Peak at 4.99 eV	Tensile (+6%): Redshifted to 4.69 eV and Compressive (-6%): Slight redshift	[140]
2019	WS2	Uniaxial Tensile Strain (0%-4%)	1.2	0% strain: 1.2 eV, 4% strain: 1.0 eV	1.2 eV	1.94 eV (Initial), 4% strain: 1.88 eV	[141]
2018	TiS3	Compressive -1.5% and Tensile +1.5%	1.12	0.246 eV (-1.5% strain), 1.12 eV (+1.5% strain)	Absorption peaks in near-infrared (750-1000 nm)	Absorption enhancement in near-IR (800-1200 nm) under compressive strain	[142]
2019	BeO	Biaxial in-plane strain	10.6	Varies with strain (Exact values not specified)	High transparency in UV (100-400 nm) and visible (400-700 nm) regions	Shifts in absorption range, stronger UV absorption at ~250-400 nm	[143]
2019	Ga2SSe	Biaxial strain -6% to +6%	2.04	2.04 eV (0% strain), decreases gradually, direct bandgap at -2% strain	Absorption begins at visible range (~450 nm), peak in UV (~350 nm)	Compression retains visible absorption (~450 nm), tensile shifts peak to near IR (~850 nm)	[144]
2019	PbI2	Uniaxial strain -12% to +12%	2.476	2.476 eV (0% strain), increases with strain, exact values vary	Strong absorption in deep UV (below 300 nm)	Wider absorption band, improved UV absorption in 250-350 nm range	[145]
2019	Perovskite	Residual tensile strain gradient	1.55	Varies with strain, reduced in tensile regions	Absorption in visible range (400-800 nm), peak at ~600 nm	Shifts in absorption, enhanced in visible (~500-850 nm)	[146]
2019	ZrSSe	Biaxial strain from -8% to +8%	1.341	Decreases with strain, transitions to metallic at 7% strain	Strong absorption in UV (100-400 nm) and visible (~450-700 nm)	Extended absorption range, stronger absorption in UV (150-500 nm)	[147]
2020	C3N	In-plane and out-of-plane strains	0.4 (PBE), 1.05 (HSE06)	Decreases under strain, semiconductor to metal transition	Absorption in visible spectrum (~450-700 nm), peak at ~500 nm	Absorption peak shifts towards IR (~600-900 nm) under tensile strain	[148]
2020	LiNbO3	External pressure from 0 GPa to 25 GPa	3.542	3.542 eV to 2.905 eV as pressure increases	Absorption mainly in deep UV (~250-400 nm)	Red shift in absorption edge, increased absorption in UV (~200-500 nm)	[73]

2020	WSSe	Biaxial strain from -6% to +6%	Varies with stacking	Tunability under strain, semiconductor-metal transition at compressive strain	Broad absorption from visible (~450-750 nm) to near-IR (~800-1000 nm)	Transformation from anisotropic to isotropic absorption, stronger near-IR absorption (~850-1200 nm)	[149]
2022	Phosphorene	Mechanical bending	Varies with ribbon type and curvature	Non-monotonic change with curvature, reduced in armchair ribbons, increases in zigzag	Absorption peaks depend on ribbon type, initial absorption in visible range (~400-800 nm)	Armchair ribbons show blue shift (~300-600 nm), zigzag ribbons show red shift (~600-900 nm)	[150]
2023	SnSe2/MoSe2	Biaxial strain from -10% to +10%	0.167	Bandgap decreases under tensile strain, increases under compressive strain	Strong UV-Visible absorption (200-700 nm), peak near 350 nm	Enhanced UV absorption (~250-600 nm), red shift under tensile strain, blue shift under compressive strain	[151]
2024	VO2	Strain engineering from -0.71% to -0.44%	Insulating phase bandgap	Metallic transition occurs with increasing strain, reducing bandgap to near zero	Strong absorption in infrared region (~1000-1500 nm)	Increased near-IR absorption (~1200-2000 nm), enhanced optical switching properties	[152]

Additionally, Zhu *et al.* [146] examined the impact of strain on perovskite solar cells, revealing that strain improves power conversion efficiency (PCE) and adjusts the bandgap for optimal carrier transport. The bandgap before the strain was 1.60 eV; however, following tensile strain (+4%), it increases to 1.65 eV, and compressive strain (-4%) decreased it to 1.55 eV, indicating a direct association between lattice deformation and modifications in band structure. Optical absorption originally ranged from 350 nm (ultraviolet) to 750 nm (visible-red light), which shifted to longer wavelengths (~800 nm, near-infrared) on application of tensile strain, enhancing light absorption for solar energy harvesting. Conversely, compressive strain resulted in a blueshift, promoting higher-energy absorption in the infrared region. The results demonstrate that strain can boost efficiency in next-generation perovskite photovoltaics by optimizing electronic band alignment and light absorption characteristics.

In perovskites, the oxide perovskite $LiNbO_3$, examined by Gillani *et al.* [73], exhibited a bandgap reduction from 3.54 eV to 2.90 eV under external pressure, resulting in a shift of the absorption edge from 350 nm (ultraviolet) to 427 nm (violet-blue) [73]. These findings demonstrate significant pressure-induced optical responses for nonlinear photonics. Overall,

strain engineering is an effective method for altering band structure, optical absorption, and carrier transport in materials like perovskites, transition metal dichalcogenides (TMDs), Janus monolayers, and nanowires. Tensile strain decreases the bandgap and induces a redshift in absorption, hence improving the efficacy of infrared photodetectors and solar cells. Compressive strain increases the bandgap and induces a blueshift in absorption, enhancing ultraviolet detection and optical coatings. Strain generates semiconductor-to-metal transitions, shifts from direct to indirect bandgaps, and anisotropic optical absorption, facilitating adjustable optoelectronic devices and polarization-sensitive photodetectors. Furthermore, it improves dielectric characteristics and carrier mobility, which are essential for flexible electronics and transparent conductors.

2.8.2 Impact of intensity of strain on optical properties

Strain intensity significantly influences the tuning of the electronic bandgap, optical absorbance, and conductivity of materials. The impact of strain is nonlinear; lower strain values (±2% to ±4%) often induce minimal alterations in band structure, whereas greater strain values (±6% and above) can result in substantial bandgap shifts, modifications to the absorption edge, and potential semiconductor-to-metal transitions. Tensile strain typically reduces the bandgap, resulting in a redshift in optical absorption, as observed in $LaNiO_3$ at +7% strain, where the interband transition energy diminished from 1.5 eV to 0.84 eV [138].

Conversely, compressive strain generally increases the bandgap or increases metallicity, as demonstrated in ZrSSe at -7% strain, where the bandgap reduced to zero, resulting in a semiconductor-to-metal transition [146]. The optical absorption response exhibits significant variation with the intensity of strain. At low strain values (~±2%), absorption shifts are mild, influencing electronic transitions without significantly modifying conductivity. At high strain intensities (~±6% and beyond), the absorption shifts noticeably, facilitating increased infrared light absorption under tensile strain (ZrSSe at +6%) or greater UV reflectivity under compressive strain ($LaNiO_3$ at -7%) [147].

Hoat *et al.* [145] investigated PbI_2 monolayers subjected to uniaxial strain ranging from −12% to +12%, revealing a significant strain effect on the bandgap and absorption spectra. The initial bandgap of 2.476 eV decreased to 2.305 eV at -6% strain and further to 2.092 eV at -12% strain. Tensile tension, on the other hand, increased the bandgap to 2.567 eV at +6% strain and 2.645 eV at +12% strain. Optical absorption exhibited significant sensitivity to strain: under tensile

strain, the absorption experienced a redshift, whereas with compressive strain, absorption penetrated further into the ultraviolet (~4.5 eV, 275 nm). The maximum reflectivity increased from 64.74% at equilibrium to 74.29% at 6% tensile strain, rendering PbI_2 exceptionally appropriate for UV-reflective coatings and optoelectronic applications. In conclusion, high strain intensities (exceeding ±6%) induce noticeable nonlinear effects, resulting in anisotropic electronic alterations, band inversion, and increased optical conductivity. This highlights strain intensity as an efficient tool for material design, enabling the customization of optical and electronic responses for optoelectronic, sensing, and energy applications.

2.9 LAYERING FOR TUNING THE PROPERTIES OF MATERIALS

Layering in 2D materials is a powerful strategy for tuning their properties, enabling precise control over electronic, optical, and mechanical characteristics. By stacking different 2D layers or introducing interfacial modifications, researchers can engineer band structures, enhance charge transport, and optimize excitonic interactions. This approach facilitates the design of materials with tailored functionalities for applications in transistors, photodetectors, energy storage, and quantum devices. Van der Waals heterostructures, for instance, offer tuneable bandgaps, improved carrier mobility, and novel quantum effects, making layered 2D materials a promising avenue for next-generation electronic and optoelectronic technologies.

In past years, many studies are carried out to evaluate the impact of heterostructure formation on optoelectronic properties, with emphasis on optical absorption and bandgap. Huong *et al.* [155] investigated the electronic and optical properties of SnS/SnSe heterostructure, and discovered type-II band alignment alongside the improvement in visible region absorption, making the formed heterostructure potential candidate for the optoelectronic and photovoltaic applications. The absorption edge for the individual layers of SnS and SnSe are in the lower wavelengths, which are significantly shifted towards the higher wavelengths, improving the solar conversion efficiency.

Further, Salunkhe *et al.* [156] stacked the layers of TiO_2 and Bi_2S_3 to form TiO_2/Bi_2S_3 heterostructure. The work also focused on the quantum size effects and reported the improvement in the visible region absorption with shifting of the absorption edges towards lower energies (redshift). It is also reported in the study that the increase in the coverage of Bi_2S_3 reduces the bandgap, improves the photocurrent generation, confirming its acceptance in solar cells.

In the similar significant work, Maniyar *et al.* [161] in 2020 formed the heterostructure of phosphorene/transition metal dichalcogenide (TMD). The monolayer of phosphorene is stacked with MoS_2, $MoSe_2$, $MoTe_2$, WS_2, WSe_2 to form heterostructure for optoelectronic applications. The value of bandgap is 1.21 eV for phosphorene, whereas transition metal dichalcogenides exhibit a bandgap in the range from 0.47 to 1.57 eV. Due to the formation of heterostructure, the bandgap is reduced to 0.25–1.01 eV, facilitating charge separation. Further, a redshift in absorption peaks also observed from ultraviolet range (~390–430 nm) to the visible spectrum (410–780 nm), in the heterostructures enhancing solar energy efficiency. The high visible region absorption and incorporation of type-II band alignment makes these formed heterostructures significant for solar and optoelectronic applications.

Table 2.9 Tuning electronic and optical properties of materials using layering.

Structure	Bandgap Individual (eV)	Bandgap Heterostructure (eV)	Absorption Individual	Absorption Heterostructure	Referances
Au/CdSe	CdSe: 1.74	Not explicitly stated	CdSe: ~700 nm (visible region)	Enhanced absorption in visible range.	[153]
ZnO/CeO2	ZnO: 3.25, CeO2: 3.08	Decreases to 3.08 eV	ZnO: ~380 nm, CeO2: ~340 nm (UV region)	Enhanced UV absorption while maintaining high visible light transparency (~400-800 nm)	[154]
BiFeO3/ZnO	BiFeO3: 2.67, ZnO: 3.4	Direct bandgap ~0.6 eV	BiFeO3: ~465 nm, ZnO: ~380 nm (UV-visible)	Enhanced absorption in visible and terahertz regions; broad absorption in ~400-800 nm range	[155]
TiO2/Bi2S3	TiO2: 3.2, Bi2S3: 1.7	Not explicitly stated	TiO2: ~380 nm (UV), Bi2S3: ~700 nm (visible)	Enhanced visible light absorption; increased photocurrent under solar illumination	[156]
Blue Phosphorene/WSe2	BlueP: 2.39, WSe2: 1.75	1.13 (Indirect)	BlueP: ~300 nm, WSe2: ~500-750 nm	Enhanced absorption in visible region; absorption enhancement observed in ~350-600 nm range	[157]
MoS2/Hg0.33Cd0.66Te	MoS2: 1.9, Hg0.33Cd0.66Te: 0.69	Negligible indirect bandgap (semi-metallic)	MoS2: 390-430 nm; Hg0.33Cd0.66Te: 310-350 nm	Enhanced absorption in visible region; red-shift observed to ~640-710 nm	[158]
HfSe2/MoTe2	HfSe2: 1.2, MoTe2: 0.88	Type-II band alignment, bandgap ~0.65 eV	HfSe2: ~1030 nm, MoTe2: ~1400 nm	Enhanced absorption in near-infrared region, peaks at ~1100-1500 nm	[159]
SnS/SnSe	SnS: 2.89, SnSe: 2.65	1.50 (Type-II band alignment)	Absorption in visible region (~430-800 nm)	Enhanced optical absorption; suitable for water splitting and photovoltaic applications; peak absorption	[160]

				in visible range (~430-800 nm).	
TMDs/Phosphorene (MoS2/P, MoSe2/P, MoTe2/P, WS2/P, WSe2/P)	MoS2: 1.9, MoSe2: 1.55, MoTe2: 1.1, WS2: 2.1, WSe2: 1.35, Phosphorene: 0.9	Varies by combination, mostly Type-II alignment	Absorption in UV-visible range (~390-780 nm)	Redshift observed; enhanced absorption in visible region, absorption peaks shift towards ~450-750 nm.	[161]
ZnSe/AlAs	ZnSe: 2.7, AlAs: 2.01	0.986 (Direct bandgap)	ZnSe: 500-600 nm, AlAs: ~600 nm	Enhanced absorption, especially in ultraviolet region; absorption peak at ~350-450 nm.	[162]
ZnSe/AlAs/GaAs	ZnSe: 2.354, AlAs: 2.388, GaAs: 1.564	0.548 eV (Direct bandgap)	Strong absorption in UV-visible region, ZnSe ~ 527 nm, AlAs ~ 520 nm, GaAs ~ 793 nm	Stronger absorption in infrared, enhanced optical properties; peak absorption shift around ~900-1000 nm.	[163]
MoS2/ZnO	MoS2: 1.52, ZnO: 3.14	MoS2/ZnO: 1.62, ZnO/MoS2: 2.67	MoS2 ~ 815 nm, ZnO ~ 395 nm (UV-visible)	Enhanced absorption in visible range, photocurrent 7 times higher than pure ZnO; peak absorption enhancement in ~450-600 nm.	[164]
MoS2/WS2	1.93 (MoS2), 2.12 (MoS2), 1.96 (WS2), 2.44 (WS2)	Indirect bandgap at Î"-point, K-point ~1.96 eV	MoS2: 1.93 eV (~642 nm), 2.12 eV (~585 nm); WS2: 1.96 eV (~632 nm), 2.44 eV (~508 nm)	Minimal change; retains monolayer optical properties, slight absorption shifts in ~632 nm region.	[165]
SnS/SnS2	2.24 (SnS2), 1.20 (SnS)	Not explicitly stated	SnS2: 2.24 eV (~553 nm); SnS: 1.20 eV (~1033 nm)	Enhanced optical response; 7 times improvement in photoresponsivity, improved absorption in visible range (550-700 nm).	[166]

Another significant work conducted by Komsa *et al.* [165] explored the electronic and optical properties of the stacked transition metal dichalcogenide (TMD) bilayers of MoS₂ and WS₂ by forming the MoS₂/WS₂ heterostructure. The work discovered induction of type-II band alignment in the formed heterostructure with availability of valence band maximum (VBM) and conduction band minimum (CBM) in different layers. The formed MoS₂/WS₂ heterostructure demonstrate efficient charge separation, reduction in bandgap, and improved optical transitions.

Similarly, Lin *et al.* [166] formed the heterostructure from the layers of SnS and SnS₂, synthesized via chemical vapor deposition. The work indicated that the photoresponsivity is

increased to 7.31×10^{-3} A/W due to heterostructure formation with improvement in optical response and fast carrier dynamics, making it a promising candidate for photodetection applications. The absorption spectra indicate improved visible-light absorption, with peaks extending to 700 nm. This broad absorption range suggests an improved capacity to harness visible light, which is highly desirable for various technological applications. Such characteristics make these materials promising candidates for advanced photodetectors, where efficient light detection across a wide spectral range is crucial.

Collectively, these studies emphasize the potential of heterostructures in fine-tuning material properties, paving the way for high-performance electronic and photonic devices as illustrated in Table 2.9. The findings reported in the mentioned papers jointly underscore the importance of layering/heterostructure in modulating optical properties, bandgap, and absorption for various optoelectronic applications. Research indicates that stacking of materials/layers result in substantial enhancements in optoelectronic performance, rendering them advantageous for applications in solar energy conversion, photocatalysis, and photodetection.

2.10 APPLICATIONS OF PERVOSKITES

Perovskite materials, particularly lead-halide and oxide perovskites, have gained significant attention in recent years due to their remarkable structural, electronic, and optical properties. These materials exhibit high charge-carrier mobility, tunable bandgaps, excellent light absorption, and ease of fabrication, making them suitable for a wide range of applications. Their unique crystal structure allows for customization through chemical and structural modifications, enhancing their performance in various technological fields. Below are the key applications of perovskites across different industries.

2.10.1 Perovskite Solar Cells (PSCs)

In comparison to the conventional solar cells, the perovskite solar cells (PSCs) exhibit notable solar conversion efficiency greater than 25%, which makes them a potential competitor conventional silicon-based solar cell [167, 134]. The turnability of the bandgap of the perovskite allow the researchers to improve their visible region absorption to improve the light-to-electricity conversion. Further, the compatibility of perovskites with the flexible and lightweight substrates, support the fabrication of portable and wearable solar panels using perovskites. The combination of silicon with perovskite is utilized to fabricate the tandem solar

cells and solar conversion efficiency of more than 30 % is achieved, thereby improving their commercial feasibility.

2.10.2 Light-Emitting Diodes (LEDs)

Perovskite are widely accepted and emerged as a potential candidate for the fabrication of next-generation lighting and display devices. The perovskite-based LEDs (PeLEDs) offer very high photoluminescence quantum yield, adjustable emission wavelengths, and narrow absorption spectra, which makes the, prominent for the high-resolution displays, televisions, and lighting applications [168]. In contrast to the convectional semiconductors, perovskite allow the modulation of the colour, enabling the production of efficient blue, green, and red-light sources. The solution-processability of the perovskite also makes them fascinating for the large-scale manufacturing of LEDs.

2.10.3. Photodetectors and Imaging Sensors

The value of the absorption coefficients is very high for the perovskites in compression to the conventional materials. Perovskites also exhibits the excellent charge transport properties and high value of photocurrent, which make them ideal for the applications of photodetectors and imaging sensors [169]. The photodetectors are widely utilized in optical communication, security, biomedical imaging, and environmental monitoring. The photodetectors and imaging sensors fabricated by utilizing perovskites offer high sensitivity across the ultraviolet (UV) to near-infrared (NIR) spectrum, offering performance in comparison to the conventional silicon-based detectors. Their ability to be integrated into flexible and transparent substrates opens possibilities for wearable and stretchable electronic applications.

2.10.4. Perovskite-Based Lasers

In optoelectronic applications, specifically in the fabrication of Lasers, perovskites played a crucial role in past few years [170]. Their high carrier recombination rates and tuneable optical and electronic properties make them attractive for the fabrication of low-threshold, high-efficiency laser diodes. The absorption of perovskite can be tuned to the ultraviolet to near-infrared using various techniques, which facilitates the operability of perovskite-based laser across the broad spectrum. The perovskite-based lasers have applications in telecommunications, medical diagnostics, and high-speed optical computing. The perovskite-based laser can be synthesised on flexible substrates at low temperatures opens up the possibility of compact and flexible laser devices.

2.10.5. Perovskite in Energy Storage and Batteries

In addition to the application in photovoltaics, perovskites are also explored for the applications in the energy storage-based devices and batteries. The lithium lanthanum titanate (LLTO) perovskite have very high ionic conductivity favourable for the utilization in fabrication of solid-state electrolytes in next-generation batteries [170]. The energy storage devices fabricated using perovskite have battery stability, energy density, and cycle life, and address key challenges in energy storage technologies in comparison to the conventional materials.

2.11 TECHNICAL GAPS

- Lithium niobate (LiNbO$_3$) has a wide band gap of 3.56 eV, primarily absorbing UV light, which constitutes only about 5% of the sunlight spectrum, limiting its effectiveness in solar applications. There is a need to shift LiNbO$_3$'s optical absorption into the visible range, and doping with various metal elements could be a promising strategy; however, a comprehensive investigation on the effects of different metal dopants on its optical properties is still lacking, highlighting a significant research opportunity.

- Strontium titanate (SrTiO$_3$) has a wide band gap of 3.24 eV, leading to significant absorption primarily in the UV range, which limits its solar cell efficiency. Plasmonic metal doping could reduce the band gap and decrease charge carrier recombination, yet a comprehensive analysis of various dopants and their effects on SrTiO$_3$'s optical properties remains unexplored, presenting a valuable research opportunity to enhance its performance in solar applications.

- Strain engineering and metal doping in materials can significantly modify its electronic and optical properties, which is crucial for enhancing performance in applications like sensors and solar cells. Despite some studies on strain effects, a comprehensive understanding of how different strain types (tensile vs. compressive) and various dopants interact to influence optical absorption and carrier dynamics remains lacking, highlighting an opportunity to explore these synergistic effects for optimizing materials in advanced optoelectronic applications.

- Two-dimensional materials can be fabricated with relatively inexpensive production methods, integrated into existing semiconductor technologies, and offer new physical and chemical properties. Hence, van der Waals heterojunctions offer the opportunity to combine layers with different properties as the building blocks to engineer new

functional materials for high-performance electronic devices, chemical sensors, water-splitting photocatalysts and optoelectronics applications.

CHAPTER-3

METAL DOPING FOR IMPROVING OPTICAL PROPERTIES OF LITHIUM NIOBATE

Among the wide variety of perovskites, Lithium Niobate ($LiNbO_3$) is a high-performance oxide perovskite, recognized for its exceptional ferroelectricity and electro-optic properties, making it a critical material for photonics, optoelectronics, and quantum applications. As a wide-bandgap material, $LiNbO_3$ exhibits non-zero absorption across a broad optical spectrum; however, its low absorption in the visible region limits its effectiveness in applications requiring strong light-matter interactions. Doping $LiNbO_3$ with metal ions can effectively enhance its optical, electrical, and structural properties, optimizing its performance in advanced applications. These tailored modifications make doped $LiNbO_3$ a promising candidate for next-generation integrated photonic and optoelectronic applications. Therefore, to determine the electronic and optical properties of $LiNbO_3$ and to investigate the impact of doping on these properties, the following objective is formed.

"Analyzing the effect of metal doping (M= Au, Ag, Cu, Al, Mn, Mo, Ni, and Fe) on electronic and optical properties of lithium niobate ($LiNbO_3$) crystal for optoelectronic applications: A First-principles Calculation."

The methodology used to achieve desired objective involved following steps: -

- The pristine hexagonal cell of lithium niobate is build using the builder tool of ATK VNL.
- Electronic and optical properties are calculated for pristine lithium niobate.
- Further, the pristine lithium niobate is doped with the various metal dopants (M= Al, Au, Ag, Cu, Fe, Mn, Mo, and Ni) with 5% doping concentration.
- Electronic and optical properties are calculated for doped lithium niobate and are compared with the pristine lithium niobate.
- The impact of metal doping on the electronic and optical properties of lithium niobate is investigated in detail.

This chapter is divided into seven sections, including the introduction in the first section. The second section provides information on the simulation setup adopted for the calculations. Following that, in the third section, the structural properties of pristine and doped $LiNbO_3$ are calculated and analyzed. The electronic properties of pristine and doped $LiNbO_3$ are plotted and explained in section four. The optical properties are plotted and elucidated in section five. In section six, the comparison of the optical properties of pristine and metal-doped $LiNbO_3$ is illustrated. Finally, the important outcomes are summarized in section seven.

3.1 INTRODUCTION

In 1963, Geologist Gustav Rose discovered the mineral CaTiO3 (Calcium titanate) in the mountains of Ural. The mineral was named as perovskite to award the gratitude to Lev Perovski, a distinguished mineralogist from Russia [171]. Any compound having formula ABC3 is named as perovskite, where B ion surrounds the C ions. Numerous varieties of electric properties and solid-state behaviors including; insulating, semiconducting, metallic, and superconducting are comprehended in the perovskite materials [172]. Therefore, these compounds are very fascinating for investigations and are applied to a large variety of applications. They also exhibit a variety of optical, magnetic, and electronic properties. Most of the elements of the periodic table are found stable in the perovskite structure [173].

Studies of these compounds are of great interest owing to their wide applicability in the photochromic, image storage, electrochromic, filtering, switching, and surface acoustic wave signal processing devices [174, 175]. Likewise, they have a virtuous impact on numerous optoelectronic, bio-sensing, photo-electrolysis based applications [176]. In recent years, a huge interest has developed in the studies of perovskite materials and in investigating their properties for the photonic and optoelectronic applications. It is owing to their adjustable optical and electrical properties that too with mechanical flexibility [177, 178]. Furthermore, their high-absorption coefficient, low diffusion length, excellent charge transportation, and low nonradioactive emission exceeds their utilization for photovoltaic and optoelectronic based devices [179-181].

Lithium niobate ($LiNbO_3$) is a notable member of the perovskite family. It exists in the ferroelectric state and liable for potential use in the electro-optical and optical systems its extraordinary piezoelectric, electro-optical, photovoltaic, photo elastic, and nonlinear optical properties [182-184]. The study of $LiNbO_3$ is interesting for the researchers due to its unique

properties that are mainly determined by its defect structure and composition. Its optical characteristics can be influenced by the significant amount of impurity which can replace Li/Nb ion and can occupy the octahedral void in the crystal [185]. In the past, $LiNbO_3$ has attracted the attention of the researcher and manufacturers for optoelectronics-based applications. Javid *et al.* [186], reported the DFT study of electronic and optical properties of $LiNbO_3$. It has been concluded in the past studies that a great shortcoming associated with the $LiNbO_3$ is its large bandgap. Due to which, the $LiNbO_3$ crystal undergoes surface photo activation under UV radiation only [187]. However, UV light (300–400 nm), is a very small fraction of the sunlight (only 5%) and a large proportion of the sunlight will be left unutilized. So, it is interesting to shift the optical response of $LiNbO_3$ to the visible range of the optical spectrum [158]. This can be achieved by the metal-doping which leads an extension in the wavelength range towards the visible spectra and thus improves the solar energy utilization efficiency [188, 189].
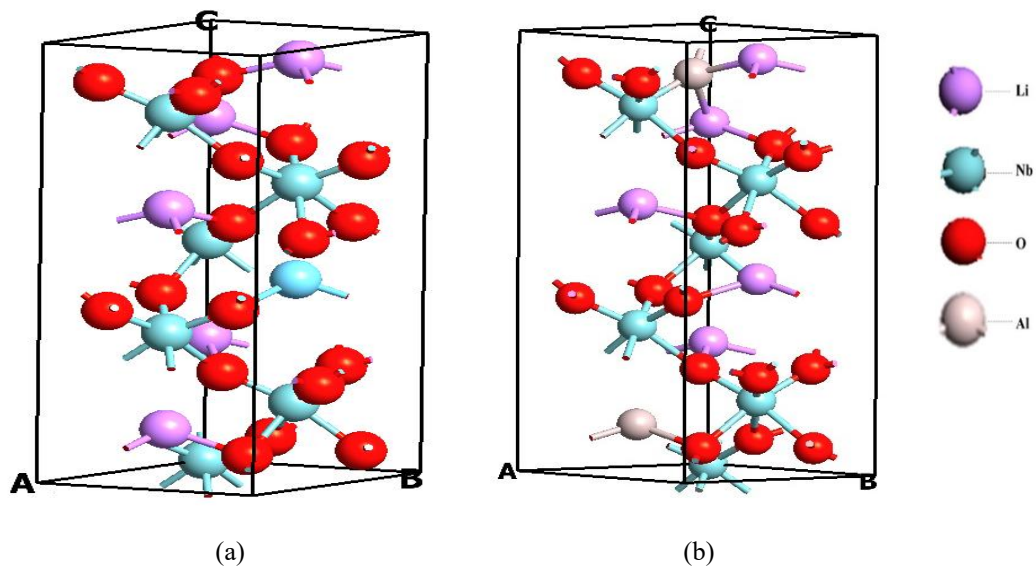
Fig. 3.1 Hexagonal unit cell of (a) Pristine $LiNbO_3$ and (b) Metal (Al) doped $LiNbO_3$.

Pathak *et al.* [118], studied the effect of Eu3+doping on the optical properties of $LiNbO_3$ and concluded that the optical properties are improved due to doping. Likewise, Huang Duo-Hui *et al.* [191], studied the effect of Fe and Mg doping on the optical properties of $LiNbO_3$. El-Bachiri *et al.* [192], also analyzed the effect of Ni doping on the properties of the $LiNbO_3$. Metal doping is an effective way to improve the optical properties by lowering the bandgap of materials for photoexcitation (red shift) and additionally reduce the recombination of charge carriers. In the category of dopants, metals can be further subcategorized based on their properties. Although there are various classes of metals, however, a superior class of the metals is plasmonic (Ag, Au, Al, and Cu) which exhibits the occurrence surface plasmonic phenomena

[193]. This phenomenon leads to the oscillation of electrons for the matched frequency of the incident radiation. The metals exhibiting surface plasmonic phenomena have unique optical properties and are exceptionally strong absorber of light. This makes them appropriate dopant for tuning the optical absorption towards the visible region [194-197].

In this chapter, initially, the electronic and optical properties of the pristine $LiNbO_3$ crystal are investigated. Further, the crystal is doped with various metals (M= Fe, Mn, Mo, and Ni) along with the metals exhibiting plasmonic effect (M=Au, Ag, Al, and Cu). Subsequently, the effects of doping on electronic and optical properties are analysed. The bandgap of pristine and doped structures is calculated for analysing the electronic properties. The primary motivation of the doping is to reduce the large bandgap and to further tune the optical properties.

For analysing the effect of doping on the optical properties, the energy and wavelength-dependent absorption coefficient are computed. Further, dielectric function and refractive index are also computed for the analysis. From the computed results, a significant improvement is observed in the optical properties due to metal-doping. These improvements are significant for the plasmonic metal dopant (M=Au, Ag, Al, and Cu) [198]. However, for the other metal dopants like Fe, Ni, Mn, and Mo, an improved absorption in visible spectra along with red shift is observed. These findings suggest M-lithium niobite (M= Au, Ag, Al, Cu, Fe, Mn, Mo, and Ni) as a suitable candidate for photovoltaic and optical applications.

3.2   COMPUTATIONAL SET UP FOR CALCULATIONS

The ground-state properties of any material can be efficaciously computed by utilizing first-principles calculations modeled on density functional theory. The plane-wave Density Functional Theory (DFT) calculator is utilized to optimize the geometry and to compute the properties of $LiNbO_3$ and its metal-doped structures. The calculations are performed on the Quantum-ATK tool kit. In geometry optimization, to represent the exchange-correlation function, the generalized gradient approximation (GGA) of perdew–purke– prnzerh is adopted [199, 200]. The geometry optimization is performed by using Monkhorst–Pack k-point mesh with the 9×9×1 k point sampling and density mesh cut off of 150 Hartree [82]. LBFGS optimization method of type quasi-Newton optimization algorithm is utilized for the geometry optimization until all forces acting on the atoms and stress became less than 0.02 eV/Å and 0.004 GPa, respectively.

To render steadiness with earlier research, GGA is adopted to compute the electronic properties [186, 201]. Nonetheless, due to the use of effective approximation algorithms, the calculated results are in good match with the previously reported results [186, 67]. The DFT in combination with meta-GGA (TB09) is used to calculate the optical properties. The 9×9×1 k-points sampling is used for the Brillouin zone to calculate the optical properties [82].
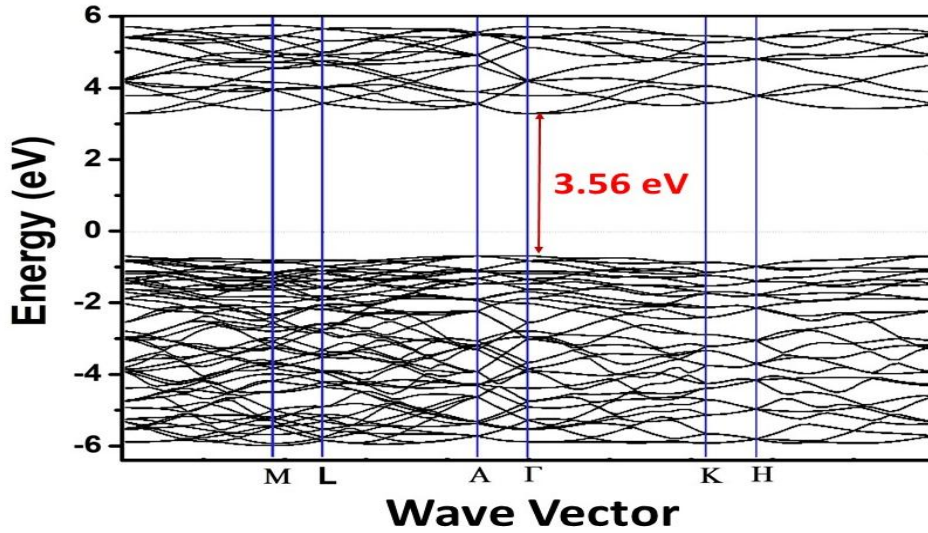
Fig. 3.2 Band structure of pristine LiNbO₃ with bandgap value Eg=3.56 eV.

The electronic and optical properties of the optimized LiNbO₃ hexagonal unit cell with various doping arrangements are calculated. Various metal dopants from the periodic table are chosen to regulate/tune the optical properties of the crystal. For the material, relationships among the dielectric constant (εr), polarizability (α), optical conductivity (σ), and susceptibility (χ) are given as [202]:

$$\varepsilon_r = 1 + \chi(\omega) \tag{3.2}$$

$$\alpha(\omega) = V\varepsilon_0\chi(\omega) \tag{3.2}$$

$$\sigma(\omega) = -img(\omega\varepsilon_0\chi(\omega)) \tag{3.3}$$

The refractive index (η), extinction coefficient (k), and dielectric constant (εr) are related as:

$$\eta + i\kappa = \sqrt{\varepsilon_r} \tag{3.4}$$

Refractive index (η) and extinction coefficient (k) can be represented in terms of real (ε_1) and imaginary parts (ε_2) of dielectric function, as:

$$\eta = \sqrt{\frac{\sqrt{\varepsilon_1^2 + \varepsilon_2^2} + \varepsilon_1}{2}} \tag{3.5}$$

$$\kappa = \sqrt{\frac{\sqrt{\varepsilon_1^2 + \varepsilon_2^2} - \varepsilon_1}{2}} \tag{3.6}$$

Coefficient of optical absorption and coefficient of extinction are related as [103]:

$$\alpha_a = 2\frac{\omega}{c}\kappa \tag{3.7}$$

Wavelength (λ) and photon energy (E) are related as:

$$\lambda(\mu m) = \frac{1.2398}{E(eV)} \tag{3.8}$$

The above equations are utilized to calculate the optical parameters from the computed values.

3.3 STRUCTURAL GEOMETRY OF PRISTINE AND DOPED LINBO₃

The hexagonal unit cell of LiNbO₃ crystal consists of six atoms of each lithium and niobate along with eighteen atoms of oxygen (total 40 atoms). The LiNbO₃ crystal structure utilized for the calculations [204], is illustrated in Fig. 3.1 (a). In the doped structures, the hexagonal unit cell of LiNbO₃ containing 40 atoms is constructed, and two host atoms are replaced by dopant atoms. All the doped models are simulated with 5% doping concentration, as shown in Fig. 3.1 (b). The doping model in Fig. 3.1 (b) is represented for the dopant; Aluminium (Al) and same analogy is adopted for the other dopants.

Table 3.1. Lattice constant of pristine LiNbO₃.

a (Å)	b (Å)	c (Å)	Vol (Å3)	References
5.204	5.204	13.976	378.492	Calculated
5.220	5.220	14.093	384.011	[104] theor.
5.057	5.057	13.942	356.542	[101] theor.
5.147	5.147	13.849	366.880	[104] expt.

For pristine LiNbO₃, the geometry is optimized and the lattice parameters of the optimized structure are found in good agreement with the previously reported results [61, 67, 186, 203, 204, 205]. The compression of the experimental lattice parameter reported in earlier studies along with the values calculated in this study for pristine LiNbO₃ are depicted in Table 3.1. The

calculated lattice constant, lattice volume and bandgap for metal doped structures are elaborated in Table 3.2.

3.4 ELECTRONIC PROPERTIES OF PRISTINE AND DOPED LINBO₃

Band structure of any material is a representation of the band of eigenvalues, which can be utilized to understand the alignment of Fermi level. For any material, there is a noteworthy influence of the location of fermi level on electronic and optical properties [206- 208]. By identifying the location and energies of the dominant bands close to the Fermi level, the electronic and optical properties of the materials can be easily understood. The band structure of pristine $LiNbO_3$ crystal is computed using GGA and is presented in Fig. 3.2. It can be observed from the figure, that the pristine $LiNbO_3$ crystal has a direct bandgap of 3.56 eV. The conduction band minima and valance band maxima are located at 2.94 eV and -0.62 eV. The valence band maximum and conduction band minimum occur at the same point Γ. The occurrence of valence band maximum and conduction band minimum at same point makes pristine $LiNbO_3$ a direct band gap material [67].

Table 3.2. Lattice constant and band gap of $LiNbO_3$ (pristine and doped).

Doped Models	Lattice Parameters			Volume	Bandgap
	a (Å)	b (Å)	c (Å)	(Å³)	(eV)
Pristine-LN	5.204	5.204	13.976	378.492	3.56
Ag-LN	5.551	5.551	14.711	453.298	1.78
Al-LN	5.505	5.505	15.068	456.635	2.02
Au-LN	5.505	5.505	14.346	434.755	1.36
Cu-LN	5.556	5.556	14.411	444.855	0.96
Fe-LN	5.483	5.483	14.333	430.897	1.38
Mo-LN	5.520	5.520	14.631	445.812	0.61
Mn-LN	5.517	5.517	14.390	437.992	0.72
Ni-LN	5.534	5.534	14.337	439.072	0.94

To understand the effect of doping on the electronic and optical properties, M-LiNbO₃ (M= Al, Au, Ag, Cu, Fe, Mn, Mo, and Ni) crystal is optimized. The calculated lattice constant, lattice volume and bandgap of pristine and metal-doped (M= Al, Au, Ag, Cu, Fe, Mn, Mo, and Ni) structures after geometry relaxation are elaborated in Table 3.2. A significant reduction in the bandgap is achieved for all the metal-doped structures (summarized in Table 3.2) as compared

to pristine LiNbO₃ due to the introduction of in-gap impurity states. It is determined from the calculated bandgap that the metal doping can be advantageous to achieve the improvement in the optoelectronic performance of LiNbO₃ due to the band gap narrowing.

3.5 OPTICAL PROPERTIES OF PRISTINE AND LINBO₃

In this section, the calculated optical properties including dielectric function, absorption coefficient, and refractive index of pristine and M-LiNbO₃ (M= Au, Ag, Al, Cu, Fe, Mn, Mo, Ni) crystal are analyzed in detail. These analyses are very interesting and are essential for finding a notable doped structure of LiNbO₃ for optoelectronics-based applications. The values represented in this section are calculated along the xx, yy and zz tensor. The results along the x-direction are discussed here, and the results in the other two directions may be interpreted in the same way [107].
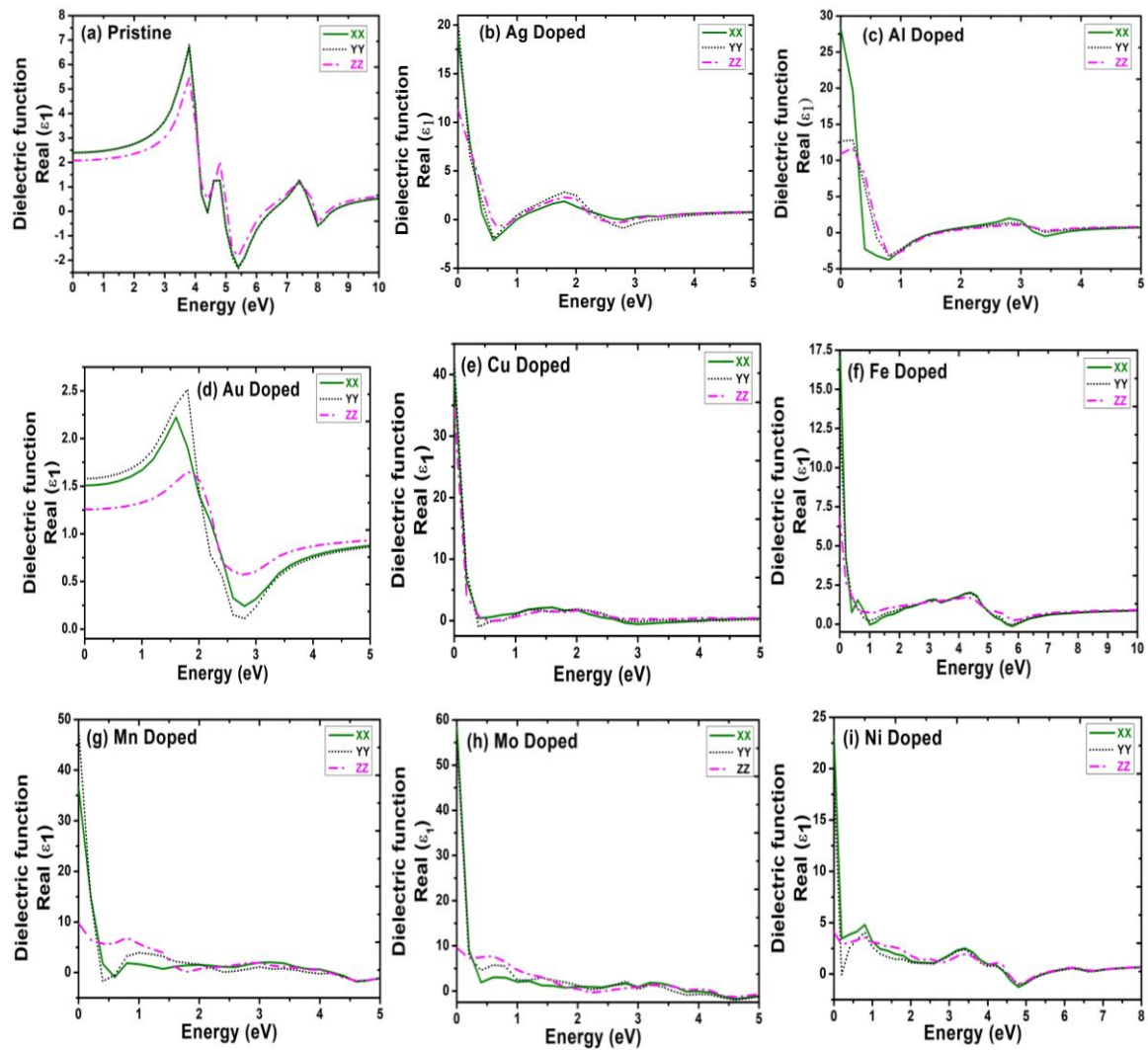
Fig. 3.3 Energy-dependent real part of dielectric function for (a) pristine LiNbO₃, and doped with (b) Ag, (c) Al, (d) Au, (e) Cu, (f) Fe, (g) Mn, (h) Mo and (i) Ni.

The real part of dielectric function is illustrated in Fig. 3.3 (a) for pristine $LiNbO_3$ and in Fig 3.3 (b)-3.3 (h) for M-$LiNbO_3$ (M= Au, Ag, Al, Cu, Fe, Mn, Mo, and Ni). The real part of dielectric function describes the phase lag between the driving and response frequency and represents the slowing down of the light in the material. For the doped $LiNbO_3$, the value of real part of dielectric function increases and the dielectric loss decreases with respect to pristine $LiNbO_3$. The decreased dielectric losses signify lesser slowing down of the light in the doped structures and better optical response in comparison to the pristine $LiNbO_3$.

3.5.1 Dielectric function of pristine and doped $LiNbO_3$

The dielectric function describes a material's response to an external electromagnetic field and is a key parameter in understanding its optical and electronic properties. The imaginary ($\varepsilon2$) portion of the energy-dependent dielectric function for pristine and metal-doped $LiNbO_3$ are illustrated in Fig. 3.4. which corresponds to absorption losses due to electronic transitions, interbond absorption, or free carrier interactions.

It is significant and fascinating to examine the imaginary ($\varepsilon2$) portion of dielectric function due to its effectiveness in determining the optical absorption. The imaginary part of dielectric function is a representation of the damping and considered as an effective parameter to investigate the optical absorption. Perovskite materials have gained significant attention in optoelectronics, particularly in solar cells, due to their excellent dielectric properties.

The dielectric constant (εr) of perovskites typically ranges between 10 and 30, depending on their composition and crystal structure. This high dielectric constant helps in efficient charge separation and reduces charge recombination, making perovskites highly efficient for photovoltaic applications. Additionally, their tunable dielectric properties allow for optimization in other optoelectronic devices such as LEDs, photodetectors, and transistors. As research progresses, improving the stability and dielectric performance of perovskites remains a key focus in advancing next-generation solar technologies.

For pristine $LiNbO_3$, as shown in Fig. 3.4 (a), there are three peaks in the imaginary part of the dielectric function, with the strongest one at around ~3.6 eV and the second-strongest one at ~5 eV followed by the smallest one at ~8 eV. Further, for all the metal-doped structures included in this analysis, the peaks are significantly shifted towards the lower energies and are broadly found in the range of ~0-1 eV, as shown in Fig. 3.4 (b)-4 (i).
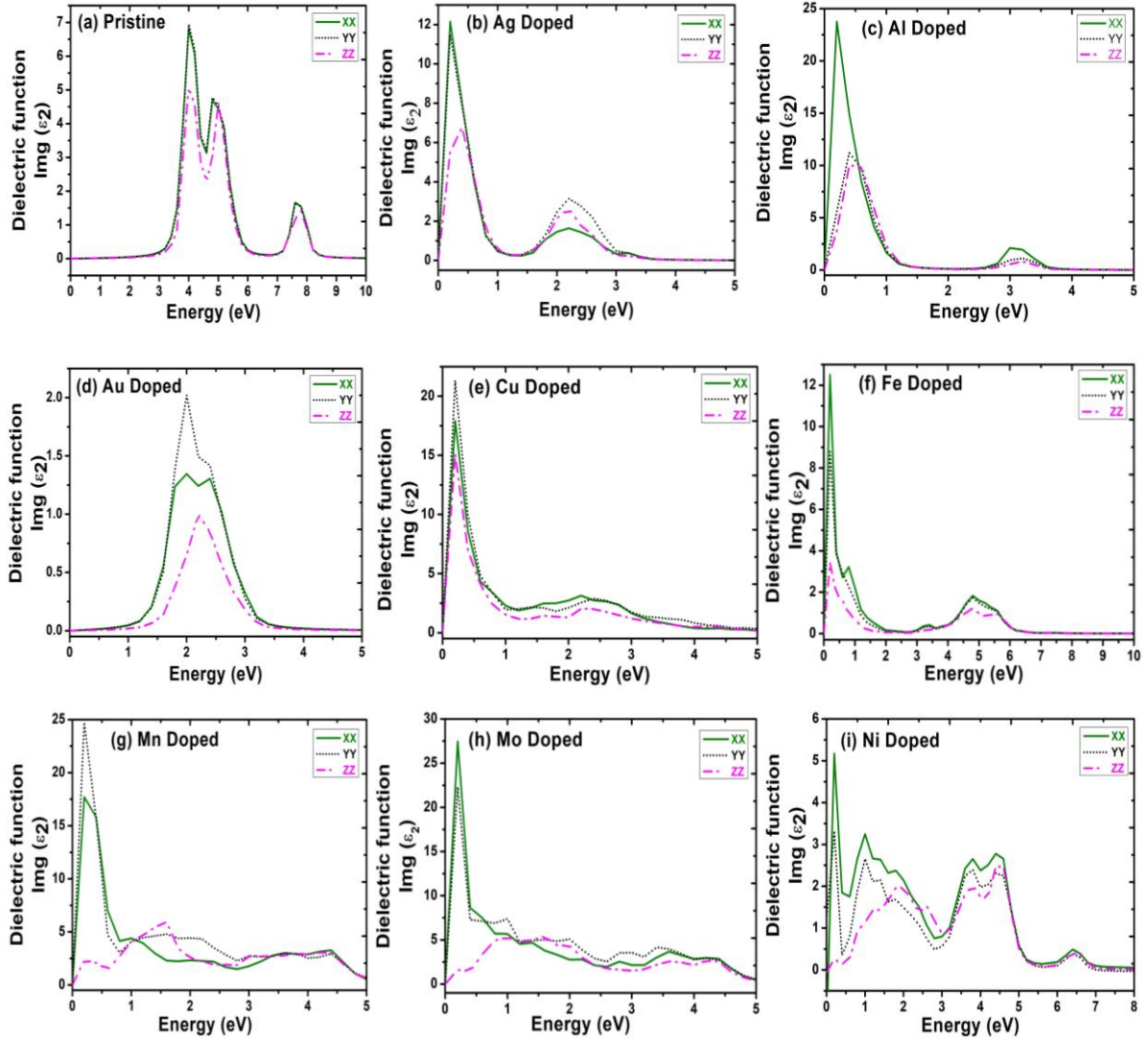
Fig. 3.4 Energy-dependent imaginary part of dielectric function for (a) pristine $LiNbO_3$, and doped with (b) Ag, (c) Al, (d) Au, (e) Cu, (f) Fe, (g) Mn, (h) Mo and (i) Ni.

For pristine and all the metal-doped structures, the peaks of the imaginary part of the dielectric function are in consistency with the energy-dependent absorption coefficient as illustrated in Fig. 3.5. The presence of these peaks of dielectric function at low energies (for all the metal-doped structures) signifies a smaller excitation binding energy that in turn results in a higher absorption in the visible region of the optical spectrum.

3.5.2 Absorption coefficient of pristine and doped $LiNbO_3$

The energy-dependent and wavelength-dependent absorption coefficient are illustrated in Fig. 3.5 and Fig. 3.6 for the pristine and metal-doped $LiNbO_3$, respectively. The absorption coefficient of any material is an effective indicative of the efficiency of solar energy conversion and signifies the propagation length of light in any material. As illustrated in Fig. 3.5 (a), the

absorption starts from ~3.6 eV which is in consistency with the bandgap calculated in the earlier section for the pristine structure. However, for metal doped LiNbO₃, the absorption edge of absorption coefficient starts at lower energies (Fig 3.5). Compared with that of pristine LiNbO₃ (3.6 eV), the absorption edge of metal-doped (M= Al, Au, Ag, Cu, Fe, Mn, Mo, and Ni) shifts to the lower energy direction (long-wave direction). This shift predominantly improves the optical performance.
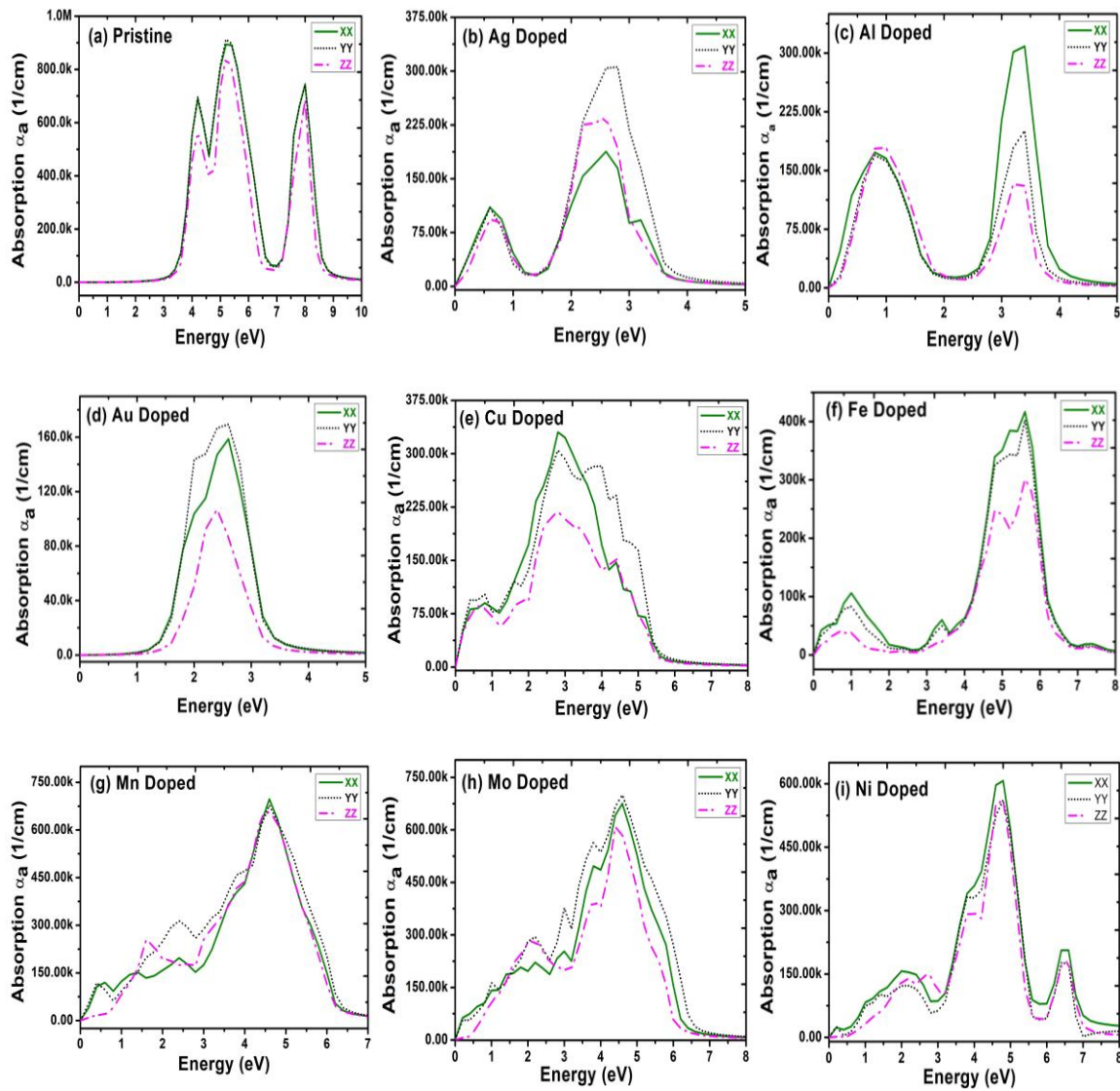
Fig. 3.5 Energy-dependent absorption coefficient for (a) pristine LiNbO₃, and doped with (b) Ag, (c) Al, (d) Au, (e) Cu, (f) Fe, (g) Mn, (h) Mo, and (i) Ni, along the xx, yy and zz tensors.

The wavelength-dependent absorption coefficient for the metal dopants; Ag, Al, Au, and Cu are illustrated in Fig. 3.6 (b)-3.6 (e). As shown in Fig. 3.6 (a), the absorption in the pristine structure lies completely in the UV region of the optical spectrum with absorption edge at ~350 nm. This absorption edge is in strong consistency with the computed bandgap (Eg = 3.56 eV).

It can be concluded from the absorption coefficient that there is a significant shift in the absorption edge towards the visible and near-visible region (NVR) of the optical spectrum for the dopant Ag, Al, Au, and Cu. It can be seen from the Fig. 3.6 (b) and 3.6 (d) that the absorption has been completely shifted to 400 nm to 800 nm for the dopant Ag and Au.

However, for dopant Al (Fig. 3.6 (b)); the absorption is in Near visible region i.e. around 400 nm and for dopant Cu (Fig. 3.6 (e)), it is in 400 nm to 600 nm. This shifting of absorption in visible region for the dopants like Au, Ag, Cu, and Al is occurred due to the surface plasmonic resonance phenomena. These dopants are in the category of plasmonic metal. The doping with these plasmonic metal leads to the oscillation of electrons matched to the frequency of incident radiation. Metals like Au, Ag, Cu, and Al are considered as potential candidate for the plasmonic applications. Among these metals, Ag is superior for the plasmonic effect because of its least optical losses in the visible region.

However, Ag oxidizes in a rapid manner and exhibits losses because of roughness at the surface. On the contrary, Au outperforms in the visible region that too with superior chemical stability. Conversely, the chemical instability of Cu and Al restricts them from the wide applicability. The above facts are strongly supported by wavelength-dependent absorption coefficient, shown in the Fig. 3.6 (b)-3.6 (e). It can be inferred from Fig. 3.6 that the optical spectrum is completely tuned in the visible region for the dopant Ag (Fig. 3.6 (b)) and Au (Fig. 3.6 (d)) due to their extraordinary absorbing and scattering efficiency. In these metals, the conduction electrons in the surface experience a collective oscillation for a specific wavelength during interaction with incident light. This oscillation may be identified as plasmon resonance, and thus results in a higher absorption in the visible region.

For the other plasmonic dopants; Al (Fig. 3.6 (c)) and Cu (Fig. 3.6 (e)), the absorption is shifted towards visible and near-visible region (NVR). The value of absorption coefficient is the highest for Ag-doped LiNbO₃ among all the metal-dopants utilized in this study and thus making it best among all. Subsequently, for other metal-dopants like Fe, Mo, Mn, Mo, and Ni, a red-shift along with slightly improved absorption in the visible spectra is observed, as illustrated in Fig. 3.6 (f)-6 (i). The amount of redshift is very significant for the plasmonic metal dopants due to plasmon resonances, leading to hybridized modes that often result in high value of red shift.
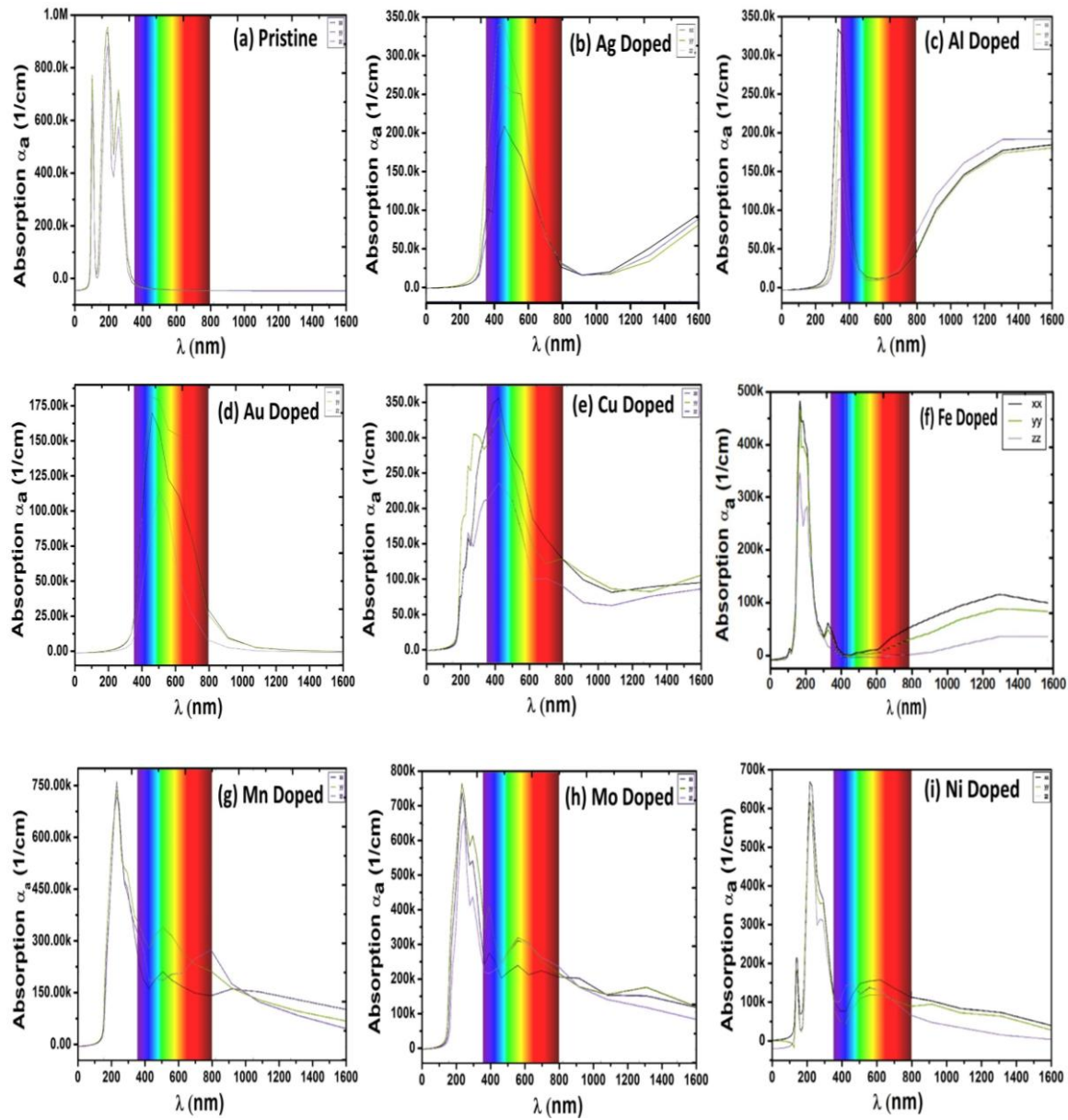
Fig. 3.6 Wavelength-dependent absorption coefficient for (a) pristine LiNbO₃, and doped with (b) Ag, (c) Al, (d) Au, (e) Cu, (f) Fe, (g) Mn, (h) Mo and (i) Ni.

Overall, the shifting of edges and improvement in absorption in the visible region for all the M-lithium niobite (M= Au, Ag, Al, Cu, Fe, Mn, Mo, Ni) are attributed to the newly created energy levels near to the filled conduction band. This results in a red-shift as illustrated in Fig. 3.6. Further, it can also be concluded that due to metal doping, the equilibrium carrier concentration got altered that leads to the formation of traps. These traps ultimately reduce the charge carrier recombination rate and thus improve the photovoltaic activity. As a conclusive remark, it can be stated that the doping with metal-dopant used in this study resulted in an improved absorption of visible light. The outcomes of the absorption coefficient are found consistent with the calculated dielectric function. Further, a broader range of absorption can

easily be observed for the structures doped with plasmonic metals (M= Au, Ag, Al, and Cu), from the Fig. 3.6 (b), 3.6 (c), 3.6 (d) and 3.6 (e). This broader range clearly signifies a stable and enhanced absorption in the visible range of the optical spectrum due to the doping of plasmonic metals. Owing to the improved visible light absorption, metal-doped LiNbO₃ structures (specifically plasmonic metal doped) are proven a prominent candidate for the optoelectronics and photonic based applications.
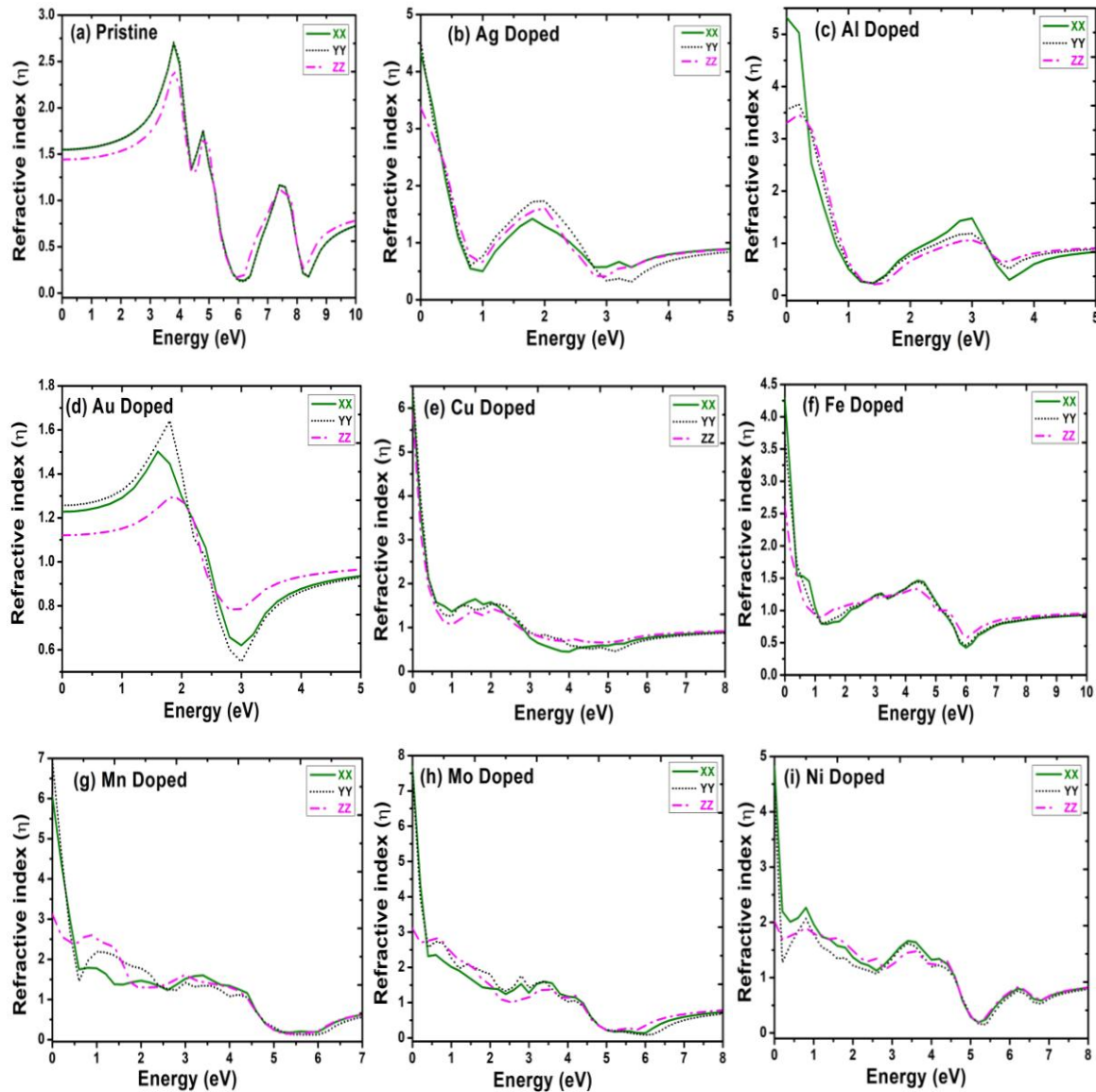
Fig. 3.7 Energy-dependent refractive index for (a) pristine LiNbO₃, and doped with (b) Ag, (c) Al, (d) Au, (e) Cu, (f) Fe, (g) Mn, (h) Mo and (i) Ni.

3.5.3 Refractive index of pristine and doped LiNbO₃

The refractive index is computed from the real part of the dielectric function and is demonstrated in Fig. 3.7 for pristine and metal-doped LiNbO₃. The peaks in the refractive index

follow the imaginary part of the dielectric function earlier shown in Fig. 3.3, which illustrates the consistency of the refractive index with dielectric function. A significant improvement is observed in the refractive index for all the metal-dopants as shown in Fig. 3.7 (b)-3.7 (i) than that of pristine LiNbO₃ shown in Fig. 3.7 (a). This implies comparatively a longer life of light in the crystal, resulting in the higher absorption of the photon in the respective spectrum range.

3.6 COMPARISON OF OPTICAL PROPERTIES OF PRISTINE AND LINBO₃

The comparative analysis of the optical properties and applications of pristine and doped LiNbO₃ (M = Au, Ag, Al, Cu, Fe, Mn, Mo, and Ni) is illustrated in Table 3.3. It is evident from the summarized data that for Au and Ag-doped LiNbO₃ are most appropriate for optoelectronic and photonic applications due to their high absorption in the visible region, which enhances light-matter interaction. The pristine LiNbO₃, despite good optoelectronic properties exhibit high absorption in ultraviolet region, making it less effective for optoelectronic applications. The doping of Al and Cu significantly improves absorption in both the visible and near-visible regions (NVR), making them better than pristine LiNbO₃ but still inferior to Ag and Au dopants. For dopants Ni, Fe, Mn, and Mo the absorption is high for ultraviolet region but exhibit low absorption in found in the visible range, resulting in moderate suitability for optoelectronic applications.

Table 3.3. Comparison of the optical properties of pristine and metal doped LiNbO₃.

Optical Properties	Pristine LiNbO₃	Ag/Au Doped	Al/Cu Doped	Ni/Fe/Mn/Mo Doped
Optical Absorption-UV region	High	Missing	Missing	High
Absorption-Visible region	Missing	High	High in visible and NVR	Low
Suitability -optoelectronic applications	Not Good	Best	Better	Good

These findings indicate that doping LiNbO₃ with appropriate metal ions can effectively modulate its optical properties, including refractive index, absorption, and nonlinear optical coefficients. Such modifications enable precise control over light propagation, frequency conversion, and electro-optic modulation, making doped LiNbO₃ a highly promising material for next-generation optoelectronic and photonic applications, such as high-speed optical modulators, wavelength converters, and integrated photonic circuits

3.7 SUMMARY OF THE IMPORTANT RESULTS

1. The electronic and optical properties of pristine and metal-doped $LiNbO_3$ are computed by using density functional theory.

2. Due to large bandgap, pristine $LiNbO_3$ cannot utilize the visible portion of the optical spectrum. The absorption in the visible region can be enhanced by means of doping with a suitable metal dopant.

3. The pristine $LiNbO_3$ is doped metal (M= Au, Ag, Al, Cu, Fe, Mn, Mo, Ni) and the impact of doping on electronic and optical properties is investigated.

4. Due to doping, the lattice parameters are changed. The calculated value of the unit cell volume for the pristine $LiNbO_3$ is 78.492 $Å^3$.

5. The largest increase in the unit cell volume is observed for Ag-doped $LiNbO_3$ (453.298 $Å^3$) and Al-doped $LiNbO_3$ (456.635 $Å^3$). However, for Fe-doped $LiNbO_3$ and Au-doped $LiNbO_3$, there is a moderate increase in the lattice volume.

6. The value of the bandgap is 3.56 eV for pristine $LiNbO_3$, which decreases significantly upon doping. Mo-doped $LiNbO_3$ and Mn-doped $LiNbO_3$ exhibit the largest drop in the bandgap with the values of bandgap 0.61 eV and 0.72 eV, respectively.

7. With the plasmonic metal dopants, the bandgap is also reduced. The reduction is moderate for the Au-doped $LiNbO_3$ (1.36 eV,) and Ag-doped $LiNbO_3$ (1.78 eV).

8. Doping with all the other dopants lowers the bandgap. Cu doped $LiNbO_3$ (0.96 eV) and Ni doped $LiNbO_3$ (0.94 eV) create notable shifts, useful for optoelectronics. In contrast, Al doped $LiNbO_3$ (2.02 eV) maintains a relatively higher bandgap, making it suitable for applications in UV photodetectors and optical Sensors.

9. There are significant improvements in the optical properties due to doping. These improvements are very significant for the plasmonic metal dopants due to surface plasmonic resonance. The optical absorption is extraordinarily enhanced in the visible region for the plasmonic metal dopants.

10. Among the plasmonic dopants, the enhancement is very much significant for the dopants Au and Ag, due to their extraordinary plasmonic properties. The other plasmonic dopants, Cu and Al, also showed an enhanced absorption in the visible region.

11. For the other metal dopants like Ni, Fe, Mn, and Mo, a slightly increased absorption in the visible region along with redshift is observed.

12. It is observed from the calculated results that the pristine $LiNbO_3$ exhibits strong UV absorption below 400 nm. Due to doping with plasmonic metal dopants Al, Au, Ag, and Cu, the bandgap reduces, and the absorption is shifted significantly toward the visible-NIR region, where Au and Cu show the most significant shifts.

13. For other dopants (Fe, Mn, Mo, Ni), good absorption in the visible-NIR region is observed with the highest redshift for Mo-doped $LiNbO_3$.

14. It has been shown that the optical properties (dielectric constant and refractive index) are also improved significantly due to the doping of metal dopants (M = Au, Ag, Al, Cu, Fe, Mn, Mo, Ni). Hence, it is envisaged that the metal-doped $LiNbO_3$ may find vital usage in photonic and optoelectronics-based applications.

CHAPTER-4

TUNING THE OPTICAL PROPERTIES OF $SrTiO_3$ FOR OPTOELECTRONIC AND PHOTOCATALYTIC APPLICATIONS

Strontium titanate (SrTiO₃), widely known as STO, is a perovskite oxide characterized by exceptional dielectric characteristics, thermal stability, and effective charge transport, making it a potential candidate for optoelectronic and photocatalytic applications. Nevertheless, its wide bandgap (~3.2 eV) limits its optical absorption predominantly to the ultraviolet spectrum, hence limiting its solar conversion efficacy in optoelectronic applications. To improve the absorption of STO, the pristine crystal may be doped with the metal dopants. The doping will result in lessening of the bandgap, broadening absorption into the visible and near-infrared (NIR) spectra, thus improving photocatalytic effectiveness. Moreover, doping also improves oxygen vacancies and enhances charge separation dynamics, hence enhancing catalytic activity. Therefore, the aim of this chapter is to investigate the impact of plasmonic metal doping on the structural, electronic, optical, and photocatalytic properties of STO. The following objective is framed to accomplish the proposed work;

"Determining the structural, electronic and optical Properties on strontium titanate (SrTiO3) crystal. Tuning the electronic and optical properties of SrTiO3 through plasmonic metal doping for optoelectronic and photocatalytic applications."

The methodology used to achieve framed objective involves following steps: -

- The 2×2×1 cubic unit cell of pristine STO is build using ATK VNL, and the geometry is relaxed before starting the density calculations.
- Further, the pristine STO is doped with plasmonic metal dopants (M= Ag, Al, Au, and Cu), and electronic and optical properties are calculated.
- To examine the influence of doping with plasmonic-metal dopant on the photocatalytic ability of STO, the band edge alignment is plotted.
- The electronic, structural, photocatalytic, and optical properties of doped STO are compared with the pristine STO, and the improvements in the properties are identified.

The present chapter is divided into ten different sections, starting with an introduction as the first section. In the second section, the DFT computations adopted for the calculations are explained. Section three focuses on the structural properties of pristine and doped STO. Section four discusses the impact of doping on the electronic properties of STO. The calculations of optical properties are explained in section five. Section six provides details on the effect of doping on the real and imaginary dielectric constant of STO. Sections seven and eight explore the effect of doping with the plasmonic dopants on the absorption and refractive index of STO, respectively. Section nine discusses the photocatalytic properties of pristine and doped STO and explains the band edge alignment. Finally, all the important outcomes are summarized in Section ten in conclusion.

4.1 INTRODUCTION

After the discovery of Calcium titanate ($CaTiO_3$) in 1939, Russian mineralogist Gustav Rose, introduced a new class of material with the formula ABX_3. These structures are named after Lev A. Perovski, a renowned Russian mineralogist. Perovskite material is a ternary oxide of formula ABO_3, where A is an element of group I or group II (a rare-earth, an alkaline-earth, or an alkali element), and B is a transition metal or post-transition metal with period 4, 5, or 6. In past studies, a tremendous variety of electric and solid-state behaviours have been comprehended in perovskites [209]. The widespread acceptability of the perovskites for electronic and optoelectronics applications are due to their highly adjustable properties. The perovskites attracted the large attention of researchers due to their ability to form stable structure with almost all the elements of the periodic table [173].

(a)   (b)
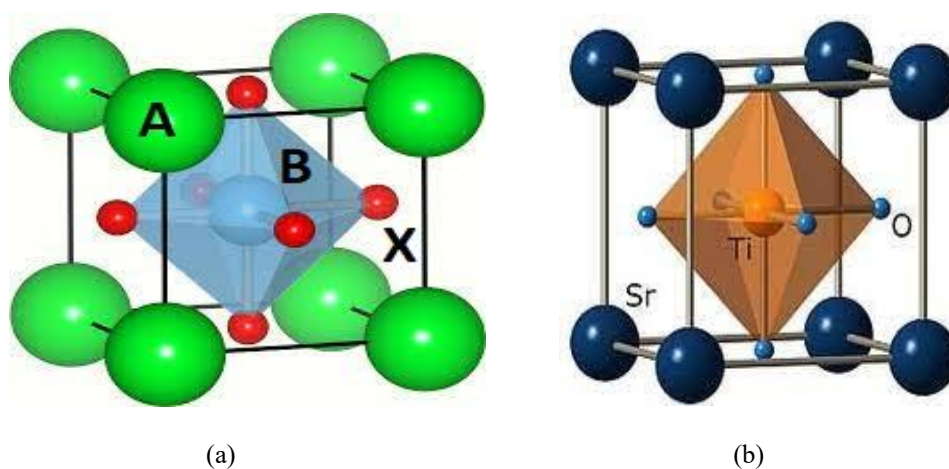
Fig. 4.1 General structure of **(a)** Perovskite and **(b)** $SrTiO_3$.

Strontium titanate ($SrTiO_3$) widely known as STO is a preeminent perovskite compound with a cubical unit cell of lattice parameters 3.905 Å [112]. The STO has widely proven its acceptance for applications such as sensors, super-lenses, photo-catalyst, electronic switches, solar cells, and fuel cell anodes. The general structure of perovskite and STO is represented in Fig. 4.1. In recent years, STO has been a focus of extensive study due to its enormous applications in optoelectronics and photocatalysis. The band gap of the STO is 3.20 eV at room temperature and it exhibits the insulating behavior [111]. It can perform water splitting even without the application of any externally applied electric field and act as a perfect photocatalyst [63]. But the main shortcoming with the pure STO is its wide band gap, which corresponds to the ultra-violate (UV) light (300–400 nm) of the solar spectrum [63, 65].

It is well known that UV light is only a small fraction of the solar spectrum (only 5%), hence a larger portion of the solar spectrum is left unutilized [111]. The large band gap of STO, severely limits its efficiency for optoelectronic and photocatalysis applications. This shortcoming can be overcome by mean of band gap narrowing, which shifts the absorption towards the visible region and ultimately improve optoelectronics and photocatalysis efficiency [177, 210]. It is revealed in previous studies that the electronic structure of materials can be altered by various approaches like doping [211], heterostructures formation [212], and vacancies creation [213].

The altered electronic structure can considerably narrow down the band gap and remarkably shift the absorption towards the visible region. This will finally result in enormous enhancements in the efficiency of the material for optoelectronics, photocatalysis, and solar applications. Numerous experimental and theoretical studies are performed to tune the properties of STO in recent times [214, 64]. In these studies, doping has been extensively used as an inevitable method to tune the properties of STO for optoelectronics and photocatalysis [112, 173, 181, 215, 216]. Xin Zhou *et al.* reported experimentally and theoretically that Fe and Mn doping in STO results in the reduction of band gap and improves the optical properties [217].

Gillani *et al.* doped the STO with Zinc and reported significant improvements in electronic and optical properties and unlocks a potential prospect for applicability of Zn-STO for optoelectronics [112]. H. Irie *et al.* studied the effect of Ag and Pb doping on STO and reported the shifting of optical absorption predominantly in the visible region [218]. Conclusively, metal doping played an excellent role in improving the optical properties of STO and in

widening its applicability for optoelectronics-based applications. In the family of metals, there is a superior category of metal widely known as plasmonic. Silver (Ag), Gold (Au), Aluminium (Al), and Copper (Ag) are members of the plasmonic family and exhibit the occurrence of the surface plasmonic phenomenon [219]. This phenomenon results in the occurrence of oscillation of electrons for the incident radiation of matched frequency. The plasmonic-metals are very strong absorbers of light and show unique optical properties, which makes them a potential dopant to extend the optical absorption towards the visible region [196, 220-221].

In this chapter, to elucidate the underlying plasmonic effect, the structural, electronic, and optical properties of plasmonic-metal doped STO (M= Ag, Al, Au, and Cu) are exmined by applying density functional theory. First, the structural, electronic, and optical properties of pristine STO are computed. Furthermore, the STO is doped by plasmonic-metal dopants, and the properties of doped STO are compared with the properties of pristine STO. Subsequently, the enhancements in optical properties and evaluation of the photocatalytic behaviour in doped STO are analyzed. For analyzing the impact of doping on electronic properties, band gap and density of states (DOS) are computed.

Likewise, wavelength-dependent and energy-dependent absorption coefficients are computed for optical properties. Furthermore, refractive index and dielectric function are also calculated for the detailed study of modified optical properties. For all the plasmonic-metal dopants, the band gap of STO reduced significantly, which completely shift the absorption towards the lower energies (Red Shift). The primary cause responsible for this shifting is surface plasmonic resonance. Additionally, the structural variation in crystal from its ideal stoichiometry due to doping is also responsible for the modified properties. Furthermore, to understand the impact of doping on photocatalytic behaviour, the calculations are conducted and band alignment for all the structures is plotted for the water redox potential.

4.2 COMPUTATIONAL SET UP

The first-principles calculations are carried out to accurately compute the structural, electronic, and optical properties of STO and its doped structures. All the calculations are computed on Quantum-ATK by employing the plane-wave-pseudopotential approach of density functional theory (DFT) [121, 158]. In DFT calculations, the Generalized Gradient Approximation (GGA) of Perdew-Burke-Ernzerh (PBE) parametrization is adopted to characterize the exchange-

correlation [199, 222]. The Monkhorst–Pack grid is used for the calculations and the brillouin zone k point sampling is fixed to $7 \times 7 \times 1$ [200].

The density mesh cut-off energy is fixed to 150 Ry for all the computations [161]. Before starting the single point energy calculations, geometry optimization is accomplished using LBFGS optimization. The quasi-newton method is used for geometry optimization. The atomic optimization is iterated until the residual forces and stress on all the atoms became below 0.05 eV/Å and 0.004 GPa, respectively. The electronic properties are calculated by using GGA. However, DFT incorporated with meta-GGA is adopted for calculations of optical properties [201]. In the calculations, the formula of Kubo-Greenwood is used for calculating the value of susceptibility tensor as [223]:

$$\chi_{i,j(\omega)} = -\frac{e^2 \hbar^4}{\varepsilon_0 m^2 \omega^2 V} \sum_{nm} \frac{f(E_m) - f(E_n)}{E_{nm} - \hbar\omega - \imath\Gamma} \pi^{\iota}_{nm} \pi^{j}_{mn} \tag{4.4}$$

In the above equation, π^{ι}_{mn} represents the ith element of the dipole matrix. V is the volume, n and m represent the state of atoms, f represents fermi function and Γ is the broadening. The dielectric constant ($\mathcal{E}_r$), polarizability (α), and optical conductivity (σ) are represented in terms of susceptibility (χ) as [202]:

$$\varepsilon_r = 1 + \chi(\omega) \tag{4.2}$$

$$\alpha(\omega) = V\varepsilon_0\chi(\omega) \tag{4.3}$$

$$\sigma(\omega) = -img(\omega\varepsilon_0\chi(\omega)) \tag{4.4}$$

The dielectric constant ($\mathcal{E}_r$), is represented in the terms of refractive index (η) and extinction coefficient (k) as:

$$\eta + i\kappa = \sqrt{\varepsilon_r} \tag{4.5}$$

Refractive index (η) and extinction coefficient (k) is calculated from real (ε_1) and imaginary (ε_2) parts of dielectric function as:

$$\eta = \sqrt{\frac{\sqrt{\varepsilon_1^2 + \varepsilon_2^2} + \varepsilon_1}{2}} \tag{4.6}$$

$$\kappa = \sqrt{\frac{\sqrt{\varepsilon_1^2 + \varepsilon_2^2} - \varepsilon_1}{2}} \tag{4.7}$$

The coefficient of optical absorption is shown below as a function of extinction coefficient [203]:

$$\alpha_a = 2\frac{\omega}{c}\kappa \qquad (4.8)$$

The above equations are utilzied to caclauatae properties of pristine and doped sturtures of STO in the subsequnet sections of this chapter.

4.3 STRUCTURAL PROPERTIES OF PRISTINE AND DOPED STO

In structural properties, the lattice constants and lattice volume of pure and M-STO (M= Ag, Al, Au and Cu) are computed. The pristine STO considered for the present study is a perovskite structure with space group pm3m (see Fig. 4.2 (a)). The 2×2×1 cubic unit cell of pristine STO is build using ATK VNL and the geometry is relaxed before starting the density calculations [111, 112]. The unit cell of pristine STO is consisting of a total of 40 atoms (see Fig. 4.2 (a)) out of which, there are 8 atoms of each strontium and titanium along with 24 oxygen atoms [224].

(a)   (b)
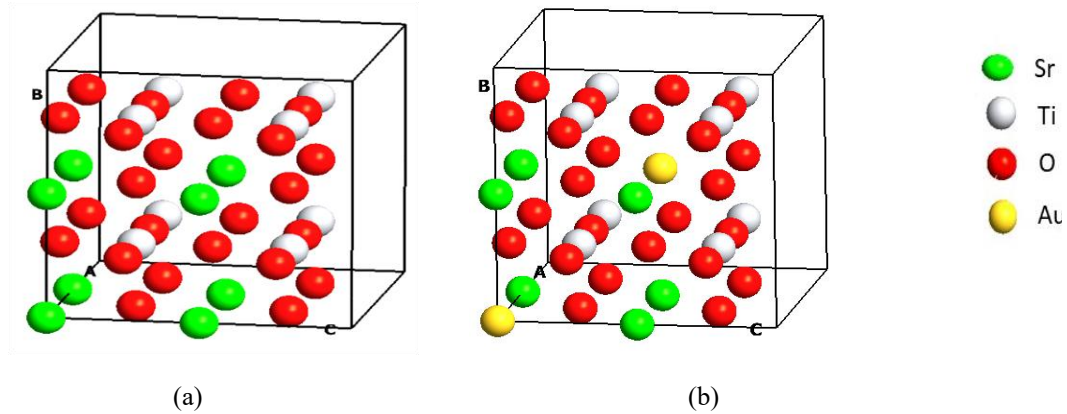
Fig. 4.2 Cubical unit cell of **(a)** Pure $SrTiO_3$ and **(b)** Au-doped $SrTiO_3$.

Table 4.1 Lattice parameters of pure $SrTiO_3$.

Structure	Methodology	Lattice Constant (Å) a = b = c	Vol (Å^3)	Reference
Cubic	Experimental Pristine	3.90	59.319	35
	DFT Pristine	3.90	59.319	4
		3.95	61.629	17
	DFT Pristine	3.94	61.162	Present work

The calculated values of lattice constants for the pristine STO shown in Fig. 4.2 (a) are a=b=c=3.945 Å and the lattice angles are $\alpha = \beta = \gamma = 90°$. The values of lattice constants

and lattice angles are in well accordance with the earlier reported experimental and theoretical results [111, 217, 225]. This proves the validity of accapted parameters of first-principles calculations. Subsequently, the pristine STO is doped with plasmonic-metal dopants (Ag, Al, Au, and Cu) with 5% doping concertation (see Fig. 4.2 (b)).

Table 4.2 Lattice parameters and band gap of pure and plasmonic-metal doped $SrTiO_3$.

Doping Model	Lattice Constant (Å) a = b = c	Volume ($Å^3$)	Band gap (eV)
Pristine-STO	3.94	61.16	2.94
Ag-STO	4.08	67.91	1.57
Al-STO	3.93	60.69	1.77
Au-STO	3.94	61.16	1.56
Cu-STO	4.07	67.41	1.54

The doped structure for dopant Au is illustrated in Fig. 4.2 (b) and the same doping model is used for all other dopants. The Ti-site of STO is considered for doping as the metal ions predominantly prefer to enter the Ti-site in STO rather than Sr-site [217, 226]. This is because of the ionic radius of metal ion, which is nearly close to Ti as compare to Sr [226]. The computed lattice constants of optimized pristine STO of present study along with previously reported values are illustrated in Table 4.1. As shown in Table 4.1 the lattice constants computed in our study are in well accordance with the earlier results.

4.4   ELECTRONIC PROPERTIES OF PRISTINE AND DOPED STO

To investigate the effect of plasmonic-metal doping on the electronic structure of pristine STO, band structure, the total density of states (TDOS), and partial density of states (PDOS) of pristine and plasmonic-metal doped STO (M= Ag, Al, Au, and Cu) are computed and plotted in Fig. 4.3 and Fig. 4.4. As illustrated in Fig. 4.3, the computed band gap of pristine STO is 2.88 eV. The computed band gap is in well accordance with the theoretical results reported in earlier studies [111, 112, 227, 228].
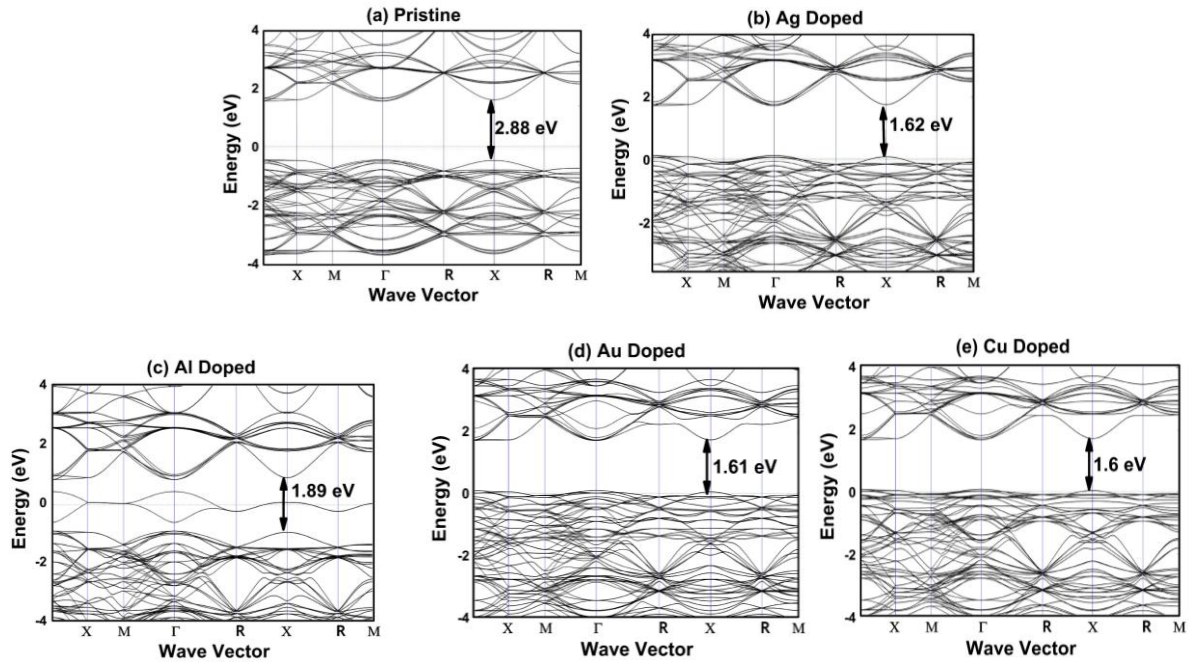
Fig. 4.3 Band structure of pure and doped SrTiO$_3$.

The band gap of M-STO (M= Ag, Al, Au, and Cu) are shown in Table 4.2. The band gap significantly lowered for the M-STO, as compared to the pure STO. This lowering down of band gap decrease the transition energy between CBM and VBM, which results in a phenomenon known as red-shift. The reduced values of band gaps are 1.57, 1.77, 1.56, and 1.54 eV for the dopants Ag, Al, Au, and Cu, respectively. These reduced band gaps of doped STO are favourable for achieving the enhanced visible-light absorption.

As illustrated in the TDOS and PDOS plot in Fig. 4.4, the band gap lowering in doped structures are due to the formation of localized states, which bring down the CBM and eventually results in enhanced visible light absorption. The dopants Ag, Al, Au, and Cu lower the value of CBM by 1.49, 0.67, 0.69, and 0.71 eV, respectively, as compared to the pure STO. For the Al-doped STO (see Fig. 4.2(c)), some impurity states can be seen in the forbidden gap. These impurity states act as electron-hole recombination centers and results in the reduction of energy conversion efficiency. Hence, degrade the photocatalytic behavior. Additionally, for Al-doped STO, the downward shift in CBM is very high, which adversely degrade its reduction power and make it ineligible for the photocatalysis process. For the dopants Ag, Au, and Cu the downward shift in CBM is very small, which is favourable for overall photocatalytic performance.
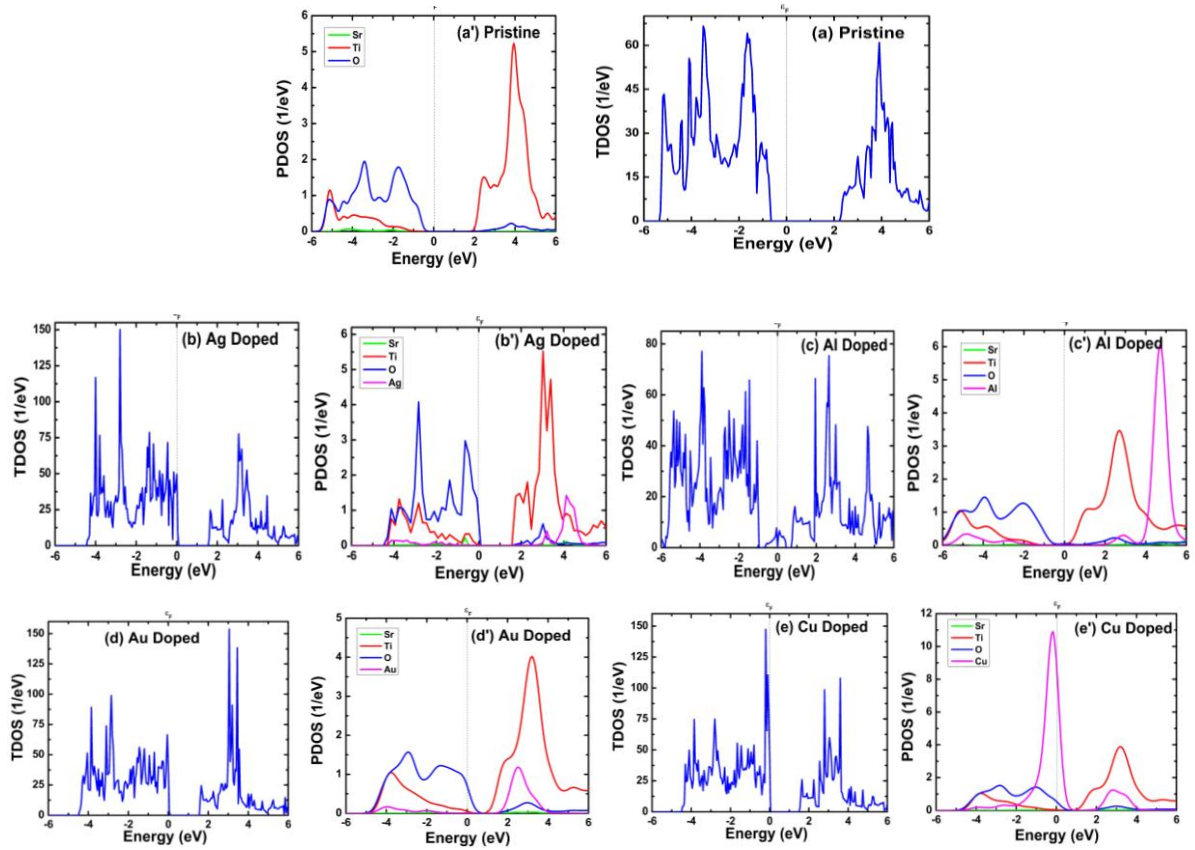
Fig. 4.4 Total density of states (TDOS) and Partial density of states (PDOS) of pure and plasmonic-metal doped $SrTiO_3$ (M= Ag, Al, Au and Cu).

The PDOS of STO (see Fig. 4.4) clearly shows that the 2p state of oxygen principally contributes to the valance band maxima (VBM) and conduction band minima (CBM) is principally composed of 3d-Ti. For dopant Ag, Al, and Au the CBM and VBM are dominantly composed of 3d-Ti and 2p-O, respectively. However, for dopant Cu, the CBM and VBM are dominantly composed of 3d-Ti and 2p-O/3d-Cu, respectively. Consequently, in the analysis of the electron structure, the calculated results assert two significant effects of the plasmonic-metal doping on the properties of STO. The first one is the lessening of the band gap, which implies the improvement of absorption in the visible region. Secondly, for all the dopants except Al, the doped STO shows properties favorable for photocatalysis water splitting. Thus, the plasmonic-metal doped STO can be considered as an efficient material for optoelectronic, photovoltaic, and photocatalysis applications.

4.5 OPTICAL PROPERTIES OF DOPED STO

STO is widely considered an active and prominent candidate for optoelectronic applications. Therefore, it is fascinating to analyse the various optical properties of STO like absorption

82

coefficient, refractive index, and dielectric function. These optical properties illustrate the interaction of the material with light and describe the emerging optical behaviour. The calculated optical properties of pure STO in this chapter are in well accordance to the results reported in earlier studies [63, 111, 112], which validate the acceptance of our computations methods. All the properties are calculated for the xx, yy, and zz tensor and, properties are described for xx tensor only. For other tensors, all the properties may be understood in the similar way as described for the xx tensor [158]. The optical properties corresponding to different tensors overlap for pure and doped STO, which indicate the isotropic behaviour. This signify that all the optical properties are unrelated to the crystallographic direction.

4.6 EFFECT OF DOPING ON DIELECTRIC FUNCTION OF STO

The dielectric function is considered as an ideal parameter to define the behaviour of the light interaction with the medium of propagation. The real part represents the dispersion and polarization effects. However, the imaginary part determines the absorption and damping. The energy-dependent real dielectric function for the pure and doped STO (M= Ag, Al, Au, and Cu) are plotted in Fig. 4.5. It can be seen from Fig 4.5, for pristine STO, the majority of the peaks of real dielectric function are found in the energy range of ~ 3- 7 eV, with the strongest peak at 3.5 eV. However, for all the doped-STO the peaks are completely shifted to the energy range of ~ 0- 1 eV, having major values of real dielectric function in lower energy range.
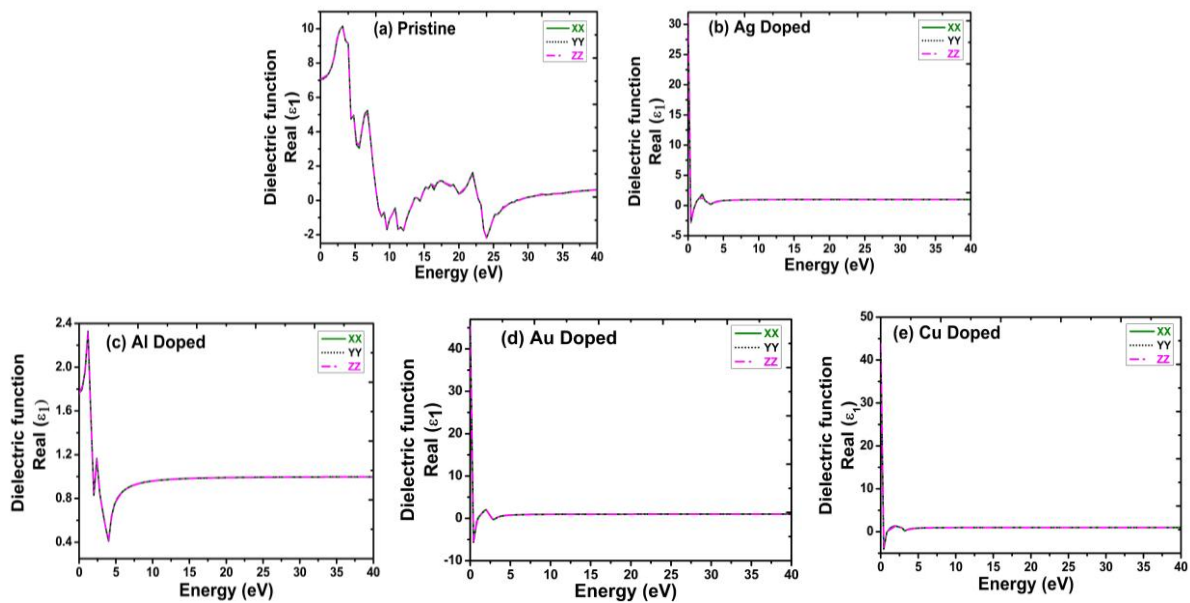
Fig. 4.5 Real dielectric function vs. Energy for pure and plasmonic-metal doped $SrTiO_3$ (M= Ag, Al, Au and Cu).
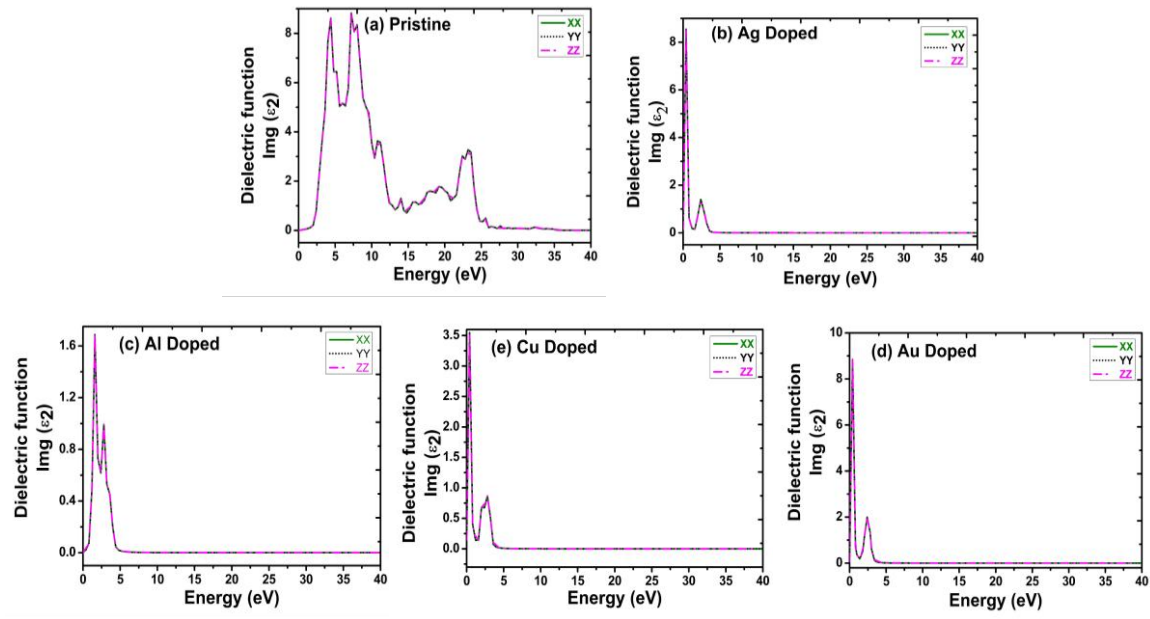
Fig. 4.6 Imaginary dielectric function vs. Energy for pure and plasmonic-metal doped $SrTiO_3$ (M= Ag, Al, Au and Cu).

For all the doped STO, the real dielectric constant increases at zero energy as compared to pure STO. This represents low dielectric losses in doped-STO compared to pristine, which eventually results in reduced slowdown of the propagation of light and improved optical response. The energy-dependent imaginary dielectric function for the pure and doped STO (M= Ag, Al, Au, and Cu) are plotted in Fig. 4.6. As shown in Fig. 4.6, for pristine STO majority of the peaks of imaginary dielectric function are found in the energy range of ~3-25 eV with the strongest peak at 3.5 eV. The peaks are located at 3.5, 7.5 and 22.5 eV.

The peaks for almost same valves of energy can be seen in the absorption (Fig. 4.7). For pure STO, the calculated values of optical properties are in well agreement with the results of previous studies [111, 112]. For doped structures, the imaginary dielectric function is found in energy range of ~0-5 eV, having the majority of peaks in lower energy range. The strongest peak doped structures is ~ 1 eV and the peaks in higher energies are completely eliminated because of doping. The peaks in lower energy for the doped structures signifies the lowering of the exciton binding energy, which results in a higher value of absorption.

4.7   EFFECT OF DOPING ON ABSORPTION OF STO

The absorption coefficient for pure and plasmonic-metal doped STO are shown in Fig. 4.7 and Fig. 4.8. Absorption is an efficient parameter to describe solar energy efficiency and light

propagation. For pure STO the absorption starts from ~ 3 eV (see Fig. 4.7), which is well consistent with the band gap reported in section 3.2. The absorption edges of the pure and doped STO are in well agreement with their band gap. For all the doped STO, the absorption edges are largely shifted in the lower energies i.e.~ 0-1 eV and the occurrence of redshift is observed. This shift is due to the reduced band gap, which ultimately results in enhanced optical absorption of doped-STO as compared to undoped structure. All the results of absorption are well consistent with the imaginary dielectric constant.

The wavelength vs. absorption for the pure and plasmonic-metal doped STO are shown in Fig. 4.8. For pristine STO the absorption is predominantly found in UV region with an absorption edge around ~300 nm. The absorption is almost zero in the visible region for the pure STO. For the dopants Ag, Au and Cu, the absorption is completely shifted towards the visible region (~ 400 - 800 nm) with a significantly large value as compared to the pure STO. For the dopant Al, the absorption starts ~ 300 nm and is found in the near-visible and visible region. The main reason of improved visible absorption for the dopants Ag, Al, Au, and Cu is the occurrence of surface plasmonic resonance (SPR).
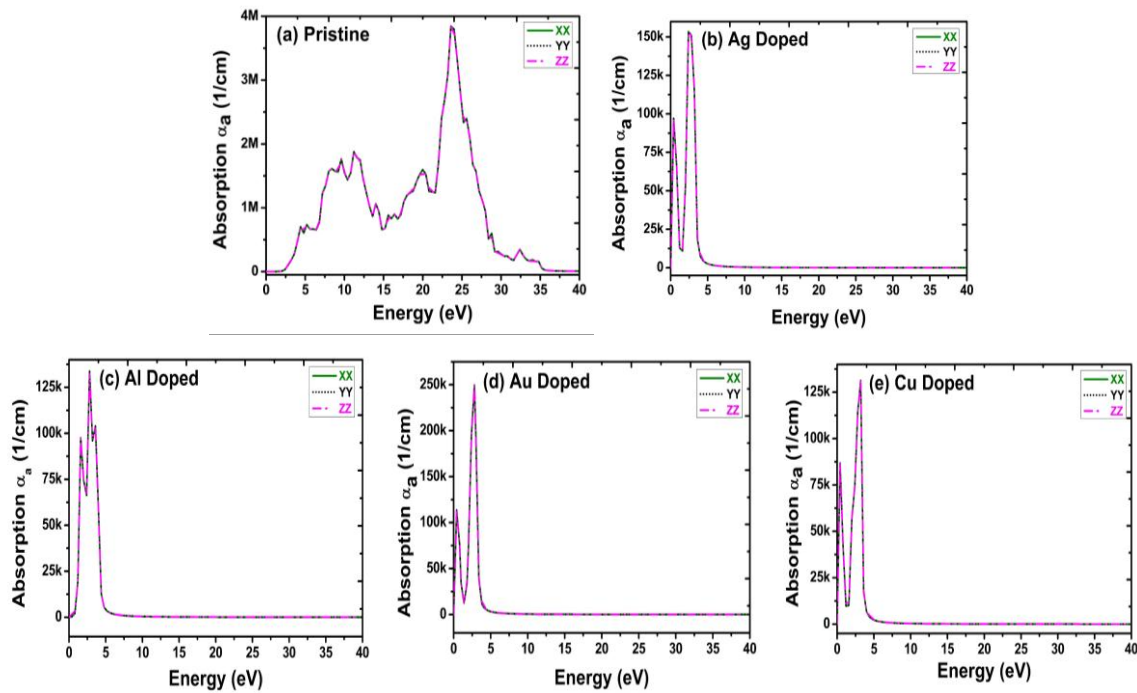
Fig. 4.7 Absorption coefficient vs. Energy for pure and plasmonic-metal doped $SrTiO_3$ (M= Ag, Al, Au and Cu).

The SPR results in oscillations of electrons for matched frequency of the radiation and improve the absorption in visible region. Additionally, due to doping, energy levels are created close to the conduction band, which results in the red shift. Moreover, the doping alters the equilibrium

concentration of charge carriers and form the traps, which reduces the recombination rate of charge carriers and results in enhanced photocatalyst activity.
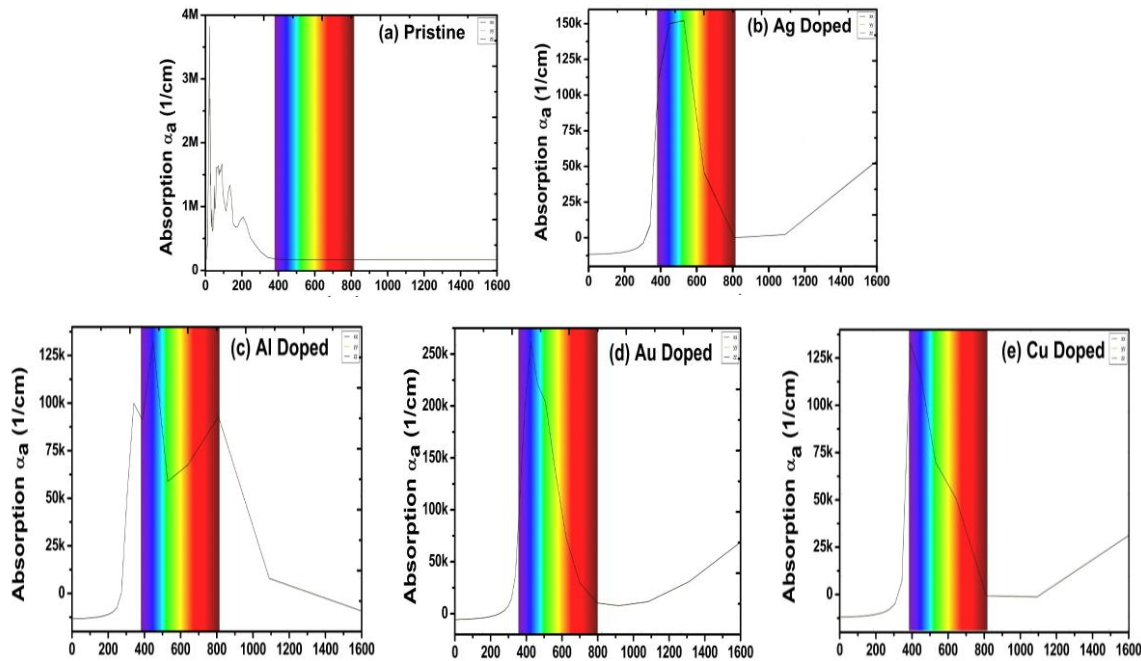
Fig. 4.8 Absorption coefficient vs. Wavelength (in nm) for pure and plasmonic-metal doped $SrTiO_3$ (M= Ag, Al, Au and Cu).

Among all the plasmonic dopants, Ag shows superior plasmonic behaviour because of the lowest optical losses for visible light. However, Ag undergoes to rapid oxidation and also have losses because of surface roughness. In contrary, Au is having an extraordinary performance for visible light along with the highest chemical stability. For Cu and Al, the uses are restricted due to their chemical instability. Among all the plasmonic-metal dopants, the absorption is highest for Au followed by Ag, Cu, and Al. Conclusively, all the plasmonic-metal doped STO (M= Au, Ag, Al, and Cu) showed enhanced absorption in visible region, which proves their potential applicability for optoelectronics and photocatalysis.

4.8 EFFECT OF DOPING ON REFRACTIVE INDEX OF STO

The value dielectric function is utilized to calculate refractive index. The calculated values of refractive index are plotted in Fig. 4.9. All the calculated values of refractive index are in line with the corresponding absorption coefficient and dielectric function (see Fig. 4.8 and Fig.4.5).
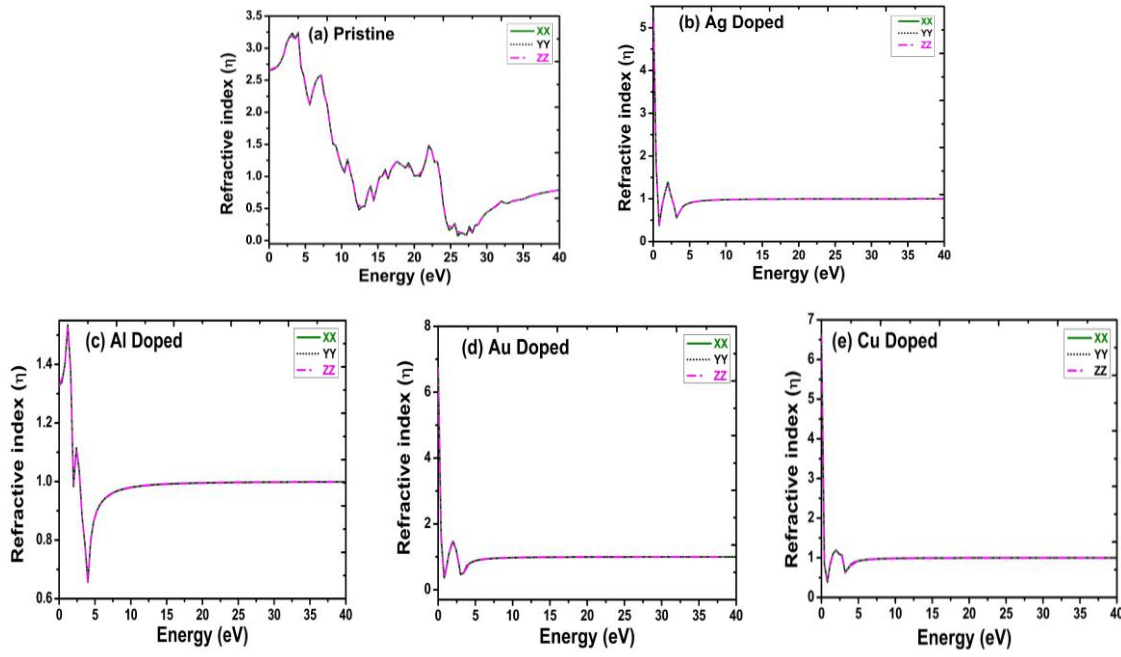
Fig. 4.9 Refractive index vs. Energy for pure and plasmonic-metal doped $SrTiO_3$ (M= Ag, Al, Au and Cu).

The plotted Fig. 4.9 depicts the relationship between the refractive index (η) and photon energy for pristine material, elucidating its optical characteristics. At lower energy levels (0–5 eV), the refractive index is comparatively elevated (~3.0), signifying robust light-matter interaction, which is essential for optoelectronic applications. As energy escalates, η diminishes, indicating a diminished optical response at elevated photon energies. The virtually equal XX, YY, and ZZ components affirm the material's optical isotropy, indicating uniform refractive characteristics across various crystallographic directions.

The identified peaks and troughs correlate to electronic transitions, indicating the material's capacity to engage with particular photon energy. Above 25 eV, η converges to a low value, signifying restricted light absorption at elevated energy levels. The energy-dependent refractive behavior is crucial in the design of photonic devices, waveguides, and optoelectronic components, where meticulous control of optical properties is vital for improved performance and efficiency.

The values of refractive index are increased due to doping in comparison to the refractive index of pure STO. The increased refractive index suggest that the light will remain much longer in the doped structure, therefore leading to better absorption in the visible region. The value of refractive index is almost negligible for higher energies, which is following the trend dielectric function.

4.9 PHOTOCATALYTIC PROPERTIES OF PRISTINE AND DOPED STO

In the process of photocatalysis water-splitting, the photocatalyst undergoes the reduction of H+ to H_2 along with oxidation of H_2O to H+ and O_2. For successful photocatalysis, the band gap of the photocatalyst should be less than or equal to the illuminated photon energy. In photocatalysis reduction, the valance band electron will drift to the conduction band and valance band holes are responsible for the oxidation process. The efficient photocatalytic behaviour of any material cannot be guaranteed only by the reduction in its band gap.

However, the appropriate position of band edges (CBM and VBM) can help to strongly guarantee the photocatalytic ability of any photocatalyst. In general, an efficient water splitting photocatalyst must have the VBM positioned below the oxidation level (O_2/H_2O) of water and the CBM above the reduction level (H+/H_2) of water. To examine the influence of doping with plasmonic-metal dopant on the photocatalytic ability of STO, first, the position of CBM and VBM are calculated for pristine STO by using the equations given below and then the position of band edges are aligned for doped structures with respect to the pristine structure [63, 217].

$$E_{CBM} = -\frac{1}{2}E_g + \chi_{STO} + E_0 \tag{4.9}$$

$$E_{VBM} = \frac{1}{2}E_g + \chi_{STO} + E_0 \tag{4.10}$$

$$\chi_{STO} = (\chi_{sr}\chi_{ti}\chi_o{}^3)^{\frac{1}{5}} \tag{4.11}$$

In above equations, E_g represents the band gap of pristine STO, E_0 represents the scaling factor with value -4.5 for normal hydrogen electrode (NHE), χ is the absolute values of electronegativity [229]. The calculated values of the positions of CBM and VBM for the pristine STO are -0.879 and 2.271 eV, respectively. These calculated values are in well accordance with the previous results [63, 217]. For the doped-STO, the positions of VBM and CBM are calculated from the DOS plots by considering the relative positions as compared to the pristine STO [217]. The band alignment along with CBM and VBM vs. NHE, for all structures, are plotted in Fig. 4.10.
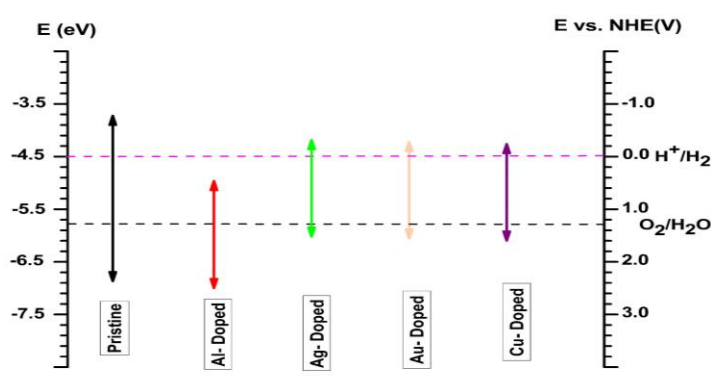
Fig. 4.10 Band edge alignment of pristine and metal (M= Ag, Al, Au and Cu) doped STO with respect to water oxidation and reduction potential.

As illustrated in Fig. 4.10, STO holds a strong reducing ability under UV light, ascribed to its negative CBM as compared to the water reduction potential H+/H_2 (0 eV vs. NHE). Moreover, it has a lower VBM as compared to the water oxidation potential O_2/H_2O (1.23 eV vs. NHE). For the dopant Al, the CBM shifts 1.43 eV, compared to pristine STO. Due to this large shift, the CBM becomes more positive compared to the oxidation potential of the water and which makes it active for photo-oxidation only. These findings oppose the acceptance of Al-doped STO as a promising candidate for the photocatalysis process. However, for the dopants Ag, Au and Cu, the downward shifts in CBM as compared to the pristine STO are 0.61, 0.63, and 0.65 eV, respectively.

Theses downward shifts improves the photo-reduction capabilities. As illustrated in Fig. 4.10, for Au, Ag and Cu doped STO, the VBM also move upward as compared with the VBM of pristine STO, which results in enhanced photo-oxidation capability. Furthermore, for dopants Ag, Au and Cu, the position of VBM and CBM is straddle to the water redox potential and the absorption is also found largely in the visible region. Thus, it is concluded that doping the STO with plasmonic-metal dopants (except the dopant Al) not only improves the absorption in the visible region but also enhances the photocatalytic ability for water splitting. These observations of our study, strongly support the applicability of M-STO (M=Ag, Au, and Cu) for photocatalysis water splitting.

4.10 SUMMARY OF THE IMPORTANT RESULTS

1. The effect of plasmonic-metal doping (M = Ag, Al, Au, and Cu) on the structural, electronic, and optical properties is investigated by employing DFT first-principles calculation.

89

2. For analyzing the electronic properties, band structure, TDOS, and PDOS are calculated. Moreover, dielectric function, refractive index, and absorption coefficient are calculated for optical analysis.

3. Furthermore, the band edge alignment is plotted for doped structures with respect to the pristine for analyzing the photocatalytic activities.

4. Doping SrTiO$_3$ (STO) with plasmonic metal dopants Ag, Al, Au, and Cu evidently affects its structural and electronic properties, resulting in an increase in lattice constant and volume, while drastically decreasing the bandgap relative to pristine STO (2.94 eV).

5. The shifting of the bandgap is significant for all the dopants with bandgap values of 1.57 eV, 1.56 eV, and 1.54 eV for Ag-STO, Au-STO, and Cu-STO, respectively.

6. The significant reduction in bandgap demonstrates their suitability for visible-light-driven optoelectronic and photocatalytic applications.

7. The results reveal that the doping with plasmonic metals reduces the band gap significantly and completely shifts the absorption towards the visible region (red shift). Among all plasmonic-metal dopants, Au and Ag exhibit superior plasmonic effects and show the highest optical absorption in the visible region.

8. Pristine STO has significant absorption in the ultraviolet spectrum, predominantly below 400 nm. Doping with Ag and Au enhances absorption in the visible spectrum, exhibiting peaks between 500 and 600 nm attributed to surface plasmon resonance phenomena.

9. Doping with Al and Cu also alters the absorption edge, resulting in significant absorption characteristics emerging within the 450–700 nm range.

10. The comprehensive redshift in absorbance for doped STO improves its photocatalytic and optoelectronic efficiency by facilitating enhanced usage of visible light, rendering it more appropriate for solar-driven applications.

11. For dopants Ag, Au, and Cu, the position of VBM and CBM is straddled to the water redox potential, which makes them potentially active for photocatalytic water splitting under visible light. However, Al-doped is active only for the photo-oxidation, which does not support the acceptance of Al-doped for the photocatalysis process.

12. Hence, it is envisaged that doping with plasmonic metal not only shifts the absorption towards the visible spectrum but also efficiently maintains the photocatalytic properties, which makes the plasmonic-metal doped a possible potential candidate for optoelectronic and photocatalysis applications.

CHAPTER-5

STRAIN ENGINEERING FOR TUNING THE OPTOELECTRONIC PROPERTIES OF PEROVSKITES

Strain engineering is a key technique for manipulating the optical and electronic properties of materials. In perovskite oxides, including $SrTiO_3$ and $LiNbO_3$, strain can lead to either bandgap narrowing or broadening, significantly affecting their optical absorption and photoluminescence. The coexistence of strain and doping enables improved control over bandgap engineering. Doping creates impurity states that combine with strain-induced alterations, facilitating the precise adjustment of optical absorption edges. Furthermore, the dopant integration in the materials may impact their stability, which can be assessed by calculating the values of formation energies, which is crucial for the sustainable performance of optoelectronic materials. Therefore, the objective of this chapter is to present a comprehensive investigation of the impact of strain on the electronic and optical properties of oxide perovskites ($LiNbO_3$ and $SrTiO_3$) and to evaluate the impact of coexistence of doping with strain, targeted to address the aforementioned need; the following objective is formed:

"Investigating the structural stability of the doped LiNbO3 and doped SrTiO3 using formation energy. Exploring the evaluation of improved visible light absorption and photocatalytic behaviour by application of strain."

The methodology used to achieve desired objective involved following steps: -

- The tensile and compressive strains of varying intensities are applied to the pristine lithium niobate and strontium titanate, and electronic and optical properties are calculated.

- To evaluate the impact of the coexistence of doping and strain on the optical properties, the plasmonic metal-doped lithium niobate and strontium titanate are applied with the compressive and tensile strain of varying intensities.

- In electronic properties, bandgap is calculated. Dielectric constant, refractive index, and absorption coefficient are calculated for investigating the optical properties.

- The formation energy calculations are carried out for the doped strontium titanate to evaluate the impact of doping on the stability.

This chapter is divided into seven sections, including the introduction in the first section. The second section provides information on the simulation setup adopted for the calculations. Following that, in the third section, the strain is applied on pristine $LiNbO_3$, and the impact of strain on electronic and optical properties is evaluated. The impact of strain on the optoelectronic properties of plasmonic metal-doped $LiNbO_3$ is investigated in the fourth section. In section five, the strain engineering is applied to the pristine and plasmonic metal-doped $SrTiO_3$. The structural stability using formation energy for the doped $SrTiO_3$ is illustrated in section six. Finally, the important outcomes are summarized in section seven.

5.1 INTRODUCTION

Lithium niobate ($LiNbO_3$) and strontium titanate ($SrTiO_3$) are promising materials for optoelectronic applications due to their excellent electro-optic, piezoelectric, and nonlinear optical properties. $LiNbO_3$ (LN) exhibits strong second-order nonlinear effects, making it valuable for frequency conversion and photonic devices, while $SrTiO_3$ (STO) demonstrates high dielectric permittivity and tunable refractive index, beneficial for optical modulators and transparent conductors. However, their wide bandgap (>2.5 eV) restricts their absorption primarily to the ultraviolet region, limiting their efficiency in visible-light-driven applications such as photovoltaics and photocatalysis. Additionally, intrinsic defects in these materials can introduce trap states, which degrade charge transport and enhance recombination losses, further reducing their performance in optoelectronic devices.

The wide bandgap of these perovskites results in the absorption in the UV region of the sunlight only, which is a small segment of the (~5%) available spectrum. Therefore, it is advantageous to modulate the electronic bandgap of lithium niobate and strontium titanate so that the optical absorption can be largely shifted toward the desired wavelengths, i.e., toward the visible region. Recently, researchers have adopted doping and strain as effective techniques to reduce the bandgap of materials and subsequently improve visible absorption [111, 225, 230- 234]. As far as doping is concerned, the dopant introduces the donor or acceptor levels in the empty forbidden band and shifts the absorption towards low energy ranges (redshift). The dopant also introduces the discrete energy gaps in the pristine material, and the electron can be exited from the valence to the conduction band using these gaps, which ultimately enhances the absorption in the visible region [63, 225].

In the past few years, several types of research have been carried out to enhance the optoelectronic behavior of materials by means of doping and strain [11, 230, 232, 235]. In these studies, Gillani *et al.* [73] and H. Irie *et al.* [218] studied the impact of doping on the $SrTiO_3$ with dopants Zn and Ag, respectively. It is found that doping with metals improves the absorption in the visible region and results in enhancement in the acceptability of doped $LiNbO_3$ and $SrTiO_3$ for optoelectronic applications. In this chapter, among the wide variety of metals available in the periodic table, silver (Ag), aluminum (Al), gold (Au), and copper (Cu) are adopted as dopants.

These dopants show plasmonic behavior and are very strong absorbers of light. Doping with these plasmonic metals can extend the absorption extraordinarily toward the visible region [112, 128]. Along with the doping, further strains of varying intensity are applied to pristine and doped perovskites (lithium niobate and strontium titanate) to improve their optical properties for optoelectronic applications. Strain engineering is a reversible and controllable process [65, 67, 223, 236] that allows precise modulation of material properties with high accuracy. Stain does not generate any additional defects or lattice damage in the crystal and advantageously alters its structure, which induces enormous prospects for various desirable applications. It demonstrates the variation in the structure of the materials and shows unique properties for various applications in the field of optoelectronics and photovoltaics [239- 242].

 Furthermore, the coexistence of doping and strain has proved itself an efficient approach to modulate the optoelectronic characteristics of the nanomaterials in the desired manner [199, 237]. Doping with metals like Ag, Al, Au, and Cu can improve the optoelectronic response, which can be further enhanced by the application of strain [196, 218, 235]. Several studies have revealed that strain can be considered an effective way to tune the optical properties of materials. In a significant work, Chen *et al.* [233] calculated the bandgap as a function of strain for $FAPbI_3$ iodide perovskite.

In the case of perovskite $LiNbO_3$, Husin *et al.* [236] studied the effect of strain on the electronic and optical properties and concluded that the compressive and tensile strain shifts the spectrum to the higher or lower wavelength, which ultimately improves the optical performance. In a similar work on strain, Ghosh D *et al.* [235] analyzed the effect of strain on the electronic and optical properties of lead iodide perovskites. These studies collectively advocate that the strain can participate significantly in modulating the optical properties of the materials. Furthermore, it is significant to evaluate the stability of doped materials via formation energy calculations

for ascertaining their thermodynamic viability. A reduced formation energy signifies improved structural stability and dopant solubility; hence, decreasing defect formation and phase separation. Consequently, stability analysis plays a vital role in optimizing material performance for optoelectronic and photovoltaic applications.

Herein, the pristine and plasmonic metal-doped $LiNbO_3$ and $SrTiO_3$ (M= Ag, Al, Au, and Cu) are subjected to the compressive and tensile strain of varying intensities. The optical, structural, and electronic properties are computed, and the impact of the strain on the properties is analyzed. For understanding the electronic structure, the bandgap is computed for all the structures. The optical behavior is understood by calculating the parameters like absorption, refractive index, and dielectric function. All the results computed, altogether, emphasize the fact that the coexistence of doping and strain is an effectual approach for modulating the optoelectronic behavior of the lithium niobate and strontium titanate for photovoltaic and optoelectronic applications.

5.2 COMPUTATIONAL SET UP FOR CALCULATIONS

In this chapter, DFT-based calculations are performed to determine the electronic and optical properties of lithium niobate ($LiNbO_3$) and strontium titanate ($SrTiO_3$) with the coexistence of strain and doping. All the simulations are performed on Quantum ATK atomic-scale modeling software. The hexagonal unit cell of $LiNbO_3$, consisting of a total of 40 atoms of lithium, niobium, and oxygen, is built using the builder tool of Quantum ATK [220]. In the same way, the cubic cell of $SrTiO_3$ containing 40 atoms of strontium (Sr), oxygen, and titanium (Ti) is build. The geometry of the pristine unit cells is optimized to achieve the structure with the lowest possible ground state energy for further calculations. All the calculations related to geometry optimization are performed on the LACO ATK-DFT calculator with k-point sampling (Monkhorst-Pack) of 7x7x7 [238, 239, 242]. The exchange correlation functional of the generalized gradient approximation (GGA-PBE) is utilized for the calculation [82, 112, 225]. For geometry optimization, the LBFGS (quasi-Newton) method is utilized [82]. The geometry is relaxed till the interatomic forces between the atoms reach the limit of force tolerance of 0.05 eV/Å [77]. The maximum number of steps is set to 200, and stress tolerance is set to 0.005 $eV/Å^3$.
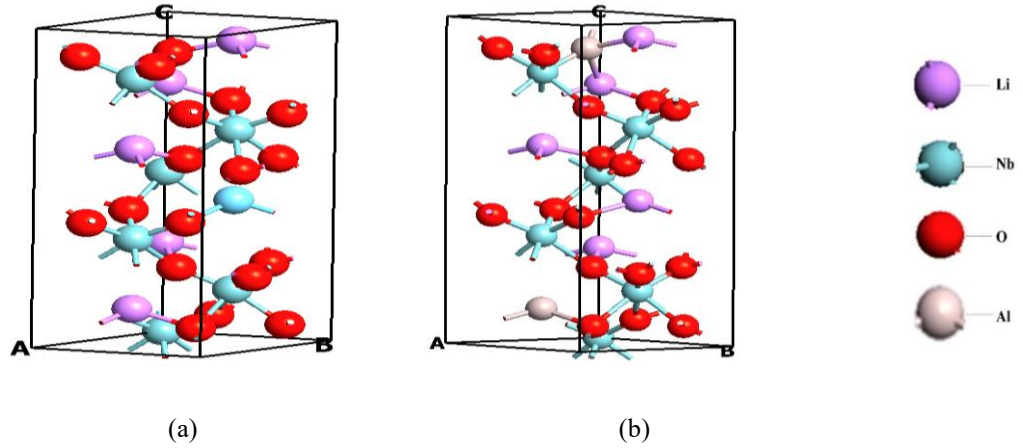
Fig. 5.1 Crystal structure of nit cell of (a) Undoped and (b) Al-doped Lithium niobate.

Afterward, the pristine crystals of $LiNbO_3$ and $SrTiO_3$ are doped with the plasmonic metal dopants (M=Al, Ag, Au, and Cu) with the 5% doping concentration. Subsequently, the tensile and compressive strains of varying intensities of 10% and 20% are applied on the pristine and M-$LiNbO_3$. On the other hand, the pristine and M-$SrTiO_3$ is applied with the compressive and tensile strain of 5% along with 10% and 20% to investigate the impact of strain on the optoelectronic properties. The appropriate value of the intensity of the strain to be subjected to these perovskites is taken from the previous research of strain engineering based on perovskite structures.

Among several studies, the Wu *et al.* [236] conducted a detailed review on the influence of strain on the properties of perovskite and concluded that the perovskite can be applied with a strain of 20% without any structural breakdown. It is also concluded that the suitable range of strain for tuning the band structure of the perovskites is 20%–13%. Further, in the similar work, the accepted range of the strain for tuning the band structure of the perovskites is from 5% to 10% [7, 8].

The same has been followed in this chapter, and the intensity of applied strain is kept between 5% and 20% to tune the electronic and optical properties of $LiNbO_3$ and $SrTiO_3$ for optoelectronic and photovoltaic applications. The electronic properties are calculated by employing the GGA approximation with the mesh cut-off of 150 Ry [18, 230]. However, meta-GGA Tran and Blaha (TB09) is used for calculating the optical properties to ensure the accuracy of the results, as indicated in the literature available on DFT calculations [210, 217]. The high-accuracy basis set of tier 3 with HGH [Z=4] pseudopotentials is adopted in the calculations to achieve computational accuracy [239, 240].

To validate the adopted DFT simulation parameters, properties of pristine LiNbO₃ and pristine SrTiO₃ are calculated and are then compared with the experimental and theoretical results reported in previous research [64, 66, 69, 101, 107]. The consistency of our calculated results with the previously reported results advocates the validity of the DFT simulation model adopted for calculations. For applying the compressive and tensile strain on the perovskites, the equation illustrated below is utilized.

$$\varepsilon = \frac{a - a_0}{a_0} \times 100\,\%$$
(5.1)

In the equation given above, ao is the value of the lattice constant perovskite (relaxed and without strain), and a represents the lattice constant after the application strain. The positive value of ε represents the tensile strain, and the negative value represents the compressive strain.

5.3 IMPACT OF STRAIN ON PRISTINE LINBO3

In this section, the pristine LiNbO₃ is applied with compressive and tensile strains of 10% and 20%. Further, the impact of strain on the electronic, structural, and optical properties is examined for optoelectronic and photovoltaic applications.

5.3.1 Structural and electronic properties of strained pristine LiNbO₃

LiNbO₃ is a perovskite, consisting of lithium, niobium, and oxygen atoms. The schematic structure of the hexagonal cell of pristine LiNbO₃, consisting of 40 atoms, is shown in Fig. 5.1 (a), the geometry of which is optimized using the GGA functional of DFT. The lattice constants for the pristine LiNbO₃ are a=5.204, b=5.204, and c=13.976, which are in good agreement with the previously calculated results [67, 118, 186, 234]. Further, the tensile strain and compressive strains of 10% and 20% intensities are applied on pristine LiNbO₃ to examine the effect of strain on various properties. Based on the DFT computation of the bandgap performed, it is found that the pristine LiNbO₃ is a wide bandgap material with a bandgap of 3.56 eV. The experimental value of the band gap of LiNbO₃ varies from 3.6 to 3.8 eV. The variation in the values of the experimental bandgap is because of the changes in the Li: Nb ratio. The calculated value of the bandgap in this chapter for strained and unstrained pristine LiNbO₃ is tabulated in Table 5.1. The value of the bandgap of pristine LiNbO₃ is in good accordance with the values reported in previous theoretical and experimental studies [67].

Table 5.1 Bandgap and lattice constants for unstrained and strained $LiNbO_3$.

$LiNbO_3$	Bandgap (eV)	VBM (eV)	CBM (eV)
Unstrained	3.56	-1.80	1.76
10% C	4.23	-0.63	3.6
20% C	4.15	-0.64	3.51
10% T	2.54	-0.66	1.88
20% T	1.71	-0.68	1.03

From Table 5.1, it is evident that the bandgap is significantly reduced for the tensile strain of 10% and 20%, which opens up the scope for possibilities of finding improved absorption in the visible region in comparison to the unstrained $LiNbO_3$. The reduced value of the bandgap is 2.54 eV for the 10% tensile strain and 1.71 eV for the tensile strain of 20%. The bandgap reduction is due to the downward shifting of the value of minima of the conduction band (CBM) and upward shifting of valence band maxima.

The calculated values of bandgaps also signify that with the increase in the intensity of strain, the decrease in bandgap increases, which indicates the possibility of more redshift with increased strain. The reduction in the value of the bandgap due to the high tensile strain implies that strain engineering is an efficient technique for tuning the positions of band edges. Further, the bandgap is increased on the application of the compressive strain of 10% and 20%, which is indicative of the blueshift. The compressive strain opens up the possibilities of the shifting of the absorption towards the hog wavelength regions.

5.3.2 Optical properties of strained pristine $LiNbO_3$

The main shortcoming associated with $LiNbO_3$ is its wide bandgap, which ultimately limits its absorption in the visible range of the optical spectrum. In this section of the chapter, the optical properties of pristine $LiNbO_3$ are calculated, and further, the effects of tensile strain and compressive strain on optical properties are investigated. The fundamental parameter for obtaining the optical properties of any material is the dielectric function, which is the elucidation of the interaction of the material with the applied electromagnetic field. The dielectric function (real) of any material is related to the slowing down of the light and resembles the refractive index. Its large value is desired as it represents the lesser slowdown of the propagating light.

The imaginary part is related to the optical absorption and represents the damping. The absorption coefficients for varied energy and wavelength for unstrained and strained LiNbO₃ are illustrated in Fig. 5.2. As illustrated in Fig. 5.2 (b), for unstrained LiNbO₃, the absorption is high in the ultraviolet region of the optical spectrum. The energy-dependent absorption of the pristine LiNbO₃ is found in the higher energy range only. From Fig. 5.2 (a), it is clear that the absorption starts around 3.5 eV, which is equal to the bandgap of the pristine LiNbO₃. On applying the compressive strain (10% and 20%), the absorption is found shifted into the low wavelength regions with no absorption in the visible region (blueshift). Most of the peaks of absorption are found in high-energy ranges (see Figs. 5.2 (g) and 5.2 (h)).

On applying the tensile strain, redshift occurs, and the absorption is shifted in the lower energy range (high wavelength) as clearly seen in Figs. 5.2 (e) and 5.2 (f). As shown in Figs. 5.2 (i) and 5.2 (j), that wavelength-dependent absorption is enhanced in the visible region for the tensile strains of 10% and 20%, which is desirable for optoelectronic applications. The value of visible region absorption is highest for the tensile strain of 20%, which is in accordance with the highest reduction in the bandgap. The peaks of the absorption are in well accordance with the calculated value of bandgaps.

The energy-dependent dielectric constants for unstrained and strained (tensile and compressive) LiNbO₃ are calculated using meta-GGA and are illustrated in Fig. 5.3. The real part and imaginary dielectric function for unstrained LiNbO₃ are illustrated in Fig. 5.3 (a) and Fig. 5.3 (b). Further, the tensile strain and compressive strain of intensities of 10% and 20% are applied on the pristine LiNbO₃, and the dielectric function is plotted with photon energy as illustrated in Fig. 5.3 (c)- 5.3 (j). As illustrated in Fig. 5.3 (b), the imaginary dielectric constant is zero for unstrained LiNbO₃ up to 3 eV. On application of the tensile strain of 10% and 20%, the imaginary dielectric constant is found shifted towards lower energies. Which can be interpreted as the reflection of electromagnetic radiation and improved optical absorption in the visible range.

For unstrained LiNbO₃, the major peaks of the imaginary dielectric constant are at ~3 eV and ~5 eV, having the largest peak at ~3.5 eV. For the compressive strains of intensities 10% and 20%, the peaks of the imaginary dielectric function are not shifted towards the lower energies. However, for the tensile strains of 10% and 20%, the peaks are found shifted in the lower energies, with the highest peak of absorption at ~2.5 eV and 1~.7 eV, respectively.
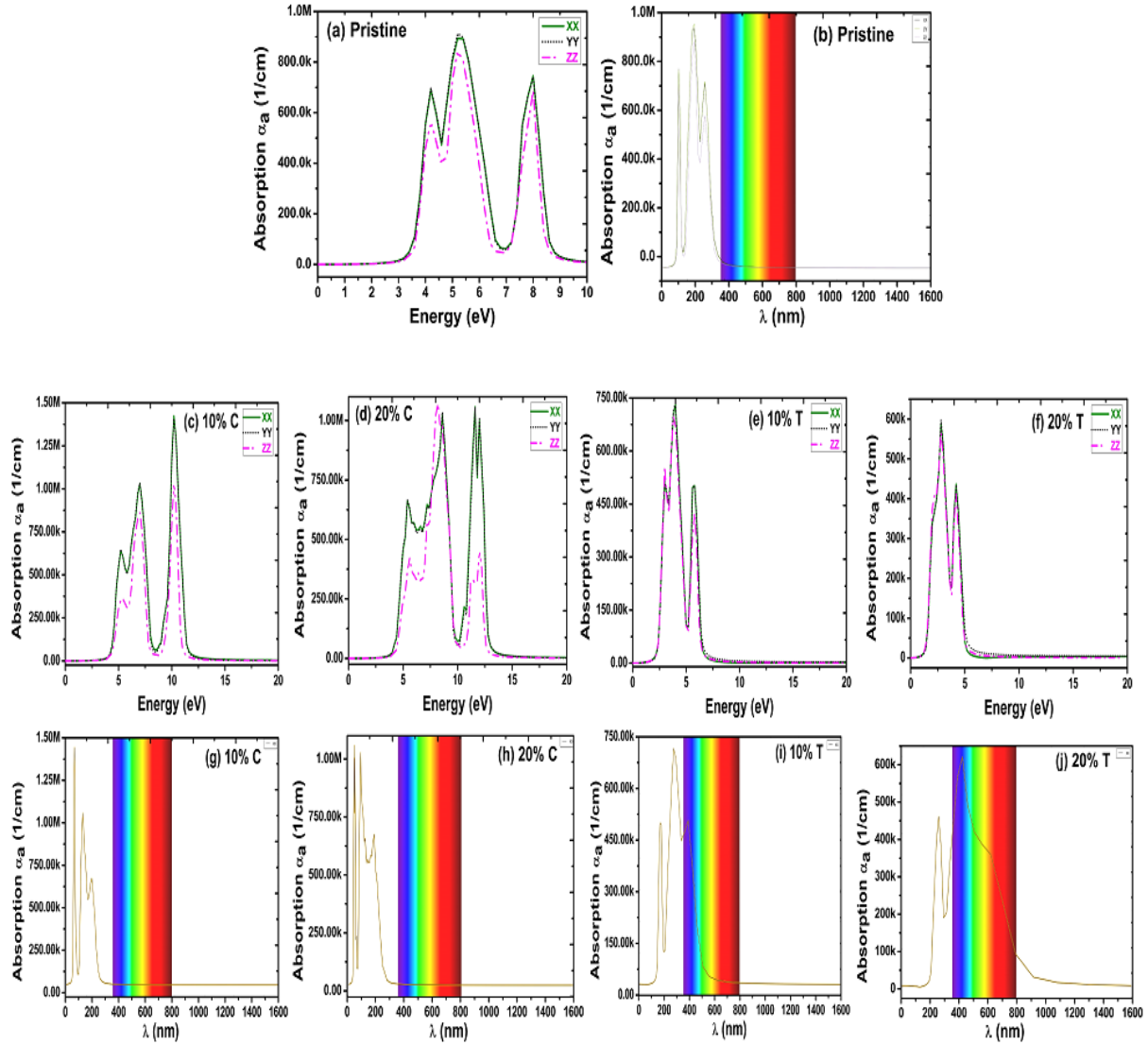
Fig. 5.2 Absorption coefficient of lithium niobite and its strained structures.

Due to the application of the tensile strain of 10% and 20%, the shifting of peaks of the imaginary dielectric constant towards lower energies can be interpreted as the narrowing of the bandgap under strain. For the tensile strain of 20%, the intensity of the peak is highest due to inter-band transition in VB and CB and is favorable for visible light absorption. The real part of the dielectric constant for unstrained $LiNbO_3$ is illustrated in Fig. 5.3 (a), and for strained $LiNbO_3$, it is illustrated in Fig. 5.3 (c)- 5.3 (f). For tensile strains of 10% and 20%, the value of the real dielectric function at zero eV is increased, and this increase is high for the high intensity of the strain.
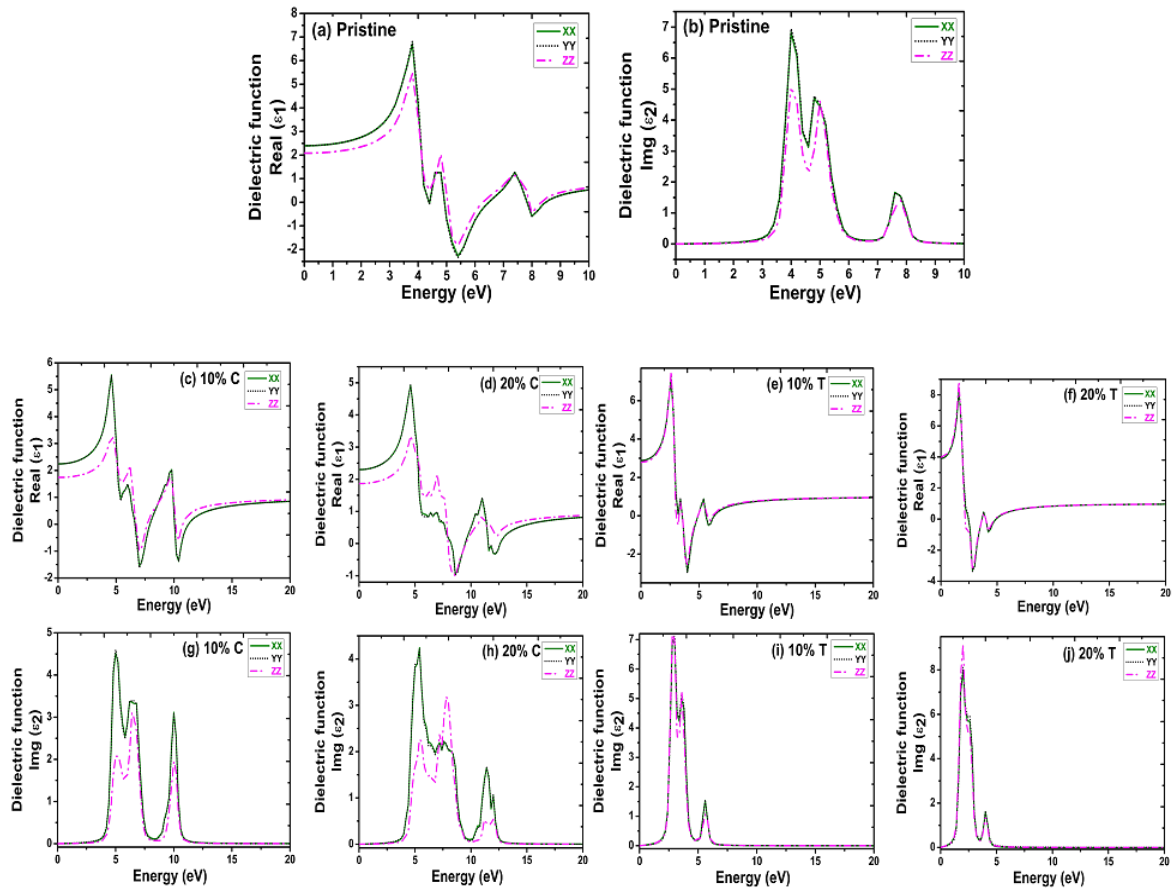
Fig. 5.3 Dielectric function of lithium niobite and its strained structures.

The peaks of the real dielectric function are shifted towards lower energies due to the application of tensile strains of 10% and 20% with the highest value of the peak for the strain of 20%. The shifting of the peaks of the dielectric function towards lower energies and amplified values of the peak for the tensile strain of 10% and 20% are favorable for optoelectronic applications). The high absorption in the visible region and improved dielectric response due to the application of tensile strain make the strained LiNbO₃ a potential candidate for optoelectronic applications.

5.4 IMPACT OF STRAIN ON PLASMONIC METAL DOPED LINBO3

This portion of the chapter focuses on the analysis of the structural, electronic, and optical properties of pristine and metal-doped LiNbO₃. Further, the metal-doped LiNbO₃ is subjected to the tensile and compressive strain of varying intensities of 10% and 20%. The electronic and optical properties of strained structures are computed, and the same is compared with the respective unstrained structure.

5.4.1 Structural and electronic properties of strained and plasmonic metal doped LiNbO₃

The hexagonal cell of LiNbO₃ is doped with the metal dopants (M= Ag, Au, Cu, and Al) and structural, and electronic properties are calculated in this section. The doping concentration is kept at 5% for all the dopants and the doping model adopted is illustrated in Fig. 5.1 (b). Further, the metal-doped LiNbO₃ is applied with tensile and compression strain of 10% and 20% to investigate the effect of strain on optical and electronic properties. Before calculating the properties, the geometry of the unit cells of all undoped and doped LiNbO₃ are relaxed. The values of lattice constants of the pristine and all doped LiNbO₃ are elucidated in Table 5.2.

Table 5.2 Lattice parameters of undoped and doped LiNbO₃.

Structure	a (Å)	b (Å)	c (Å)	Volume (Å3)	Bandgap (eV)
Pristine	5.20	5.20	13.97	378.49	3.56
Ag-doped	5.55	5.55	14.71	453.29	1.78
Al-doped	5.50	5.50	15.06	456.63	2.02
Au-doped	5.50	5.50	14.34	434.75	1.36
Cu-doped	5.55	5.55	14.41	444.85	0.96

Further to understand the impact of doping and strain on the electronic structure, bandgap is calculated. The bandgap is an effective measure of understating the alignment of bands and position of fermi levels in any material. It is significant to calculate the bandgap due to its notable influence on the optical properties [34, 35]. The computed value of the bandgap of undoped and unstrained LiNbO₃ is 3.56 eV, which is in good accordance with the previously reported values of experimental and theoretical research.

Table 5.3 Bandgap (eV) of tensile and compressive strained LiNbO₃.

Structure	GGA				Meta GGA			
	Compressive		Tensile		Compressive		Tensile	
	10%	20%	10%	20%	10%	20%	10%	20%
Ag-doped	1.26	0.86	2.31	0.61	1.43	0.07	0.36	0.61
Al-doped	0.81	1.33	1.45	0.23	0.47	1.41	0.49	0.35
Au-doped	1.55	1.06	1.24	0.73	2.37	1.28	2.62	0.91
Cu-doped	1.18	0.78	0.96	0.41	0.07	0.04	0.22	0.13

The calculated bandgaps of the metal-doped LN after the application of tensile and compression strains of 10% and 20% are elucidated in Table 5.3. The bandgaps for all the strained structures are calculated with the exchange correlation functionals GGA and meta-GGA to make the optical spectra more consistent with bandgaps. For Ag-doped LN, the bandgap is 1.78 eV. On the applied compressive strain, the bandgap reduces to 1.26 eV and 0.86 eV for the intensity of 10% and 20%, respectively, signifying increased electronic delocalization. For the applied tensile strain, the bandgap initially rises to 2.31 eV for 10% strain, but decreases to 0.61 eV for 20% strain, indicating a shift towards increased conductivity.

The bandgap of Al-doped LN is 2.02 eV; nevertheless, compressive strain makes a significant decrease to 0.81 eV at 10% strain; subsequently, the bandgap is increased to 1.33 eV at 20% strain. For tensile strain, the bandgap remains comparatively steady with a value of 1.45 eV at 10% strain but significantly decreases to 0.23 eV at 20% strain, indicating a strain-dependent modulation of the bandgap.

For Au-doped LN, the value of the bandgap is 1.36 eV. Compressive strain initially elevates it to 1.55 eV (10%), then decreases it to 1.06 eV (20%). However, the tensile strain modulated the bandgap to 1.24 eV at 10% but diminishes to 0.73 eV at 20%, suggesting a propensity for bandgap narrowing at high tensile strain. In Cu-doped LN, the unstrained bandgap is 0.96 eV, which increases marginally to 1.18 eV at 10% compressive strain and decreases to 0.78 eV at 20%. Under tensile strain, the bandgap remains 0.96 eV at 10% strain but significantly reduces to 0.41 eV at 20% strain, indicating a transition to a more conductive state at elevated strain levels. These results illustrate the significant interaction between strain and electrical structure, presenting prospects for bandgap engineering in optoelectronic applications.

5.4.2 Optical properties of strained and plasmonic metal doped LiNbO$_3$

The optical properties of strained metal-doped LiNbO$_3$ are calculated and plotted in this section. For pristine LN, most of the absorption peaks are in higher energy ranges, and the absorption is limited to the UV range (~350 nm) of the optical spectrum. The presence of absorption in the UV region only limits the applicability of undoped and unstrained LN for optoelectronic and photovoltaic applications. The imaginary dielectric constant for undoped and unstrained LN has the strongest peak ~3.5 eV, which is in line with the absorption. The lower energy peaks of the imaginary dielectric constant signify the low excitation energy and

are responsible for the lower visible light absorption. The aim of the coexistence of doping and strain is to shift the optical absorption towards the visible range of the optical spectrum through metal doping and strain engineering.
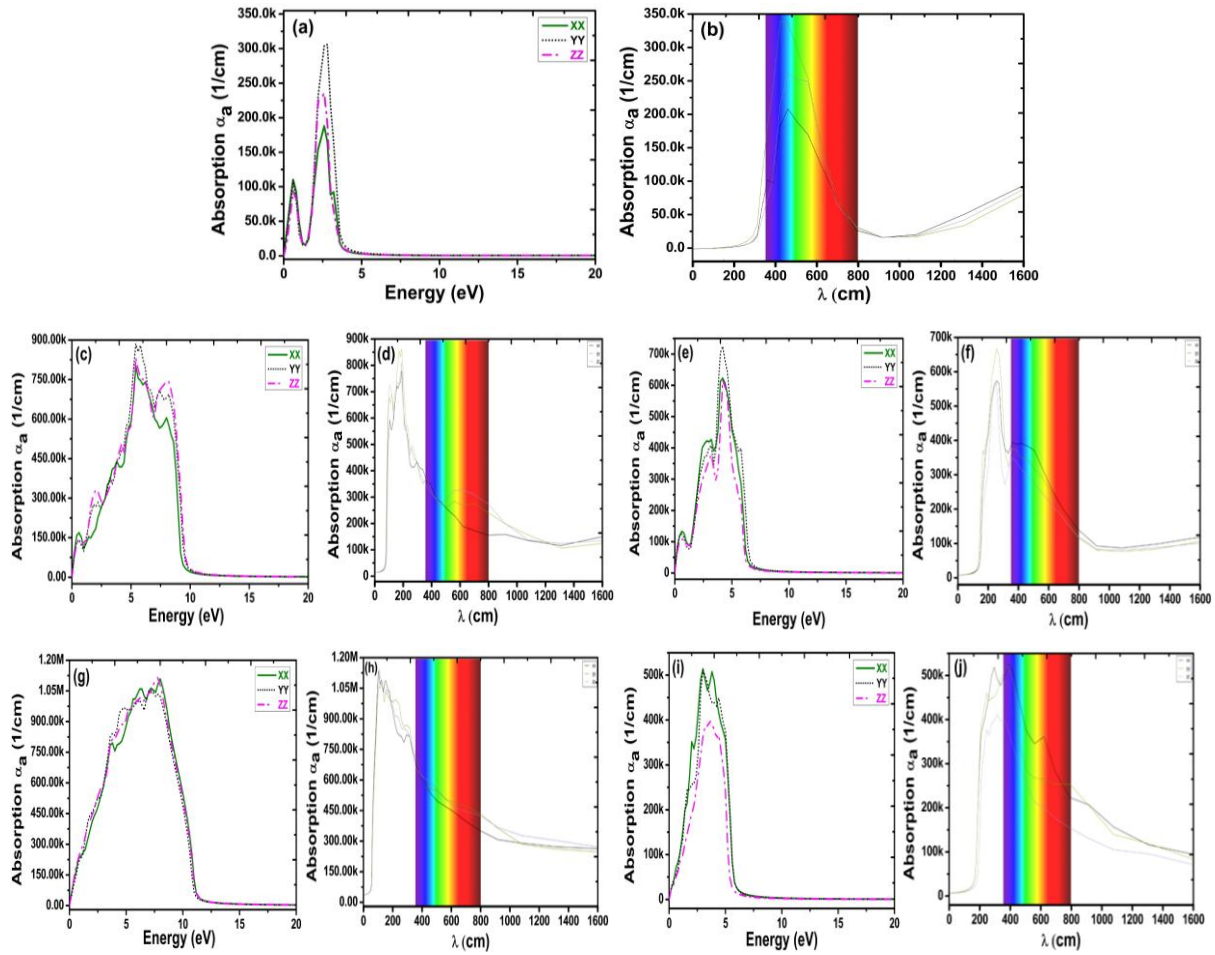
Fig. 5.4 Absorption coefficient for Ag- doped LN (a) and (b) unstrained, (c) and (d) 10% compressive strain, (e) and (f) 20% compressive strain, (g) and (h) 10% tensile strain and (i) and (j) 20% tensile strain.

Fig. 5.4 elucidates the absorption coefficient (energy and wavelength-dependent) of unstrained and strained Ag-doped $LiNbO_3$. For Ag-doped $LiNbO_3$, the peaks of absorption are found at lower energies (Fig. 5.4 (a)) as compared to the undoped $LiNbO_3$. The absorption of the Ag-doped $LiNbO_3$ is shifted completely in the visible region due to surface plasmonic resonance as compared to the undoped structure (Fig. 5.4 (b)). The absorption peaks are predominately found from ~400 nm to ~800 nm, which is favorable for optoelectronic and photovoltaic applications. Further, the absorption coefficient (energy and wavelength-dependent) is plotted for LN for the varying tensile and compressive strains of 10% and 20%. For 10% tensile and compressive strain, the absorption peaks are found from 0 to 10 eV (Figs. 5.4 (c) and 5.4 (g)).
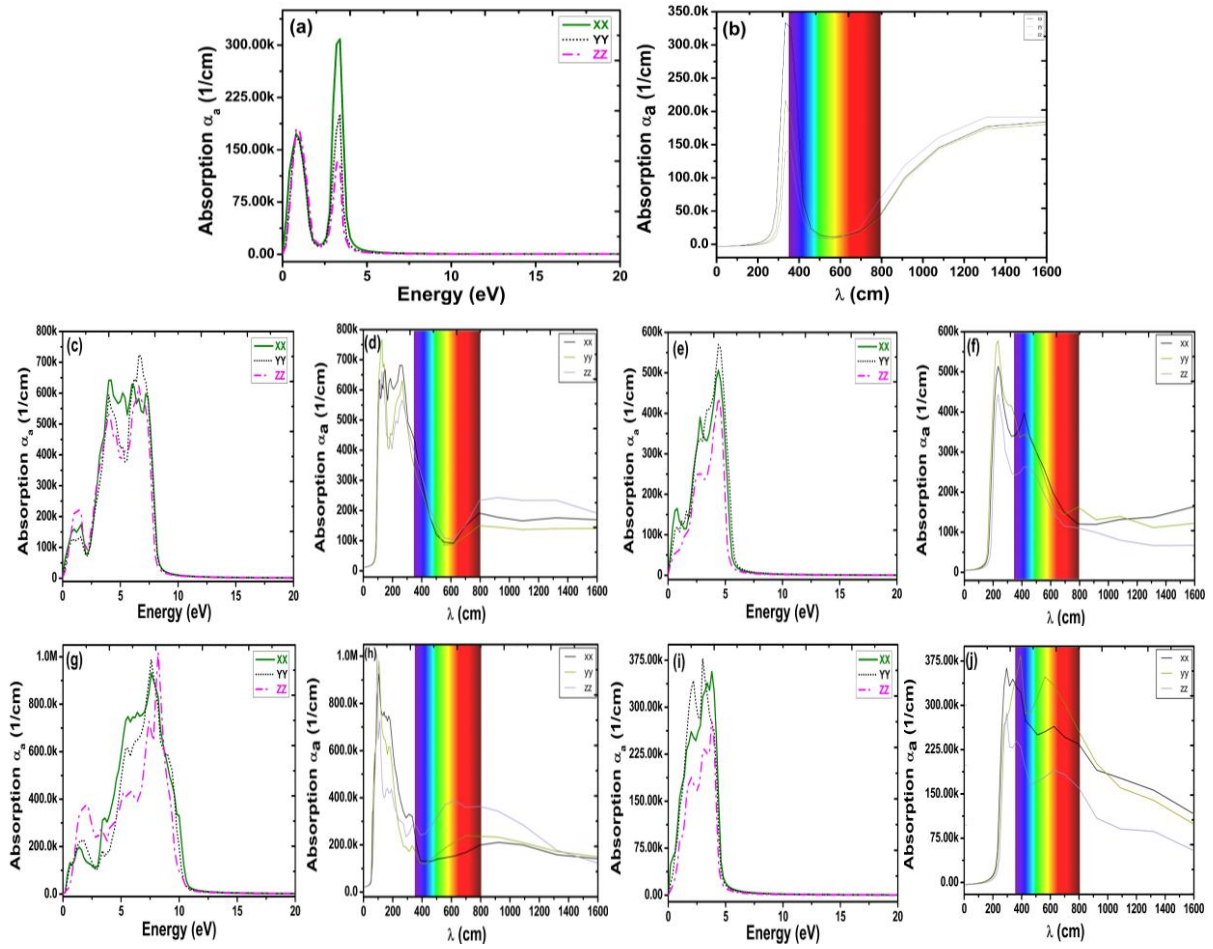
Fig. 5.5 Absorption coefficient for Al- doped LN (a) and (b) unstrained, (c) and (d) 10% compressive strain, (e) and (f) 20% compressive strain, (g) and (h) 10% tensile strain and (i) and (j) 20% tensile strain.

The absorption is slightly shifted towards higher energies for these strains and has non-zero values for ~600 nm to ~800 nm (redshift) (Fig. 5.4 (d) and 5.4 (h)). For higher values of the tensile and compressive strain of 20% (Figs. 5.4 (e) and 5.4 (i)), the absorption peaks are found in lower energy ranges, i.e., from 0 to 5 eV. The optical absorption is shifted significantly towards the visible region of the optical spectrum for high tensile and compressive strain. For the tensile strain of 20%, the absorption peak attains a value of ~500 k, which is higher than the unstrained structures.

For unstrained and strained Al-doped LiNbO₃, the absorption coefficients (energy and wavelength-dependent) are plotted in Fig. 5.5. For lower values of tensile and compressive strain, the absorption peaks are found in low energy ranges, and a very small absorption is found in the visible region of the optical spectrum (redshift) (Figs. 5.5 (c), 5.5 (d), 5.5 (g), and 5.5 (h)). For the high value of tensile and compressive strain (20%), the absorption peaks are predominantly available in the lower energy ranges, i.e., from 0 eV to 5 eV (Figs. 5.5 (e) and

5.5 (i)). The absorption is significantly shifted to higher wavelengths with increased value for the 20% compressive strain (Fig. 5.5 (f)). For 20% compressive strain, the absorption is largely found in the visible region (~300 nm to 800 nm) with a value higher than the unstrained Al-doped LiNbO₃. This evidences the improvement in the optical properties of Al-doped LiNbO₃ for optoelectronic applications.
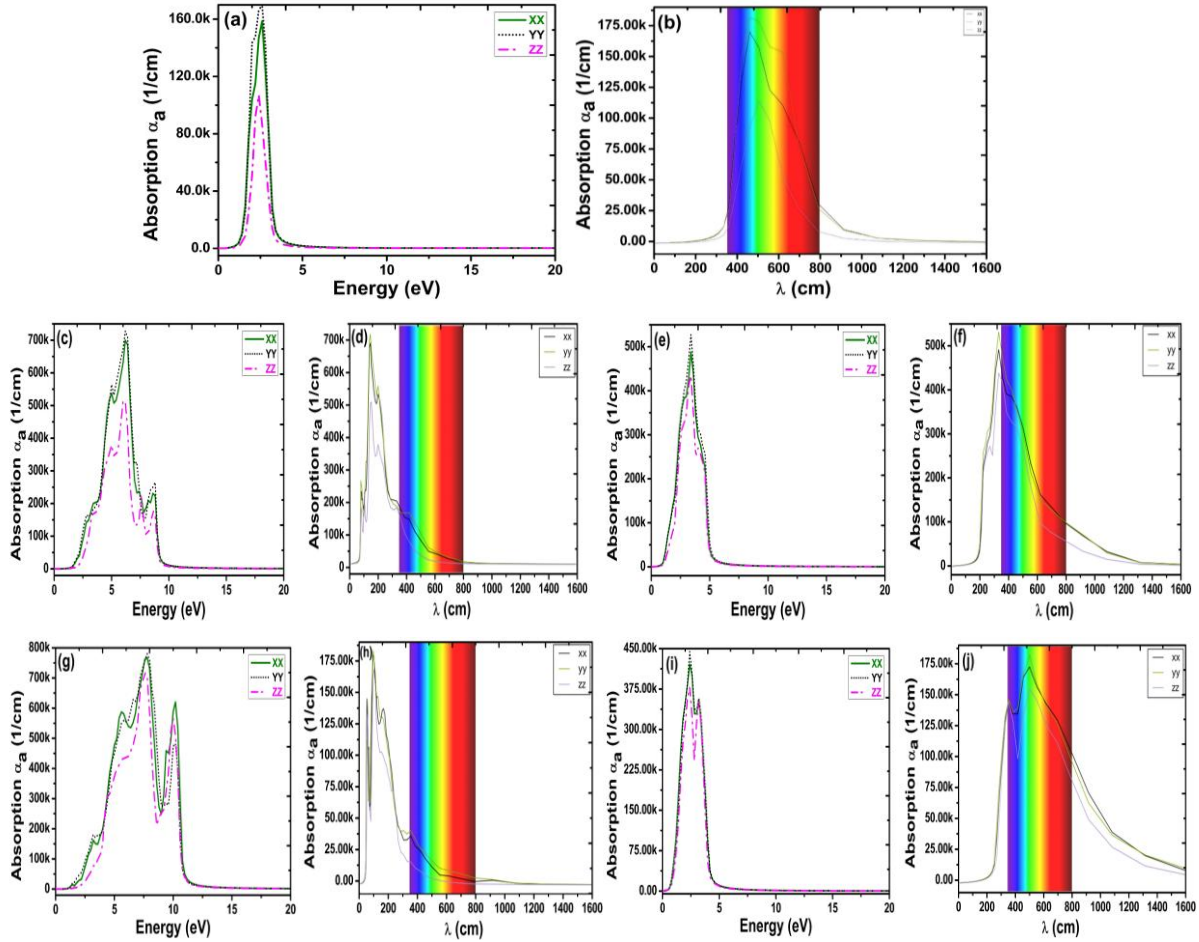
Fig. 5.6 Absorption coefficient for Au- doped LN (a) and (b) unstrained, (c) and (d) 10% compressive strain, (e) and (f) 20% compressive strain, (g) and (h) 10% tensile strain and (i) and (j) 20% tensile strain.

The absorption coefficient (energy and wavelength-dependent) for the strained and unstrained Au-doped LiNbO₃ is represented in Fig 5.6. Au is one of the best metal dopants with tremendous chemical stability. As seen in Figs. 5.6 (a) and 5.6 (b), due to doping of Au in LiNbO₃, the absorption is shifted in low energy ranges and is found completely in the visible region (~400 nm to ~800 nm).

This improved visible light absorption makes Au-doped LN LiNbO₃ a promising candidate for optoelectronic and photovoltaic applications. On application of tensile and compressive strain of low intensity (10%), the absorption is found in the energy range 0 eV to 10 eV and shifted

slightly towards the higher wavelengths (red-shift) (Figs. 5.6 (c), 5.6 (d), 5.6 (g), and 5.6 (h)). Furthermore, for a high value of the tensile and compressive strain (20%), the absorption is found completely in the visible region (Figs. 5.6 (f) and 5.6 (j)). Specifically, for the tensile strain of 20%, the value of the absorption is high as compared to the unstrained structure, which makes it prominent for optoelectronic and photovoltaic applications.
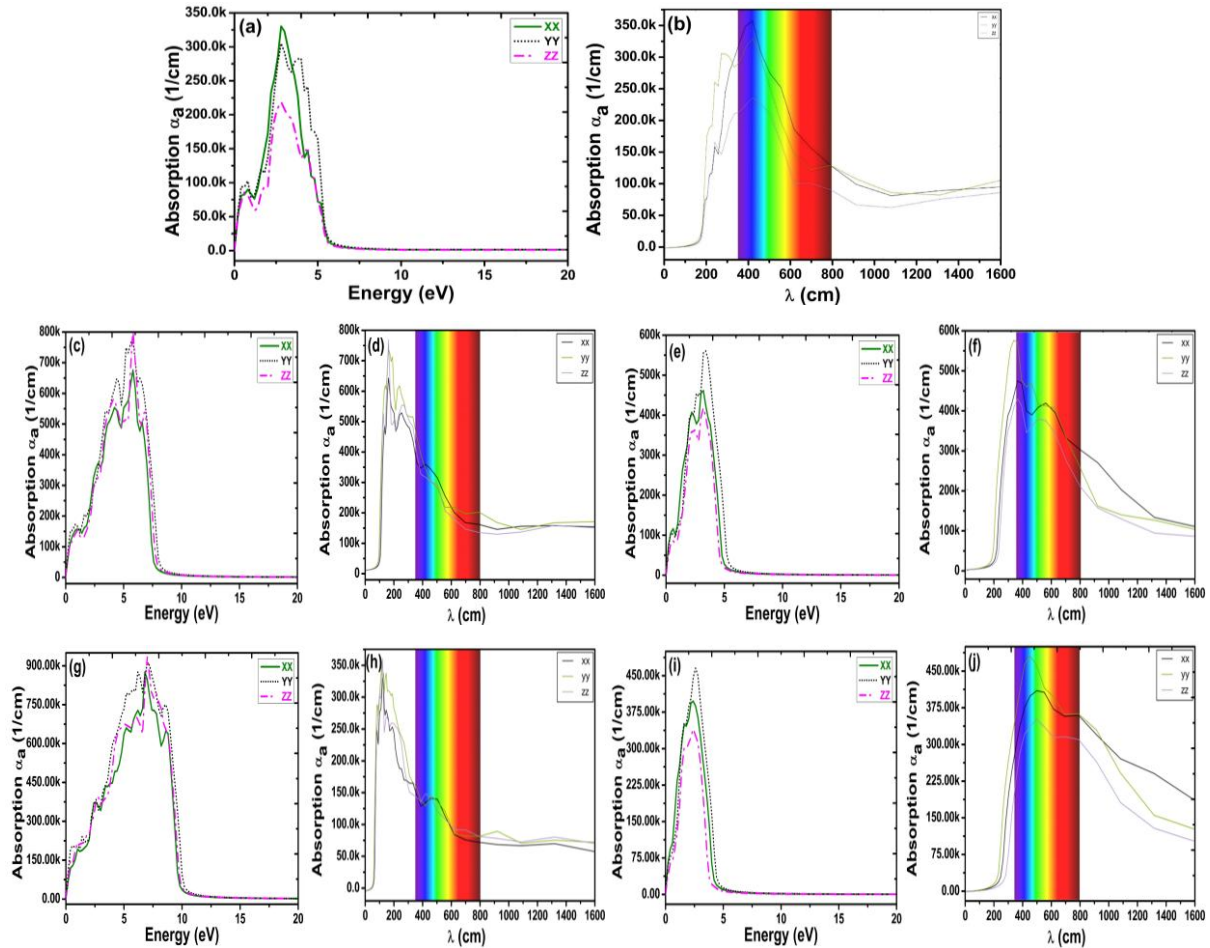
Fig. 5.7 Absorption coefficient for Cu- doped LN (a) and (b) unstrained, (c) and (d) 10% compressive strain, (e) and (f) 20% compressive strain, (g) and (h) 10% tensile strain and (i) and (j) 20% tensile strain.

The absorption coefficient (energy and wavelength-dependent) for the strained and unstrained Cu-doped LiNbO₃ is represented in Fig 5.7. For a strain of low intensity (10%), the absorption is slightly found in the visible region (redshift) (Figs. 5.7 (d) and 5.7 (h)). For the high value of compressive and tensile strain (20%), the absorption peaks are limited to the low energy ranges. For these values of strain, the absorption is predominantly shifted to the visible region. The value of the absorption peak is high in comparison to the absorption peak of the unstrained structure for 20% tensile and compressive strain, which makes it more suitable for optoelectronic-based applications.
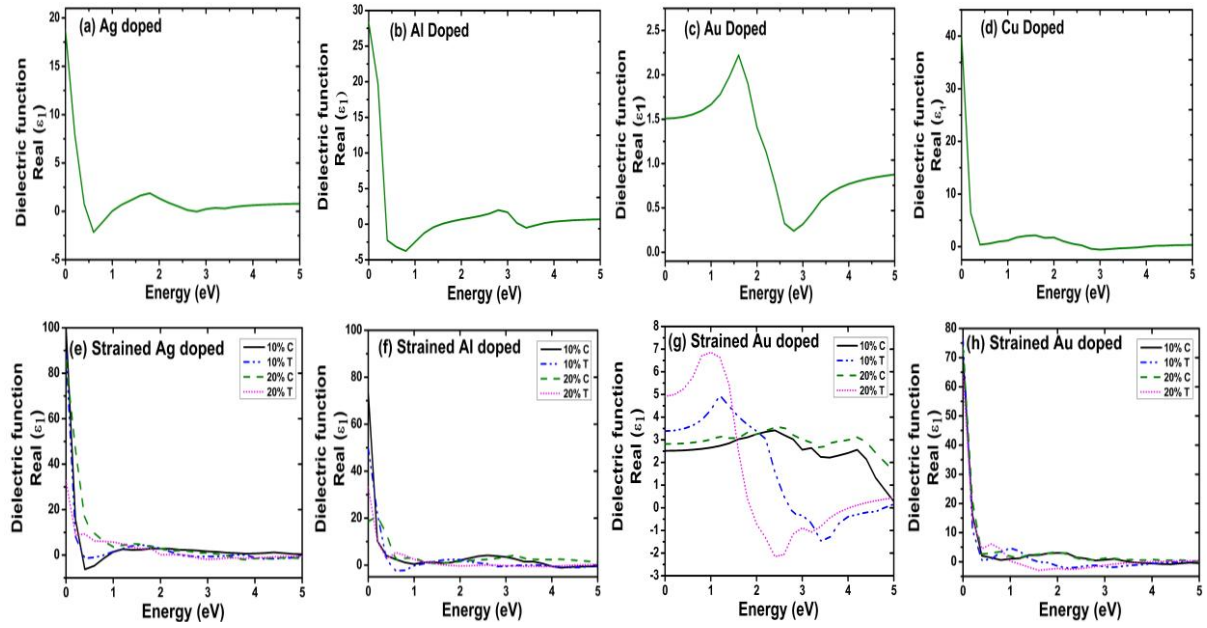
Fig. 5.8 Real dielectric constant for unstrained and strained LN (a) and (e) Ag-doped, (b) and (f) Al-doped, (c) and (g) Au-doped and (d) and (e) Cu-doped.

Concussively, for all the doped LiNbO$_3$, the effect of the compressive and tensile strain of low intensity (10%) is not prominent to tune the optical properties. A small amount of redshift is absorbed in all the metal-doped LiNbO$_3$ on the application of small compressive and tensile strain. For the high value of compressive and tensile strain, the absorption is significantly tuned in the visible region. This tuning is very much prominent for the tensile strain. Owing to the enhanced visible light absorption, the application of the high value of tensile strain can be considered a prominent approach for improving the optoelectronic and photovoltaic efficiency of LiNbO$_3$.

The real and imaginary dielectric constants for all the metal-doped LiNbO$_3$ for varying tensile and compressive strains are shown in Fig. 5.8 and Fig. 5.9. For all the structures, the imaginary dielectric constants have peaks in line with the absorption coefficient. Due to strain, the values of the imaginary dielectric constant are increased in comparison to the unstrained structures, which signifies the smaller value of excitation energy and results in an improved value of visible light absorption.

Further, there is a shifting in the peaks of imaginary dielectric constants due to the application of tensile and compressive strain, in accordance with the shifting of absorption peaks. For all the doped and strained structures, the imaginary dielectric constant values are consistent with the absorption. The refractive index for strained and unstrained metal-doped LiNbO$_3$ is plotted

in Fig. 5.10. The peaks of the refractive index are following the peaks of the real dielectric constant, which shows the steadiness of the calculated results.
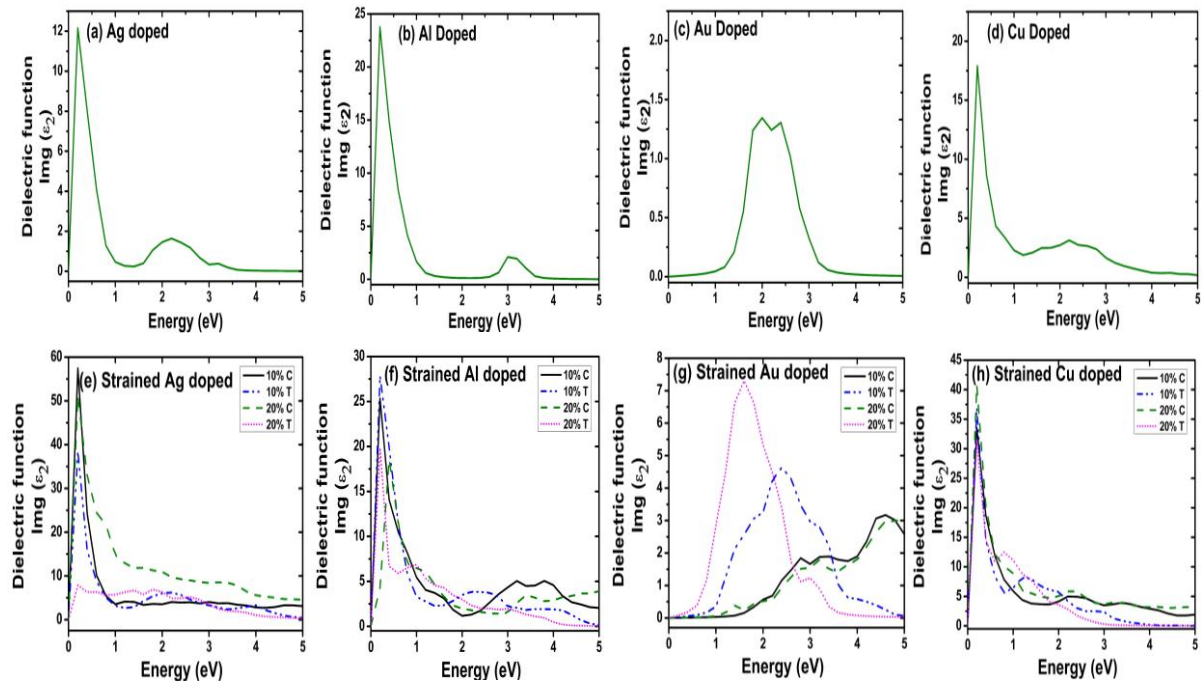
Fig. 5.9 Imaginary dielectric constant for unstrained and strained LN (a) and (e) Ag-doped, (b) and (f) Al-doped, (ac and (g) Au-doped and (d) and (e) Cu-doped.
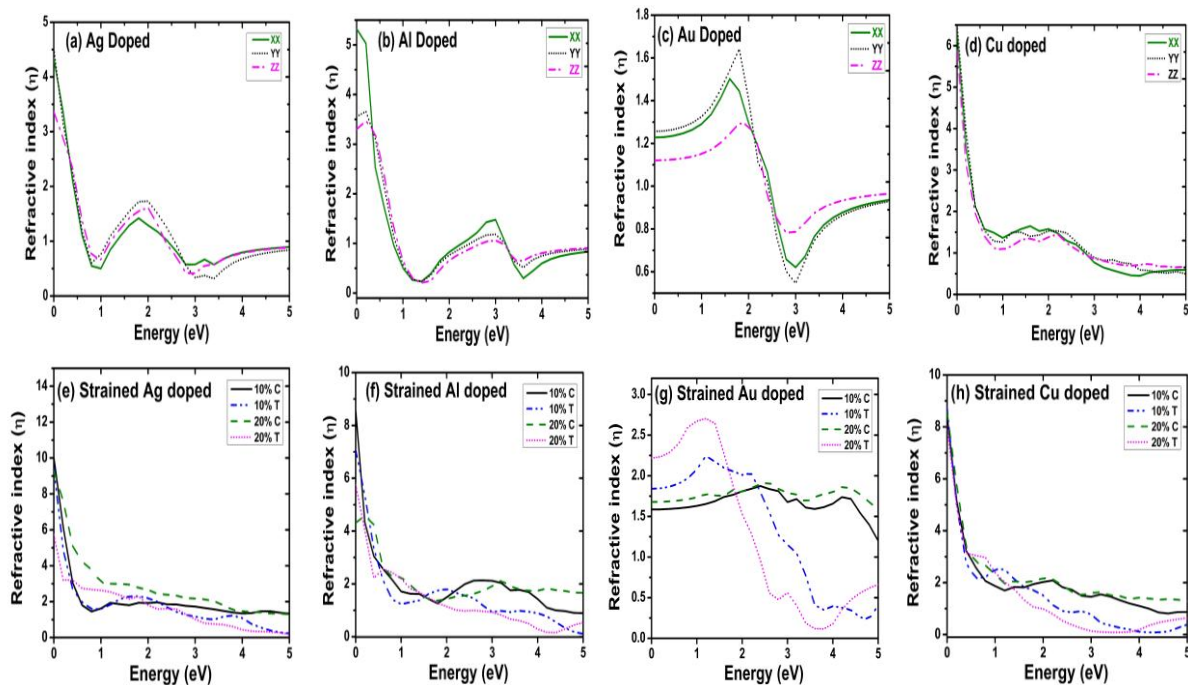
Fig. 5.10 Refractive index for unstrained and strained LN (a) and (e) Ag-doped, (b) and (f) Al-doped, (c) and (g) Au-doped and (d) and (e) Cu-doped.

The values of the refractive index are increased for all the doped structures, which is indication of the increased life of the light propagating in the doped and strained LiNbO₃. The increase in the refractive index is further increased on the application of strain. The absorption peaks in the strained and unstrained metal-doped LiNbO₃ shifted towards the lower energy values, due to which more photons will get absorbed in the visible range. This is also justified by the wavelength-dependent absorption plotted in the earlier section.

5.4.3 Compression of the optical properties of pristine, doped, and strained LiNbO₃

A brief comparison of the calculated optical absorption of the pristine and doped LiNbO₃ (strained and unstrained) computed is tabulated in Table 5.4. From Table 5.4, it is evident that the absorption is improved in the visible region due to doping in comparison to the pristine structure, for which it was found in the UV region only. Furthermore, on the application of the strain, the absorption is extraordinarily enhanced in the visible region, specifically for the compressive and tensile strain of 20% intensity.

Table 5.4 Compression of the optical properties of pristine, doped, and strained LiNbO₃.

	Doping	Optical absorption			
LiNbO3		Ultra-violate	Visible	Absorption Peak	Absorption
Pristine	Pristine	High	Zero	1000 k UV	UV
Unstrained	Ag-doped	Low	High	350 k visible	Visible
	Al-doped	Low	Low	350 k UV	IR
	Au doped	Low	High	175 k Visible	Visible
	Cu doped	Low	High	350 K Visible	Visible
10% Compressive	Ag-doped	High	Low	800 k UV	UV
	Al-doped	High	Low	700 k UV	UV
	Au doped	High	Low	700 k UV	UV
	Cu doped	High	Low	700 k UV	UV
20% Compressive	Ag-doped	High	Low	650 k UV	Visible
	Al-doped	High	Low	550 k UV	Visible
	Au doped	Low	High	500 k Visible	Visible

	Cu doped	Low	High	550 k Visible	Visible
10% Tensile	Ag-doped	High	Low	1000 k UV	UV
	Al-doped	High	Low	1000 k UV	UV
	Au doped	High	Low	175 k UV	UV
	Cu doped	High	Low	350 k UV	UV
20% Tensile	Ag-doped	Low	High	550 k visible	Visible
	Al-doped	Low	High	350 K visible	Visible
	Au doped	Low	High	175 k Visible	Visible
	Cu doped	Low	High	500 k Visible	Visible

In this chapter, the coexistence of two methods, i.e., doping and strain, is adopted, which is a more effective approach for tuning the optical properties. The doped $LiNbO_3$ responds strongly to the compressive strain and tensile strain specifically of 20% intensity and improves the optical absorption, which is beneficial for optoelectronic-based applications.

5.5 STRAIN ENGINNERING ON PRISTINE AND PLASMONIC METAL DOPED SRTIO3

In this segment of the chapter, the optical, structural, and electronic properties of pristine and doped structures of $SrTiO_3$ are computed by employing the DFT computations. Further, the structures of pristine and doped $SrTiO_3$ are subjected to strain (tensile and compressive) with intensities of 5%, 10%, and 20%. All the properties of strained $SrTiO_3$ are calculated, and variations in the properties due to strain are analyzed.

5.5.1 Structural and electronic properties of strained M-SrTiO3

Under this segment, the structural and electronic properties of the strained M-$SrTiO_3$ (M=Ag, Al, Au, and Cu) are computed. The cubic cell ($2\times2\times1$) of $SrTiO_3$ (space group pm3m) is build for the calculations. As shown in Fig. 5.11, the cubic cell of $SrTiO_3$ has 8 atoms of strontium and titanium each and 24 oxygen atoms [112]. The computed lattice constants of pristine and doped $SrTiO_3$ after the geometry relaxation are illustrated in Table 5.5.
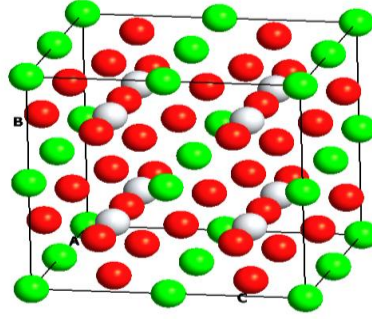
Fig. 5.11 Cubic unite cell of pristine SrTiO₃ crystal.

To validate our computational reliability, the calculated geometrical parameters of pure SrTiO₃ are equated with the previous research results. Our computation results show that the lattice constants of pristine SrTiO3 are a=b=c=3.945 Å. These values of structural parameters for pristine SrTiO₃ are in good agreement with the previous research results [64, 107, 111, 112]. Subsequently, the SrTiO₃ is doped through the metal dopants Ag, Al, Au, and Cu (doping concentration of 5%). The doping in SrTiO₃ is performed on the Ti site only, as the existing research on SrTiO₃ advocates that the metal ions enter the Ti site preferably due to the comparable ionic radius [112].

Table 5.5 Lattice parameters and bandgap of pure and doped SrTiO₃.

Model	a=b=c (Å)	Volume (Å³)	Bandgap (eV)	References
Pristine	-	-	3.25	Experimental [243]
Pristine	3.90	59.31	-	Experimental [111]
Pristine	3.94	61.39	2.15	DFT [112]
Pristine	3.94	61.16	2.94	DFT Calculations of this chapter
Ag- SrTiO₃	4.08	67.91	1.57	
Al- SrTiO₃	3.93	60.69	1.77	
Au- SrTiO₃	4.09	68.41	1.56	
Cu- SrTiO₃	4.07	67.41	1.54	

The lattice constants of pristine and plasmonic-doped SrTiO₃ are tabulated in Table 5.5. Furthermore, the pure and metal-doped SrTiO₃ are subjected to the strain of compressive and tensile with intensities of 5%, 10%, and 20%. The values of the intensities applied are taken from the available research on strain engineering of the materials. According to the previous research, the suitable range of the strain to be applied for tuning the band structure of the perovskites is from 10% to 20%. The band structure of pure and doped SrTiO₃ are computed

111

and the effects of the applied strain (tensile and compressive) on the bandgap are analyzed. The calculated value of the bandgap for pristine $SrTiO_3$ is 2.94 eV.

Table 5.6 Bandgap (eV) of pure and doped $SrTiO_3$ under strain.

Structure		Compressive			Tensile		
	5%	10%	20%	5%	10%	20%
Ag-doped	0.198	0.249	0.406	0.13	0.031	0.058
Al-doped	0.02	0.008	0.091	0.25	0.030	0.174
Au-doped	0.108	0.145	0.914	0.091	0.031	0.011
Cu-doped	0.104	0.148	0.012	0.074	0.026	0.049

The bandgap of the pristine and M-$SrTiO_3$ (M=Ag, Al, Au, and Cu) are illustrated in Table 5.6. For all the dopants, the bandgap is remarkably lowered. The bandgap is decreased due to the introduction of impurity states due to doping. The lowering of the bandgap is further increased on the application strain of intensities 5%, 10%, and 20%. The bandgaps of strained M-$SrTiO_3$ are illustrated in Table 5.6. The lessening of the bandgap because of doping and strain is favorable for the possibilities of enhancement of the optical properties of the photovoltaic and optoelectronics applications.

5.5.2 Optical properties of strained M-SrTiO3

In this section, the optical properties of pure and doped (M = Al, Ag, Au, and Cu) $SrTiO_3$ are calculated. Subsequently, the influence of the applied strain (tensile and compressive) of intensities of 5%, 10%, and 20% on the optical properties of $SrTiO_3$ (pure and doped) is evaluated. The calculations of the optical parameters are important to categorize the prospective utilization of the materials for various applications. The optical properties of all the structures of $SrTiO_3$ (pristine, doped, and strained) are calculated by utilizing the computed values of the dielectric function (real and imaginary). The acceptance of computation is validated by comparing our results calculated for pristine $SrTiO_3$ with the existing research work [111, 112].

Fig. 5.12 Absorption coefficient of pristine SrTiO₃: Unstrained ((a) and (b)), and Strained (5% compressive (c) and (d), 5% tensile (e) and (f), 10% compressive (g) and (h), 10% tensile (i) and (j), 20% compressive (k) and (l) and 20% tensile (m) and (n)).

To understand the impact of the applied biaxial strain on the optical response of SrTiO₃, the pristine structure of SrTiO₃ is subjected to the strain (tensile and compressive) of 5%, 10%, and 20% intensities. Furthermore, the absorption coefficients (a function of energy and wavelength) of the strained crystals are calculated and compared with the unstrained crystal (Fig. 5.12). For the pristine crystal of SrTiO₃, the absorption is limited only in the region of lower wavelengths and high energies, which limits its solar efficiency. The optical absorption for the pristine unstrained crystal of SrTiO₃ (Figs. 5.12 (a) and 5.12 (b)) is predominantly found in the UV region (~0 to 200 nm) with height peaks of the absorption in the high energy range (at ~25 eV). The absorption of the pristine SrTiO₃ begins around ~3 eV, which resembles the bandgap. On the applied strain, the optical absorption modulates depending on the type and intensity of the applied strain.

For the compressive strain of 5% and 10%, the absorption is found to shift significantly towards the visible and near-visible region, starting from ~200 nm and available till ~800 nm range (Figs. 5.12 (c), 5.12 (d), 5.12 (g), and 5.12 (h)). For the compressive strain of 20%, the absorption is enhanced drastically in the visible region, but there are non-zero absorption values for the high wavelengths region (IR) (Fig. 5.12 (k) and 5.12 (l)). For the tensile strains of 5%, 10%, and 20%, the absorption starts from ~400 nm and has a high value in the visible region. For the biaxial tensile strains of 5%, 10%, and 20%, the absorption is zero in the UV region and completely shifted towards the low energies (redshift), with improved value in the visible region absorption as compared to the unstrained crystal of SrTiO$_3$ (Figs. 5.12 (e), 5.12 (f), 5.12 (i), 5.12 (j), 5.12 (m), and 5.12 (n)).
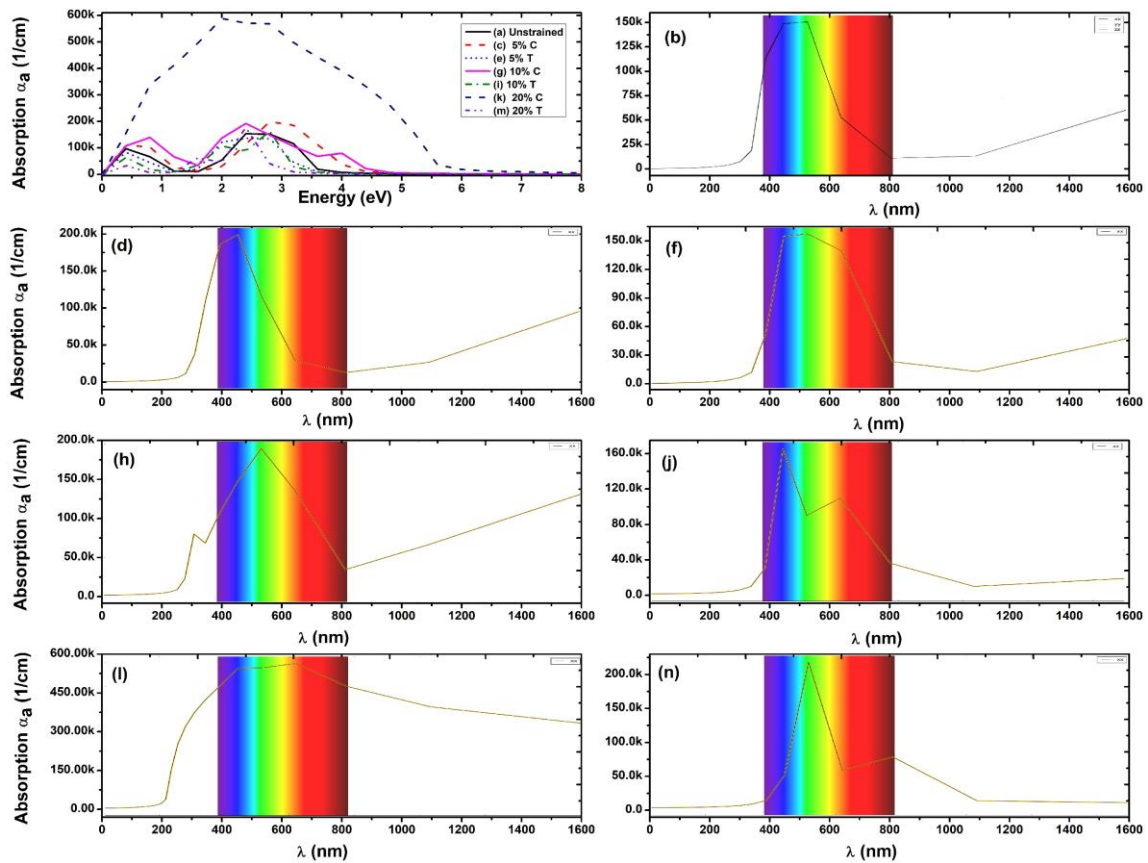
Fig. 5.13 Absorption coefficient of Silver-doped SrTiO$_3$: unstrained ((a) and (b)), and Strained (5% compressive (c) and (d), 5% tensile (e) and (f), 10% compressive (g) and (h), 10% tensile (i) and (j), 20% compressive (k) and (l) and 20% tensile (m) and (n)).

Conclusively, the tensile and compressive strain enhances the visible light absorption of SrTiO$_3$, which improves solar efficiency and is desired for optoelectronic applications. Further, the crystal of SrTiO$_3$ is doped through the metal dopants Ag, Al, Au, and Cu, and subsequently,

strain is applied to the doped crystals. The implementation of the coexistence of techniques (strain and doping) might be a more efficient method for modulating the optical properties of SrTiO₃ for desired applications.

The absorption coefficients for the Ag-doped SrTiO₃ and its strained structure (tensile and compressive) are plotted in Fig. 5.13. Due to the doping of Ag, the absorption starts at low energy (Figs. 5.13 (a) and 5.13 (b)), and the peak of the absorption is found at ~2.5 eV (redshift). The non-zero absorption in the UV region of the pristine crystal is shifted towards the high wavelengths and is predominantly available in ~300 to 800 nm. Furthermore, on the applied compressive strains of intensities of 5% and 10%, the absorption is available in the ~300 to 800 nm range with the enhanced value of visible region absorption (Figs. 5.13 (c), 5.13 (d), 5.13 (g), and 5.13 (h)).

Fig. 5.14 Absorption coefficient of Aluminum-doped SrTiO₃: unstrained ((a) and (b)), and Strained (5% compressive (c) and (d), 5% tensile (e) and (f), 10% compressive (g) and (h), 10% tensile (i) and (j), 20% compressive (k) and (l) and 20% tensile (m) and (n)).

Subsequently, the Ag-doped SrTiO₃, applied with the tensile biaxial strain of intensities of 5%, 10%, and 20%, has almost zero absorption in the UV region, but the absorption in the visible

region is narrow and low as compared to the compressive strain (Fig. 5.13). For the compressive strain of 20%, the absorption curve contains the peak at ~600 nm with an amplitude of ~650k, which is the highest among all the crustal of strained and unstrained Ag-doped SrTiO₃.
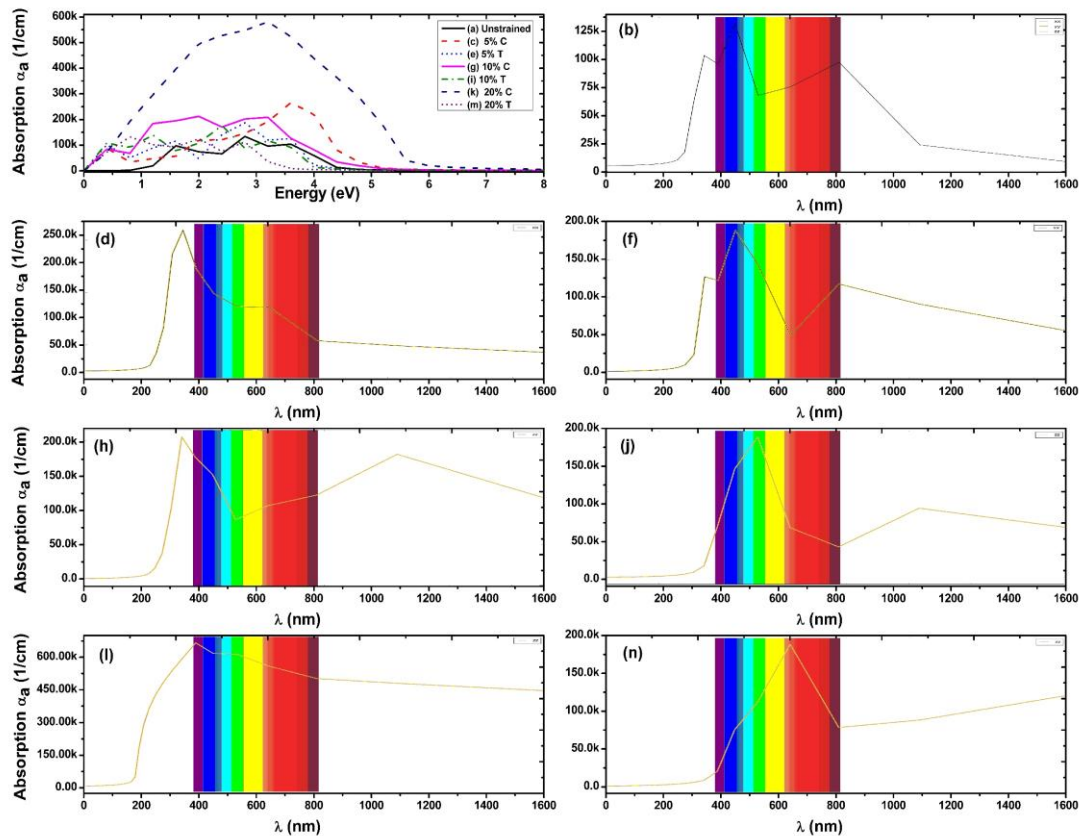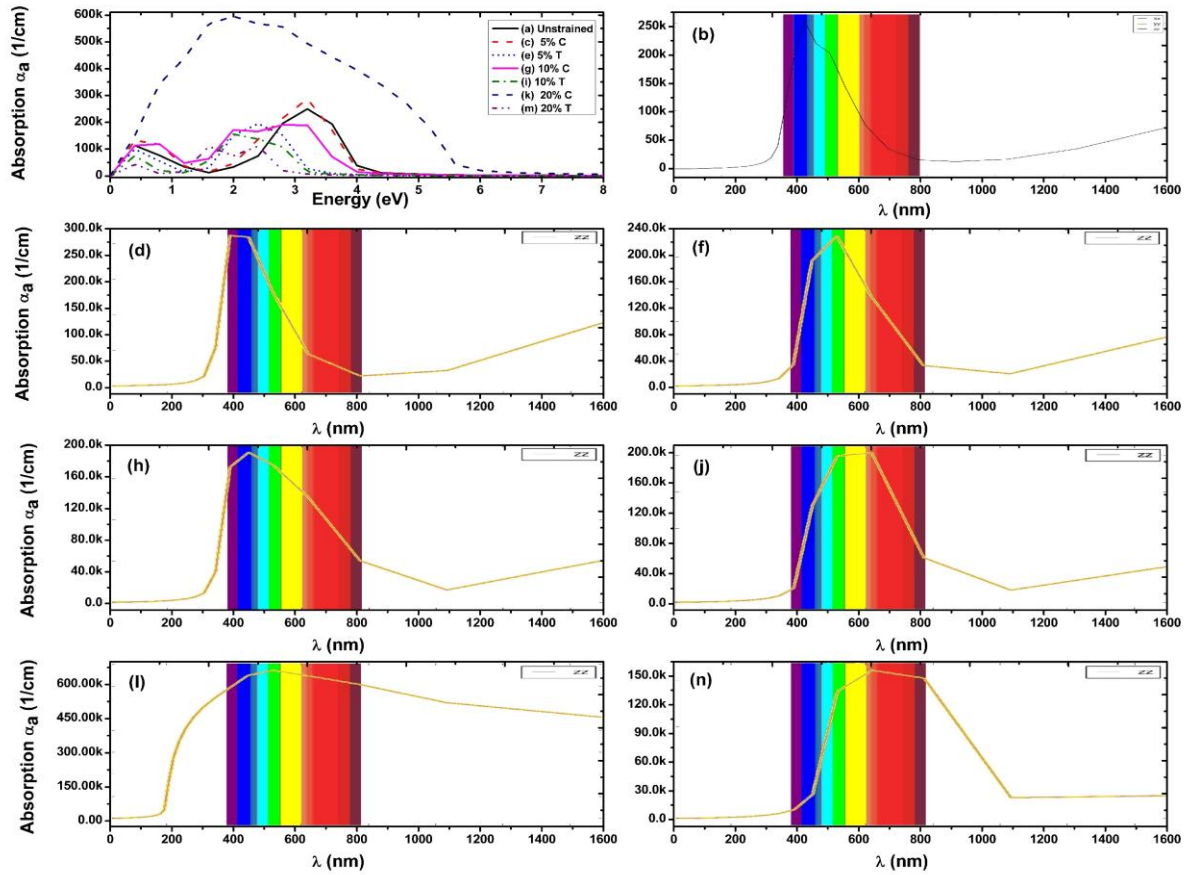

Fig. 5.15. Absorption coefficient of Gold-doped SrTiO₃: unstrained ((a) and (b)), and Strained (5% compressive (c) and (d), 5% tensile (e) and (f), 10% compressive (g) and (h), 10% tensile (i) and (j), 20% compressive (k) and (l) and 20% tensile (m) and (n)).

For the Al-doped crystal of SrTiO₃, the absorption is shown in Fig. 5.14. As shown in Fig. 5.14 (a) and 5.14 (b), as a result of doping with Al, the absorption begins at ~0.5 eV and has non-zero peaks in the range of wavelengths ~300 to 1100 nm. The non-zero absorption is available in the high wavelength range, and the values of absorption are amplified in the visible range as compared to the pure crystal of SrTiO₃. The Al-doped crystal of SrTiO₃, with the compressive applied strain of 5%, 10%, and 20%, has an enhanced visible absorption. Specifically, for the high compressive strain of 20%, the amplitude of the highest absorption peak is found at ~450 nm with an amplitude of ~600 k.

The applied tensile strain on Al-doped SrTiO₃ shifts the absorption in the visible region with some extension towards the IR region. All the crystals of Al-doped SrTiO₃ under tensile strain have an absorption peak with a value of ~200k, which is larger than the absorption peak of unstrained crystals. Further, the doping of the Au on the crystal of SrTiO₃ tunes the absorption from ~400 to 800 nm, with an absorption peak of ~250k at ~500 nm (Fig. 5.15). Also, the applied compressive strain shifts the absorption in the visible and near-visible regions (300 to 800 nm). The absorption peak is highest in the visible region for the compressive biaxial strain of large intensity of 20%. Nevertheless, the compressive strain also increases the absorption in the IR region slightly. The Cu doping on SrTiO₃ also tunes the absorption in the visible region, which further improves due to the strain having the highest value of visible region absorption for the compressive strain of 20% (Fig. 5.16).
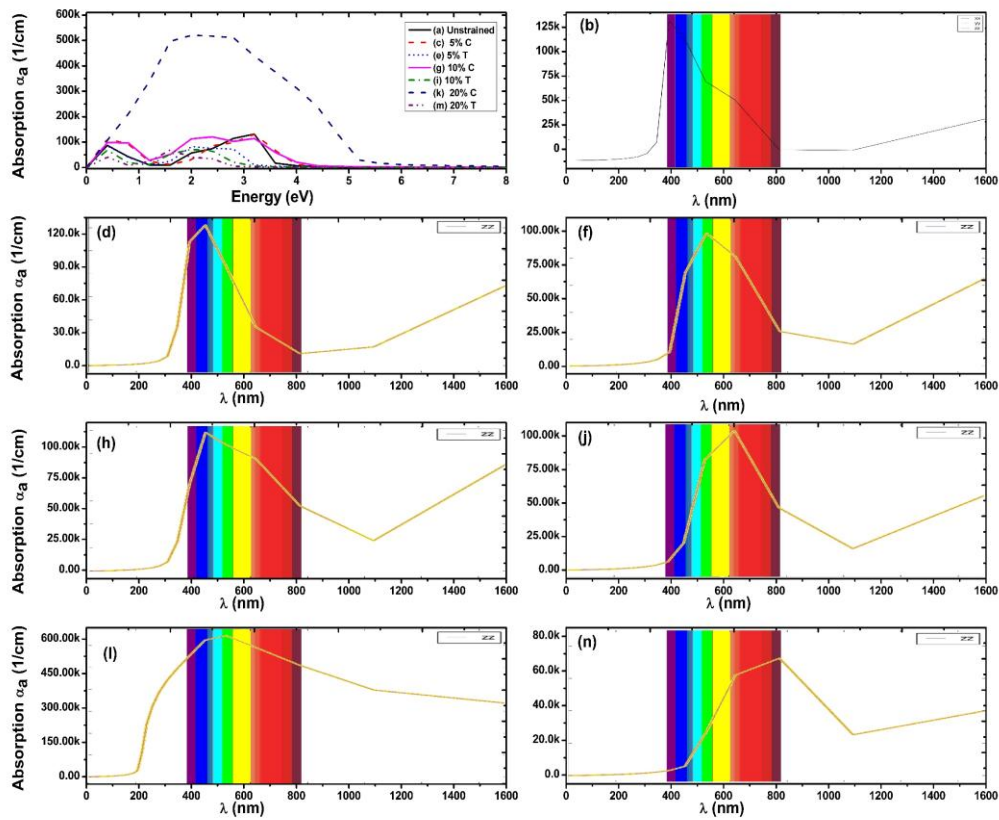
Fig. 5.16 Absorption coefficient of Copper-doped SrTiO₃: unstrained ((a) and (b)), and Strained (5% compressive (c) and (d), 5% tensile (e) and (f), 10% compressive (g) and (h), 10% tensile (i) and (j), 20% compressive (k) and (l) and 20% tensile (m) and (n)).

It is evident from Figs. 5.12 (b), 5.13 (b), 5.14 (b), 5.15 (b), and 5.16 (b) that the UV region absorption of the pure SrTiO₃ is completely tuned towards the visible and near-visible region

due to the doping of plasmonic metal dopants. The increased absorption is due to the collective oscillation of the charge carriers (surface plasma effect). Among the plasmonic dopants, the Ag and Au show better plasmonic behavior in comparison to the Al and Au. Additionally, gold has excellent chemical stability and shows remarkable properties in the visible region. The reduction in the bandgap due to doping is lowest for the dopant Al because of its lowest ionic radius among all the plasmonic dopants. Further, the large size of the dopant ion reduces the scattering of the light and increases the plasmonic effect. The same is evident from the lowest improvement in visible light absorption due to the doping of the Al (smallest ionic radius among all dopants).
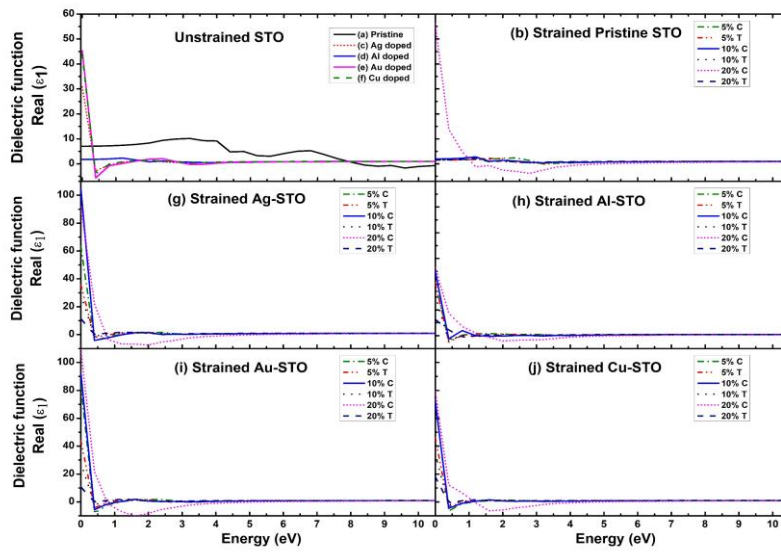
Fig. 5.17 Dielectric function (real) of SrTiO₃ (undoped, doped and strained).

The dielectric constants for the pristine, doped, and strained SrTiO₃ are shown in Fig. 5.17 and Fig. 5.18. As the dielectric constant is directly related to the absorption coefficient, the peaks of the dielectric constants are in accordance with the absorption coefficient. The value of the dielectric constants (imaginary) is increased due to the applied strain (Fig. 5.18), which indicates the low value of the energy of excitation and improves the absorption. The value of the dielectric constant is highest for the compressive strain of 20%. The strained SrTiO₃ results in the border and stable absorption as compared to the pristine structure, which is useful for optoelectronics applications. The refractive indexes for all the structures of SrTiO₃ are calculated from the value of the dielectric function and are represented in Fig. 5.19. As shown in Fig. 5.19, the refractive index of all the structures of SrTiO₃ completely follows the trends of the absorption coefficient and dielectric function. The peak of refractive index for the pristine SrTiO₃ is ~3 eV, which is in accordance with the peak of the dielectric constant. After doping,

the values of the corresponding refractive index are high in the low energy region, and the value of the refractive index is further increased on the application of the strain.
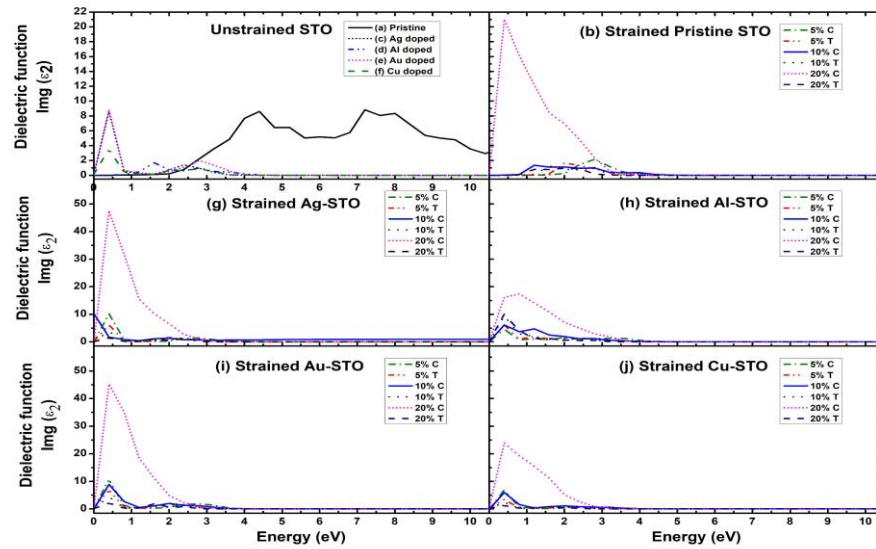
Fig. 5.18 Dielectric function (imaginary) of $SrTiO_3$ (undoped, doped and strained)
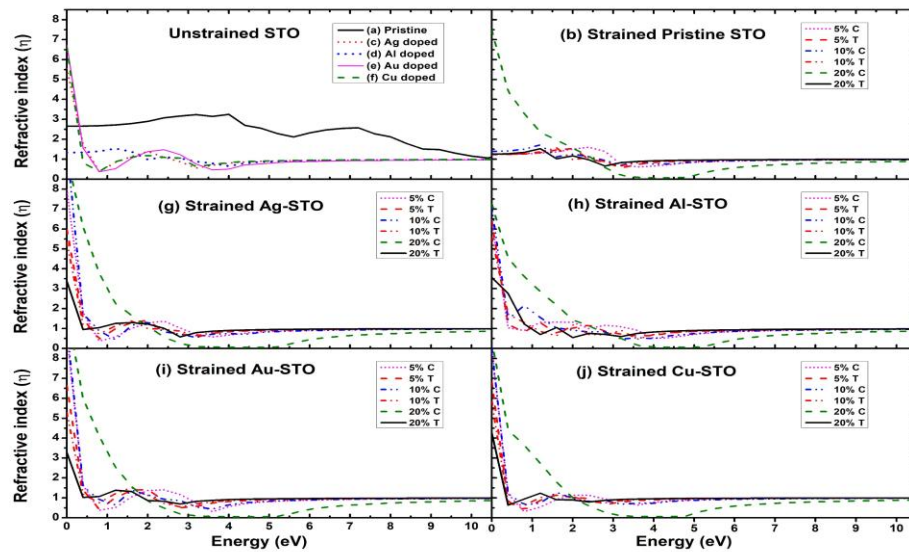
Fig. 5.19 Refractive index of $SrTiO_3$ (undoped, doped and strained).

The large value of the refracting index corresponds to the large absorption and results in the long life of the light in the material. Similarly, the low values of the refractive index for high energy, after the doping and strain, represent the lower absorption. The value of the intrinsic refractive index is ~2.7 for the pristine $SrTiO_3$, and the same becomes ~7 due to the applied compressive biaxial strain of intensity 20%. Similarly, the computed value of the intrinsic refractive index improved due to doping and increased further with strain, having the largest

value for the compressive strain of 20%. Improvements in the refractive index of SrTiO₃ due to the coexistence of doping and strain increase photon absorption, which is favorable for solar and optoelectronics applications.

5.6 STRUCTURAL STABILITY OF DOPED SRTIO3

To investigate the structural stabilities of doped structures, the total energy calculations are performed on pristine and doped SrTiO₃. The stability of any nanostructure can be effectively defined by utilizing the formation energy and binding energy. The formation and binding energy of pure and doped SrTiO₃ are computed by using the ground state total energy as illustrated in Table 5.7 with the relation given below [37].

$$E_{Binding} = -\frac{(E_T - xE_{Sr} - yE_{Ti} - zE_O - kE_{M(Au,Al,Au,Cu)})}{x+y+z} \tag{5.2}$$

In the equation given above ET is the computed energy (SrTiO3 and M-SrTiO3), Esr is the computed energy of Sr, E is the computed energy of O, ETi is the computed energy of Ti, and Em is the computed energy of the dopant. x, y, z, k, and N are the number of atoms. The formation energy is calculated by using the equation given below.

$$E_{Formation} = -\frac{(E_{Doped} - E_{Pristine} - xE_{M(Au,Al,Au,Cu)})}{N} \tag{5.3}$$

In the equation given above, SrTiO₃ is the computed energy of doped SrTiO₃, Epristine is the computed energy of pure SrTiO₃, and EM is the computed energy of the dopant. x and N are the total numbers of dopant atoms and the total number of atoms in the nanocrystal, respectively.

The results of binding energy and formation energy are illustrated in Table 5.7. As shown in the table, the value of the binding energies is negative for all the structures of SrTiO₃, which indicates the stability in the doped and pristine SrTiO₃.

Table 5.7 Formation energy of pure and doped SrTiO₃.

Structure	Total Energy	Binding energy	Formation energy
Pure-SrTiO₃	-12239.6	-581.026	
Ag- Doped Al- Doped	-14248.96	-683.888	-145.213
	-12453.64	-627.449	-88.7743
Au- Doped	-14159.82	-678.331	-139.657

The values of the binding energy of the doped $SrTiO_3$ are more negative in comparison to the pristine $SrTiO_3$, which shows that the doped structures reach more stability. In the doped structures of $SrTiO_3$, the value of binding and formation energy is the largest negative for the dopant Cu, which indicates that this structure is highly stable among all the doped structures and energetically more favorable for doping.

5.7 SUMMARY OF THE IMPORTANT RESULTS

1. First principles DFT (Density Functional Theory) calculations are performed to investigate the electronic and optical properties of pristine and metal-doped (Ag, Al, Au, Cu) $LiNbO_3$ and $SrTiO_3$ under compressive and tensile strain.

2. Doping and strain caused lattice distortions and volume expansion in $LiNbO_3$ and $SrTiO_3$, significantly affecting its crystal structure. These modifications influenced the electronic and optical properties of the material.

3. The bandgap of pristine $LiNbO_3$ is 3.56 eV, limiting its optical absorption to the UV region (300–400 nm). Doping significantly reduced the bandgap, enabling absorption in the visible spectrum.

4. In $LiNbO_3$, the compressive strain (20%) reduces the bandgap of Ag-doped $LiNbO_3$ from 1.78 eV to 0.86 eV, Al-doped from 2.02 eV to 1.33 eV, Au-doped from 1.36 eV to 1.06 eV, and Cu-doped from 0.96 eV to 0.78 eV. Tensile strain (20%) further lowers the bandgap for Cu-doped $LiNbO_3$ to 0.41 eV, while other dopants show varying degrees of bandgap reduction, making the material highly tunable for optoelectronic applications.

5. The absorption spectrum of $LiNbO_3$ shifts towards the visible region under high tensile and compressive strain, particularly at 20% strain, where the absorption peak reaches ~500k, significantly higher than the unstrained structure. High tensile strain is especially effective in enhancing visible light absorption, making it a promising strategy for improving optoelectronic and photovoltaic performance.

6. The bandgap of pristine $SrTiO_3$ is 2.94 eV (GGA calculations), which aligns well with experimental results (~3.25 eV). Doping significantly reduced the bandgap, with Cu-doped $SrTiO_3$ showing the most substantial decrease.

7. The pristine STO, due to wide bandgap of 2.94 eV, primarily absorb the light in the UV range. Under strain, the bandgap reduces significantly, facilitating improved absorption

in the visible range. The combination of doping and strain further lowers the bandgap, making STO a strong candidate for optoelectronic applications.

8. In SrTiO$_3$, compressive strain (10% and 20%) significantly increased the absorption coefficient, with 20% compressive strain shifting the absorption peak of Ag-doped SrTiO$_3$ to ~600 nm (visible region), while Cu-doped SrTiO$_3$ exhibited the highest absorption enhancement. Tensile strain (10% and 20%) generally reduced absorption intensity, with a lesser impact on shifting the absorption edge.

9. The study confirms that strain engineering, in combination with metal doping, effectively modulates the optoelectronic properties of LiNbO$_3$ and SrTiO$_3$. The coexistence of doping and strain tuning resulted in superior visible-light absorption, with 20% tensile and compressive strain leading to the most significant improvements.

10. The shift in the absorption spectrum, bandgap narrowing, and enhanced dielectric properties highlight the potential of strained and doped perovskite (LiNbO$_3$ and SrTiO$_3$) in next-generation solar and photonic devices.

CHAPTER-6

LAYERING AND STRAIN FOR TUNING THE OPTICAL PROPERTIES OF MONOLAYERS

Tin-monochalcogenides (SnS, SnSe) and zinc-monochalcogenides (ZnS, ZnSe) are promising materials for optoelectronic applications due to their tunable bandgaps and strong light absorption. SnS and SnSe, with their layered structure and high carrier mobility, are excellent for photodetectors, solar cells, and transistors. Similarly, ZnS and ZnSe, known for their wide bandgaps and high exciton binding energies, are widely used in UV photodetectors and LEDs. Applying strain can significantly alter their electronic and optical properties, enabling bandgap engineering for enhanced absorption in the visible spectrum. Tensile strain typically induces a redshift, improving absorption in the desired wavelength range, while compressive strain modifies optical transitions. Additionally, forming heterostructures between Sn- and Zn-based monochalcogenides can enhance charge separation and broaden spectral response, improving device efficiency. Strain-engineered heterostructures offer tailored optoelectronic properties, making them ideal for next-generation photonic and photovoltaic devices with improved performance and energy conversion efficiency.

"Analysing the structural, electronic, & optical properties of heterostructures of metal oxides/alkali metals/2D materials and tuning their properties for optoelectronic and photocatalytic applications."

The methodology used to achieve desired objective involved following steps: -

- Systematic investigation of the electronic, structural, and optical properties of monolayers of tin-monochalcogenides (SnS and SnSe) and zinc-monochalcogenides (ZnS and ZnSe) is performed.

- Further the monolayer of SnS is stacked with SnSe, ZnS, and ZnSe, to form SnS/SnSe, SnS/ZnS, and SnS/ZnSe to form heterostructures and optoelectronic properties are calculated.

- Subsequently, to determine the effect of strain, the positive and negative strain of varied intensities (2%, 5%, and 10%) is applied to the SnSe, SnS, ZnSe, and ZnS monolayers.

This chapter is divided into five sections, including the introduction in the first section. The second section provides information on the simulation setup adopted for the calculations. Following that, in the third section, the SnS monolayer is stacked with the monolayers of SnSe, ZnSe, and ZnS and the impact of layering on optoelectronic properties is investigated. Further, the strain is applied on the monolayers of SnSe, SnS, ZnSe, and ZnS and the optical properties are calculated in section four. Finally, the important outcomes are summarized in section five.

6.1 INTRODUCTION

In recent years, the remarkable optical, electronic, and structural properties of layered two-dimensional materials, widely known as 2D materials attracted the attention of researchers for their usability in optoelectronic and photovoltaic applications [157, 244 - 246]. After the breakthrough of the successful fabrication of the monolayer of graphene in 2014, 2D materials gained the immense attention of researchers in the domain of nanoelectronics [19, 247]. This came into being due to the exceptional and distinctive optoelectronic properties of two-dimensional materials [248, 249]. 2D materials like germane, silene, tin monochalcogenides, zinc monochalcogenides, and transition metal chalcogenides (TMD) have been widely utilized in recent times for the fabrication of optoelectronics and photovoltaic devices [250].

With the increasing need for material applications, the functional constraints of single-layer materials cannot fulfill the intensified and diverse demand of the industry [251, 252]. Additionally, the layered materials exhibit functionalities such as magnetic properties, conductivity, photocatalytic and semi-conductivity. Due to these reasons, researchers extensively attempted to focus on modulating the properties of layered materials to cater to the growing demands of the industry [253].

In the past years, the pathway of modulating the electronic, optical, magnetic, mechanical, and chemical properties of 2D materials without altering their composition has been identified as a new aspect of the design of novel functional materials [161]. Over the last few years, researchers have performed several theoretical and experimental studies to tune the properties of layered two-dimensional materials by utilizing techniques like the application of external strain and application of external electric field, doping, and stacking the two-dimensional materials to form layered structures [82]. Among all the above techniques for altering the properties of 2D materials for optoelectronics applications, another field of coupling 2D materials to fabricate heterostructures has evolved drastically in recent times [254, 255]. The

fundamental principle of making the heterostructure of layered materials is the stacking of two layers with weak van der Waals (vdW) forces to make a stable structure for various applications [158]. The heterostructures are fabricated by employing the different layers and overcoming the limitation of lattice matching, as no defect chemical bonding is required to form a stable heterostructure [159].

Advantageously, the assembly of materials in the creation of heterostructure does not involve one-to-one chemical bonding or direct chemical treatment/interaction of the individual materials [160]. However, it results in the combination of the properties of two monolayers. Heterostructures with vdW by stacking 2D materials are suitable for various optoelectronic and photonic applications with modulated interlayer energy of charge separation [158, 160, 162, 255]. It is evident from past studies that the 2D vdW heterostructures demonstrate overall enhanced characteristics and performance in compression to the single-layer two-dimensional material [162, 256, 257]. This makes the 2D vdW heterostructure a potential candidate for the fabrication of optoelectronics, and photovoltaic devices such as phototransistor, photodetector, solar-cell, and light-emitting-diode [258-260].

As far as the studies of 2D materials are concerned, among the 2D materials, graphene has been found fascinating in the past few decades and has attracted the attention of researchers due to its acceptance for various applications [160, 248]. However, the absence of bandgap in the sheet of graphene has become a prominent hurdle for its applicability in optoelectronic applications [261]. The zero bandgap of graphene derived the researchers for tuning its bandgap with external strain, doping, external electric field, and stacking of its two layers for various applications [160, 162, 262].

Subsequently, it motivated the researchers to find new novel 2D materials and fabricate their heterostructures for various applications. Many graphene-like materials like transition metal dichalcogenides (TMDCs), boron nitride, zinc monochalcogenides, tin monochalcogenides, and graphitic carbon nitrides are investigated by the researchers to find the possibilities of their wide applications in the domain of optoelectronics. Among all these materials, Group IV chalcogenide captured the attention due to advantageous properties, such as flexibility, stability, and moderate bandgap matching with the absorption energy of the incident solar radiation [162, 263]. These properties of Group IV chalcogenide are advantageous for optical and solar applications. Among the family of Group IV chalcogenides, the well-known Sn-monochalcogenides (SnS and SnSe) show very high absorption efficiency due to optimal

bandgap [264]. The Sn- monochalcogenides are widely utilized in the fabrication of photodetectors, photovoltaic cells, electrochemical switching devices, lithium-ion batteries, and thermoelectric devices [265, 266].
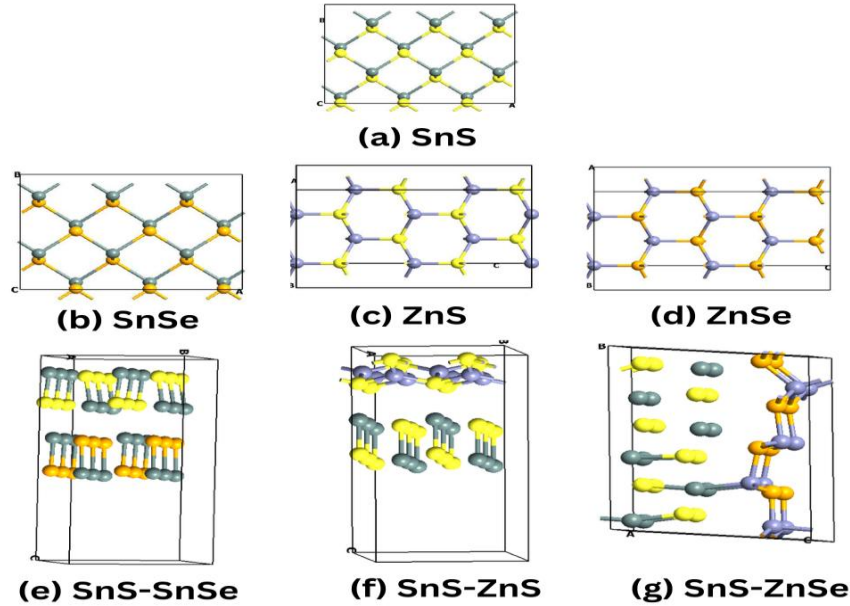
Fig. 6.1 The structure of 2d-monolayers ((a) SnS, (b) SnSe, (c) ZnS and (d) ZnSe) and their heterostructures ((e) SnS/SnSe, (f) SnS/ZnS and (g) SnS/ZnSe).

The limitation of these materials is their low carrier mobility, which is not favorable for optical applications. Along with the Group IV chalcogenide, the II-VI zinc chalcogenides (ZnS and ZnSe) are also useful for optoelectronics applications [263]. ZnS with a honeycomb structure is an excellent choice for optoelectronics applications [267- 269]. The 2D ZnS has a hexagonal wurtzite phase and stable structure with good absorption ability in the UV region [270, 271]. Experiments show that monolayer ZnS is suitable for optoelectronic applications. However, its large bandgap limits its optical absorption in the visible spectrum. The monolayer of II-VI zinc chalcogenides can be stacked for optoelectronic applications by layering them with the Group IV chalcogenide SnS to build a novel bilayer heterostructure for optoelectronics applications such as light-emitting devices, photodetectors, and solar cells.

In the past few years, several researchers attempted to build the heterostructures of monolayers of various elements to tune the properties for optoelectronic applications. The primary aim was to narrow down the bandgap of the monolayers by the formation of the heterostructures and to further improve the optical properties. Trung *et al.* [272] Synthesised the ZnS/ZnO heterostructure-alloy and explored the structural and optical properties and tuned them by

controlling the substrate temperature and indicated potential applications of the ZnS/ZnO heterostructure alloy in optoelectronic and photonic applications.

Further, Maniyar *et al.* [161] used density functional theory to investigate heterostructures of black phosphorene with MoS2, MoSe2, MoTe2, WS2, and WSe2. They found these combinations enhance UV and visible light absorption, with absorption peaks shifting to lower energies. This makes them promising for optoelectronics and solar cells. The structures exhibit type-II band alignment, beneficial for efficient charge separation in solar energy conversion and optoelectronic applications. Further, Li *et al.* [273] investigated a two-dimensional MoS2/SnS heterostructure via first-principles methods and explored the enhanced photocatalytic performance, attributing synergistic effects between MoS2 and SnS layers. The heterostructure demonstrates improvement in the visible light region, which is beneficial for optoelectronic applications.

Along with layering, strain has also been utilized widely to modify the bandgap and carrier mobility in past few years, which enables band alignment and introduces new optoelectronic phenomena in materials [230, 288]. The appropriate value and type of applied strain adjust the optical absorption toward the lower energies and improve the emission characteristics of materials for advanced photonic applications. The applied strain also improves the optical properties, including the dielectric function, absorption coefficient, and refractive index. As per Kramers-Kronig relations, there is a significant impact of applied strain on the refractive index of materials.

In recent times, the impact of applied strain on various properties of two-D materials and TMMCs has been extensively studied for optoelectronic applications. Wang *et al.* [274] investigated the impact of strain on the properties of MoS₂. The research concluded that the tensile strain reduces the bandgap, enhancing the absorption in the visible spectrum. Similarly, Peng *et al.* [275] reviewed the work based on tuning the optoelectronic properties of TMDCs and graphene for optoelectronic applications. This tunability of bandgap and optical properties because of strain accommodates the development of optoelectronic devices, as it allows for the modulation of light emission properties. Considering strain as an efficient and controllable method for tuning the properties of materials, strain can be employed on the monolayer of tin and zinc monochalcogenides for tuning their properties for photonic and optoelectronic applications.

6.2 COMPUTATIONAL SET UP FOR CALCULATIONS

In this chapter, the electronic, structural, and optical properties of the monolayers of tin-monochalcogenides (SnS and SnSe), zinc-monochalcogenides (ZnS and ZnSe), and their heterostructures (SnS/SnSe, SnS/ZnS, and SnS/ZnSe) are calculated. All the simulations are performed by utilizing the DFT calculations of the Atomistix Tool Kit. The generalized gradient approximation (GGA) of Perdew–Burke–Ernzerhof (PBE) is applied for the approximation of the exchange-correlation energy in all the calculations performed [199, 222, 276]. The monolayer of SnS is combined with the monolayers of SnSe, ZnS, and ZnSe to form the SnS/SnSe, SnS/ZnS, and SnS/ZnSe vdW heterostructures. The energy of all the atoms of monolayers and their heterostructures is relaxed with a force of 0.05 eV. The value of the mesh cut of is fixed to 150 Ry with 15x15x1 Brillouin- zone sampling k-points for geometry optimization [200].

In the performed calculations the value of the muffin-tin radii utilized are 2.1 ˚A, 2.2 ˚A, 1.9 ˚A, and 2.1 ˚A for Zn, Sn, S, and Se, respectively. For the formation of vdW interactions, the semi-empirical Grimme DFT-D2 are selected for corrections as the same are not defined in the PBE function [277]. Electronic parameters are calculated by applying the GGA approximations. However, DFT along with meta-GGA combined with Tran and Blaha (TB09) with 15x15x1 Brillouin-zone sampling k-points is applied for performing the precise calculations of optical parameters [201]. The equation of Kubo-Greenwood given below is utilized to calculate the value of the susceptibility tensor [270].

$$\chi_{i,j(\omega)} = -\frac{e^2\hbar^4}{\varepsilon_0 m^2 \omega^2 V} \sum_{nm} \frac{f(E_m)-f(E_n)}{E_{nm}-\hbar\omega-\iota\Gamma} \pi_{nm}^{\iota} \pi_{mn}^{j} \tag{6.5}$$

To analyze the stability of the heterostructures, the binding energy is also calculated using the equation illustrated below.

$$E_B = \frac{E-(E_1-E_2)}{N} \tag{6.2}$$

In the above equation, E is the total energies of SnS/SnSe, SnS/ZnS, and SnS/ZnSe heterostructure, E1 is the total energy of free-standing SnSe, ZnS, and ZnSe, and E2 is the total energy of SnS monolayer. N represents the total number of atoms in the heterostructure.

Further, to modulate the properties of SnS, SnSe, ZnS, and ZnSe, strain is applied. For applying the compressive and tensile strain on the perovskites, the equation illustrated below is utilized.

$$\varepsilon = \frac{a - a_0}{a_0} \times 100\ \%$$
(6.3)

In the equation given above, ao is the value of the lattice constant perovskite (relaxed and without strain), and a represents the lattice constant after the application strain. The positive value of ε represents the tensile strain, and the negative value represents the compressive strain.

6.3 IMPACT OF LAYERING ON PROPERTIES OF MONOLAYERS

In this section of the chapter, the structural, electronic, and optical properties of the monolayers SnS, SnSe, ZnS, and ZnSe are elucidated. Further, the impact of the formation of the heterostructure of SnS with SnSe, ZnS, and ZnSe is also analyzed in detail along with the applicability of the formed heterostructures in optoelectronic and solar applications.

6.3.1 Electronic and structural properties of monolayers and formed heterostructures

To develop the heterostructures of monolayers of SnS with SnSe, ZnS, and ZnSe, the structural properties of the monolayers of tin-monochalcogenides (SnS and SnSe) and zinc-monochalcogenides (ZnS and ZnSe) are calculated. The calculated values of the lattice constants for the monolayers of SnS, SnSe, ZnS, and ZnSe are tabulated in Table 6.1. The values of the lattice constant are consistent with the results of previous studies [264-268, 278-281]. Further, the monolayer of SnS is combined with SnSe, ZnS, and ZnSe to build the heterostructures SnS/SnSe, SnS/ZnS, and SnS/ZnSe.

The monolayers and formed heterostructures are relaxed for the geometry optimization to reduce the forces on the atoms. The lattice mismatch of the monolayer of SnS with SnSe, ZnS, and ZnSe is evaluated and found +4.27% -3.81% and +1.01% respectively. These calculated values of lattice mismatch are within the acceptable range of experimental synthesis required for the formation of heterostructures [82, 161]. The acceptable range lattice mismatch is an indication of the low impact of the induced strain on electronic properties due to the formation of heterostructure. The interlayer spacings of the optimized heterostructures of SnS/SnSe, SnS/ZnS, and SnS/ZnSe are 2.96 (˚A), 3.71 (˚A), and 2.88 (˚A), respectively.

To investigate the electronic behavior of the monolayers of SnS, SnSe, ZnS, and ZnSe, the bandgap is calculated. Further, the bandgap of the heterostructures SnS/SnSe, SnS/ZnS, and

SnS/ZnSe are also calculated to investigate the effect of heterostructure formation on the bandgap of monolayers. It is found from the calculated results that the bandgap of the monolayers of SnS, SnSe, ZnS, and ZnSe are 1.70 eV, 1.46 eV, 2.35 eV, and 1.46 eV, respectively. All the calculated values of the bandgap of the monolayers agree with the values calculated in previous studies [264-268, 278-281].

The bandgap of the SnS/SnSe heterostructure is 1.04 eV. However, the value of the bandgap is 0.6 eV and 0.9 eV for the SnS/ZnS and SnS/ZnSe heterostructures, respectively. It is observed that the bandgap is significantly narrowed due to the formation of the heterostructure of SnS with SnSe, ZnS, and ZnSe. The formation of heterostructures can find potential applications in optoelectronics, which is a simple p-n junction device. The applicability of these formed heterostructures in optoelectronics is dependent on their light absorption capabilities.

Table 6.1 Lattice constant and bandgap of the monolayers and heterostructures.

Structure	Lattice constant a(A˚)	Bandgap (eV)	References
SnS	3.957	1.70	[264]
SnSe	4.126	1.461	[264- 266]
ZnS	3.806	2.35	[266, 268]
ZnSe	3.997	1.46	[266]
SnS/SnSe	3.957	1.04	[282]
SnS/ZnS	4.126	0.6	[283]
SnS/ZnSe	3.806	0.9	[284]

Therefore, the analysis of the optical properties of the formed heterostructures is performed in the next section. The decrease in bandgap is very significant for the heterostructures SnS/ZnS and SnS/ZnSe due to the combined properties of zinc and tin, which is an indication of the improvement in optical absorption in the visible region. This lowering of the bandgap due to the formation of heterostructure opens up the possibility of further improvement in the optical properties for optoelectronic applications.

 It can be seen from the results of the absorption coefficient elucidated in the next section that the formation of heterostructures will result in high and wide absorption in visible region compression to the individual monolayers due to the bandgap lowering. The lowering of the bandgap is responsible for the direct excitement of the photogenerated electron from the conduction band of SnS to the valance band of SnSe, ZnS, and ZnSe, subsequently improving

the visible light absorption. The interlayer distances are calculated for all the heterostructures to investigate the interlayer atomic interactions and their influence on the bandgap. The interlayer distances for the SnS/SnSe, SnS/ZnS, and SnS/ZnSe heterostructures are 2.93 Å, 2.76 Å, and 2.75 Å, respectively.

The interlayer distance for SnS/SnSe is the largest at 2.93 Å, indicating a relatively weaker interaction compared to the shorter distances of 2.76 Å for SnS/ZnS and 2.75 Å for SnS/ZnSe. Notably, SnS/SnSe exhibits a strong binding energy of -228.38 meV, suggesting robust interlayer interactions that enhance its structural stability. In contrast, SnS/ZnS presents a binding energy of 0.055 meV, indicating weak interactions and potential instability, which likely leads to its lowest bandgap of 0.6 eV. SnS/ZnSe, with a binding energy of -8.93 meV, shows moderate stability and an intermediate bandgap of 0.9 eV. These results indicate a clear trend: stronger interlayer interactions correlate with higher bandgap values. The significant bandgap of 1.04 eV in SnS/SnSe, linked to its favourable binding energy, highlights its potential for optoelectronic applications.

6.3.2 Optical properties of monolayers and formed heterostructures

In this segment, the optical properties of monolayers of tin-monochalcogenides (SnS and SnSe), zinc-monochalcogenides (ZnS and ZnSe), and their heterostructures (SnS/SnSe, SnS/ZnS, and SnS/ZnSe) are investigated. In optical properties, the absorption coefficient, dielectric function, and refractive index are calculated and analyzed. To understand the optical behavior of all the monolayers and heterostructures, the absorption coefficient is plotted for different values of energy and wavelength [158, 285]. The other optical properties (dielectric function, and refractive index) are calculated and plotted for varying energy.

The optical properties are plotted along all the tensors (xx, yy, and zz). However, the discussions of the calculated and plotted properties are carried out along the x tensor only, and properties along two other tensors (y and z) can be interpreted in the same way [208]. The calculated values of the energy-dependent dielectric constant for monolayers SnS, SnSe, ZnS, and ZnSe and their heterostructures SnS/SnSe, SnS/ZnS, and SnS/ZnSe are plotted in Fig. 6.2 and Fig. 6.3. The dielectric constant of any material is a representation of its capacity to store energy. It also indicates the interaction of the light with the material when propagating through it [157].

The real part of the dielectric constant is the measurement of the polarization and dispersion of the light in the material. However, the imaginary part is a measurement of energy absorption and represents the absorption capacity of the material [82, 157]. The presence of negative values for the real part of the dielectric constant (see Fig. 6.2) can lead to novel optical and electronic effects, such as enhanced light absorption, modified electronic properties, and unique interface interactions (plasmonic effect) in the monolayer of SnS, SnSe, ZnS, and ZnSe.

The SnS, SnSe, ZnS, and ZnSe are not typically plasmonic materials on their own, in certain conditions or when engineered at the nanoscale due to quantum size effects or surface plasmon resonances, they might exhibit behaviors where the real part of the dielectric constant can become negative. In the monolayers and formed heterostructure, the presence of negative values for the real part of the dielectric constant can lead to novel optical and electronic effects, such as enhanced light absorption, modified electronic properties, and unique interface interactions.
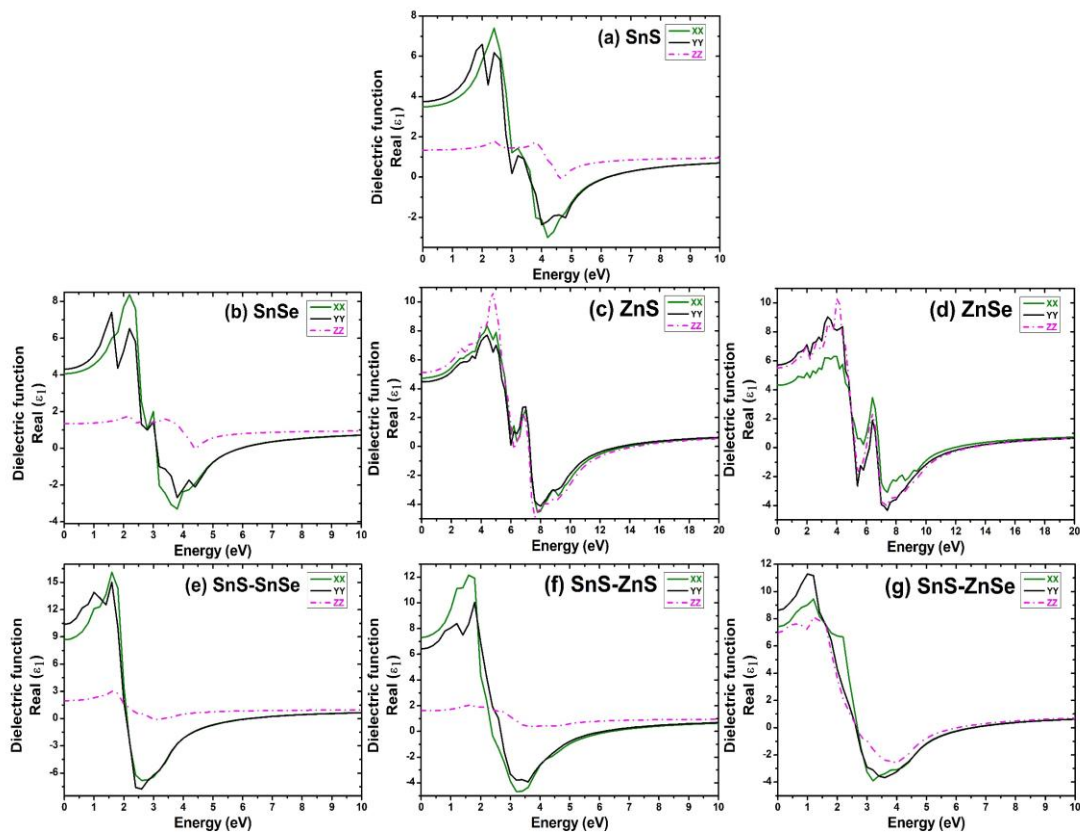
Fig. 6.2 Real part of dielectric constant for monolayers (SnS, SnSe, ZnS and ZnSe) and their heterostructures (SnS/ SnSe, SnS/ZnS and SnS/ZnSe).
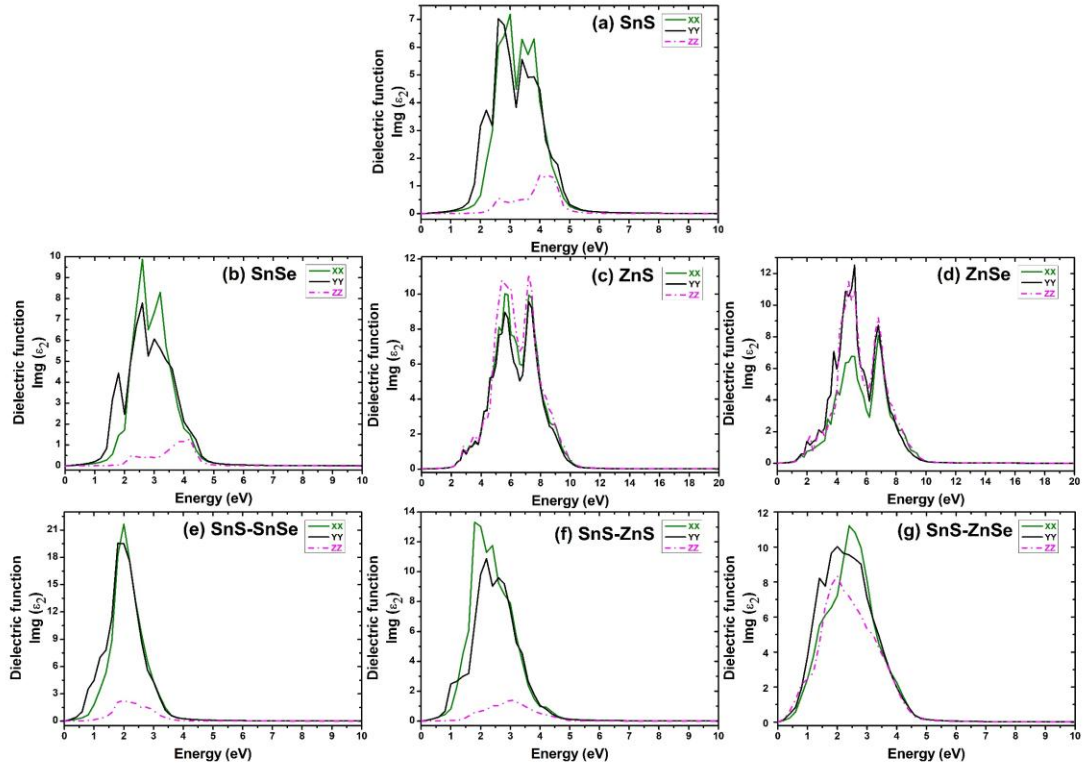
Fig. 6.3 Imaginary part of dielectric constant for monolayers (SnS, SnSe, ZnS and ZnSe) and their heterostructures (SnS/ SnSe, SnS/ZnS and SnS/ZnSe).

It can be observed from Fig. 6.3 that for the monolayer of tin-monochalcogenides (SnS and SnSe), all the peaks of the imaginary dielectric constant are in the range of 1.5 to 5.0 eV. The strongest peak appears around 3.0 eV and 2.5 eV for SnS and SnSe, respectively. It is observed that the peaks of the imaginary dielectric constants are in lower energy ranges for both SnS and SnSe monolayers. However, for the monolayers of tin-monochalcogenides (ZnS and ZnSe), the peaks of the imaginary dielectric constant are found in the higher energy ranges, i.e., from 3.0 to 10 eV.

The strongest peak is seen around 8.0 eV for ZnS and around 4.0 eV for ZnSe. These calculated values of the imaginary dielectric constant for the monolayers are in accordance with previous results of various studies. It is evident from Fig. 6.3 that the tin-monochalcogenides have peaks of imaginary dielectric constant in lower energy ranges. However, the zinc-monochalcogenides have peaks in higher energy ranges. The peaks of imaginary dielectric constants in higher energies are undesirable for optoelectronic applications.
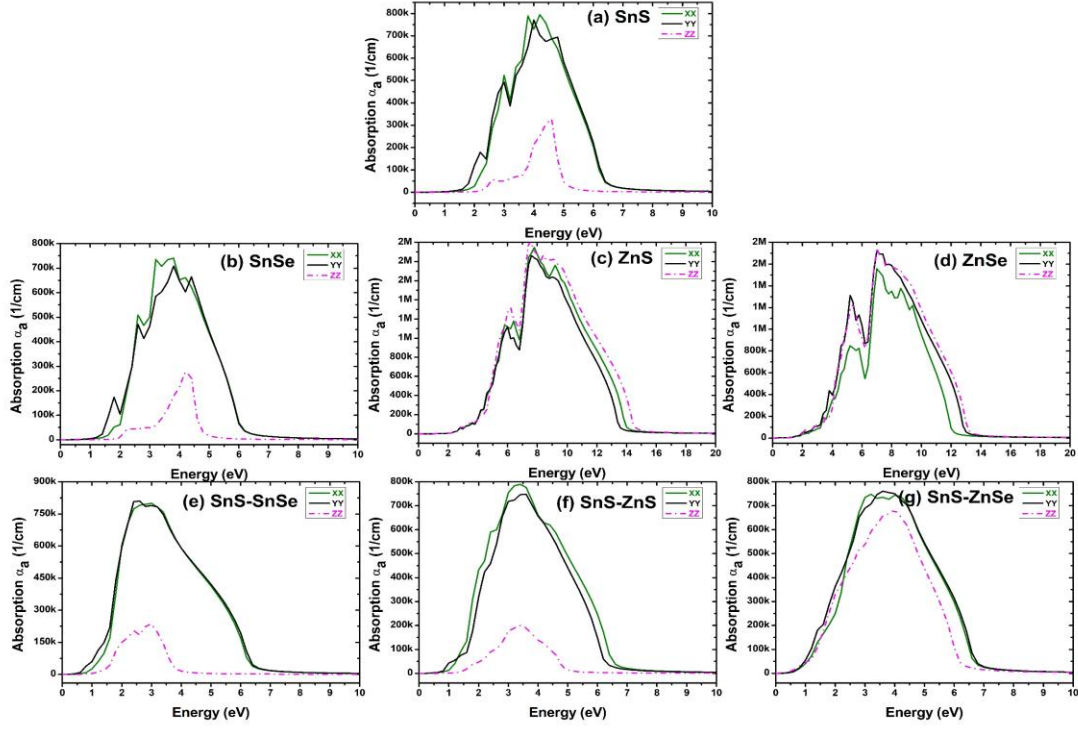
Fig. 6.4 Energy dependent absorption coefficient for monolayers (SnS, SnSe, ZnS and ZnSe) and their heterostructures (SnS/ SnSe, SnS/ZnS and SnS/ZnSe).

For heterostructures SnS/SnSe, SnS/ZnS, and SnS/ZnSe, as shown in Fig. 6.3, the peaks of imaginary dielectric constant are in the range of 1.0 to 4.0 eV, with the highest peak around 2.0 eV for all the heterostructures. The edges of the imaginary dielectric constant for all the monolayers and their heterostructures agree with their calculated bandgap. Due to the formation of heterostructures (SnS/SnSe, SnS/ZnS, and SnS/ZnSe), the peaks of the imaginary dielectric constant are found to be shifted towards the lower energy ranges due to the combined properties of monolayers of tin and zinc. Further, due to the formation of heterostructures, the value of binding energy becomes smaller in comparison to the individual monolayers, which results in more absorption in lower energy ranges.

The energy-dependent absorption coefficients for the monolayers SnS, SnSe, ZnS, and ZnSe and their heterostructures SnS/SnSe, SnS/ZnS, and SnS/ZnSe are shown in Fig. 6.4. It can be seen from Fig. 6.4 that for the monolayers SnS and SnSe, absorption the absorption is in the range of 1.5-6.5 eV (lower energies). However, for ZnS and ZnSe, the absorption is in the range of 4.0-14 eV (higher energies). The peaks of the absorption for the heterostructures SnS/SnSe, SnS/ZnS, and SnS/ZnSe are in the range of 1.0-6.5 eV (lower energies). The peaks of absorption appear in lower energy ranges for heterostructures, which indicates that more photons are absorbed in the visible region due to the formation of heterostructures or redshift.

The absorption peaks of the heterostructures are consistent with the imaginary dielectric constant shown in Fig. 6.3.
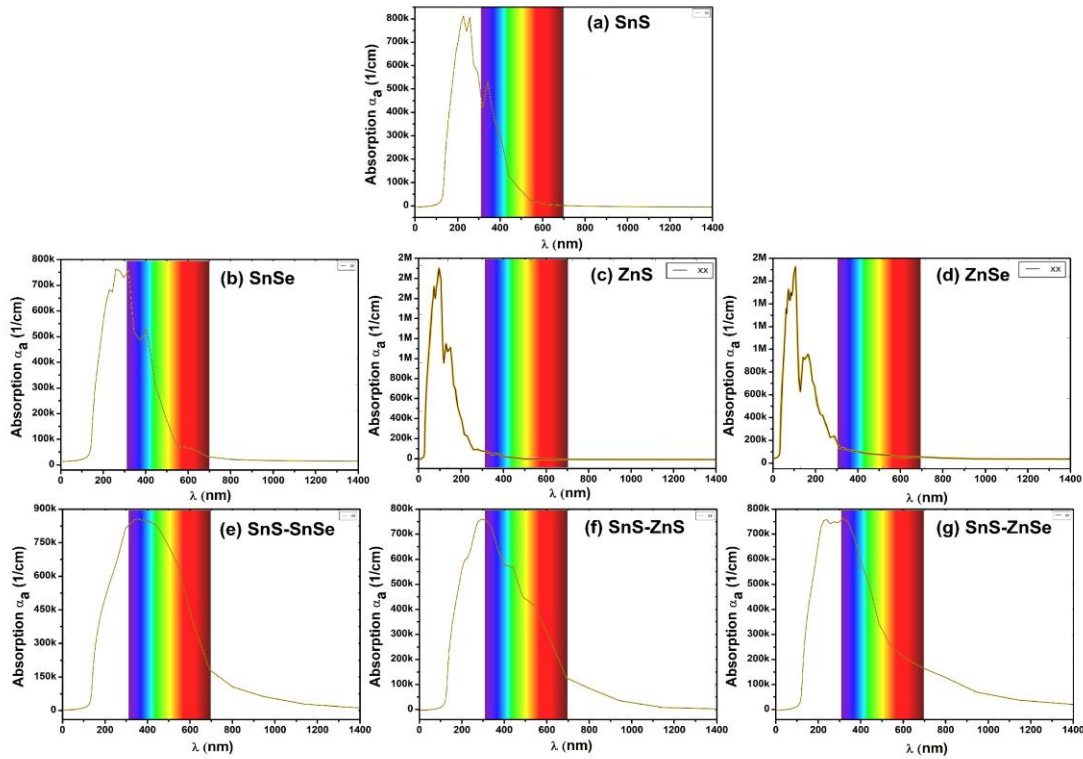

Fig. 6.5 Wavelength dependent Absorption coefficient for monolayers (SnS, SnSe, ZnS and ZnSe) and their heterostructures (SnS/ SnSe, SnS/ZnS and SnS/ZnSe).

The wavelength-dependent absorption coefficients of the monolayers of SnS, SnSe, ZnS, and ZnSe and their heterostructures SnS/SnSe, SnS/ZnS, and SnS/ZnSe are shown in Fig. 6.5. It is evident from the figure that the absorption of the tin-monochalcogenides (SnS and SnSe) is mostly in the UV region (100 to 300 nm), with small absorption in the near-visible region (380 to 500 nm). It can be indicated from the results of optical absorption that monolayers of the SnS and SnSe have high absorption in the unwanted UV region. This high absorption in the UV region is responsible for the high heating and low power efficiency.

For the zinc-monochalcogenides (ZnS and ZnSe), the absorption is negligible in the visible region, with most of the absorption in the UV region only (50 to 205 nm). It can be seen from Fig. 6.5 that for the heterostructures SnS/SnSe, SnS/ZnS, and SnS/ZnSe, the absorption is found to be shifted towards the visible region (350 to 650 nm) in compression to the monolayers of SnSe, ZnS, and ZnSe. The heterostructures SnS/SnSe, SnS/ZnS, and SnS/ZnSe have stable and high absorption in the visible range, which indicates that the absorption is largely shifted

towards the visible region or larger wavelength (redshift) due to the formation of heterostructures. The stable and broader absorption in the visible region of heterostructures is useful in optoelectronic and photovoltaic applications. Furthermore, it is found from the calculated optical properties that the monolayers SnS and SnSe and the heterostructures SnS/SnSe and SnS/ZnS have overlapping of the YY and XX tensors. However, the ZZ tensor is not overlapping. This indicates the anisotropic or isotropic behavior of the monolayers SnS and SnSe and the heterostructures SnS/SnSe and SnS/ZnS [286, 287].
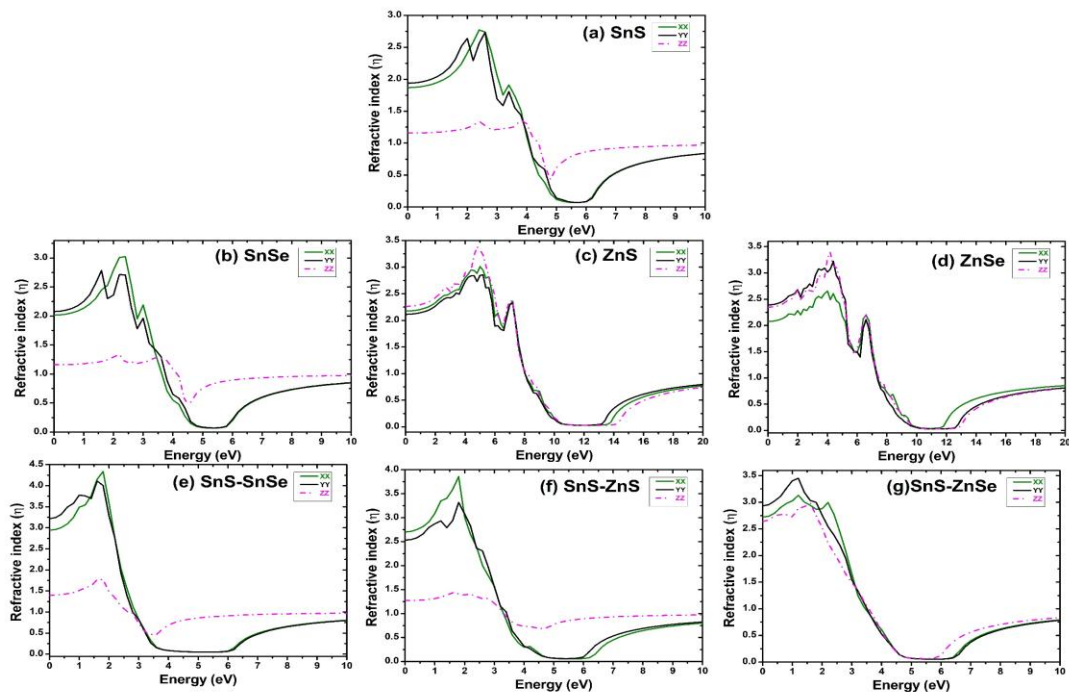
Fig. 6.6 Refractive index for monolayers (SnS, SnSe, ZnS and ZnSe) and their heterostructures (SnS/ SnSe, SnS/ZnS and SnS/ZnSe).

The values of refractive index vs energy for the monolayers SnS, SnSe, ZnS, and ZnSe and their heterostructures SnS/SnSe, SnS/ZnS, and SnS/ZnS are plotted in Fig. 6.6. It can be seen from the figure that the peaks of the refractive index are in line with the peaks of the absorption coefficient and the real dietetic constant. The peaks of the refractive index for the monolayers SnS and SnSe are found between 1.5-3.5 eV. For the monolayers ZnS and ZnSe, the peaks are between 2.8-6.0 eV. The highest peak of refractive index is around 2.0 eV for the monolayers SnS and SnSe and around 4.0 eV for the monolayers ZnS and ZnSe.

For the formed heterostructures SnS/SnSe, SnS/ZnS, and SnS/ZnSe, the major peaks of the refractive index are in lower energies with highest peaks around 2.0 eV, 1.5 eV, and 1.0 eV,

respectively. The value of the refractive index is increased due to the formation of heterostructures, which indicate that the incident light will propagate longer and will result in high absorption of the photon in the visible region. The increased value of the refractive index due to the formation of heterostructure is favorable for optoelectronic applications.

6.4 IMPACT OF STRAIN ON PROPERTIES OF MONOLAYERS

In this section, the effect of strain of varied intensity on various optoelectronic properties of tin and zinc monochalcogenides monolayers are investigated by employing density functional method. To determine the effect of strain, the positive and negative strain of varied intensities (2%, 5%, and 10%) is applied to the SnSe, SnS, ZnSe, and ZnS monolayers. The bandgap is calculated to evaluate the electronic structure, and the refractive index, absorption coefficient, and dielectric function are calculated for analyzing the optical behavior. The one-to-one comparison of the electronic properties and optical properties of unstrained monolayers with strained monolayers is performed to analyze the effect of strain.

6.4.1 Strain engineering of the electronic and structural properties of monolayers

The bandgap for the SnSe, SnSE, ZnSe, and ZnS under tensile strain and compressive strain of varied intensities (2%, 5%, and 10%) is illustrated in Table 6.2. As illustrated in Table 6.1, the computed values of the bandgaps for the unstrained SnS, ZnS, SnSe, and ZnSe monolayers are 1.70 eV, 2.35 eV, 1.46 eV, and 1.46 eV, respectively. Upon the application of strain, there is a change in the lattice constants of all the monolayers, which alters the overlapping of orbits and ultimately affects bandgap values. Subsequently, the applied strain enables the lessening of the bandgap in the monolayers for most of the values and types of the applied strain, which eventually results in the shifting of absorption towards the high wavelengths (redshift).

On the application of strain, the SnS monolayer undergoes a reduction in the bandgap under the applied compressive strain of 2% (1.7033 eV to 1.6 eV). Which is further decreased to 1.36 eV and increased to 1.78 eV for the applied compressive strains of 5% and 10% respectively. This originates due to the possible structural alteration at a large value of strain. Conversely, for the tensile strain, the bandgap is elevated to 1.86 eV for 2% and to 1.99 eV for 5%, thereafter reducing to 1.64 eV for 10% tensile strain. Which represents initial expansion of the bandgap followed by a reduction at high strain. In SnSe there is a reduction in the bandgap for the applied strain of compresive type with inetnsities 2% and 5%, and the value bandgap is elevated for the high value of compressive strain. SnSe exhibits an increase in bandgap for the applied

tensile strain of 2% and 5%, followed by a decrease at 10% tensile strain, indicating a complicated reaction where high strain ultimately reduces the bandgap. In ZnS, the applied compressive strain increases the bandgap from 2.35 eV (pristine) to 2.46 eV and 2.58 eV for the applied strain of compressive type with intensities 2% and 5% respectively. Due to applied tensile strain, the bandgap is reduced for the strain of 2%, 5%, and 10%. Moreover, the monolayer of ZnSe followed the same variation in the bandgap upon the applied strain as ZnS.

Table 6.2 Bandgap (eV) of strained monolayers.

Monolayer	Compressive			Tensile		
	2%	5%	10%	2%	5%	10%
SnS	1.6	1.36	1.78	1.86	1.99	1.64
SnSe	1.11	0.81	1.23	1.53	1.83	1.49
ZnS	2.46	2.58	2.53	2.17	1.82	1.35
ZnSe	1.58	1.7	1.53	1.29	0.96	0.58

Overall, the applied compressive strain leads to the widening of the bandgap for SnS and ZnS, while tensile strain increases the bandgap for SnS and SnSe but reduces it for ZnS and ZnSe. These findings align with the typical behavior of semiconductors under strain, where compressive strain tends to enhance the bandgap and tensile strain tends to narrow it. There is a widening of the bandgap in SnS and SnSe under tensile strain, notably for the low strain of 2%, due to the separation between the bands. Conversely, ZnS and ZnSe show a significant narrow downing of the bandgap under tensile strain. The results deduce that the applied strain may induce a metallic or semi-metallic transition, predominantly for the high value of the applied strain. The calculated results correspond with the conventional behavior of materials under strain, wherein compressive strain generally increases the bandgap and tensile strain typically reduces it. The narrow downing of the bandgap under strain may be favorable for the improvement in visible region absorption, which is investigated in the next section.

6.4. 2 Strain engineering of the optical properties of monolayers

To evaluate the effect of applied strain on optical absorption, the compressive and tensile strain (2%, 5%, and 10%) is applied on the monolayers of SnSe, SnS, ZnSe, and ZnS. Further, the

energy-dependent and wavelength-dependent absorption coefficients for the unstrained SnS monolayer along with strained SnS monolayer are illustrated in Fig. 6.7. As shown in Fig. 6.7 (a), for the unstrained SnS, the absorption begins from ~1.7 eV, which resembles its bandgap with peaks in the 1.7-6.5 eV energy range. The largest absorption peak of SnS is located in the area of high energy around ~5 eV. Due to the applied strain of both type (compressive and tensile), there is a notable shifting in the absorption towards the low energy ranges. The magnitude of the shifting is largest for the 5% compressive strain and 10% tensile strain applied on SnS, which opens a possibility of finding maximum augmentation in the visible absorption. The wavelength-dependent absorption for the unstrained SnS monolayer is plotted in Fig. 6.7 (b). As shown in Fig. 6.7 (b), the wavelength-dependent absorption for unstrained SnS is found in the ~150- 600 nm range with the maximum part of absorption located in the undesired ultra-violate region. When the strain of intensities 2%, 5%, and 10% of both types (compressive and tensile) is applied on the SnS, the absorption is noticed utterly shifted in the visible spectrum, and existence of redshift is observed. For the compressive strain of 5% and tensile strain of 10%, the most of the absorption of ultraviolet region is found shifted towards the desired visible spectrum, which is in line with the energy-dependent absorption.
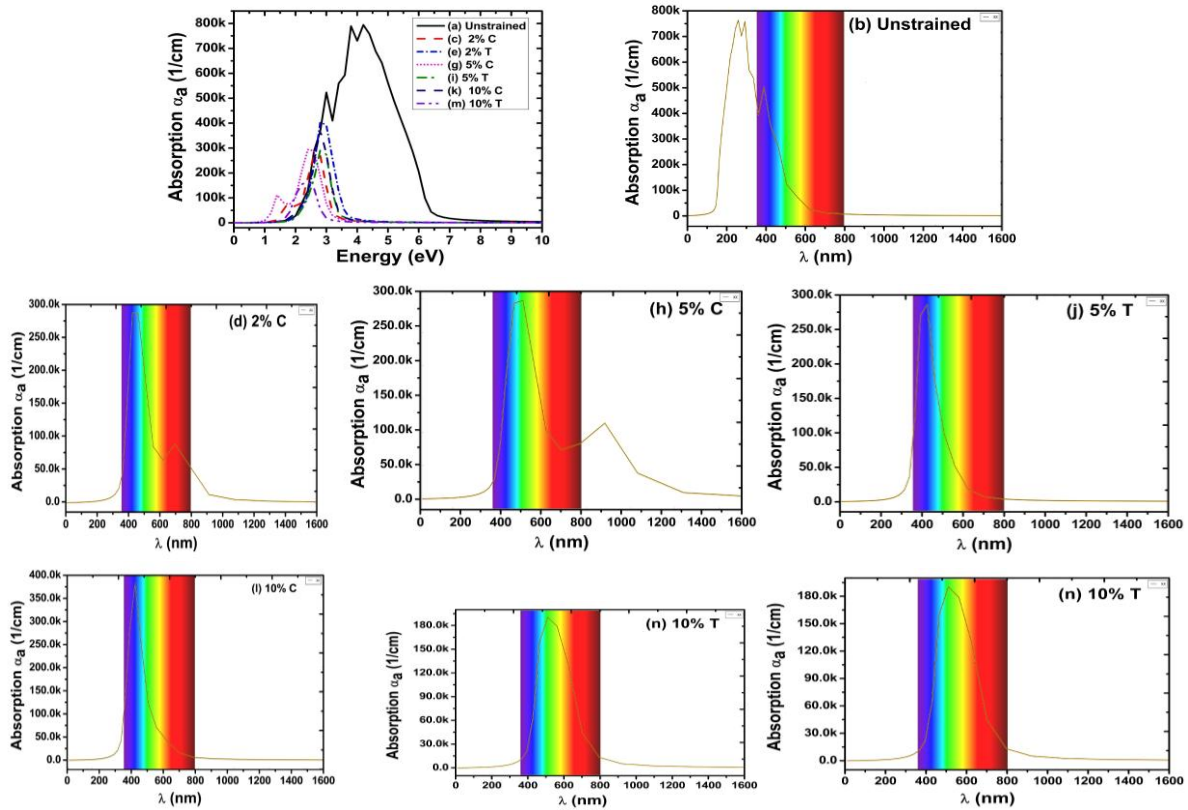
Fig. 6.7 Absorption coefficient of unstrained and strained SnS monolayer (C: Compressive strain and T: Tensile Strain).

For SnSe, energy and wavelength-dependent absorption coefficients are shown in Fig. 6.8. As shown in the figure, the absorption begins from the low energy value around ~1.5 eV for unstrained SnSe, with peaks located in the ~1.5 to 5.5 eV energy range, with the location of highest peak at 4.5 eV. As shown in Fig 6.8 (b), the wavelength-dependent optical absorption is largely available in undesired ultra-violate region for unstrained SnSe. The imposed strain on SnSe results in shifting of the peaks of absorption from higher to lower energies with the largest peaks located in 2.0-3.0 eV range. This shift is observed for all the intensities of applied compressive and tensile strain.
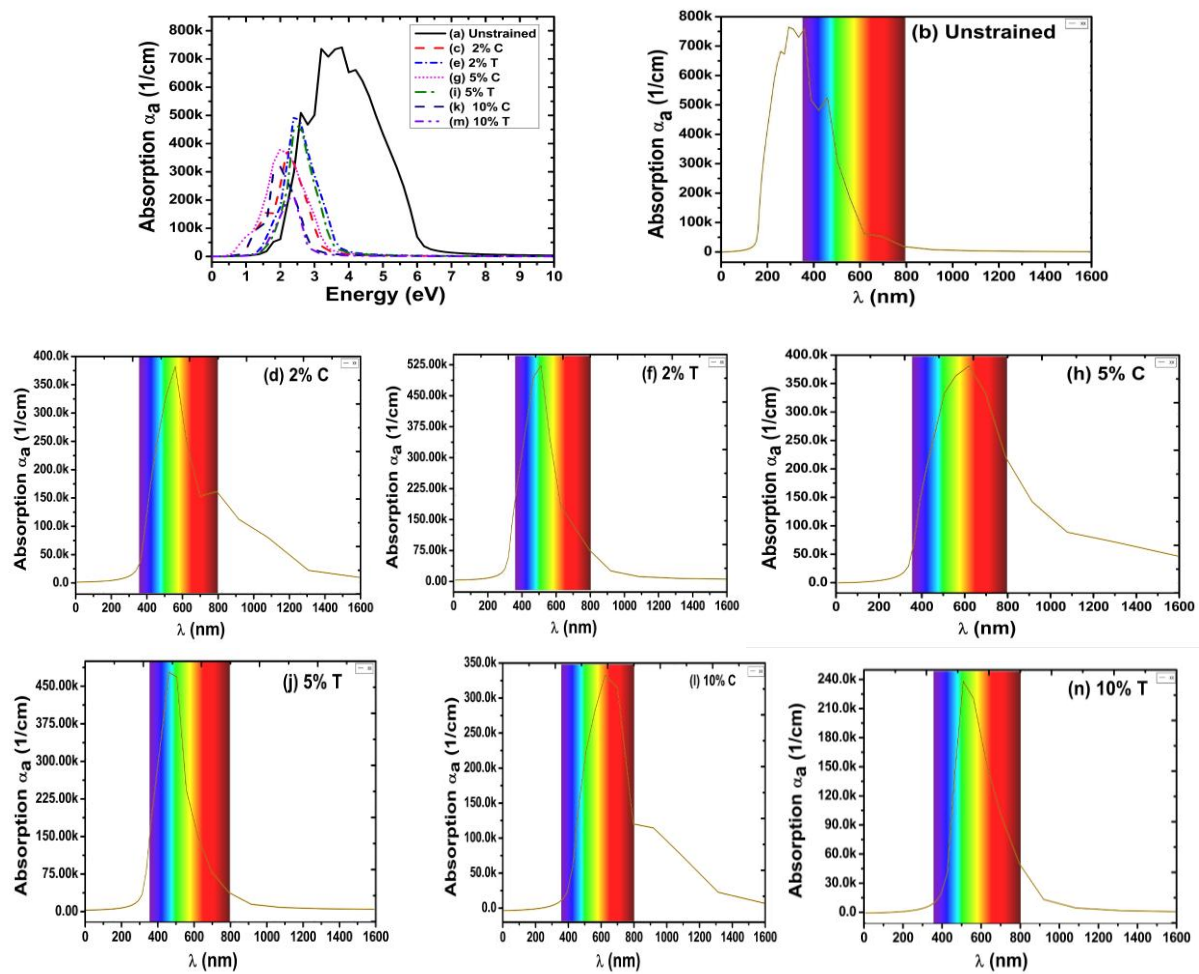
Fig. 6.8 Absorption coefficient of unstrained and strained SnSe monolayer (C: Compressive strain and T: Tensile Strain)

Furthermore, as shown in Fig. 6.8, the wavelength-dependent visible region absorption is also improved for the applied tensile strain and compressive strain compared to the unstrained SnSe. This improvement is highest for the high intensities of strain with the existence of the redshift phenomena. Conclusively, the high intensity of compressive and tensile strain results in

maximum redshift in optical properties of SnSe and SnS, shifting absorption and emission towards longer wavelengths. This tunability of optical properties enhances the suitability of SnSe and SnS monolayer for optoelectronic applications like infrared detectors, LEDs, solar, and photodetectors.

The energy and wavelength-dependent absorption coefficient for the monolayer of ZnS (unstrained and strained) is plotted in Fig. 6.9. In the monolayer of ZnS, due to the exitance of a wide bandgap (2.35 eV), a very high amount of absorption is available in the UV range (100-400 nm). Undesirably, due to wide bandgap of ZnSe and ZnS, there is a nonexistence of absorption peaks in the visible range. It is discovered from the results that the monolayer of ZnS can only absorb the photon of UV wavelengths, which limits its usability for optoelectronic applications. Due to the high bandgap, only the photons of UV energy can jump from the valance band to the conduction band. However, the photons of visible energy fail to cross it due to low energies.

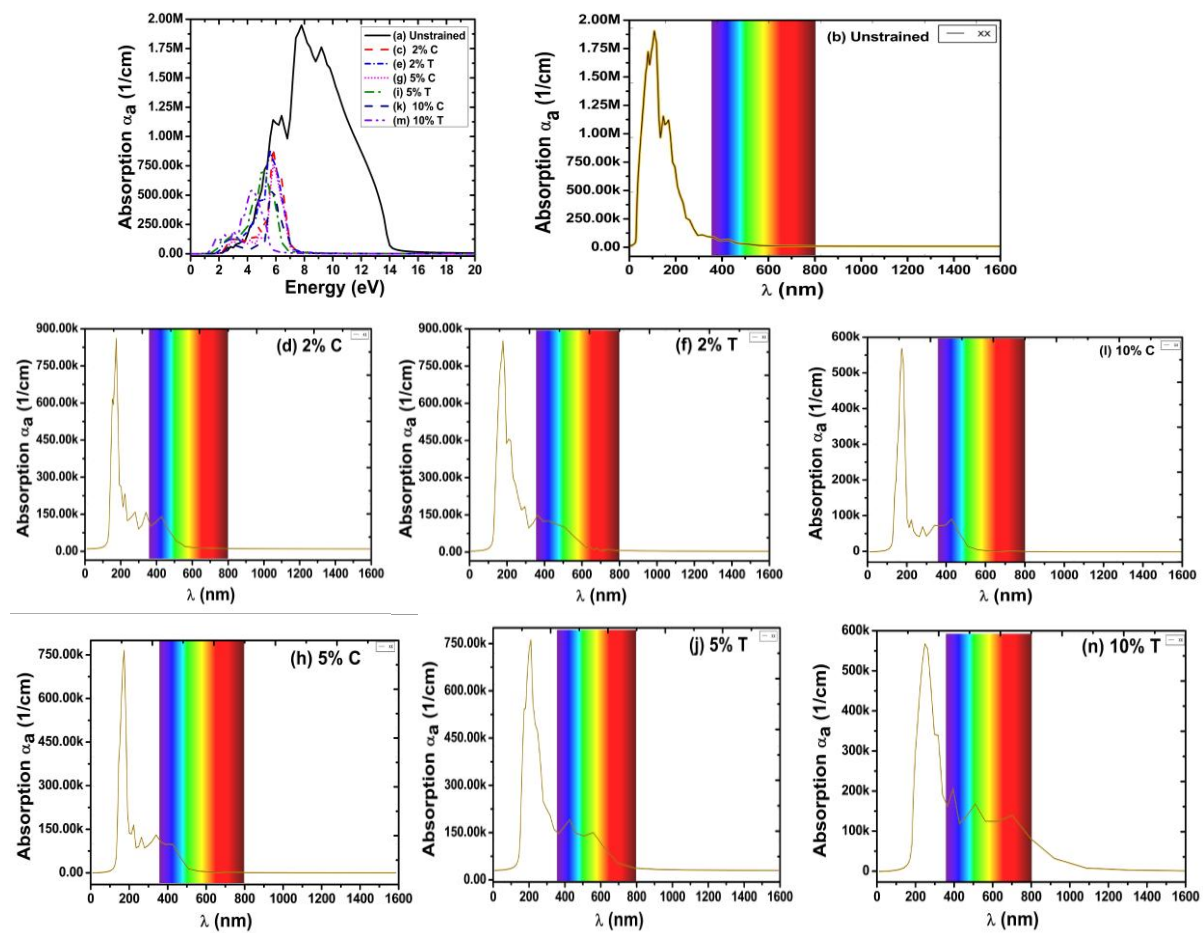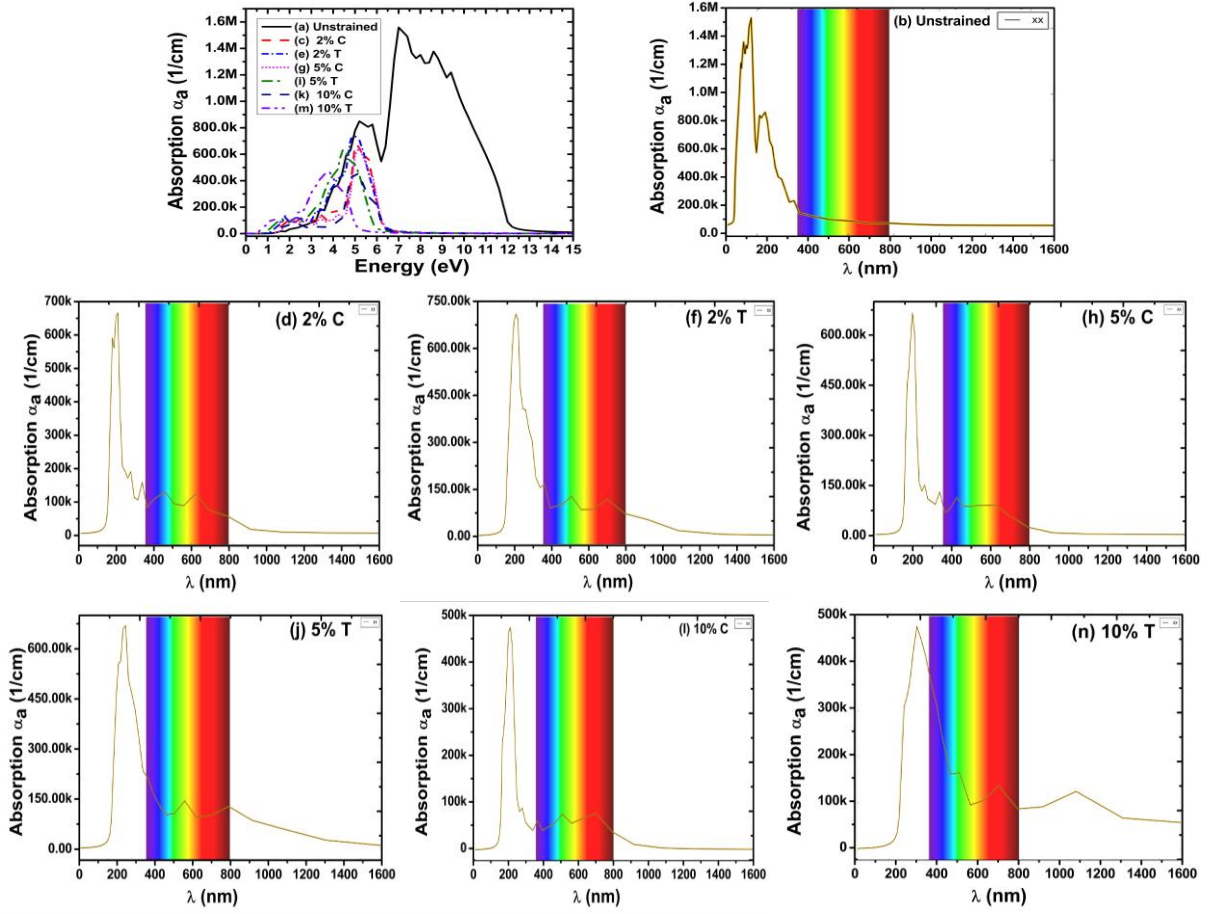**Fig. 6.9** Absorption coefficient of unstrained and strained ZnS monolayer (C: Compressive strain and T: Tensile Strain)

141

As shown in Fig. 6.9, the absorption in unstrained ZnS starts from ~2.3 eV with the largest peak of absorption located around ~9 eV. On the applied strain of compressive and tensile type with varied intestines, it is observed that the absorption peaks are predominantly found shifted towards lower energies. The highest peaks of absorption are located at ~6.5 eV, ~6 eV, and ~5.5 eV for compressive strain of intensities 2%, 5% and 10%, respectively. For the applied tensile strain of 2%, 5%, and 10%, the absorption peaks are at ~6.5 eV, ~6 eV, and ~4.5 eV, respectively. Furthermore, the wavelength-dependent absorption of the ZnS monolayer is primarily in the lower wavelength region (~0 to 300 nm).

Upon the applied strain, the most of the peaks of absorption of ZnS is found shifted from ultraviolet region to the visible region. For the low intensity of compressive and tensile strain of 2%, the non-zero absorption is noticed only in some portions of the visible region (~300 to 600 nm) with absorption peak of value ~150 k (see Fig. 6.9 (d) and (f)). Further, the ZnS monolayer applied with tensile strain of intensity 5%, exhibit non-zero absorption in the visible range till ~650 nm with a max absorption value of ~200 k. Advantageously, the high value of tensile strain (10%), exhibit non-zero absorption in the entire visible region with a maximum value of ~200k around ~400 nm. For strain of compressive type with intensities 5% and 10%, a slight improvement in visible region absorption is observed in compression to the unstrained ZnS.

Similarly, the wavelength and energy-dependent absorption for ZnSe are elucidated in Fig. 6.10 For the unstrained monolayer of ZnSe, absorption is only available in the high energy ranges with an absorption peak located around ~8ev (see Fig 6.10 (a)). Due the strain, the shifting of absorption is observed towards the lower energy ranges. As elucidated in Fig 6.10 (b), the wavelength-dependent absorption of ZnSe is primarily located in the ultra-violate region with zero visible region absorption. For the tensile strain and compressive strain of low intensity (2%), there is significant reduction in the absorption available in the undesired UV region. The non-zero absorption peaks are located in 400 to 700 nm range (viable region) with highest peak of value ~100k. For compressive and tensile strain of intensity 5%, further improvements in the visible region absorption are noticed and an absorption peak of value ~150 k found in the visible region.

Fig. 6.10 Absorption coefficient of unstrained and strained ZnSe monolayer (C: Compressive strain and T: Tensile Strain)

Furthermore, the high intensity of tensile strain of 10%, the maximum redshift is observed in ZnSe with an absorption peak of value ~350k at ~450 nm. Conclusively, in ZnS and ZnSe, the applied strain-induced bandgap reduction results in the shifting of absorption peaks towards lower energies (red-shift). Additionally, the applied strain modulates the bandgap, reduces the UV absorption, and aids the broader and more significant absorption in the desired visible range, predominantly for the high intensity of tensile strain which is favorable for optoelectronic applications.

The real part and imaginary part of energy-dependent dielectric function are plotted in Fig. 6.11 and 6.12. The real part defines the polarization phenomena and is directly aligned with the refractive index. On the other hand, the imaginary part describes the energy absorption and is associated with the absorption coefficient. It is discovered from the plotted graphs that the real dielectric function corresponds to the refractive index, nevertheless, the imaginary part is lined up with the absorption coefficient. As shown in Fig. 6.12, the strongest peaks of the imaginary

143

part are located at ~2.5 eV, ~2.7 eV, ~7.0 eV, ~7.5 eV. for SnSe, SnS, ZnSe, and ZnS, respectively.

For all the unstrained monolayers, the imaginary dielectric function is primarily non-zero in the high energy region and follows the trend of the absorption. On applying strain, the non-zero values of imaginary dielectric function start from the lower energy with peaks significantly shifted toward the lower energies (visible region). Similarly, the real part of dielectric function in plotted in Fig. 6.11. The peaks of refractive index translate into the peaks of real part of dielectric function. There is a notable shifting in the peaks towards the lower energies due to the application of strain in compression to the constituent unstrained monolayer.
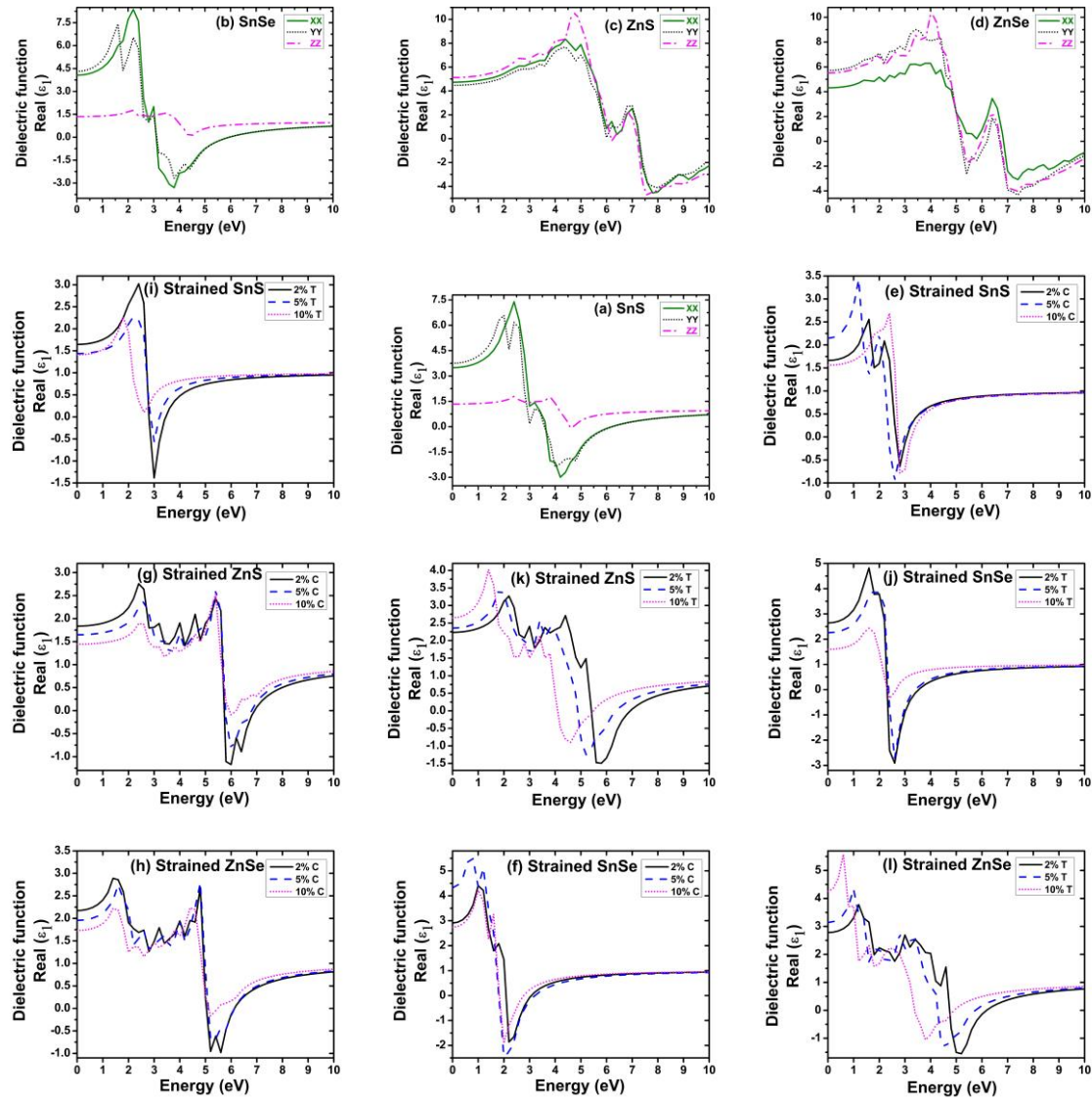
Fig. 6.11 Real Dielectric function: SnS, SnSe, ZnS and ZnSe monolayers.

The refractive index for the unstrained and strained SnSe, SnS, ZnSe, and ZnS is plotted in Fig. 6.12. The dielectric function is utilized to calculate the values of refractive index and the peaks of the refractive constant follow the real dielectric function. As illustrated in Figures 6.12 (a) and 6.12 (b), SnS and SnSe have peaks of refractive index are located in the range 1.5–3.5 eV. The highest peak is located at ~2.5 eV for both the monolayers. For ZnS and ZnSe monolayers (figure 6.12 (e) and 6.12 (f)), the refractive index peaks are available between 2.8–6.0 eV with the highest peaks at ~1.5 eV and 1 eV, respectively. Due to stain, refractive index of SnS is shifted towards lower energies. This shifting is highest in the case of high-intensity tensile strain of 10% and compressive strain of intensity 5%. A similar impact of the application of stain on the refractive index of the SnSe monolayer is observed.
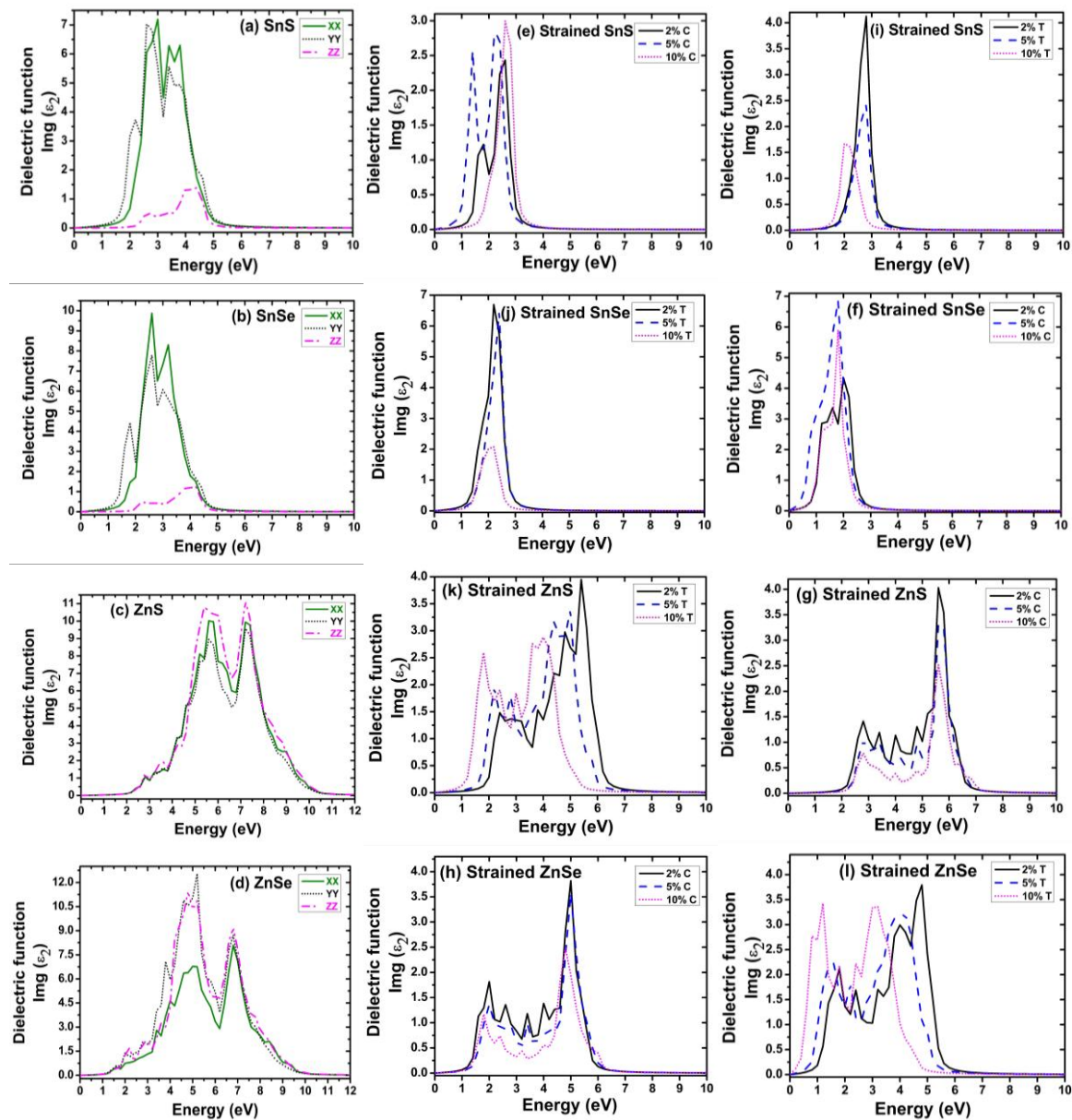
Fig. 6.12 Imaginary Dielectric function: SnS, SnSe, ZnS and ZnSe monolayers.

In ZnS and ZnSe monolayers, strain shift the peaks of refractive index in lower energies along with some peaks in the high energy range which represent the non-zero infrared absorption. Certainly, due to applied strain on the monolayer of SnSe, SnS, ZnSe, and ZnS, the refractive index peaks shift toward low energies, enhancing light retention and absorption in the desired visible range and ultimately improving utilization in optoelectronic applications.

6.5   SUMMARY OF THE IMPORTANT RESULTS

1. DFT calculations are executed to investigate the electronic, structural, and optical properties of monolayers of tin monochalcogenides (SnS and SnSe) and zinc monochalcogenides (ZnS and ZnSe).

2. Further, the monolayer of SnS is stacked with monolayer SnSe, ZnS, and ZnSe to form the heterostructure SnS/SnSe, SnS/ZnS, and SnS/ZnSe, and the effect of stacking on electronic, structural, and optical properties is analyzed.

3. It is found from the calculated results that the bandgap of the monolayer of SnS, SnSe, ZnS, and ZnSe are 1.70 eV, 1.46 eV, 2.35 eV, and 1.46 eV, respectively. However, due to the formation of the heterostructure, the bandgap is narrowed down to 1.04 eV, 0.6 eV, and 0.9 eV for the SnS/SnSe, SnS/ZnS and SnS/ZnSe, respectively.

4. The monolayer of ZnS and ZnSe have zero absorption in the visible region. Due to the formation of the heterostructure of SnS with SnSe, ZnS, and ZnSe, the absorption is improved significantly in the visible spectrum (380 to 700 nm).

5. The shifting of the absorption towards the higher energies due to the formation of heterostructure is an indication of the existence of redshift in the formed heterostructures.

6. The narrowed bandgap and improved optical properties due to the formation of the heterostructure SnS/SnSe, SnS/ZnS, and SnS/ZnSe advocate their usefulness in the fabrication of optoelectronic, photovoltaic, and solar devices.

7. Furthermore, the impact of compressive strain and tensile strain on the optical properties and electronic properties of monolayers of tin and zinc monochalcogenides are examined.

8. The applied tensile strain and compressive strain (2%, 5%, and 10%) on the monolayers resulted in a significant reduction in the bandgap across all the monolayers.

9. Furthermore, the absorption shifts towards the lower energies, giving rise to the red-shift phenomenon under the applied strain.

10. The effect of strain on SnS monolayers reveals a shift in optical absorption. Unstrained SnS absorbs in the ultraviolet region (~150-600 nm, ~1.7-6.5 eV). Applying 2%, 5%, and 10% strain\ (compressive/tensile) shifts absorption into the visible spectrum, with 5% compressive and 10% tensile strain causing the most significant redshift.

11. The absorption in unstrained ZnS begins at ~2.3 eV, peaking around ~9 eV. Applied compressive and tensile strains shift absorption to lower energies, with peaks at ~4.5-6.5 eV. Strain also moves absorption from the ultraviolet to the visible spectrum, with 10% tensile strain enabling continuous absorption across the visible range (~300-650 nm).

12. The sifting is very significant in the case of a high value of applied strain. The lessening of the bandgap and improvements in the visible region absorption due to applied strain, advocate the potential applicability of the strained SnSe, SnS, ZnSe, and ZnS for various optoelectronic applications.

CHAPTER - 7

CONCLUSIONS AND FUTURE SCOPE

Oxide perovskites, particularly $SrTiO_3$ (STO) and $LiNbO_3$, exhibit unique structural, electronic, and optical properties that make them highly suitable for optoelectronic applications. $SrTiO_3$ is a wide-bandgap semiconductor (2.94 eV) that primarily absorbs in the UV region, while $LiNbO_3$ has an even larger bandgap of 3.56 eV. However, their inherent limitations in visible-light absorption necessitate bandgap engineering through doping and strain modulation to expand their application potential. The tunability of $SrTiO_3$ and $LiNbO_3$ makes them highly promising for various optoelectronic applications. In solar cells, metal-doped STO is used as a photoanode due to its ability to absorb visible light efficiently and facilitate charge transfer processes.

$LiNbO_3$, with its strong nonlinear optical properties, is employed in second-harmonic generation and electro-optic modulators, enhancing laser technology and optical communication. The oxide perovskite has immense potential in advancing optoelectronics, photovoltaics, and sustainable energy solutions, reinforcing their role as key materials for next-generation electronic and photonic technologies. In this chapter, the key findings of all the preceding chapters are summarized in section 7.1. Further, in section 7.2, the future scope for further research and development is elaborated.

7.1 CONCLUSIONS

This work has presented the density functional theory (DFT) analysis of pristine and metal-doped $LiNbO_3$ reveals significant improvements in its electronic and optical properties. The large bandgap of pristine $LiNbO_3$ limits its absorption to the UV region, but doping with metals such as Au, Ag, Al, Cu, Fe, Mn, Mo, and Ni effectively reduces the bandgap, shifting absorption into the visible spectrum. This bandgap reduction is most pronounced in Mo-doped (0.61 eV) and Mn-doped (0.72 eV) $LiNbO_3$, making them particularly suitable for optoelectronic applications. Plasmonic dopants such as Au and Ag demonstrate remarkable optical enhancements due to their surface plasmon resonance effects.

Additionally, metal doping induces lattice parameter changes, with Ag and Al showing the highest unit cell volume expansion. The overall findings indicate that metal-doped $LiNbO_3$

holds great promise for photonic and optoelectronic applications, with its tunable electronic and optical properties enabling its potential use in UV photodetectors, optical sensors, and visible-light-driven technologies.This research explored the investigation into plasmonic-metal-doped $SrTiO_3$ (STO) using DFT first-principles calculations underscores the transformative effect of Ag, Al, Au, and Cu doping on its structural, electronic, and optical behavior.

The introduction of these dopants leads to a significant reduction in bandgap, with Ag-STO (1.57 eV), Au-STO (1.56 eV), and Cu-STO (1.54 eV) displaying the most substantial shifts. This reduction enhances visible-light absorption, particularly in the 450–700 nm range, rendering these materials highly efficient for optoelectronic and photocatalytic applications. The study further establishes that Ag and Au exhibit the highest optical absorption due to their strong plasmonic effects. Moreover, the alignment of the valence and conduction bands of Ag, Au, and Cu-doped STO with the water redox potential suggests their viability for photocatalytic water splitting under visible light. The findings indicate that plasmonic-metal-doped STO not only enhances absorption in the visible spectrum but also retains its photocatalytic efficiency, making it a highly promising candidate for solar-driven applications and optoelectronics.

Further the first-principles DFT calculations performed on pristine and metal-doped (Ag, Al, Au, Cu) $LiNbO_3$ and $SrTiO_3$ under strain reveal significant modifications in their electronic and optical properties. Doping introduces lattice distortions, causing volume expansion and leading to notable bandgap reductions, thereby improving visible-light absorption. For $LiNbO_3$, compressive and tensile strains further tune the bandgap, with Cu-doped $LiNbO_3$ reaching as low as 0.41 eV under 20% tensile strain, demonstrating high tunability for optoelectronics. Similarly, strain-induced modifications in $SrTiO_3$ result in improved absorption characteristics, with Ag- and Cu-doped STO exhibiting peak absorption shifts towards the visible region. The combination of metal doping and strain engineering significantly enhances the optoelectronic and photocatalytic performance of these materials, offering promising avenues for next-generation photonic devices, solar cells, and water-splitting applications.

Furthermore, the electronic and optical properties of monolayers of tin and zinc monochalcogenides (SnS, SnSe, ZnS, and ZnSe) and their heterostructures were analyzed using DFT calculations. The formation of heterostructures significantly narrows the bandgap and enhances absorption in the visible spectrum, improving their optoelectronic performance. The SnS/SnSe, SnS/ZnS, and SnS/ZnSe heterostructures exhibit bandgap reductions to 1.04

eV, 0.6 eV, and 0.9 eV, respectively, making them ideal for photovoltaic applications. Moreover, the application of tensile and compressive strain leads to further bandgap tuning and a redshift in absorption. Strained ZnS and ZnSe exhibit notable absorption shifts from the UV to the visible range, with 10% tensile strain enabling continuous absorption across 300-650 nm. These findings highlight the immense potential of strained and heterostructured tin and zinc monochalcogenides in the development of advanced optoelectronic and solar energy devices.

7.2 FUTURE SCOPE

Based on the research conducted in this thesis and the results reported, several future scopes can be suggested for further research and development. Future research can focus on the experimental realization of metal-doped and strain-engineered materials to validate theoretical predictions. Synthesis techniques such as pulsed laser deposition, sol-gel methods, and molecular beam epitaxy can be explored to fabricate high-quality doped $LiNbO_3$, $SrTiO_3$, and monochalcogenide heterostructures. Advanced characterization techniques, including X-ray diffraction (XRD), Raman spectroscopy, and ultrafast spectroscopy, will be essential to assess structural, electronic, and optical modifications. Furthermore, investigating the stability of these materials under varying environmental conditions, such as temperature, humidity, and prolonged light exposure, will be crucial for their practical applications.

Strain engineering remains a promising strategy for bandgap tuning, but further studies may explore its application under real fabrication conditions. Investigating strain effects in thin films grown on lattice-mismatched substrates or through mechanical strain application in flexible electronic devices can provide deeper insights into strain-induced modifications. Additionally, combining strain engineering with external electric or magnetic fields may offer new ways to control electronic transitions and enhance optoelectronic performance. Future work can also explore the synergistic effects of multiple dopants or defect engineering to achieve precise control over the optical absorption range and electronic band structure.

Computational advancements can further refine material discovery by incorporating machine-learning models and high-throughput screening methods. The use of hybrid functionals, many-body perturbation theory (GW approximation), and time-dependent DFT can provide more accurate predictions of electronic and optical properties. Expanding research to other perovskites, transition metal oxides, and layered van der Waals materials can help identify novel candidates for next-generation optoelectronic and photocatalytic applications.

Additionally, integrating these materials into real-world devices, such as UV photodetectors, transparent conductive films, and solar-driven water-splitting systems, will be essential for transitioning from theoretical studies to practical applications.

REFERENCES

[1]   S. Rai and A. Rai, "Nanotechnology-the secret of fifth industrial revolution and the future of next generation," Nusantara Biosci., vol. 7, no. 2, pp. 61-66, 2017.

[2]   M. Boholm, "The use and meaning of nano in American English: Towards a systematic description," Ampersand, vol. 3, pp. 163-173, 2016.

[3]   V. P. Sharma, U. Sharma, M. Chattopadhyay, and V. N. Shukla, "Advance applications of nanomaterials: a review," Mater. Today:. Proc., vol. 5, no. 2, Part 1, pp. 6376-6380, 2018.

[4]   N. Kumar and S. Kumbhat, "Carbon-based nanomaterials," in Essentials in Nanoscience and Nanotechnology, John Wiley & Sons, Ltd, pp. 189-236, 2016.

[5]   D. Jariwala, V. K. Sangwan, L. J. Lauhon, T. J. Marks, and M. C. Hersam, "Carbon nanomaterials for electronics, optoelectronics, photovoltaics, and sensing," Chem. Soc. Rev., vol. 42, no. 7, pp. 2824-2860, 2013.

[6]   E. O. Ogunsona, R. Muthuraj, E. Ojogbo, O. Valerio, and T. H. Mekonnen, "Engineered nanomaterials for antimicrobial applications: a review," Appl. Mater. Today, vol. 18, p. 100473, 2020.

[7]   A. Saravanan, P. S. Kumar, R. V. Hemavathy et al., "A review on synthesis methods and recent applications of nanomaterial in wastewater treatment: challenges and future perspectives," Chemosphere, vol. 307, p. 135713, 2022.

[8]   A. Adewuyi and W. J. Lau, "Nanomaterial development and its applications for emerging pollutant removal in water," in Handbook of Nanomaterials, Eds. Elsevier, pp. 67-97, 2021.

[9]   S. Bayda, M. Adeel, T. Tuccinardi, M. Cordani, and F. Rizzolio, "The history of nanoscience and nanotechnology: from chemical-physical applications to nanomedicine," Molecules, vol. 25, no. 1, pp. 1-15, 2020.

[10]   P. Sciau, "Nanoparticles in ancient materials: the metallic lustre decorations of medieval ceramics," The Delivery of Nanoparticles, vol. 115, pp. 525-540, 2012.

[11]   S. K. Kulkarni, Nanotechnology: Principles and Practices. Springer, 2015.

[12]   G. Mie, "Beitrage zur Optik truber Medien, speziell kolloidaler Metallosungen," Ann. Phys., vol. 330, no. 3, pp. 377-445, 1908.

[13] M. Riordan, L. Hoddeson, and C. Herring, "The invention of the transistor," Rev. Mod. Phys., vol. 71, no. SUPPL 2, 1999.

[14] J. D. Watson and F. H. C. Crick, "Molecular structure of nucleic acids: a structure for deoxyribose nucleic acid," Nature, vol. 171, no. 4356, pp. 737-738, 1953.

[15] A. K. Singh, Engineered Nanoparticles: Structure, Properties and Mechanisms of Toxicity, 2015.

[16] S. Iijima and T. Ichihashi, "Single-shell carbon nanotubes of 1-nm diameter," Nature, vol. 363, no. 6430, pp. 603-605, 1993.

[17] W. H. Hunt, "Nanomaterials: nomenclature, novelty, and necessity," JOM, vol. 56, no. 10, pp. 13-18, 2004.

[18] U.S. Congress, 21st Century Nanotechnology Research and Development Act, S. Rept. 108-147, 108th Congress, 2003.

[19] A. K. Geim and K. S. Novoselov, "The rise of graphene," Nature Mater., vol. 6, no. 3, pp. 183–191, 2007.

[20] N. Panneerselvam, D. Sundaramurthy, and A. Maruthapillai, "Pectin/Xylitol incorporated with various metal oxide based nanocomposite films for its antibacterial and antioxidant activity," J. Polym. Environ., vol. 31, no. 4, pp. 1598–1609, 2023.

[21] National Nanotechnology Initiative (NNI), "Glossary," 2021. [Online]. Available: https://www.nano.gov/about-nni/glossary.

[22] F. S. Ligler et al., "Optical biosensors: today and tomorrow," in Nanoparticles for Biosensors, 2nd ed. Elsevier B.V., 2008. [Online]. Available: https://doi.org/10.1016/B978-0-444-53125-4.50017-6.

[23] T. Commission, "Commission recommendations," Nurs. Stand., vol. 24, no. 26, p. 6, 2010.

[24] R. Hayami et al., "Preparation and properties of organic–inorganic hybrid materials using titanium phosphonate cluster," Polym. J., vol. 49, no. 9, pp. 665–669, 2017.

[25] K. M. L. Taylor-Pashow et al., "Hybrid nanomaterials for biomedical applications," Chem. Commun., vol. 46, no. 32, pp. 5832–5849, 2010.

[26] V. V. Pokropivny and V. V. Skorokhod, "Classification of nanostructures by dimensionality and concept of surface forms engineering in nanomaterial science," Mater. Sci. Eng., C, vol. 27, no. 5, pp. 990–993, 2007.

[27] J. Jeevanandam et al., "Review on nanoparticles and nanostructured materials: History, sources, toxicity and regulations," Beilstein J. Nanotechnol., vol. 9, no. 1, pp. 1050–1074, 2018.

[28] T. A. Saleh, "Nanomaterials: classification, properties, and environmental toxicities," Environ. Technol. Innov., vol. 20, p. 101067, 2020.

[29] Kumar and S. Kumbhat, Carbon-based nanomaterials, in Essentials in Nanoscience and Nanotechnology, John Wiley & Sons, Ltd, pp. 189–236, 2016.

[30] A. B. Asha and R. Narain, Nanomaterials properties, in Polymer Science and Nanotechnology, Elsevier, pp. 343–359, 2020.

[31] T. Y. Poh, N. A. T. B. M. Ali, M. Mac Aogáin, M. H. Kathawala, M. I. Setyawati, K. W. Ng, and S. H. Chotirmall, "Inhaled nanomaterials and the respiratory microbiome: clinical, immunological and toxicological perspectives," Part. Fibre Toxicol., vol. 15, no. 1, pp. 1-16, 2018.

[32] S. Ali, I. Khan, S. A. Khan, M. Sohail, R. Ahmed, A. ur Rehman, and M. A. Morsy, "Electrocatalytic performance of Ni@Pt core-shell nanoparticles supported on carbon nanotubes for methanol oxidation reaction," J. Electroanal. Chem., vol. 795, pp. 17-25, 2017.

[33] V. Georgakilas, J. A. Perman, J. Tucek, and R. Zboril, "Broad family of carbon nanoallotropes: classification, chemistry, and applications of fullerenes, carbon dots, nanotubes, graphene, nanodiamonds, and combined superstructures," Chem. Rev., vol. 115, no. 11, pp. 4744-4822, 2015.

[34] S. Choudhary and S. Qureshi, "Theoretical study on the effect of dopant positions and dopant density on transport properties of a BN co-doped SiC nanotube," Phys. Lett. A, vol. 377, no. 5, pp. 430-435, 2013.

[35] A. S. Bhalla, R. Guo, and R. Roy, "The perovskite structure—a review of its role in ceramic science and technology," Mater. Res. Innov., vol. 4, no. 1, pp. 3–26, 2000.

[36] E. A. Katz, "Perovskite: name puzzle and German-Russian odyssey of discovery," Helv. Chim. Acta, vol. 103, no. 6, p. e2000061, 2020.

[37] Y. Choi, S. Han, B. I. Park, Z. Xu, Q. Huang, S. Bae, and S. H. Bae, "Perovskite nanocomposites: synthesis, properties, and applications from renewable energy to optoelectronics," Nano Convergence, vol. 11, no. 1, p. 36, 2024.

[38] T. T. Dang, T. L. A. Nguyen, K. B. Ansari, V. H. Nguyen, N. T. Binh, T. T. N. Phan, and Q. T. Trinh, "Perovskite materials as photocatalysts: Current status and future perspectives," in Nanostructured Photocatalysts, pp. 169-216, 2021.

[39] L. Zhang, L. Mei, K. Wang, Y. Lv, S. Zhang, Y. Lian, and L. Ding, "Advances in the application of perovskite materials," Nano-Micro Lett., vol. 15, no. 1, p. 177, 2023.

[40] H. Wang, Y. Sun, J. Chen, F. Wang, R. Han, C. Zhang, and J. Yang, "A review of perovskite-based photodetectors and their applications," Nanomaterials, vol. 12, no. 24, p. 4390, 2022.

[41] L. Lin, Y. Liu, W. Wu, L. Huang, X. Zhu, Y. Xie, and A. Pan, "Self-powered perovskite photodetector arrays with asymmetric contacts for imaging applications," Adv. Electron. Mater., vol. 9, no. 10, p. 2300106, 2023.

[42] H. Zhang, Y. Luo, F. Tang, C. Wu, and B. Lin, "First-principle prediction of one-dimensional silicon allotropes: Promising new candidate for chemical and electrochemical hydrogen storage," Int. J. Hydrogen Energy, vol. 48, no. 14, pp. 5552-5564, 2023.

[43] P. Fu, Q. Shan, Y. Shang, J. Song, H. Zeng, Z. Ning, and J. Gong, "Perovskite nanocrystals: synthesis, properties and applications," Sci. Bull., vol. 62, no. 5, pp. 369-380, 2017.

[44] M. H. Miah, M. U. Khandaker, M. B. Rahman, M. Nur-E-Alam, and M. A. Islam, "Band gap tuning of perovskite solar cells for enhancing the efficiency and stability: issues and prospects," RSC Adv., vol. 14, no. 23, pp. 15876-15906, 2024.

[45] H. Dong, C. Ran, W. Gao, M. Li, Y. Xia, and W. Huang, "Metal halide perovskite for next-generation optoelectronics: progresses and prospects," eLight, vol. 3, no. 1, p. 3, 2023.

[46] N. K. Elangovan, R. Kannadasan, B. B. Beenarani, M. H. Alsharif, M. K. Kim, and Z. H. Inamul, "Recent developments in perovskite materials, fabrication techniques, band gap engineering, and the stability of perovskite solar cells," Energy Rep., vol. 11, pp. 1171-1190, 2024.

[47] M. V. Kovalenko, L. Protesescu, and M. I. Bodnarchuk, "Properties and potential optoelectronic applications of lead halide perovskite nanocrystals," *Science*, vol. 358, no. 6364, pp. 745-750, 2017.

[48] Y. Liu, Y. Liu, and Y. Guo, "Organic-inorganic hybrid perovskite materials and their application in transistors," Mater. Chem. Front., vol. 7, no. 21, pp. 5215-5246, 2023.

[49] V. Chauhan, D. Tripathi, P. Singh, A. Sharma, M. K. Khanna, R. Kumar, and T. Kumar, "Prospects for lead free perovskite for photovoltaic applications and biological impacts: challenges and opportunities," Inorg. Chem. Commun., vol. 157, p. 111421, 2023.

[50] D. A. Egger, A. M. Rappe, and L. Kronik, "Hybrid organic-inorganic perovskites on the move," Acc. Chem. Res., vol. 49, no. 3, pp. 573-581, 2016.

[51] D. Yang, M. Cao, Q. Zhong, P. Li, X. Zhang, and Q. Zhang, "All-inorganic cesium lead halide perovskite nanocrystals: synthesis, surface engineering and applications," J. Mater. Chem. C, vol. 7, no. 4, pp. 757-789, 2019.

[52] Q. Tai, K. C. Tang, and F. Yan, "Recent progress of inorganic perovskite solar cells," Energy Environ. Sci., vol. 12, no. 8, pp. 2375-2405, 2019.

[53] R. L. Hoye, J. Hidalgo, R. A. Jagt, J. P. Correa-Baena, T. Fix, and J. L. MacManus-Driscoll, "The role of dimensionality on the optoelectronic properties of oxide and halide perovskites, and their halide derivatives," Adv. Energy Mater., vol. 12, no. 4, p. 2100499, 2022.

[54] C. He and X. Liu, "The rise of halide perovskite semiconductors," Light Sci. Appl., vol. 12, no. 1, p. 15, 2023.

[55] S. I. Seok and T. F. Guo, "Halide perovskite materials and devices," MRS Bull., vol. 45, no. 6, pp. 427-430, 2020.

[56] X. Ye, X. Wang, Z. Liu, B. Zhou, L. Zhou, H. Deng, and Y. Long, "Emergent physical properties of perovskite-type oxides prepared under high pressure," Dalton Trans., vol. 51, no. 5, pp. 1745-1753, 2022.

[57] A. Zuzic, A. Ressler, and J. Macan, "Perovskite oxides as active materials in novel alternatives to well-known technologies: A review," Ceram. Int., vol. 48, no. 19, pp. 27240-27261, 2022.

[58] T. A. Chowdhury, M. A. B. Zafar, M. S. U. Islam, M. Shahinuzzaman, M. A. Islam, and M. U. Khandaker, "Stability of perovskite solar cells: issues and prospects," RSC Adv., vol. 13, no. 3, pp. 1787-1810, 2023.

[59] C. C. Boyd, R. Cheacharoen, T. Leijtens, and M. D. McGehee, "Understanding degradation mechanisms and improving stability of perovskite photovoltaics," Chem. Rev., vol. 119, no. 5, pp. 3418-3451, 2018.

[60] H. Li, C. Lai, Z. Wei, X. Zhou, S. Liu, L. Qin, and Y. Li, "Strategies for improving the stability of perovskite for photocatalysis: A review of recent progress," Chemosphere, vol. 344, p. 140395, 2023.

[61] R. S. Weis and T. K. Gaylord, "Lithium niobate: Summary of physical properties and crystal structure," Appl. Phys. A, vol. 37, pp. 191-203, 1985.

[62] V. Mishra, A. Sagdeo, V. Kumar, M. K. Warshi, H. M. Rai, S. K. Saxena, and P. R. Sagdeo, "Electronic and optical properties of BaTiO3 across tetragonal to cubic phase transition: An experimental and theoretical investigation," J. Appl. Phys., vol. 122, no. 6, 2017.

[63]   C. E. Ekuma, M. Jarrell, J. Moreno, and D. Bagayoko, "First principle electronic, structural, elastic, and optical properties of strontium titanate," AIP Advances, vol. 2, no. 1, 2012.

[64]   A. R. Benrekia, N. Benkhettou, A. Nassour, M. Driz, M. Sahnoun, and S. Lebègue, "Structural, electronic and optical properties of cubic SrTiO3 and KTaO3: Ab initio and GW calculations," Physica B: Condensed Matter, vol. 407, no. 13, pp. 2632-2636, 2012.

[65]   S. Adjokatse, H. H. Fang, and M. A. Loi, "Broadly tunable metal halide perovskites for solid-state light-emission applications," Materials Today, vol. 20, no. 8, pp. 413-424, 2017.

[66]   F. Alarab, J. Minár, P. Šutta, L. Prušáková, R. Medlín, O. Heckmann, and K. Hricovini, "Study and characterization of SrTiO3 surface," in AIP Conference Proceedings, vol. 1996, no. 1, 2018.

[67]   M. M. Hossain, "First-principles study on the structural, elastic, electronic and optical properties of LiNbO3," Heliyon, vol. 5, no. 4, 2019.

[68]   Y. Fu, H. Zhu, J. Chen, M. P. Hautzinger, X. Y. Zhu, and S. Jin, "Metal halide perovskite nanostructures for optoelectronic applications and the study of physical properties," Nature Reviews Materials, vol. 4, no. 3, pp. 169-188, 2019.

[69]   B. L. Phoon, C. W. Lai, J. C. Juan, P. L. Show, and C. H. Chen, "A review of synthesis and morphology of SrTiO3 for energy and other applications," International Journal of Energy Research, vol. 43, no. 10, pp. 5151-5174, 2019.

[70]   J. K. Kar, N. Dharmale, and S. Chaudhury, "DFT based studies on the structural, electronic and optical properties of LiNbO3 using some hybrid techniques," Phys. Scr., vol. 96, no. 12, p. 125854, 2021.

[71]   L. Chouhan, S. Ghimire, C. Subrahmanyam, T. Miyasaka, and V. Biju, "Synthesis, optoelectronic properties and applications of halide perovskites," Chemical Society Reviews, vol. 49, no. 10, pp. 2869-2885, 2020.

[72]   M. I. Kholil and M. T. H. Bhuiyan, "Effects of Cr-and Mn-alloying on the band gap tuning, and optical and electronic properties of lead-free CsSnBr3 perovskites for optoelectronic applications," RSC Advances, vol. 10, no. 71, pp. 43660-43669, 2020.

[73]   S. S. A. Gillani, R. Ahmad, I. Zeba, M. Shakil, M. Rizwan, M. Rafique, and S. S. Hassan, "Effect of external pressure on the structural stability, electronic structure, band gap engineering and optical properties of LiNbO3: an ab-initio calculation," Materials Today Communications, vol. 23, p. 100919, 2020.

[74]   M. Z. Rahaman, S. Ge, C. H. Lin, Y. Cui, and T. Wu, "One-dimensional molecular metal halide materials: structures, properties, and applications," Small Structures, vol. 2, no. 4, p. 2000062, 2021.

[75]   R. Sharif, A. Khalid, S. W. Ahmad, A. Rehman, H. G. Qutab, H. H. Akhtar, and F. Saleem, "A comprehensive review of the current progresses and material advances in perovskite solar cells," Nanoscale Advances, vol. 5, no. 15, pp. 3803-3833, 2023.

[76]   X. Liu, Y. Wang, Y. Wang, Y. Zhao, J. Yu, X. Shan, and H. C. Kuo, "Recent advances in perovskites-based optoelectronics," Nanotechnology Reviews, vol. 11, no. 1, pp. 3063-3094, 2022.

[77]   K. Burke and L. O. Wagner, "DFT in a nutshell," Int. J. Quantum Chem., vol. 113, no. 2, pp. 96-101, 2013.

[78]   M. Segall, P. J. Lindan, M. J. Probert, C. J. Pickard, P. J. Hasnip, S. Clark, and M. Payne, "First-principles simulation: ideas, illustrations and the CASTEP code," Journal of Physics: Condensed Matter, vol. 14, no. 11, pp. 2717-2744, 2002.

[79]   J. A. Owolabi, M. Y. Onimisi, S. G. Abdu, and G. O. Olowomofe, "Determination of band structure of gallium-arsenide and aluminium-arsenide using density functional theory," Comput. Chem., vol. 4, no. 3, pp. 73-82, 2016.

[80]   D. Bagayoko, "Understanding density functional theory (DFT) and completing it in practice," AIP Adv., vol. 4, no. 12, 2014.

[81]   F. Oba, M. Choi, A. Togo, and I. Tanaka, "Defect energetics in ZnO: A hybrid Hartree-Fock density functional study," Science and Technology of Advanced Materials, vol. 12, no. 3, p. 034302, 2011.

[82]   R. Kochar and S. Choudhary, "MoS2/Phosphorene Heterostructure for Optical Absorption in Visible Region," IEEE Journal of Quantum Electronics, vol. 54, no. 4, pp. 1-6, 2018.

[83]   K. Harun, N. A. Salleh, B. Deghfel, M. K. Yaakob, and A. A. Mohamad, "First-principles calculations of electronic and optical properties of orthorhombic LiNbO3," Results in Physics, vol. 16, pp. 102829-102840, 2020.

[84]   S. Dudarev, G. Botton, S. Savrasov, C. Humphreys, and A. Sutton, "Electron-energy-loss spectra and the structural stability of nickel oxide: An LSDA+U study," Physical Review B, vol. 57, no. 3, pp. 1505-1509, 1998.

[85]   C. Delerue, G. Allan, and M. Lannoo, "Optical band gap of Si nanoclusters," Journal of Luminescence, vol. 80, no. 1-4, pp. 65-73, 1998.

[86]   W. Kang and M. S. Hybertsen, "Quasiparticle and optical properties of rutile and anatase TiO2," Physical Review B, vol. 82, no. 8, p. 085203, 2010.

[87]   C. Stampfl, W. Mannstadt, R. Asahi, and A. J. Freeman, "Electronic structure and physical properties of early transition metal mononitrides: Density-functional theory LDA, GGA, and screened-exchange LDA FLAPW calculations," Phys. Rev. B, vol. 63, no. 15, p. 155106, 2001.

[88]   M. S. Abu-Jafar, A. M. Abu-Labdeh, and M. El-Hasan, "The energy band gap of ScN in the rocksalt phase obtained with LDA/GGA+USIC approximations in FP-LAPW method," Comput. Mater. Sci., vol. 50, no. 2, pp. 269-273, 2010.

[89]   C. E. Ekuma, D. Bagayoko, M. Jarrell, and J. Moreno, "Electronic, structural, and elastic properties of metal nitrides XN (X=Sc, Y): A first principle study," AIP Advances, vol. 2, no. 3, 2012.

[90]   S. X. Tao, X. Cao, and P. A. Bobbert, "Accurate and efficient band gap predictions of metal halide perovskites using the DFT-1/2 method: GW accuracy with DFT expense," Sci. Rep., vol. 7, no. 1, p. 14386, 2017.

[91]   N. Hernandez-Haro, J. Ortega-Castro, Y. B. Martynov, R. G. Nazmitdinov, and A. Frontera, "DFT prediction of band gap in organic-inorganic metal halide perovskites: An exchange-correlation functional benchmark study," Chem. Phys., vol. 516, pp. 225-231, 2019.

[92]   M. Arrigoni and G. K. Madsen, "Comparing the performance of LDA and GGA functionals in predicting the lattice thermal conductivity of III-V semiconductor materials in the zincblende structure: The cases of AlAs and BAs," Comput. Mater. Sci., vol. 156, pp. 354-360, 2019.

[93]   Y. Zhang, J. A. Alarco, A. S. Best, G. A. Snook, P. C. Talbot, and J. Y. Nerkar, "Re-evaluation of experimental measurements for the validation of electronic band structure calculations for LiFePO4 and FePO4," RSC Adv., vol. 9, no. 2, pp. 1134-1146, 2019.

[94]   A. Patra, S. Jana, P. Samal, F. Tran, L. Kalantari, J. Doumont, and P. Blaha, "Efficient band structure calculation of two-dimensional materials from semilocal density functionals," J. Phys. Chem. C, vol. 125, no. 20, pp. 11206-11215, 2021.

[95]   N. H. Harun, R. B. S. Mydin, S. Sreekantan, K. A. Saharuddin, and A. Seeni, "In vitro bio-interaction responses and hemocompatibility of nano-based linear low-density polyethylene polymer embedded with heterogeneous TiO2/ZnO nanocomposites for biomedical applications," J. Biomater. Sci. Polym. Ed., vol. 32, no. 10, pp. 1301-1311, 2021.

[96] P. Makkar and N. N. Ghosh, "A review on the use of DFT for the prediction of the properties of nanomaterials," RSC Adv., vol. 11, no. 45, pp. 27897-27924, 2021.

[97] A. M. Ghaleb, R. A. Munef, and S. F. Mohammed, "First principles study the effect of Zn doped MgO on the energy band gap using GGA approximation," J. Ovonic Res., vol. 18, no. 1, 2022.

[98] J. Alvarez, M. Boutchich, J. P. Kleider, T. Teraji, and Y. Koide, "Direct observation of the leakage current in epitaxial diamond Schottky barrier devices by conductive-probe atomic force microscopy and Raman imaging," J. Phys. D: Appl. Phys., vol. 47, no. 35, p. 355102, 2014.

[99] K. Kabita, J. Maibam, B. I. Sharma, R. B. Singh, and R. K. Thapa, "First principles phase transition, elastic properties and electronic structure calculations for cadmium telluride under induced pressure: density functional theory, LDA, GGA and modified Becke-Johnson potential," Mater. Res. Express, vol. 3, no. 1, p. 015901, 2016.

[100] W. Li, Z. Wang, X. Xiao, Z. Zhang, A. Janotti, S. Rajasekaran, and B. Medasani, "Predicting band gaps and band-edge positions of oxide perovskites using density functional theory and machine learning," Phys. Rev. B, vol. 106, no. 15, p. 155156, 2022.

[101] I. Derkaoui, M. Achehboune, R. I. Eglitis, A. I. Popov, I. Boukhoubza, M. A. Basyooni-M. Kabatas, and A. Rezzouk, "Influence of the Hubbard U Correction on the Electronic Properties and Chemical Bands of the Cubic (Pm3m) Phase of SrTiO3 Using GGA/PBE and LDA/CA-PZ Approximations," Molecules, vol. 29, no. 13, p. 3081, 2024.

[102] R. R. Pela, C. L. Hsiao, L. Hultman, J. Birch, and G. K. Gueorguiev, "Electronic and optical properties of core-shell InAlN nanorods: a comparative study via LDA, LDA-1/2, mBJ, HSE06, G0W0 and BSE methods," Phys. Chem. Chem. Phys., vol. 26, no. 9, pp. 7504-7514, 2024.

[103] D. P. Joseph and C. Venkateswaran, "Bandgap engineering in ZnO by doping with 3d transition metal ions," J. At. Mol. Phys., vol. 2011, p. 270540, 2011.

[104] R. Mariappan, V. Ponnuswamy, M. Ragavendar, D. Krishnamoorthi, and C. Sankar, "The effect of annealing temperature on structural and optical properties of undoped and Cu doped CdS thin films," Optik, vol. 123, no. 12, pp. 1098-1102, 2012.

[105] H. Yan, X. Wang, M. Yao, and X. Yao, "Band structure design of semiconductors for enhanced photocatalytic activity: The case of TiO2," Prog. Nat. Sci.: Mater. Int., vol. 23, no. 4, pp. 402-407, 2013.

[106] V. B. Taxak, S. Singh, and S. P. Khatkar, "Synthesis and optical properties of red emitting Eu doped CaZrO3 phosphor," Optik, vol. 125, no. 20, pp. 6340-6343, 2014.

[107] T. Shen, C. Hu, H. L. Dai, W. L. Yang, H. C. Liu, C. L. Tan, and X. L. Wei, "First principles calculations of magnetic, electronic and optical properties of (Mn-Fe) co-doped SrTiO3," Optik, vol. 127, no. 5, pp. 3055-3058, 2016.

[108] H. Kafashan, R. Ebrahimi-Kahrizsangi, F. Jamali-Sheini, and R. Yousefi, "Effect of Al doping on the structural and optical properties of electrodeposited SnS thin films," Phys. Status Solidi A, vol. 213, no. 5, pp. 1302-1308, 2016.

[109] G. Pan, X. Bai, D. Yang, X. Chen, P. Jing, S. Qu, and H. Song, "Doping lanthanide into perovskite nanocrystals: highly improved and expanded optical properties," Nano Lett., vol. 17, no. 12, pp. 8005-8011, 2017.

[110] Y. Iriani, R. Afriani, and F. Nurosyid, "Co-precipitation Synthesis and Photocatalytic Activity of Mn-doped SrTiO3 for the Degradation of Methylene Blue Wastewater," J. Phys.: Conf. Ser., vol. 1912, no. 1, p. 012039, 2021.

[111] M. Rizwan, A. Ali, Z. Usman, N. R. Khalid, H. B. Jin, and C. B. Cao, "Structural, electronic and optical properties of copper-doped SrTiO3 perovskite: a DFT study," Physica B, vol. 552, pp. 52-57, 2019.

[112] S. S. A. Gillani, R. Ahmad, M. Rizwan, M. Shakil, M. Rafique, G. Murtaza, and H. B. Jin, "First-principles investigation of structural, electronic, optical and thermal properties of Zinc doped SrTiO3," Optik, vol. 201, p. 163481, 2020.

[113] A. Farhat, R. A. Khera, S. Iqbal, and J. Iqbal, "Tuning the optoelectronic properties of Subphthalocyanine (SubPc) derivatives for photovoltaic applications," Opt. Mater., vol. 107, p. 110154, 2020.

[114] S. Azam, Z. Abbas, Q. Bilal, M. Irfan, M. A. Khan, S. H. Naqib, and X. Wang, "Effect of Fe doping on optoelectronic properties of CdS nanostructure: Insights from DFT calculations," Physica B, vol. 583, p. 412056, 2020.

[115] Z. Suo, J. Dai, S. Gao, and H. Gao, "Effect of transition metals (Sc, Ti, V, Cr and Mn) doping on electronic structure and optical properties of CdS," Results Phys., vol. 17, p. 103058, 2020.

[116] M. Kumar, P. Basera, S. Saini, and S. Bhattacharya, "Role of defects in photocatalytic water splitting: monodoped vs codoped SrTiO3," J. Phys. Chem. C, vol. 124, no. 19, pp. 10272-10279, 2020.

[117] S. Suzuki, A. Iwase, and A. Kudo, "Long wavelength visible light-responsive SrTiO3 photocatalysts doped with valence-controlled Ru for sacrificial H2 and O2 evolution," Catal. Sci. Technol., vol. 10, no. 15, pp. 4912-4916, 2020.

[118] N. Pathak, P. S. Ghosh, S. Mukherjee, and B. P. Mandal, "Simultaneous tuning of optical and electrical properties in a multifunctional LiNbO3 matrix upon doping with Eu3+ ions," RSC Adv., vol. 10, no. 52, pp. 31070-31086, 2020.

[119] A. A. Al-Ghamdi, O. A. Al-Hartomy, M. El Okr, A. M. Nawar, S. El-Gazzar, F. El-Tantawy, and F. Yakuphanoglu, "Semiconducting properties of Al doped ZnO thin films," Spectrochim. Acta A Mol. Biomol. Spectrosc., vol. 131, pp. 512-517, 2014.

[120] Y. Guo, J. Su, L. Wang, Z. Lin, Y. Hao, and J. Chang, "Improved doping and optoelectronic properties of Zn-doped CsPbBr3 perovskite through Mn codoping approach," J. Phys. Chem. Lett., vol. 12, no. 13, pp. 3393-3400, 2021.

[121] A. Rauf, M. Adil, S. A. Mian, G. Rahman, E. Ahmed, Z. Mohy Ud Din, and W. Qun, "Tuning the optoelectronic properties of hematite with rhodium doping for photoelectrochemical water splitting using density functional theory approach," Sci. Rep., vol. 11, no. 1, p. 41, 2021.

[122] S. Jiao, J. Yan, G. Sun, and Y. Zhao, "Electronic structures and optical properties of Nb-doped SrTiO3 from first principles," J. Semicond., vol. 37, no. 7, p. 072001, 2016.

[123] R. V. Nair, V. S. Gummaluri, and M. V. Matham, "A review on optical bandgap engineering in TiO2 nanostructures via doping and intrinsic vacancy modulation towards visible light applications," J. Phys. D: Appl. Phys., vol. 55, no. 31, p. 313003, 2022.

[124] Q. A. Alsulami, Z. Arshad, M. Ali, and S. Wageh, "Efficient tuning of the opto-electronic properties of sol-gel-synthesized al-doped titania nanoparticles for perovskite solar cells and functional textiles," Gels, vol. 9, no. 2, p. 101, 2023.

[125] M. B. Kanoun, F. Ahmed, C. Awada, C. Jonin, and P. F. Brevet, "Band gap engineering of Au doping and Au-N codoping into anatase TiO2 for enhancing the visible light photocatalytic performance," Int. J. Hydrogen Energy, vol. 51, pp. 907-913, 2024.

[126] A. U. R. Khan, M. Ramzan, S. J. Alanazi, A. M. Al-Mohaimeed, S. Ali, M. Imran, and M. H. Sarfraz, "Structural, Optical, Electrical and Photocatalytic Investigation of n-Type Zn2+-Doped α-Bi2O3 Nanoparticles for Optoelectronics Applications," ACS Omega, vol. 9, no. 21, pp. 22650-22659, 2024.

[127]   L. Yao, X. Wu, S. Yang, and Y. Zhang, "Structural and optical properties of Ca doped BiFeO3 thin films prepared by a sol-gel method," Ceram. Int., vol. 43, pp. S470-S473, 2017.

[128]   M. Choi, A. B. Posadas, C. A. Rodriguez, A. O'Hara, H. Seinige, A. J. Kellock, and A. A. Demkov, "Structural, optical, and electrical properties of strained La-doped SrTiO3 films," J. Appl. Phys., vol. 116, no. 4, 2014.

[129]   V. R. Akshay, B. Arun, G. Mandal, and M. Vasundhara, "Visible range optical absorption, Urbach energy estimation and paramagnetic response in Cr-doped TiO2 nanocrystals derived by a sol-gel method," Phys. Chem. Chem. Phys., vol. 21, no. 24, pp. 12991-13004, 2019.

[130]   B. Kiss, T. D. Manning, D. Hesp, C. Didier, A. Taylor, D. M. Pickup, and M. J. Rosseinsky, "Nano-structured rhodium doped SrTiO3-Visible light activated photocatalyst for water decontamination," Appl. Catal. B: Environ., vol. 206, pp. 547-555, 2017.

[131]   V. D. Pon, K. J. Wilson, K. Hariprasad, V. Ganesh, H. E. Ali, H. Algarni, and I. S. Yahia, "Enhancement of optoelectronic properties of ZnO thin films by Al doping for photodetector applications," Superlattices Microstruct., vol. 151, p. 106790, 2021.

[132]   Z. Li, M. Xiong, X. Li, J. Li, N. Wang, and S. Zhang, "First principle study of electronic structure and optical properties of Mo doped ZnO with different concentrations," Optik, vol. 228, p. 166136, 2021.

[133]   H. Bantawal, U. S. Shenoy, and D. K. Bhat, "Vanadium-Doped SrTiO3 Nanocubes: Insight into role of vanadium in improving the photocatalytic activity," Appl. Surf. Sci., vol. 513, p. 145858, 2020.

[134]   Y. Rong, Y. Hu, A. Mei, H. Tan, M. I. Saidaminov, S. I. Seok, and H. Han, "Challenges for commercializing perovskite solar cells," Science, vol. 361, no. 6408, p. eaat8235, 2018.

[135]   C. K. Ghosh, D. Sarkar, M. K. Mitra, and K. K. Chattopadhyay, "Electronic structure and optical properties of CuAlO2 under biaxial strain," J. Phys.: Condens. Matter, vol. 24, no. 23, p. 235501, 2012.

[136]   B. Mohan, A. Kumar, and P. K. Ahluwalia, "Electronic and optical properties of silicene under uni-axial and bi-axial mechanical strains: a first principle study," Physica E, vol. 61, pp. 40-47, 2014.

[137]   S. Yang, C. Wang, H. Sahin, H. Chen, Y. Li, S. S. Li, and S. Tongay, "Tuning the optical, magnetic, and electrical properties of ReSe2 by nanoscale strain engineering," Nano Lett., vol. 15, no. 3, pp. 1660-1666, 2015.

[138]   D. Misra and T. K. Kundu, "Effect of strain on the optical properties of LaNiO3: A first-principle study," Comput. Mater. Sci., vol. 112, pp. 113-119, 2016.

[139]   J. Jalilian, M. Naseri, S. Safari, and M. Zarei, "Tuning of the electronic and optical properties of single-layer indium nitride by strain and stress," Physica E, vol. 83, pp. 372-377, 2016.

[140]   H. Huan, L. Chen, and X. Ye, "Strain effect on the electronic and optical properties of CdSe nanowires," Nanoscale Res. Lett., vol. 12, no. 1, p. 6, 2017.

[141]   F. Colangelo, A. Morandi, S. Forti, F. Fabbri, C. Coletti, F. V. Di Girolamo, and S. Roddaro, "Local tuning of WS2 photoluminescence using polymeric micro-actuators in a monolithic van der Waals heterostructure," Appl. Phys. Lett., vol. 115, no. 18, 2019.

[142]   J. A. Silva-Guillén, E. Canadell, F. Guinea, and R. Roldán, "Strain tuning of the anisotropy in the optoelectronic properties of TiS3," ACS Photonics, vol. 5, no. 8, pp. 3231-3237, 2018.

[143]   A. A. Aloufi, Z. A. Alahmed, A. Laref, and H. A. Albrithen, "Strain effects on structural, electronic, and optical properties of BeO by DFT," Mater. Res. Bull., vol. 114, pp. 52-60, 2019.

[144]   H. R. Jappor, M. M. Obeid, T. V. Vu, D. M. Hoat, H. D. Bui, N. N. Hieu, and R. Khenata, "Engineering the optical and electronic properties of Janus monolayer Ga2SSe by biaxial strain," Superlattices Microstruct., vol. 130, pp. 354-360, 2019.

[145]   D. M. Hoat, T. V. Vu, M. M. Obeid, and H. R. Jappor, "Assessing optoelectronic properties of PbI2 monolayer under uniaxial strain from first principles calculations," Superlattices Microstruct., vol. 130, pp. 354-360, 2019.

[146]   C. Zhu, X. Niu, Y. Fu, N. Li, C. Hu, Y. Chen, and Q. Chen, "Strain engineering in perovskite solar cells and its impacts on carrier dynamics," Nat. Commun., vol. 10, no. 1, p. 815, 2019.

[147]   T. V. Vu, H. D. Tong, D. P. Tran, N. T. Binh, C. V. Nguyen, H. V. Phuc, and N. N. Hieu, "Electronic and optical properties of Janus ZrSSe by density functional theory," RSC Adv., vol. 9, no. 70, pp. 41058-41065, 2019.

[148] A. Bafekry, M. Yagmurcukardes, M. Shahrokhi, and M. Ghergherehchi, "Electro-optical properties of monolayer and bilayer boron-doped C3N: tunable electronic structure via strain engineering and electric field," Carbon, vol. 168, pp. 220-229, 2020.

[149] J. Guo, C. Ke, Y. Wu, and J. Kang, "Strain engineering on the electronic and optical properties of WSSe bilayer," Nanoscale Res. Lett., vol. 15, no. 1, p. 9, 2020.

[150] B. Neupane, H. Tang, N. K. Nepal, and A. Ruzsinszky, "Bending as a control knob for the electronic and optical properties of phosphorene nanoribbons," Phys. Rev. Mater., vol. 6, no. 1, p. 014010, 2022.

[151] Y. Feng, H. Bai, M. An, Y. Wu, and X. Wang, "Density functional theory study of the electronic and optical properties of SnSe2/MoSe2 heterostructures under strain and electric field: implications for optoelectronic devices," ACS Appl. Nano Mater., vol. 6, no. 17, pp. 15795-15806, 2023.

[152] A. Kamat, K. Gurukrishna, R. Kumar, A. Mishra, A. K. Verma, S. Tripathi, and S. Misra, "Tunable insulator-metal transition in epitaxial VO2 thin films via strain and defect engineering," Nanoscale Adv., vol. 6, no. 22, pp. 5625-5635, 2024.

[153] K. K. Haldar, G. Sinha, J. Lahtinen, and A. Patra, "Hybrid colloidal Au-CdSe pentapod heterostructures synthesis and their photocatalytic properties," ACS Appl. Mater. Interfaces, vol. 4, no. 11, pp. 6266-6272, 2012.

[154] G. He, H. Fan, and Z. Wang, "Enhanced optical properties of heterostructured ZnO/CeO2 nanocomposite fabricated by one-pot hydrothermal method: fluorescence and ultraviolet absorption and visible light transparency," Opt. Mater., vol. 38, pp. 145-153, 2014.

[155] H. J. Feng, K. Yang, W. Deng, M. Li, M. Wang, B. Duan, and X. Guo, "The origin of enhanced optical absorption of the BiFeO3/ZnO heterojunction in the visible and terahertz regions," Phys. Chem. Chem. Phys., vol. 17, no. 40, pp. 26930-26936, 2015.

[156] D. B. Salunkhe, D. P. Dubal, J. V. Sali, and B. R. Sankapal, "Linker free synthesis of TiO2/Bi2S3 heterostructure towards solar cell application: Facile chemical routes," Mater. Sci. Semicond. Process., vol. 30, pp. 335-342, 2015.

[157] Q. Peng, Z. Wang, B. Sa, B. Wu, and Z. Sun, "Electronic structures and enhanced optical properties of blue phosphorene/transition metal dichalcogenides van der Waals heterostructures," Sci. Rep., vol. 6, no. 1, p. 31994, 2016.

[158] S. Choudhary and A. K. Garg, "Enhanced absorption in MoS2/Hg0.33Cd0.66Te Heterostructure for application in solar cell absorbers," IEEE Trans. Nanotechnol., vol. 18, pp. 989-994, 2019.

[159] X. Yang, X. Qin, J. Luo, N. Abbas, J. Tang, Y. Li, and K. Gu, "HfS2/MoTe2 vdW heterostructure: bandstructure and strain engineering based on first-principles calculation," RSC Adv., vol. 10, no. 5, pp. 2615-2623, 2020.

[160] T. N. Do, M. Idrees, B. Amin, N. N. Hieu, H. V. Phuc, L. T. Hoa, and C. V. Nguyen, "First principles study of structural, optoelectronic and photocatalytic properties of SnS, SnSe monolayers and their van der Waals heterostructure," Chem. Phys., vol. 539, p. 110939, 2020.

[161] A. Maniyar and S. Choudhary, "Visible region absorption in TMDs/phosphorene heterostructures for use in solar energy conversion applications," RSC Adv., vol. 10, no. 53, pp. 31730-31739, 2020.

[162] F. Yao, X. Zhou, and A. Xiong, "Tunable electronic and optical properties of two-dimensional ZnSe/AlAs van der Waals heterostructure," Appl. Phys. A, vol. 126, no. 5, p. 364, 2020.

[163] J. Li and X. Zhou, "The Structural, Electronic, and Optical Properties of a Novel Multilayer Heterostructure ZnSe/AlAs/GaAs: First-Principles Study," Phys. Status Solidi B, vol. 258, no. 6, p. 2100034, 2021.

[164] M. I. Khan, S. Ali, N. Alwadai, M. Irfan, H. Albalawi, A. H. Almuqrin, and M. Iqbal, "Structural, electrical and optical properties of hetrostructured MoS2/ZnO thin films for potential perovskite solar cells application," J. Mater. Res. Technol., vol. 20, pp. 1616-1623, 2022.

[165] H. P. Komsa and A. V. Krasheninnikov, "Electronic structures and optical properties of realistic transition metal dichalcogenide heterostructures from first principles," Phys. Rev. B, vol. 88, no. 8, p. 085318, 2013.

[166] D. Y. Lin, H. P. Hsu, K. H. Liu, P. H. Wu, Y. T. Shih, Y. F. Wu, and C. F. Lin, "Enhanced optical response of SnS/SnS2 layered heterostructure," Sensors, vol. 23, no. 10, p. 4976, 2023.

[167] H. Zhang, X. Ji, H. Yao, Q. Fan, B. Yu, and J. Li, "Review on efficiency improvement effort of perovskite solar cell," Sol. Energy, vol. 233, pp. 421-434, 2022.

[168] K. Zhang, N. Zhu, M. Zhang, L. Wang, and J. Xing, "Opportunities and challenges in perovskite LED commercialization," J. Mater. Chem. C, vol. 9, no. 11, pp. 3795-3799, 2021.

[169] H. Wang and D. H. Kim, "Perovskite-based photodetectors: materials and devices," Chem. Soc. Rev., vol. 46, no. 17, pp. 5204-5236, 2017.

[170] N. S. Kumar and K. C. B. Naidu, "A review on perovskite solar cells (PSCs), materials and applications," J. Materiomics, vol. 7, no. 5, pp. 940-956, 2021.

[171] N. F. Atta, A. Galal, E. E. Ads, and L. Pan, "Perovskite nanomaterials-synthesis, characterization, and applications," in Perovskite Materials-Synthesis, Characterisation, Properties, and Applications, Intech, pp. 107-151, 2016.

[172] L. N. Quan, B. P. Rand, R. H. Friend, S. G. Mhaisalkar, T. W. Lee, and E. H. Sargent, "Perovskites for next-generation optical sources," Chem. Rev., vol. 119, pp. 7444-7477, 2019.

[173] H. Huang, L. Polavarapu, J. A. Sichert, A. S. Susha, A. S. Urban, and A. L. Rogach, "Colloidal lead halide perovskite nanocrystals: synthesis, optical properties and applications," NPG Asia Mater., vol. 8, p. e328, 2016.

[174] F. Hu, H. Zhang, C. Sun, C. Yin, B. Lv, C. Zhang, W. W. Yu, X. Wang, Y. Zhang, and M. Xiao, "Superior optical properties of perovskite nanocrystals as single photon emitters," ACS Nano, vol. 9, pp. 12410-12416, 2015.

[175] A. M. A. Amri, B. Cheng, and J. He, "Perovskite methylammonium lead trihalide heterostructures: Progress and challenges," IEEE Trans. Nanotechnol., vol. 18, pp. 1-12, 2018.

[176] F. Dogan, H. Lin, M. G. Viry, and O. Pena, "Focus on properties and applications of perovskites," Sci. Technol. Adv. Mater., vol. 16, p. 020301, 2015.

[177] S. Negi, P. Mittal, and B. Kumar, "In-depth analysis of structures, materials, models, parameters, and applications of organic light-emitting diodes," J. Electron. Mater., vol. 49, pp. 4610-4636, 2020.

[178] O. A. J. Quintero, R. S. Sanchez, M. Rincon, and I. M. Sero, "Bright visible-infrared light emitting diodes based on hybrid halide perovskite with Spiro-OMeTAD as a hole-injecting layer," J. Phys. Chem. Lett., vol. 6, pp. 1883-1890, 2015.

[179] Z. K. Tan, R. S. Moghaddam, and M. L. Lai, "Bright light-emitting diodes based on organometal halide perovskite," Nat. Nanotechnol., vol. 9, pp. 687-692, 2014.

[180] S. Negi, P. Mittal, and B. Kumar, "Numerical modeling and parameters extraction of novel triple hole block layer based organic light emitting diode for display," J. Soc. Inf. Disp., vol. 28, pp. 1-9, 2020.

[181] S. Negi, P. Mittal, and B. Kumar, "Impact of different layers on performance of OLED," Microsyst. Technol., vol. 24, pp. 1-9, 2018.

[182] P. R. Prezas and M. P. F. Graça, "Structural characterization of lithium niobate nanoparticles prepared by the sol-gel process, using X-ray and Raman spectroscopy

and scanning electron microscopy," in Applications of Molecular Spectroscopy to Current Research in the Chemical and Biological Sciences, Intech, p. 32, 2016.

[183] R. S. Klein, G. E. Kugel, A. Maillard, K. Polgar, and A. Peter, "Absolute non-linear optical coefficients of LiNbO3 for near stoichiometric crystal compositions," Opt. Mater., vol. 22, pp. 171-174, 2003.

[184] W. Sohler, H. Hu, R. Ricken, V. Quiring, C. Vannahme, H. Herrmann, D. Buchter, S. Reza, W. Grundkötter, S. Orlov, H. Suche, R. Nouroozi, and Y. Min, "Integrated optical devices in lithium niobate," Opt. Photon. News, vol. 19, pp. 24-31, 2008.

[185] F. Abdi, M. D. Fontana, M. Aillerie, and P. Bourson, "Defect structure in pure LiNbO3 and its relationship to optical properties," Appl. Phys. A, vol. 83, pp. 427-434, 2016.

[186] A. Javid, Z. Khan, Z. Mehmood, and A. Nabi, "Structural, electronic and optical properties of LiNbO3 using GGA-PBE and TB-mBJ functionals: A DFT study," Int. J. Mod. Phys. B, vol. 32, p. 1850168, 2018.

[187] B. Sun, J. Gou, J. Wang, and Y. Jiang, "Composition dependence of the ultraviolet absorption edge in lithium tantalate films," in Proc. 9th Int. Symp. Adv. Opt. Manuf. Test. Technol.: Optoelectron. Mater. Devices Sens. Imag., 2019.

[188] M. Rahaman and A. K. M. Hossain, "Effect of metal doping on the visible light absorption, electronic structure and mechanical properties of non-toxic metal halide CsGeCl3," RSC Adv., vol. 8, pp. 33010-33018, 2018.

[189] K. Song and X. Han, "Electronic properties of rutile TiO2 doped with 4d transition metals: First-principles study," J. Alloys Compd., vol. 551, pp. 118-124, 2013.

[190] P. Chamola and P. Mittal, "Zinc telluride material properties for solar cell application: Absorber layer," Optik, vol. 224, p. 165626, 2020.

[191] H. D. Hui, Y. J. Sheng, C. Q. Long, W. M. Jie, L. Qilong, S. Liang, and W. F. Hou, "Effect of Mg and Fe doping on optical absorption of LiNbO3 crystal through first principles calculations," Chin. Phys. Lett., vol. 31, p. 037103, 2014.

[192] A. E. Bachiri, M. E. Hasnaoui, F. Bennani, and M. Bousselamti, "Effect of Ni-doping charge on structure and properties of LiNbO3," J. Mater. Environ. Sci., vol. 7, pp. 3353-3361, 2016.

[193] D. Vilela, M. C. González, and A. Escarpa, "Sensing colorimetric approaches based on gold and silver nanoparticles aggregation," Anal. Chim. Acta, vol. 751, pp. 24-43, 2012.

[194]   X. Huang and M. A. E. Sayed, "Gold nanoparticles: Optical properties and implementations in cancer diagnosis and photothermal therapy," J. Adv. Res., vol. 1, pp. 13-28, 2010.

[195]   M. Li, L. Shi, T. Xie, C. Jing, G. Xiu, and Y. T. Long, "Plasmonic metallic nanostructures as colorimetric probes for environmental pollutants," ACS Sens., vol. 2, pp. 263-267, 2017.

[196]   M. Jabeen and S. Haxha, "Increased optical absorption and light-matter interaction in silicon thin-film solar cell nanostructure using graphene and 2-dimensional Au/Ag," IEEE J. Quantum Electron., vol. 54, pp. 1-12, 2018.

[197]   S. Negi, P. Mittal, B. Kumar, and P. Juneja, "Microelectronic engineering," vol. 218, p. 111154, 2019.

[198]   P. Sena, P. K. Sen, R. Bhatt, S. Kar, V. Shukla, and K. S. Bartwal, "The effect of MgO doping on optical properties of LiNbO3 single crystals," Solid State Commun., vol. 129, pp. 747-752, 2004.

[199]   J. P. Perdew, K. Burke, and M. Ernzerhof, "Generalized gradient approximation made simple," Phys. Rev. Lett., vol. 77, pp. 3865-3868, 1996.

[200]   H. J. Monkhorst and J. D. Pack, "Special points for Brillouin-zone integrations," Phys. Rev. B, vol. 13, pp. 5188-5192, 1976.

[201]   F. Tran and P. Blaha, "Accurate band gaps of semiconductors and insulators with a semilocal exchange-correlation potential," Phys. Rev. Lett., vol. 102, p. 226401, 2009.

[202]   R. M. Martin, Electronic Structure: Basic Theory and Practical Methods, Cambridge University Press, New York, 2014.

[203]   D. J. Griffiths, Introduction to Electrodynamics, 3rd ed., Prentice Hall, 1999.

[204]   X. Liu, W. Que, Y. He, and H. Zhou, "A first-principle study on the electronic properties of substitutionally Cu (I, II)-doped LiNbO3," J. Adv. Dielectr., vol. 8, p. 1820002, 2018.

[205]   J. Yu and X. Liu, "Hydrothermal synthesis and characterization of LiNbO3 crystal," Mater. Lett., vol. 61, pp. 355-358, 2007.

[206]   P. Mittal, "Ditch and elevated organic thin film transistor-based improved common source voltage amplifier: Frequency response characteristics and analytical modeling," J. Soc. Inf. Disp., vol. 29, pp. 642-658, 2021.

[207]   N. E. H. Fares and N. Bouarissa, "Band structure, charge distribution and optical properties of AlPxSb1-x ternary semiconductor alloys," Mater. Res., vol. 21, p. e20170964, 2014.

[208]   L. J. Kong, G. H. Liu, and Y. J. Zhang, "Tuning the electronic and optical properties of phosphorene by transition-metal and nonmetallic atom co-doping," RSC Adv., vol. 6, pp. 10919-10929, 2016.

[209]   B. Yang, D. B. Geohegan, and K. Xiao, "Perovskite materials: Solar cell and optoelectronic applications," in Encyclopedia of Inorganic and Bioinorganic Chemistry, pp. 1-14, 2011.

[210]   G. Yadav and S. Choudhary, "Tuning the optical properties of zinc sulfide nanotube," IEEE Trans. Nanotechnol., vol. 17, pp. 807-813, 2018.

[211]   Y. Bi, M. F. Ehsan, Y. Huang, J. Jin, and T. He, "Synthesis of Cr-doped SrTiO3 photocatalyst and its application in visible-light-driven transformation of CO2 into CH4," J. CO2 Util., vol. 12, pp. 43-48, 2015.

[212]   J. Lim, H. Lim, and Y. S. Lee, "Ambient dependence of visible emissions in SrTiO3," Curr. Appl. Phys., vol. 19, pp. 1177-1181, 2019.

[213]   H. Che, J. Chen, and K. Huang, "Construction of SrTiO3/Bi2O3 heterojunction towards to improved separation efficiency of charge carriers and photocatalytic activity under visible light," J. Alloys Compd., vol. 688, pp. 882-890, 2016.

[214]   T. Jarlborg, "Tuning of the electronic screening and electron-phonon coupling in doped SrTiO3 and WO3," Phys. Rev. B, vol. 61, p. 9887, 2000

[215]   S. Suzuki, T. Yamamoto, H. Suzuki, K. Kawaguchi, K. Takahashi, and Y. Yoshisato, "Fabrication and characterization of Ba1-xKxBiO3/Nb-doped SrTiO3 all-oxide-type Schottky junctions," J. Appl. Phys., vol. 81, pp. 6830-6836, 1997.

[216]   X. Liu, Z. Xing, H. Zhang, W. Wang, Y. Zhang, Z. Li, X. Wu, X. Yu, and W. Zhou, "Fabrication of 3D mesoporous black TiO2/MoS2/TiO2 nanosheets for visible-light-driven photocatalysis," ChemSusChem, vol. 9, pp. 1118-1124, 2016.

[217]   X. Zhou, J. Shi, and C. Li, "Effect of metal doping on electronic structure and visible light absorption of SrTiO3 and NaTaO3 (Metal=Mn, Fe, and Co)," J. Phys. Chem. C, vol. 115, pp. 8305-8311, 2011.

[218]   H. Irie, Y. Maruyama, and K. Hashimoto, "Ag+- and Pb2+-doped SrTiO3 photocatalysts. A correlation between band structure and photocatalytic activity," J. Phys. Chem. C, vol. 111, pp. 1847-1852, 2007.

[219]   H. Yu, Y. Peng, and Y. Yang, "Plasmon-enhanced light-matter interactions and applications," npj Comput. Mater., vol. 5, p. 45, 2019.

[220] F. Scotognella, G. D. Valle, A. R. S. Kandada, M. Z. Rossi, S. Longhi, S. Lanzani, and F. Tassone, "Plasmonics in heavily-doped semiconductor nanocrystals," Eur. Phys. J. B, vol. 86, p. 154, 2013.

[221] Z. Liang, J. Sun, and Y. Jiang, "Plasmonic enhanced optoelectronic devices," Plasmonics, vol. 9, pp. 859-866, 2014.

[222] G. Kresse and J. Furthmüller, "Efficient iterative schemes for ab initio total-energy calculations using a plane-wave basis set," Phys. Rev. B, vol. 54, p. 11169, 1996.

[223] G. R. Berdiyorov, "Optical properties of functionalized $Ti_3C_2T_2$ (T=F, O, OH) MXene: First-principles calculations," AIP Adv., vol. 6, p. 055105, 2016

[224] R. H. Mitchell, A. R. Chakhmouradian, and P. M. Woodward, "Crystal chemistry of perovskite-type compounds in the tausonite-loparite series, $(Sr_{1-2x}Na_xLa_x)TiO_3$," Phys. Chem. Miner., vol. 27, pp. 583-589, 2000.

[225] M. Barrimi, R. Aalouane, C. Aarab, H. Hafidi, H. Baybay, M. Soughi, N. Tachfouti, C. Nejjari, F. Z. Mernissi, I. Rammouz, and R. B. McKenzie, "An investigation of thermoelectric power factor of Mn and Nb doped $SrTiO_3$ ceramics," Encephale, vol. 53, pp. 59-65, 2013.

[226] Y. Wang, Y. Liu, Q. Zhai, M. Zhang et al., "Effect of doping concentration on electronic, magnetic and optical properties of (Fe, Mn) co-doped $SrTiO_3$: A first-principles study," Optoelectron. Adv. Mater., vol. 12, pp. 579-583, 2018.

[227] Y. Xu and M. A. A. Schoonen, "The absolute energy positions of conduction and valence bands of selected semiconducting minerals," Am. Mineral., vol. 85, pp. 543-556, 2000.

[228] R. W. Godby, M. Schlüter, and L. J. Sham, "Accurate exchange-correlation potential for silicon and its discontinuity on addition of an electron," Phys. Rev. Lett., vol. 56, p. 2415, 1986.

[229] G. Z. Wang, H. Chen, X. K. Luo, H. K. Yuan, and A. L. Kuang, "Bandgap engineering of $SrTiO_3/NaTaO_3$ heterojunction for visible light photocatalysis," Int. J. Quantum Chem., vol. 117, p. e25424, 2017.

[230] A. Ali, M. Rizwan, M. Shakil, S. S. A. Gillani, and M. F. Ehsan, "First-principles investigation on electronic structure, magnetic states and optical properties of Mn-doped SnS_2 monolayer via strain engineering," *Phys. E Low-dimens. Syst. Nanostruct.*, vol. 134, p. 114842, 2021.

[231] H. Bentour, M. El Yadari, A. El Kenz, and A. Benyoussef, "DFT study of electronic and optical properties of (S–Mn) co-doped $SrTiO_3$ for enhanced photocatalytic hydrogen production," *Solid State Commun.*, vol. 312, p. 113893, 2020.

[232] Y. Bi, M. F. Ehsan, Y. Huang, J. Jin, and T. He, "Synthesis of Cr-doped $SrTiO_3$ photocatalyst and its application in visible-light-driven transformation of CO_2 into CH_4," *J. CO_2 Util.*, vol. 12, pp. 43–48, 2015.

[233] Y. Chen, S. Lei, Y. Li, W. Li, J. Yu, and J. Luo, "Strain engineering and epitaxial stabilization of halide perovskites," *Nature*, vol. 577, no. 7789, pp. 209–215, 2020.

[234] A. Dhar and A. Mansingh, "Optical properties of reduced lithium niobate single crystals," *J. Appl. Phys.*, vol. 68, no. 10, pp. 5804–5809, 1990.

[235] D. Ghosh, A. Aziz, J. A. Dawson, A. B. Walker, and M. S. Islam, "Putting the squeeze on lead iodide perovskites: Pressure-induced effects to tune their structural and optoelectronic behavior," *Chem. Mater.*, vol. 31, no. 11, pp. 4063–4071, 2019.

[236] R. Husin, F. W. Badrudin, M. F. M. Taib, and M. Z. A. Yahya, "Effects of strain on electronic and optical properties of $LiNbO_3$: A first principles study," *Mater. Res. Express*, vol. 6, no. 11, p. 114002, 2019.

[237] D. P. Ngurah Made, M. R. Sahar, and M. R. Sudin, "Interrelation of intrinsic defects and optical absorption properties of lithium niobate ($LiNbO_3$) crystals," *J. Nonlinear Opt. Phys. Mater.*, vol. 14, no. 2, pp. 237–243, 2005.

[238] A. Srivastava, M. I. Khan, N. Tyagi, and P. Swaroop Khare, "Doping induced structural stability and electronic properties of GaN nanotubes," *Sci. World J.*, vol. 2014, 2014.

[239] K. van Benthem, C. Elsässer, and R. H. French, "Bulk electronic structure of $SrTiO_3$: Experiment and theory," *J. Appl. Phys.*, vol. 90, no. 12, pp. 6156–6164, 2001.

[240] K. Xu, "Silicon electro-optic micro-modulator fabricated in standard CMOS technology as components for all silicon monolithic integrated optoelectronic systems," *J. Micromech. Microeng.*, vol. 31, no. 5, p. 054001, 2021.

[241] Y. Zhou, G. Cheng, and J. Li, "Coexistence of Co doping and strain on arsenene and antimonene: Tunable magnetism and half-metallic behavior," *RSC Adv.*, vol. 8, no. 3, pp. 1320–1327, 2018.

[242] L. Zhao, H. Chang, W. Zhao, Z. Luan, X. Tian, C. Tan, and Y. Huang, "Coexistence of doping and strain to tune electronic and optical properties of GaN monolayer," Superlattices Microstruct., vol. 130, pp. 93–102, 2019.

[243] K. van Benthem, C. Elsasser, and R. H. French, "Bulk electronic structure of $SrTiO_3$: Experiment and theory," J. Appl. Phys., vol. 90, no. 12, pp. 6156-6164, 2001.

[244] X. Liu, Z. Tao, W. Luo, and T. Chakraborty, "Interlayer excitons in double-layer transition metal dichalcogenide quantum dots," *Phys. Rev. B*, vol. 111, no. 8, p. 085424, 2025.

[245] T. Tan, X. Jiang, C. Wang, B. Yao, and H. Zhang, "2D material optoelectronics for information functional device applications: Status and challenges," Adv. Sci., vol. 7, no. 11, p. 2000058, 2020.

[246] S. Yadav, P. Mittal, and S. Negi, "Characteristic performance and analysis of the positional variation of the charge generation layer to enhance the performance of OLEDs," J. Comput. Electron., vol. 22, no. 6, pp. 1696-1705, 2023.

[247] H. Liu, A. T. Neal, Z. Zhu, Z. Luo, X. Xu, D. Tománek, and P. D. Ye, "Phosphorene: An unexplored 2D semiconductor with a high hole mobility," ACS Nano, vol. 8, no. 4, pp. 4033-4041, 2014.

[248] P. Vogt, P. De Padova, C. Quaresima, J. Avila, E. Frantzeskakis, M. C. Asensio, A. Resta, B. Ealet, and G. Le Lay, "Silicene: Compelling experimental evidence for graphenelike two-dimensional silicon," Phys. Rev. Lett., vol. 108, no. 15, p. 155501, 2012.

[249] X. Duan, C. Wang, A. Pan, R. Yu, and X. Duan, "Two-dimensional transition metal dichalcogenides as atomically thin semiconductors: Opportunities and challenges," Chem. Soc. Rev., vol. 44, no. 24, pp. 8859-8876, 2015.

[250] G. Shan, H. Tan, R. Ma, H. Zhao, and W. Huang, "Recent progress in emergent two-dimensional silicene," Nanoscale, vol. 15, no. 7, pp. 2982-2996, 2023.

[251] O. P. Singh and V. P. Gupta, "Electronic properties of tin monochalcogenides (SnS, SnSe, SnTe)," Phys. Status Solidi B, vol. 136, no. 1, 1986.

[252] S. Ferahtia, S. Saib, and N. Bouarissa, "Computational studies of mono-chalcogenides ZnS and ZnSe at high-pressures," Results Phys., vol. 15, p. 102626, 2019.

[253] A. T. Hoang, L. Hu, A. K. Katiyar, and J.-H. Ahn, "Two-dimensional layered materials and heterostructures for flexible electronics," Matter, vol. 5, no. 12, pp. 4116-4132, 2022.

[254] J. Zhou, "Recent progress on 2D group II-VI binary chalcogenides ZnX and CdX (X=S, Se, Te): From a theoretical perspective," Adv. Theory Simul., vol. 2, no. 8, p. 1900061, 2019.

[255] A. Dahiya, P. Mittal, and R. Rohilla, "Variation-tolerant sense amplifier using decoupling transistors for enhanced SRAM read performance," Circuits Syst. Signal Process., vol. 42, no. 10, pp. 5799-5810, 2023.

[256] A. S. I. Al-Shammari, B. A. Nia, and S. Rezaee, "Ab initio calculation of electronic and optical properties of vdWHs HfX2/BSb (X=Se, S) using density functional theory," Phys. Scr., vol. 99, no. 6, p. 065970, 2024.

[257] D. S. Aditya and S. K. Nataraj, "Structural, optical, and electronic properties of two-dimensional nanomaterials," in Two-Dimensional Nanomaterials-Based Polymer Nanocomposites: Processing, Properties and Applications, 2024, pp. 167-194.

[258] L.-Y. Huang, X. Zhang, M. Zhang, and G. Lu, "Optically inactive defects in monolayer and bilayer phosphorene: A first-principles study," Phys. Rev. Mater., vol. 2, no. 5, p. 054003, 2018.

[259] J. Feng, X. Qian, C.-W. Huang, and J. Li, "Strain-engineered artificial atom as a broad-spectrum solar energy funnel," Nat. Photonics, vol. 6, no. 12, pp. 866-872, 2012.

[260] J. Han et al., "Band splitting under strain: A route to broad-spectrum absorption," Mater. Today Phys., vol. 39, p. 101286, 2023.

[261] X. Fan, L. Liu, J.-L. Kuo, and Z. Shen, "Functionalizing single- and multi-layer graphene with Br and Br2," J. Phys. Chem. C, vol. 114, no. 35, pp. 14939-14945, 2010.

[262] M. X. Low et al., "Strain modulation of optoelectronic properties in nanolayered black phosphorus: Implications for strain-engineered 2D material systems," ACS Appl. Nano Mater., vol. 5, no. 9, pp. 12189-12195, 2022.

[263] P. Priyadarshini, S. Das, and R. Naik, "A review on metal-doped chalcogenide films and their effect on various optoelectronic properties for different applications," RSC Adv., vol. 12, no. 16, pp. 9599-9620, 2022.

[264] A. Batool et al., "DFT study of the structural, electronic, and optical properties of bulk, monolayer, and bilayer Sn-monochalcogenides," Appl. Surf. Sci. Adv., vol. 11, p. 100275, 2022.

[265] M. Alam et al., "Optoelectronics properties of Janus SnSSe monolayer for solar cells applications," Phys. B, vol. 625, p. 413487, 2022.

[266] Y. E. Xu and J. H. Chu, "Tuning electronic and optical properties of SnSe by external strain," Optik, vol. 218, p. 165260, 2020.

[267] R. Gangadharan et al., "Electronic and structural properties of zinc chalcogenides ZnX (X=S, Se, Te)," J. Alloys Compd., vol. 359, no. 1-2, pp. 22-26, 2003.

[268] M. Majidiyan Sarmazdeh et al., "Investigation of the electronic and optical properties of ZnS monolayer nanosheet: First principles calculations," J. Mater. Sci., vol. 52, pp. 3003-3015, 2017.

[269]   S. H. Mirza et al., "First-principles quantum analysis of structural, optoelectronic, and thermophysical properties of Co/Ni doped ceria Ce1-xTmxO2 (Tm=Co, Ni) for solar cell applications," Phys. Scr., 2024.

[270]   S. G. Thoma et al., "Synthesis, optical properties, and growth mechanism of blue-emitting CdSe nanorods," J. Am. Chem. Soc., vol. 127, no. 20, pp. 7611-7614, 2005.

[271]   P. Chamola, P. Mittal, and B. Kumar, "Organic solar cells: Structural variety, effect of layers, and applications," ECS J. Solid State Sci. Technol., vol. 13, no. 3, p. 035001, 2024.

[272]   D. Q. Trung et al., "Synthesis, structural and optical properties of ZnS/ZnO heterostructure-alloy hexagonal micropyramids," Opt. Mater., vol. 125, p. 112077, 2022.

[273]   X. Li, S. Zhang, X.-J. Wang, G.-F. Huang, L.-X. Xia, W. Hu, and W.-Q. Huang, "A two-dimensional MoS2/SnS heterostructure for promising photocatalytic performance: First-principles investigations," Physica E, vol. 126, p. 114453, 2021.

[274]   C. Wang, S. Li, S. Wang, P. Zhao, and R. Zhuo, "First principles study of the effect of uniaxial strain on monolayer MoS2," Physica E, vol. 144, p. 115401, 2022.

[275]   Z. Peng et al., "Strain engineering of 2D semiconductors and graphene: From strain fields to band-structure tuning and photonic applications," Light Sci. Appl., vol. 9, no. 1, p. 190, 2020.

[276]   M. S. Khan et al., "Insight into the optoelectronic and thermoelectric properties for zinc-based TMCs: First principle-based study," Physica B, p. 416322, 2024.

[277]   S. Grimme, "Semiempirical GGA-type density functional constructed with a long-range dispersion correction," J. Comput. Chem., vol. 27, no. 15, pp. 1787-1799, 2006.

[278]   J. Henry et al., "Structural and optical properties of SnS nanoparticles and electron-beam-evaporated SnS thin films," J. Exp. Nanosci., vol. 10, no. 2, pp. 78-85, 2015.

[279]   R. Nandee et al., "Band gap formation of 2D material in graphene: Future prospect and challenges," Results Eng., vol. 15, p. 100474, 2022.

[280]   B. Liu, W.-S. Su, and B.-R. Wu, "A first-principles study of electronic and optical properties of the tetragonal phase of monolayer ZnS modulated by biaxial strain," RSC Adv., vol. 12, no. 10, pp. 6166-6173, 2022.

[281]   M. S. Halati et al., "Electronic and optical properties of ZnSe by theoretical simulation TB-mBJ associated to analysis techniques XPS, REELS and PLS," Appl. Surf. Sci., vol. 566, p. 150690, 2021.

[282] C. Lu, Y. Zhang, L. Zhang, and Q. Yin, "Preparation and photoelectrochemical properties of SnS/SnSe and SnSe/SnS bilayer structures fabricated via electrodeposition," Appl. Surf. Sci., vol. 484, pp. 560-567, 2019.

[283] H. Choi et al., "Tuning the electronic band structure and optoelectrical characteristics of ALD-grown Zn (O, S) buffer layers for SnS solar cells," Optik, vol. 228, p. 165921, 2021.

[284] J. Xu and Y. Yang, "Study on the performances of SnS heterojunctions by numerical analysis," Energy Convers. Manage., vol. 78, pp. 260-265, 2014.

[285] P. R. Parmar et al., "A first principle study of structural and optoelectronic properties of monolayer PdPtX4 (X=Se, Te)," Interactions, vol. 245, no. 1, pp. 1-12, 2024

[286] M. Zhao et al., "Interlayer coupling in anisotropic/isotropic van der Waals heterostructures of ReS2 and MoS2 monolayers," Nano Res., vol. 9, pp. 3772-3780, 2016.

[287] A. Jain and A. J. H. McGaughey, "Strongly anisotropic in-plane thermal transport in single-layer black phosphorene," Sci. Rep., vol. 5, no. 1, p. 8501, 2015.

[288] H. S. Ra, S. H. Lee, S. J. Jeong, S. Cho, and J. S. Lee, "Advances in heterostructures for optoelectronic devices: Materials, properties, conduction mechanisms, device applications," Small Methods, vol. 8, no. 2, p. 2300245, 2024.

LIST OF PUBLICATIONS

Papers Published in SCI/SCIE Indexed International Journal

1. Ashish Raturi, Poornima Mittal and Sudhanshu Choudhary, "Effect of metal doping on visible light absorption and optical properties of lithium niobate (LiNbO33) crystal: a first-principles calculation", **Bulletin of Materials Science**, vol. 44, pp. 237, 2021. (**IF: 1.9, Springer**).

2. Ashish Raturi, Poornima Mittal and Sudhanshu Choudhary, "Electronic and optical properties of lithium niobate (LiNbO3) under tensile and compressive strain for optoelectronic applications: Insights from DFT-computations", **Materials Science in Semiconductor Processing**, vol. 144, pp. 106606, 2022. (**IF: 4.2, Elsevier**).

3. Ashish Raturi, Poornima Mittal and Sudhanshu Choudhary, "Tuning the electronic and optical properties of SrTiO3 for optoelectronic and photocatalytic applications by plasmonic-metal doping: a DFT-computation", **Optical and Quantum Electronics**, vol. 54, pp. 1-19, 2022. (**IF: 3.3, Springer**).

4. Ashish Raturi, Poornima Mittal and Sudhanshu Choudhary, "Strain engineering for tuning the electronic and optical properties of lithium niobate for optoelectronic applications," **Solid State Communications**, vol. 361, pp. 115074, 2023. (**IF: 2.1, Elsevier**).

5. Ashish Raturi, Poornima Mittal and Sudhanshu Choudhary, "Density Functional Characterization of Electronic and Optical Properties of Strontium Titanate Under Doping and Strain for Optoelectronic Applications," **IEEE Transactions on Nanotechnology**, vol. 22, pp. 481-489, 2023. (**IF: 2.4, IEEE**).

6. Ashish Raturi, Poornima Mittal and Sudhanshu Choudhary, "Strain tunability of the properties of Fe- doped lithium niobate for optoelectronic applications: Theoretical insights," **Main Group Chemistry**, vol. 23, pp. 31-40, 2024. (**IF: 1.3, IOS Press**).

7. Ashish Raturi, Poornima Mittal and Sudhanshu Choudhary, "Enhanced absorption in SnS/SnSe, SnS/ZnS, and SnS/ZnSe vdW heterostructures for optoelectronic applications: DFT insights," **Physica Scripta**, vol. 99, pp.125508, 2024. (**IF: 2.6, IOP**).

8. Ashish Raturi, Poornima Mittal and Sudhanshu Choudhary, "Engineering the electronic and optical properties of perovskite nanomaterials for optoelectronic applications: A review," **Materials Science in Semiconductor Processing**, vol. 203, pp. 110250, 2026. (**IF: 4.6, Elsevier**).

Paper Under-Process in SCI/SCIE International International Journal

1. Ashish Raturi, Poornima Mittal and Sudhanshu Choudhary, "Strain-induced modulation of optical properties of SnS, SnSe, ZnS, and ZnSe monolayers for optoelectronic applications."

Papers Published in Scopus Indexed International Conference

1. Ashish Raturi, Poornima Mittal and Sudhanshu Choudhary, "Analysis of Electronic and Optical Properties of Pristine LiNbO3 Using First-Principle Calculations", *International Conference on Electrical and Electronics Engineering (ICE3-2020),* organized by MMMUT, Gorakhpur, UP, India, 14-15 Feb, 2020, pp. 601-605 (**Published by IEEE, Scopus Indexed**).

2. Ashish Raturi, Poornima Mittal and Sudhanshu Choudhary, "Effect of Rare Earth Metal (Lanthanum) Doping on Optical and Electronic Properties of Lithium Niobate (LiNbO3): DFT Insights", *3rd International Conference on Functional Materials,* Manufacturing and Performances (ICFMMP-2022), organized by Division of Research and Development, Lovely Professional University, Punjab, India, 29-30 July, 2022, pp. 1. (**Published by AIP, Scopus Indexed**).

Effect of metal doping on visible light absorption and optical properties of lithium niobate (LiNbO₃) crystal: a first-principles calculation

ASHISH RATURI[1], **POORNIMA MITTAL**[1],* and **SUDHANSHU CHOUDHARY**[2]

[1]Department of Electronics and Communication Engineering, Delhi Technological University, Delhi 110042, India
[2]Department of Electronics and Communication Engineering, National Institute of Technology, Kurukshetra 136119, India
*Author for correspondence (poornimamittal@dtu.ac.in)

Abstract. Electronic and optical properties of pristine and metal-doped lithium niobate crystals are investigated by using first-principles DFT calculations. The results on optical properties suggest that there is a shift in the absorption edge towards visible region (red-shift) for metal-doped structures, in comparison with the pristine lithium niobite. A series of metals are used for doping and it is found that the absorption edge is shifted significantly to the visible region for the dopants; gold (Au), silver (Ag), aluminium (Al) and copper (Cu) due to surface plasma resonance. However, for other metal dopants like iron (Fe), manganese (Mn), molybdenum (Mo) and nickel (Ni), the absorption is slightly improved in the visible region and red-shift is observed. The bandgap of all the doped structures is found to be reduced, this might be proven advantageous for photovoltaic applications, which requires high optical absorption in the visible region. The dielectric constant and refractive index of the pristine and doped structures are also calculated and it is observed that the absorption trend is in accordance with dielectric constant. The optical absorption is enhanced in the visible region due to doping of selected metals (M = Au, Ag, Al, Cu, Fe, Mn, Mo and Ni) making M-lithium niobite a promising material for optoelectronic- and photonic-based applications.

Keywords. Absorption; dielectric function; density function theory; doping; lithium niobate (liNbo₃); optoelectronic.

1. Introduction

In 1963, geologist Gustav Rose discovered the mineral CaTiO₃ (calcium titanate) in the mountains of Ural. The mineral was named as perovskite to award the gratitude to Lev Perovski, a distinguished mineralogist from Russia [1]. Any compound having formula ABC₃ is named as perovskite, where B ion surrounds the C ions. Numerous varieties of electric properties and solid-state behaviours including: insulating, semiconducting, metallic and superconducting are comprehended in the perovskite materials [2]. Therefore, these compounds are very fascinating for investigations and are applied to a large variety of applications. They also exhibit a variety of optical, magnetic and electronic properties. Most of the elements of the periodic table are found stable in the perovskite structure [3]. Studies of these compounds are of great interest owing to their wide applicability in the photochromic, image storage, electrochromic, filtering, switching and surface acoustic wave signal processing devices [4,5]. Likewise, they have a virtuous impact on numerous optoelectronic-, bio-sensing-, photo-electrolysis-based applications [6]. In recent years, a

huge interest has developed in the studies of perovskite materials and investigating their properties for the photonic and optoelectronic applications. It is due to their adjustable optical and electrical properties, that too with mechanical flexibility [7,8]. Furthermore, their high-absorption coefficient, low diffusion length, excellent charge transportation and low non-radioactive emission exceed their utilization for photovoltaic- and optoelectronic-based devices [9–11].

Lithium niobate (LiNbO₃) is a notable member of the perovskite family. It exists in the ferroelectric state and liable for potential use in the electro-optical and optical systems due to its extraordinary piezoelectric, electro-optical, photovoltaic, photo elastic and nonlinear optical properties [12–14]. The study of LiNbO₃ is interesting for the researchers due to its unique properties that are mainly determined by its defect structure and composition. Its optical characteristics can be influenced by the significant amount of impurity, which can replace Li/Nb ion and can occupy the octahedral void in the crystal [15]. In the past, LiNbO₃ has attracted the attention of the researchers and manufacturers for optoelectronics-based applications. Javid
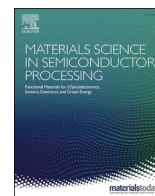
Electronic and optical properties of lithium niobate (**LiNbO₃**) under tensile and compressive strain for optoelectronic applications: Insights from DFT-computations

Ashish Raturi [a], Poornima Mittal [a,*], Sudhanshu Choudhary [b]

[a] *Department of Electronics and Communication Engineering, Delhi Technological University Delhi, India*
[b] *Department of Electronics and Communication Engineering, National Institute of Technology Kurukshetra, India*

A B S T R A C T

The electronic and optical properties of metal-doped (gold, silver, aluminum, and copper) lithium niobite are examined by employing density functional theory-based calculations. The metal-doped lithium niobates are applied with the varying tensile and compressive strain of intensity 10% and 20%. The results indicate that the bandgap is significantly narrowed down for all the metal-doped structures and this narrow downing of bandgap increase with the application of strain. The undoped lithium niobate shows absorption only in the UV region of the optical spectrum. For all the metal dopants the absorption is significantly improved in the visible region of optical spectrum, which is desired for optoelectronic and photovoltaic-based applications. In all the metal dopants, specifically, for the dopants silver and gold, due to superior properties, a widespread visible absorption is found. Further, the application of varying strain on doped lithium niobate results in red-shift, and the absorption peaks are shifted to lower energies. On application of the tensile and compressive strain of 20%, the value of the absorption coefficient is remarkably improved in the visible region. The other optical parameters like dielectric constant and refractive index are also calculated to understand the optical behavior. The improved visible absorption in the lithium niobite due to the application of strain may find several potential applications in the field of optoelectronic and photovoltaic applications.

1. Introduction

Perovskites are the compound of structure ABO₃, discovered in the Ural Mountains by Russian mineralogists. In the compound ABO₃, A represents alkali earth metal, B is a member of the family of transition metal ions and O represents the oxygen atom [1–3]. In the present scenario, researching eco-friendly lead-free materials has come out as a fascinating research objective among researchers. In lead-free materials, niobite-based materials are found to be engrossing and emerged as a promising material for optoelectronic applications. Perovskites captured a large interest of the research fraternity for their several applications in optoelectronic and photovoltaic [4]. These compounds exhibit metallic, semiconducting, and insulating behavior, which make them attractive for research and support their applicability for various applications [5, 6]. Perovskites structures can be formed by elements of different sizes and charges. Perovskites exhibit flexible composition and form stable structure with most of the elements of the periodic table [7].

Additionally, various properties of the perovskites can be modified by substitution of A and/or B ion. In the widely available perovskite structures, lithium niobate (LiNbO₃), widely known as LN, is an alkaline perovskite, which grabbed the huge attention of researchers due to its versatile properties [8]. LN is a man-made material and was fabricated in bell laboratory through the well-known czochralski process [9]. It is generally found in two phases termed as room temperature and low-temperature phase. In the room temperature phase, LN exhibits hexagonal or rhombohedral geometry. The LN is largely used in a variety of applications due to its versatile pyrometric, photocatalytic, electro-optic, piezoelectric, and nonlinear optical properties [10–12].

In recent decades, LiNbO₃ has gained the extensive attention of researchers owing to its excellent optoelectronic properties. The LN is a large bandgap perovskite having the value of bandgap of 3.54 eV at ambient temperature [13]. Owing to its large bandgap the optical absorption of LN is entirely limited only in the ultra-violate range of the optical spectrum (300–400 nm) [14]. Most of the non-zero peaks of the

---

* Corresponding author.
E-mail addresses: ashish.raturi121@gmail.com (A. Raturi), poornimamittal@dtu.ac.in (P. Mittal), sudhanshu@nitkkr.ac.in (S. Choudhary).

Tuning the electronic and optical properties of SrTiO$_3$ for optoelectronic and photocatalytic applications by plasmonic-metal doping: a DFT-computation

Ashish Raturi[1] · Poornima Mittal[1] · Sudhanshu Choudhary[2]

Abstract

In this work, first-principles calculations based on density functional theory are presented to explore the effect of plasmonic-metal doping on structural, electronic, and optical properties of Strontium Titanate (SrTiO$_3$). All the computations are performed on the ATK-VNL package with generalised-gradient approximation. The pristine SrTiO$_3$ is a wide band gap material and its absorption is limited to the ultra-violate region only. Therefore, its absorption can be extended towards the visible region, by reducing the band gap through doping with plasmonic-metals Ag, Al, Au, and Cu. The computed results reveal that the absorption for all the plasmonic-metal doped SrTiO$_3$ is completely shifted towards the visible region, resulting in widely known red-shift phenomena. This high absorption in the visible region makes doped-SrTiO$_3$ a potential candidate for optoelectronic applications. The dielectric constant and refractive index of the pristine and doped structures are also calculated and it is found that the absorption trend closely follows the dielectric constant. Furthermore, the evaluation of photocatalytic properties is also explored in the doped structures. Plasmonic-metal doping improves photocatalytic performance for all the dopants except Al. The doping with plasmonic-metals Ag, Al, Au, and Cu improves the optical properties (visible light absorption) and photocatalytic properties of pristine SrTiO$_3$, which opens a new prospect for potential applications in the field of optoelectronics.
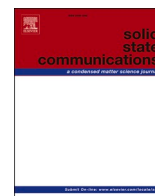
✉ Poornima Mittal
  poornimamittal@dtu.ac.in

  Ashish Raturi
  ashish.raturi121@gmail.com

  Sudhanshu Choudhary
  sudhanshu@nitkkr.ac.in

[1] Department of Electronics and Communication Engineering, Delhi Technological University, Delhi, India

[2] Department of Electronics and Communication Engineering, National Institute of Technology Kurukshetra, Kurukshetra, India

🖄 Springer

Strain engineering for tuning the electronic and optical properties of lithium niobate for optoelectronic applications

Ashish Raturi [a], Poornima Mittal [a,*], Sudhanshu Choudhary [b]

[a] Department of Electronics and Communication Engineering, Delhi Technological University Delhi, India
[b] Department of Electronics and Communication Engineering, National Institute of Technology Kurukshetra, India

ARTICLE INFO

ABSTRACT

In this paper, the first-principles calculations are presented to examine the effect of strain on the electronic and optical properties of Lithium niobate ($LiNbO_3$). Recent advancements in the use of strain engineering for tuning the properties of the materials advocate investigating the effect of strain on the properties of $LiNbO_3$. In this work, the influence of the strain of varying intensities of 10% and 20% (tensile and compressive) is investigated on the electronic and optical response of $LiNbO_3$. The $LiNbO_3$ is a wide bandgap material with a bandgap of 3.56 eV, which can be narrowed down by the application of strain. On the application of a tensile strain of 10%, the bandgap is reduced to 2.54 eV, which is further reduced to 1.71 eV for the tensile strain of 20%. The optical absorption which was in the ultra-violate region for unstrained structure is significantly shifted in the visible region for the applied tensile strain of 10% and 20% (Redshift). For the compressive strain, the bandgap is increased and the absorption is found more in the UV region (Blueshift). The high absorption in the visible region due to the application of tensile strain makes the strained $LiNbO_3$ a potential candidate for optoelectronic applications.

1. Introduction

Multifunctional materials have always gained the attention of researchers because of their considerable technological, scientific, and versatile applications [1,2]. Among the wide variety of available multifunctional materials, perovskites have distinguished and extraordinary properties. Due to this, they came up as the potential material for numerous optoelectronic, photovoltaic, and photonics-based applications [3]. The generalized formula to represent any perovskite structure is ABO_3. In the cubical structure of ABO_3 perovskite, A-atom generally occupies the (0,0,0) position, the B-atom occupies the (1/2,1/2,1/2) position, and the oxygen atom is positioned at the face center i.e., at the position (1/2,1/2,0). In the ABO_3 structure, A, and B atoms are the representation of the cation of unequal atomic radios. A and B atoms can be from any of the families of metal or semimetal of the periodic table [4,5]. The large value of the absorption coefficient, exceptional charge transportation ability, low losses, and high diffusion coefficient claims the suitability of the perovskites for optoelectronics, and photovoltaic-based device applications [6]. These materials are widely accepted in the fabrication of light-emitting diodes, photodetectors, lasers, and waveguides. In the wide availability of perovskites, lithium

niobite ($LiNbO_3$), widely known as LN, is a ferroelectric oxide with prodigious significance in the field of photonics and optoelectronics-based applications. Owing to its astounding and extraordinary piezoelectric, electronic, pyroelectric, and optical properties, $LiNbO_3$ is an obligatory material for a variety of optoelectronic and photonics-based applications. $LiNbO_3$ is first synthesized in Bell Laboratory, by the czochralski process and is certainly considered a human-made artificial material [7].

The $LiNbO_3$ compound is comprised of NbO_6 octahedra having shared corners, building an asymmetric structure. Though the geometry of the $LiNbO_3$ corresponds to the perovskite structure ABO_3, however, $LiNbO_3$ has octahedra that are distorted and are surrounded by six oxygen ions [8]. Unlike, in ABO_3 perovskites the A and B ions form a perfect cubical structure with oxygen ions [9,10]. The exceptional property of $LiNbO_3$ is that its structure is constituted of two different ions having different charge values. This structural property of $LiNbO_3$ opens up the scope of regulating the optical properties by various techniques like doping, substitution, strain, and heterostructure [11–14]. Tunable optical, electronic, and, structural properties of $LiNbO_3$ make it a material of large interest in the diversified field of multifunctional materials. The properties of $LiNbO_3$ were extensively

Density Functional Characterization of Electronic and Optical Properties of Strontium Titanate Under Doping and Strain for Optoelectronic Applications

Ashish Raturi, Poornima Mittal ⓘ, *Senior Member, IEEE*, and Sudhanshu Choudhary ⓘ

Abstract—**We perform first-principles calculations, to investigate the effect of doping of metal dopants (silver, gold, aluminum, and copper) on the electronic, structural, and optical properties of strontium titanate $SrTiO_3$. We further explore the impact of varying strains (compressive and tensile) on the optical and electronic properties of pristine and doped $SrTiO_3$. Our results suggest that the undoped $SrTiO_3$ exhibit a wide bandgap of 2.94 eV with high optical absorption only in the ultraviolet (UV) region. On doping the $SrTiO_3$ by metal dopants, the bandgap is significantly narrowed and most of the absorption peaks are found to shift towards the lower energies (red-shift). Subsequently, the absorption is enhanced in the visible region (∼380 to 800 nm) of the optical spectrum. The decrease in the bandgap is highest for the dopant Cu. Further, on the application of the biaxial strain (tensile and compressive) on the doped-$SrTiO_3$, the optical absorption is enhanced in the visible region, particularly for the high compressive strain of 20%. The calculated refractive index and dielectric function for all the structures of $SrTiO_3$ are found to follow the trend of absorption. The enhanced absorption in the desired visible region through doping and strain may find prospective applications in the fabrication of photovoltaic, optoelectronic, and solar devices.**

Index Terms—**Absorption, strain, optical, doping, Perovskite.**

I. INTRODUCTION

PEROVSKITE material is comprised of many compounds, which came into existence after the discovery of the mineral calcium titanate ($CaTiO_3$) in Russia in 1939 by Gustav Rose [1], [2]. Rose investigated its composition and named it after the renowned Russian mineralogist Lev Perovski [3]. Ideal perovskite exhibits the P-nma space group with cubical geometry. The fundamental formula of perovskite is ABO_3, where site A and site B are cations with site A larger than site B [4], [5]. The exceptional ability of perovskites to form complex structures by utilizing any element of the periodic table makes them favorable for the investigation of existing properties and promising for tuning them for the desired properties. The perovskites have tremendous structural and compositional diversity, which allows
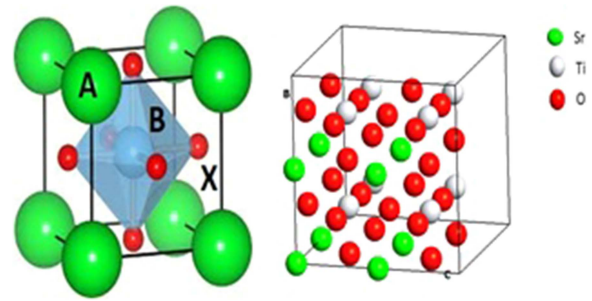
Fig. 1. (a) Perovskite structure (b) $SrTiO_3$ crystal.

the structured synthesis of materials from perovskites by chemical and/or structural modification [6], [7], [8]. In the studies of optoelectronic devices, K Wu et al. [9] designed and fabricated a polycrystalline silicon light-emitting device and found visible light absorption in the range from 400 nm to 900 nm.

Among a wide volume of perovskites, Strontium titanate ($SrTiO_3$), widely known as STO is an interesting complex oxide having B site occupied by Ti [10], [11], [12]. STO has wide applicability in the fabrication of nano-electronic devices due to its exceptional and unique ferroelectric, and optical properties [10], [12], [13]. STO has usages in the fabrication of LED, optical switches, waveguides, memory cells, and gas sensors [14]. The experimentally reported bandgap of STO is 3.25 eV, which attributes the transitions of oxygen states (2p) to titanium states (3d) [15]. The stable stoichiometry with the simple cubic structure of STO attracts the attention of researchers, which has perspective applications in the various fields of optoelectronics and microelectronics [3], [10], [13], [15]. Fig. 1 illustrates the structural geometry of perovskite and STO. The STO is the most ascribed material for optoelectronic and solar applications and has extensively attracted the attention of researchers in recent years [10], [12], [14], [15]. It exhibits a significantly large dielectric constant value and behaves as paraelectric material in bulk form. In the low-temperature state, STO exhibits a growing ferroelectric state and prohibits long-range ferroelectric formation. Owing to the wide intrinsic bandgap, despite having so many tremendous properties, the applicability of STO is restricted and the optical and photovoltaic effectiveness of the STO is severely delimited [16], [17]. The wide bandgap of STO (>3 eV) results in the absorption in the UV region of the sunlight only, which is a small segment of the (∼5%) available spectrum

Strain tunability of the properties of Fe-doped lithium niobate for optoelectronic applications: Theoretical insights

Ashish Raturi[a], Poornima Mittal[a,*] and Sudhanshu Choudhary[b]

[a]*Department of Electronics and Communication Engineering, Delhi Technological University, New Delhi, India*
[b]*Department of Electronics and Communication Engineering, National Institute of Technology, Kurukshetra, India*

Abstract. This work elucidates the impact of strain on the optical and electronic properties of Fe-doped lithium niobate using density functional theory. The Fe-doped lithium niobate is applied with the tensile and compressive strain (10% and 20%) and optical properties are analyzed. Lithium niobate, a large bandgap material (bandgap 3.56 eV), has absorption limited to the UV region of the optical spectrum only. For the Fe-doped lithium niobate, the bandgap is 1.38 eV, with low absorption in the visible region. The computed results show that the tensile and compressive strains have significantly narrowed down the bandgap of Fe-doped lithium niobate in compression to the unstrained structures. The decrease in the bandgap is largest for the tensile strain of 20% among all the applied strains. Further, visible light absorption is also improved due to the application of strain. The improvement in visible light absorption is highest for the tensile strain of 20%, with absorption completely shifted in the desired visible region. The improved visible absorption due to the applied strain makes Fe-doped lithium niobate a potential candidate for optoelectronics and solar applications.

Keywords: Dielectric, perovskites, optoelectronics, absorption

1. Introduction

Perovskites have high absorption, excellent charge transport capability, low optical absorption losses, and extraordinary diffusion coefficient [1]. These properties of widely used perovskites make them appropriate for optoelectronics-based applications [1, 2]. These materials are extensively accepted in the optoelectronics industry for the fabrication of LED, photodetectors, and optical waveguides [2–4]. Among the available perovskite structures, lithium niobate is an oxide with ferroelectric properties and showed significant importance in the production of photonic and optoelectronic-based devices [6]. Lithium niobate (LiNbO3 widely known as LN) is a widely used dielectric oxide that can be grown using common pulling techniques [5, 6]. It exhibits stable chemical and physical properties and is abundant in raw materials. LN has exceptional piezoelectric, pyroelectric, nonlinear optical, and electro-optic properties, making it a versatile material for nonlinear optical and photonic devices [7–10]. It is often referred to as the "silicon of nonlinear optics" or "silicon of photonics". The extraordinary piezoelectric

---

*Corresponding author: Poornima Mittal, Department of Electronics and Communication Engineering, Delhi Technological University, New Delhi, 110042, India. E-mail: poornimamittal@dtu.ac.in.

Physica Scripta

PAPER

Enhanced absorption in SnS/SnSe, SnS/ZnS, and SnS/ZnSe vdW heterostructures for optoelectronic applications: DFT insights

Ashish Raturi[1], Poornima Mittal[1,]* and Sudhanshu Choudhary[2]

[1] Delhi Technological University, Delhi, India
[2] SEECS- University of North Dakota, Grand Forks, United States of America
* Author to whom any correspondence should be addressed.

E-mail: ashish.raturi121@gmail.com, poornimamittal@dtu.ac.in and sudhanshu.choudhary@und.edu

Abstract

The electronic and optical properties of monolayers of tin monochalcogenides and zinc monochalcogenides are elucidated by utilizing density functional theory. The calculated results indicate that the monolayers of tin monochalcogenides (SnS and SnSe) have low bandgap and significant absorption in some segments of the visible region (~400 nm to ~500 nm). However, the monolayers of zinc monochalcogenides (ZnS and ZnSe) have wide bandgap and negligible absorption in the visible region, which limits their optical performance. Despite low absorption in visible region, ZnS and ZnSe exhibit fascinating properties such as wide band gap, cheapness, low toxicity, earth abundance, structural stability, and high refractive index. To identify the combined potential of zinc and tin, the van der Waals heterostructures SnS/SnSe, SnS/ZnS, and SnS/ZnSe are formed, and their optical and electronic properties are calculated. The calculated results illustrate that the formed heterostructures exhibit bandgap lowering and enhanced visible light absorption. The optical absorption is entirely shifted towards the visible region due to the formation of heterostructure (redshift). The enhanced visible light absorption and narrowed bandgap of the formed heterostructures make them a potential candidate for the fabrication of optoelectronic devices and solar cells.

1. Introduction

In recent years, the remarkable optical, electronic, and structural properties of layered two-dimensional materials, widely known as 2D materials attracted the attention of researchers for their usability in optoelectronic and photovoltaic applications [1–3]. After the breakthrough of the successful fabrication of the monolayer of graphene in 2014, 2D materials gained the immense attention of researchers in the domain of nanoelectronics [4, 5]. This came into being due to the exceptional and distinctive optoelectronic properties of two-dimensional materials [6, 7]. 2D materials like germane, silene, tin monochalcogenides, zinc monochalcogenides, and transition metal chalcogenides (TMD) have been widely utilized in recent times for the fabrication of optoelectronics and photovoltaic devices [8]. With the increasing need for material applications, the functional constraints of single-layer materials cannot fulfill the intensified and diverse demand of the industry [9, 10]. Additionally, the layered materials exhibit functionalities such as magnetic properties, conductivity, photocatalytic and semi-conductivity [11]. Due to these reasons, researchers extensively attempted to focus on modulating the properties of layered materials to cater to the growing demands of the industry [12]. In the past years, the pathway of modulating the electronic, optical, magnetic, mechanical, and chemical properties of 2D materials without altering their composition has been identified as a new aspect of the design of novel functional materials [13]. Over the last few years, researchers have performed several theoretical and experimental studies to tune the properties of layered two-dimensional materials by utilizing techniques like the application of external strain and application of external electric field, doping, and stacking the two-dimensional materials to form layered structures [14]. Among all the above techniques for altering the properties of 2D materials for optoelectronics applications, another field of coupling 2D materials to fabricate
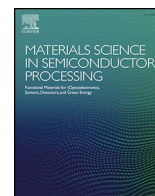
Review

Engineering the electronic and optical properties of perovskite nanomaterials for optoelectronic applications: A review

Ashish Raturi [a], Poornima Mittal [a],[*] , Sudhanshu Choudhary [b]

[a] *Department of Electronics and Communication Engineering, Delhi Technological University, Delhi, India*
[b] *SEECS-University of North Dakota, Grand, Forks, ND, USA*

ARTICLE INFO

ABSTRACT

Over the past few decades, the exceptional electronic and optical properties of perovskite have attracted the attention of researchers for material applications. Over the past few years, several studies have been conducted by researchers to investigate the structural, optical, and electronic properties of perovskites. The utilization of perovskites in the fabrication of optoelectronic devices is beneficial, resulting in high photoelectric conversion efficiency, improved quantum efficiency, flexibility, and numerous other advantages over conventional semiconductors. This review highlights the evaluation of the perovskites and advancements in their structural, electronic, and optical properties for various applications. The review elaborates various methodologies for tuning the electronic and optical properties of perovskites for various optoelectronic, photovoltaic, and solar applications. It has been found from the literature that various techniques are available for tuning the properties of the materials. Among all the available techniques, the focus of the review is on tuning the optoelectronic properties of perovskite by applying doping, strain, and layering. The latest progress on the calculation of various electronic and optical properties of perovskites using density functional theory is also discussed in detail. The review also includes the shortcomings of LDA/GGA in predicting bandgap and optical properties and highlights the enhancements observed from LDA and GGA to HSE. The outlook of the potential of perovskite-based materials in the fabrication of optoelectronic, photovoltaic, and solar devices has also been discussed. The review concludes that tuning the properties of perovskite by applying doping, strain, and layering can help researchers to identify novel materials for a variety of applications.

1. Introduction

The last few decades played a vital role in the evolution of nanotechnology and flourished it to a large extent. Nowadays, many types of research are being carried out by researchers in the field of nanotechnology. The advancement in the field of nanotechnology in the past few decades is mainly concentrated on developing the crystal of nanomaterial, synthesis and characterization, and further augmentation in the size and shape of the synthesized nanomaterial at the nanoscale for desired characteristics [1,9,10]. In the field of material science, the word nano is taken from the Greek word nanos or the Latin word nanus. The meaning of nanos or nanus is dwarf, which is a mixture of chemistry, physics, solid state, and material science [2]. The study of nanomaterials involves the study of physics, chemistry, and its derived field, material science, and solid state [3]. Nanoscience study also involves the understanding of the arrangement of atoms in the materials and the

synthesis of novel materials along with characterization [4,13]. The advancement in the field of nanotechnology gained the attention of the industry and is responsible for the widespread use of nanotechnology in the manufacturing of optoelectronic devices [5–7]. Nanotechnology evolved with the vast applications in engineering, environment, electronics, and defense [8,14]. Even though a lot of advancement has happened in nanotechnology in the past few years, there is still scope in identifying new novel nanomaterials for various applications. By seeing the ongoing development in the field of nanotechnology, it can be anticipated that in the upcoming years, the devices based on nanotechnology will control the living environment and communication [11, 12,14]. This increases the interest of the research community to elaborate on the topics of nanotechnology in detail.

The fundamental element of nanotechnology is the nanomaterial, used for the fabrication of various electronic and optical devices for potential applications [15–17]. The materials having crystals with a size

---

Analysis of Electronic and Optical Properties of Pristine LiNbO₃ Using First-Principle Calculations

Ashish Raturi and Poornima Mittal

Department of Electronics and Communication Engineering, Delhi Technological University Delhi, India

ashish.raturi121@gmail.com and poornimamittal@dtu.ac.in

Abstract—The electronic-optical properties of lithium niobate (LiNbO₃) are identified by utilizing the first principle calculation based on density function theory (DFT) executed in the ATK VNL. The exchange-correlation function of generalized-gradient-approximation utilizing density functional theory is performed to extract the electronic-optical properties of lithium niobate crystal. The lattice constants and unit cell volume are investigated from the optimized structure, that is in good resemblance with the previous reported research work. Electronic band structure and density of states (DOS) exhibited its semiconducting nature demonstrating a bandgap equal to 3.56eV. Optical properties, like absorption coefficient, complex dielectric function, refractive index is also determined and matched to the practical values. The optical spectrum of LiNbO₃ is analyzed and found appropriate for applications such as optical waveguides, piezoelectric sensors, and optical modulators.

Keywords—Density of state, Density function theory, lithium niobate, exchange-correlation, generalized gradient approximation.

I. INTRODUCTION

Due to the exceptional optoelectronic properties of Perovskite materials, the researcher has shown interest in the study of such types of materials. The perovskite materials are having chemical ABX3, where A atom and B atom represents the position of the cation. X atom represents the position of anions. The A-site cation is the large site and B-site cation is the smaller site, which allows forming [BX6]4− octahedral to corner-share if represented in a 3D framework [1]. Perovskite materials show many interesting properties such as ferroelectricity, superconductivity, and magnetization. Moreover, these materials exhibit high absorption coefficients, a high value of the mobility of, a high value of the diffusion lengths of the minority carrier, and the low value of the trap densities. These certain remarkable properties are responsible for making all the perovskites an excellent choice of semiconducting material for the solar cells-based application. Besides these properties, perovskites materials also hold properties of interest for optical sources i.e. intense photoluminescence, thin light emission, tunable binding energy, and balanced charge carrier mobility [2-3]. Among the variety of available perovskite materials lithium niobate (LiNbO₃) is a ferroelectric oxide. The LiNbO₃ gained the significant interest of the researchers in the past few years due to due to unique incorporation of piezoelectric properties and electronic-optical characteristics in LiNbO₃ [4-5]. Over the most recent few decades, the computational technique has shown a noteworthy significance in the research of the field material sciences. Various variety of properties of the materials like optical, structural and electronic properties may be computed in detail with high accuracy using the computational strategies [6-7]. In recent electronics and photonic devices, the application of thin-film technology is extremely significant and it is possible to be fabricated using a variety of available methodology. LiNbO₃ has significant advantages in the process of thin-film growth due to the crystalline structure [8].

As long as the previous studies of the attempts on the study of LiNbO₃ material are considered, Inbar and Cohen analyzed and explained the presence of the ferroelectric behavior in LiNbO₃ [9]. The crystal structure and physical characteristics of lithium niobate have been presented by the Weis and Gaylord [10]. The experimental study of the optical characteristics of LiNbO₃ has been presented by Dhar and Mansingh [11]. Kochi has made the correlation of theoretical energy-loss of an electron with the reported experimental values. The correlation established was based on the X-ray photoemission spectrum. Several studies on first-principle calculations, using available computational methods have been performed in previous studies to discover and analyze the properties of the lithium niobate crystal [12-13-14]. Optical and electronic characteristics of LiNbO₃ material are estimated by using Local-density-approximation (LDA) and Generalized-gradient approximation (GGA) functions. But theoretical estimated results are still far apart from the reported experimental data [15].

In this article, we conduct first-principles calculations for LiNbO₃ crystal using Density function theory (DFT) on the ATK-VNL software package [16]. We study the Density of States of lithium niobate (LiNbO₃) crystal and calculate the direct bandgap. Along with the electronic-optical properties of crystal of lithium niobate have been analyzed, using the Meta-generalized gradient approximation (MGGA) method, which takes the exchange-correlation into account. The optical spectrum of the crystal has been studied and the optical properties like absorption coefficient, reflectivity and refractive index are reported in the article.

II. COMPUTATIONAL PARAMETERS

To investigate the electronic- optical characteristics of the LiNbO₃, first-principle method density functional theory is being utilized. All the simulations are carried out by Atomistix Tool Kit by utilizing the density functional theory based on pseudo-potential. In DFT calculations for the computation of density of states and band structure, the generalized-gradient-approximation utilizing Perdew-Burke-Ernzerhofer has been utilized for describing the exchange-correlation function [19-20]. The Monkhorst-Pack method is utilized for sampling. Brillouin-zone sampling with sampling points 9x9x1 is used. 150 Ry Energy cut-off is utilized for performing the calculations [21].

Effect of Rare Earth Metal (Lanthanum) Doping on Optical and Electronic Properties of Lithium Niobate (LiNbO$_3$): DFT Insights

Ashish Raturi[1, a)], Poornima Mittal[1, b)] and Sudhanshu Choudhary[2, c)]

[1]*Department of Electronics and Communication Engineering, Delhi Technological University, Delhi, India*
[2]*Department of Electronics and Communication Engineering, National Institute of Technology, Kurukshetra, India*

[a)] Corresponding author: ashish.raturi121@gmail.com
[b)] poornimamittal@dtu.ac.in
[c)] sudhanshu@nitkkr.ac.in

Abstract. In this paper the optical properties and electronic strcuture of rare earth metal lanthanum doped lithium niobite are presented. All the computations are achieved on ATK VNL tool kit by utilizing density functional theory. In electronic properties the computations are performed to calculate the band gap of the lanthanum doped lithium niobite is calculated. For optical properties, dielectric function, refractive index and reflection coefficient are calculated. The undoped lithium niobite is a wide band material with absorption in UV region. It is illustrated from the results obtained that value the band gap is decreased significantly due to doping with lanthanum, which shifts the absorption in the higher wavelengths region in compression of the undoped crystal of lithium niobite. The shift in the absorption towards higher wavelengths is identified as red shift. The decrease in the band gap and relocation of the absorption in the higher wavelengths opens up an opportunity of utilizing the lanthanum doped lithium niobite for the optoelectronic applications.

Keywords: optoelectronic, DFT, perovskites, absorption

INTRODUCTION

In the wide availability of the materials, materials with ferroelectric properties have proved them promising for the optoelectronic applications [1-3]. Theses material are fascinating for the various applications due to their extraordinary and versatile piezoelectric and optical properties. Lithium niobite widely known as LN, is a famous and widely acceptable material for the optoelectronic applications, because of its excellent optoelectronic properties [4-5]. LiNbO$_3$ is a perovskite with the formula ABO3, in which A is the lithium atom an B is niobite atom. LN is usually found in hexagonal crystal structure and researched by the several scholars due to its wide optical, piezoelectric, photonic and electro-optic properties. It has wide acceptability in the manufacturing of optical storage, modulators, wave guides and acoustic devices [6].

The LiNbO$_3$ is a wide band gap material with a band gap of value 3.56 eV [7]. Due to wide band gap the non-zero values of the absorption for the undoped LiNbO$_3$ is available in the ultra-violate (UV) region only. As the UV region is only 5% of the sun light, a significantly high proportion of the sun light remains unutilized [8]. This is not favourable for the utilization of the materials for photonic and optoelectronic applications. In order to shift the absorption in the visible wavelength, several techniques like doping, strain, heterostructure are utilized by the researchers past to tune the optoelectronic properties of various materials and structures [9-10]. Among all, doing proved itself and accepted by the researchers as an efficient way to optimize the optoelectronic properties of the various structures and materials [11-13]. In past, researchers calculated and examined the various optical properties of pure and doped LiNbO$_3$ for various photonic and optoelectronics applications. Hossain et al. calculated the optoelectronic properties of LiNbO$_3$ and reported the band gap and other optical parameters of LiNbO$_3$ using DFT

DELHI TECHNOLOGICAL UNIVERSITY
(Formerly Delhi College of Engineering)
Shahbad Daulatpur, Main Bawana Road, Delhi-42

PLAGIARISM VERIFICATION

Title of the Thesis: Investigating Electronic, Optical and Structural Properties of Materials/Structures for Optoelectronic and Photocatalytic

Total Pages: 200

Name of the Scholar: Ashish Raturi (Roll No. 2K19/PHDEC/15)

Supervisor (s)

(1) Prof. Poornima Mittal, Department of Electronics and Communication Engineering, Delhi Technological University, Delhi, India

(2) Dr. Sudhansu Choudhary, School of Electrical Engineering and Computer Science (SEECS), University of North Dakota (UND), USA

Department: Electronics and Communication Engineering

This is to report that the above thesis was scanned for similarity detection. Process and outcome is given below:

Software used: Turnitn, Similarity Index: 5%, Total Word Count: 60,882 Words

Date: 27-03-2025

ASHISH RATURI

(Roll No. 2K19/PHDEC/15)

Dr. SUDHANSHU CHOUDHARY
Joint Supervisor
School of EE and CS
University of North Dakota, USA

Prof. POORNIMA MITTAL
Supervisor
Department of ECE
DTU, Delhi, India

Ashish Raturi

Thesis_Ashish.pdf

Delhi Technological University

Document Details

Submission ID

trn:oid:::27535:88166117

Submission Date

Mar 27, 2025, 5:02 PM GMT+5:30

Download Date

Mar 27, 2025, 5:11 PM GMT+5:30

File Name

Thesis_Ashish.pdf

File Size

2.8 MB

200 Pages

60,882 Words

335,023 Characters

5% Overall Similarity

The combined total of all matches, including overlapping sources, for each database.

Filtered from the Report

- ▸ Bibliography
- ▸ Quoted Text
- ▸ Cited Text
- ▸ Small Matches (less than 14 words)

Exclusions

- ▸ 10 Excluded Sources

Match Groups

105 Not Cited or Quoted 5%
Matches with neither in-text citation nor quotation marks

0 Missing Quotations 0%
Matches that are still very similar to source material

0 Missing Citation 0%
Matches that have quotation marks, but no in-text citation

0 Cited and Quoted 0%
Matches with in-text citation present, but no quotation marks

Top Sources

1% 🌐 Internet sources

1% 📖 Publications

3% 👤 Submitted works (Student Papers)

Integrity Flags

1 Integrity Flag for Review

🚩 **Replaced Characters**
52 suspect characters on 24 pages
Letters are swapped with similar characters from another alphabet.

Our system's algorithms look deeply at a document for any inconsistencies that would set it apart from a normal submission. If we notice something strange, we flag it for you to review.

A Flag is not necessarily an indicator of a problem. However, we'd recommend you focus your attention there for further review.

Match Groups

105 Not Cited or Quoted 5%
Matches with neither in-text citation nor quotation marks

0 Missing Quotations 0%
Matches that are still very similar to source material

0 Missing Citation 0%
Matches that have quotation marks, but no in-text citation

0 Cited and Quoted 0%
Matches with in-text citation present, but no quotation marks

Top Sources

1% 🌐 Internet sources

1% 📖 Publications

3% 👤 Submitted works (Student Papers)

Top Sources

The sources with the highest number of matches within the submission. Overlapping sources will not be displayed.

1	Submitted works	
National Institute of Technology, Kurukshetra on 2020-06-19		2%

2	Internet	
www.jctjournals.com		<1%

3	Internet	
ebin.pub		<1%

4	Internet	
dspace.lboro.ac.uk		<1%

5	Internet	
dspace.dtu.ac.in:8080		<1%

6	Submitted works	
Delhi Technological University on 2020-05-27		<1%

7	Internet	
mdpi-res.com		<1%

8	Internet	
pubs.rsc.org		<1%

9	Publication	
neha kapila, Hitesh Sharma, Vivek mahajan, Rajendra Adhikari. "Effect of biaxial s...		<1%

10	Publication	
Fan Yang, Shiwei Lin, Liang Yang, Jianjun Liao, Yongjun Chen, Cai-Zhuang Wang. "...		<1%

11 Submitted works

Birla Institute of Technology and Science Pilani on 2021-01-28   <1%

12 Publication

Lili Widarti Zainuddin, Mohd Hazrie Samat, Fadhlul Wafi Badrudin, Oskar Hasdino...   <1%

13 Internet

idr.aus.ac.in   <1%

14 Internet

www.researchgate.net   <1%

15 Submitted works

Jaypee University of Information Technology on 2018-03-16   <1%

16 Publication

Ashish Raturi, Poornima Mittal, Sudhanshu Choudhary. "Strain tunability of the p...   <1%

17 Submitted works

University of Zakho on 2023-10-04   <1%

18 Publication

Zhaojun Tang, Xiaohua Li, Yuying Zhao, Leiming Chen, Fengzhu Ren, Shengquan ...   <1%

19 Publication

"Springer Handbook of Electronic and Photonic Materials", Springer Science and ...   <1%

20 Publication

Nguyen, Bach T.. "Computational Studies of Enzyme Catalyzed Decarboxylation M...   <1%

21 Publication

L.W. Zainuddin, M.H. Samat, N.H.M. Zaki, F.W. Badrudin, N. Osman, A.M.M Jani, O....   <1%

22 Internet

corescholar.libraries.wright.edu   <1%

23 Internet

ujcontent.uj.ac.za   <1%

24 Submitted works

National Institute of Technology, Kurukshetra on 2020-06-23   <1%

25 Publication

Rahil Kochar, Sudhanshu Choudhary. " MoS /Phosphorene Heterostructure for O... <1%

26 Publication

Rivera Mora, Ernesto. "Essays on Information Exchange", The University of Arizon... <1%

27 Publication

Y. Selmani, H. Labrim, S. Ziti, L. Bahmad. "Electronic, optical and thermoelectric pr... <1%

28 Internet

arxiv.org <1%

29 Internet

lib.buet.ac.bd:8080 <1%

30 Publication

Azeem Ghulam Nabi, Maryam Hayat, Shahbaz Khan, Salman Nazir et al. "Photoca... <1%

31 Submitted works

Higher Education Commission Pakistan on 2019-10-07 <1%

32 Publication

Jayanta Kumar Kar, Ruma Rano, Saurabh Chaudhury. " Optoelectronic Properties ... <1%

33 Publication

Lhouceine Moulaoui, Abdelhafid Najim, Marouane Archi, Mohamed Al-Hattab et a... <1%

34 Publication

Rasidul Islam, Kong Liu, Zhijie Wang, Soyaeb Hasan, Yulin Wu, Shengchun Qu, Zh... <1%

35 Submitted works

Universiti Teknologi MARA on 2018-06-04 <1%

36 Submitted works

University of Rwanda on 2024-12-04 <1%

37 Internet

mrs.org <1%

38 Internet

www.science.gov <1%

ASHISH RATURI

https://www.linkedin.com/in/ashish-raturi-04bba3327/
ashish.raturi121@gmail.com

Experience Overview

A strong background in VLSI design and a proven track record in scientific research. Experienced in government and corporate environments with enthusiasm for leveraging technical skills to deliver impactful results.

Scientist
Government of India — Leading initiatives in software and web development in public sector projects.

September 2016 to Present
(9 years, 2 months)

- Led software & web development, API integration, IoT, and VLSI projects.
- Managed IT systems, training, and examination platforms for government agencies.
- Executed automation and monitoring initiatives using IoT technology.
- Developed scalable web platforms for enhancing government operations.
- Contributed to VLSI simulation projects, supporting research and innovation.
- Streamlined and modernized examination systems, enhancing transparency and efficiency.

Assistant Manager
Aditya Birla Group

July 2016 to September 2016
(2 months)

- Contributed to technical management and operational improvements.
- Supported cross-departmental collaboration for project success.
- Assisted in streamlining processes for enhanced efficiency.

Skills

- Project coordination
- Analytical skills
- Technical documentation
- Leadership
- Public engagement

Education

M.Tech in VLSI Design
Institution: NIT Kurukshetra

Year of Graduation: 2016

- Research publication in SCI-indexed Journal
- Hands on experience with ATK VNL
- Hands-on experience with FPGA boards
- Proficient in using Xilinx Vivado/ISE tools

B.Tech in Electronics & Communication
Institution: Graphic Era University

Year of Graduation: 2013

- Academic scholarship recipient
- Qualified GATE with good rank
- Proficient in MATLAB for simulation and data analysis
- Multisim, PSpice, AutoCAD, and Keil for circuit design
- Microcontroller programming